Controlled Trapping in Laser Wakefield Accelerators

Hansson, Martin

2016

Document Version:
Förlagets slutgiltiga version

Controlled Trapping in Laser Wakefield Accelerators

Martin Hansson

Doctoral Dissertation
2016

Lund University

Controlled Trapping in
Laser Wakefield Accelerators

Printed in Sweden by Media-Tryck, Lund, 2016

Division of Atomic Physics
Department of Physics
Faculty of Engineering, LTH
Lund University
P.O. Box 118
221 00 Lund
Sweden
www.atomic.physics.lu.se

ISSN 0281-2762
Lund Reports on Atomic Physics, LRAP 516 (2016)
ISBN 978-91-7623-806-6 (print)
ISBN 978-91-7623-807-3 (pdf)

Abstract

Experimental studies of laser-driven acceleration of charged particles, in particular electrons and protons, are described in this dissertation. Tightly focused femtosecond laser pulses with intensities exceeding $10^{18}\,\mathrm{W/cm^2}$ were used to accelerate charged particles to high energies over distances of a few millimeters. Although the transverse fields of such laser pulses are sufficient to directly accelerate electrons to relativistic energies, the direction of the fields changes rapidly. Thus, direct acceleration using the electromagnetic fields of such laser pulses is not suitable for generating beams of charged particles. Instead, the directed electric fields that are generated in the interaction between the laser pulses and plasmas can be used to accelerate particles to high energies.

The laser wakefield acceleration technique is based on the excitation of a plasma wave by a laser pulse that propagates through an underdense plasma. Electric fields on the order of 100 MV/mm, directed along the optical axis, are associated with the plasma wave with a wavelength on the order of 10 μm. A short pulse of electrons, with a length of only a fraction of the plasma wavelength, may be accelerated in the wave to several hundreds of megaelectron-volts. Simultaneously, strong electric fields act as a radially restoring force on the electrons undergoing acceleration, which therefore perform transverse oscillations. This leads to the generation of X-rays with energies on the order of a kiloelectron-volt in a beam directed along the optical axis, with an opening angle on the order of a hundred milliradians.

The physical processes involved in laser wakefield acceleration are highly nonlinear, and the resulting beams of electrons are therefore sensitive to small fluctuations in the properties of the laser pulses, and to density variations in the plasma. Controlling the amount of charge in the electron bunches and the energy of the electrons is crucial to increase the possibility of using laser wakefield accelerators in practical applications. One step towards stable generation of beams of electrons using laser wakefield accelerators is to control the location at which the electrons are trapped in the accelerator and, at the same time, control the number of trapped electrons. This dissertation describes studies on different methods of controlled trapping of electrons in laser wakefields. The methods described include trapping triggered by plasma density modulations, trapping of tightly bound electrons released by photoionization, and trapping triggered by heating of electrons in the beat wave generated by two colliding laser pulses.

The properties of the electron beams generated using different trapping techniques are then compared. The experimental studies showed that both the amount of charge and the electron energy distribution can be controlled using any one of these methods,

and that shot-to-shot fluctuations in charge and peak electron energy below 10 % and 5 %, respectively, can be achieved.

The target-normal sheath acceleration technique for proton and positive ion acceleration is based on the interaction between a focused femtosecond laser pulse and a micrometer-thick metallic foil. The surface of the foil is irradiated by a laser pulse at an intensity above $10^{19}\,\mathrm{W/cm^2}$. Electrons heated in the interaction between the laser pulse and the plasma formed on the foil surface are driven through the foil and exit from the rear side. The resulting charge separation leads to an electric sheath field of the order of TV/m, which is quasi-static on the time scale of a few picoseconds. Contaminants, typically water molecules and hydrocarbon compounds, on the rear surface of foil, are ionized in the strong field and the positive ions, predominantly protons because of their high charge-to-mass ratio, are accelerated toward the electrons.

Studies on spatial shaping of the proton beams generated in this process are described in the Appendix of this dissertation. The shape of the sheath field on the rear side of the foil was manipulated by modifying the profile of the laser pulse irradiating the foil. The divergence of the beam of protons generated using this technique could be decreased by splitting the laser beam, and irradiating the foil using two spatially separated pulses.

Populärvetenskaplig sammanfattning

Partikelacceleratorer används för att skapa strålar av elektriskt laddade partiklar med hög rörelseenergi och har många tillämpningar inom flera områden av forskning och medicin samt inom industrin. Till de moderna acceleratoranläggningarna som används för att studera beståndsdelarna av materia hör CERNs Large Hadron Collider i Schweiz med en omkrets på hela 27 kilometer. Elektronacceleratorer används vid så kallade synkrotronljusanläggningar, såsom DESY i Hamburg, Tyskland, och MAX IV-laboratoriet i Lund, för generering av intensiv röntgenstrålning. Vid dessa anläggningar används den genererade röntgenstrålningen för en mängd olika tillämpningar inom bland annat materialforskning, medicinsk forskning och kärnfysik. Inom medicinsk forskning och behandling används partikelacceleratorer i ett flertal tillämpningar. Inom medicin används strålar av accelererade elektroner till exempel för att generera röntgenstrålning som kan användas för att avbilda olika kroppsdelar och för att bestråla vissa former av cancer. Strålar av accelererade elektroner, och i sällsynta fall även protoner, kan också användas direkt för strålbehandling av cancertumörer.

I den enklaste formen av partikelaccelerator används en elektrisk spänning för att skapa ett elektriskt fält mellan två metalliska poler. Laddade partiklar som placeras i detta fält kommer då röra sig mot en av polerna och samtidigt öka sin rörelseenergi. Acceleratortekniken har under åren utvecklats och de acceleratorer som byggs idag är betydligt mer avancerade men bygger fortfarande på elektriska fält begränsade av metalliska strukturer. Detta leder till en fundamental begränsning i styrkan på det accelererande elektriska fältet. När fältet blir för starkt splittras nämligen atomerna på de metalliska ytorna som då delas upp i positivt laddade joner och negativt laddade elektroner. Dessa laddade partiklar accelereras av de elektriska fälten och skapar gnistor som både minskar styrkan på det elektriska fälten men också skadar utrustningen. Den vanligaste metoden, som används vid samtliga moderna acceleratoranläggningar, för att minska detta problem går ut på att applicera de elektriska fälten med hög frekvens, så kallad radiofrekvens, vilket gör att atomerna är mindre benägna att splittras. Trots detta är den maximala elektriska fältstyrkan begränsad till storleksordningen 100 miljoner volt per meter. Detta kan verka mycket i jämförelse med de elektriska fält man påträffar i vardagen, men för att nå de energier som krävs i dagens moderna acceleratoranläggningar måste partiklarna ändå accelereras över flera hundra meter.

I denna avhandling presenteras experimentella studier av acceleration av laddade

partiklar med hjälp av elektriska fält som skapas i plasmor istället för i metalliska strukturer. Ett plasma kan beskrivas som en blandning av positivt laddade joner och fria negativt laddade elektroner. Beståndsdelarna i ett plasma kan inte vidare splittras av de elektriska fälten, och betydligt högre accelererande fält kan därmed bibehållas i ett plasma. De accelererande fälten som används i de experiment som presenteras i denna avhandling är ca 1000 gånger starkare än de fält som kan hanteras vid konventionella acceleratoranläggningar. Fälten skapas i dessa experiment med hjälp av laserpulser som är endast några tiotals femtosekunder långa (en femtosekund motsvarar 0,000 000 000 000 001 sekunder) och fokuserade till en diameter av några fåtal mikrometer. De elektroner i plasmat som kommer i närheten av laserpulsens framfart trycks då undan medan de tyngre positiva jonerna förblir nästan oberörda. Detta skapar en separation av positiv och negativ elektrisk laddning vilket motsvaras av starka elektriska fält.

Metoden för att accelerera elektroner till höga energier kallas på engelska *laser wakefield acceleration*, och som namnet antyder går det ut på att utnyttja de starka fält som skapas i kölvågen bakom en laserpuls. I detta fall låter man laserpulsen färdas genom ett tunt plasma, skapat genom jonisation av en gas av till exempel väte. Laserpulsen trycker undan elektronerna i plasmat likt en plog. Bakom laserpulsen återstår endast de positivt laddade jonerna som verkar attraherande på de omgärdande elektronerna som börjar röra sig tillbaka till sin ursprungsposition. Det bildas på så vis en *bubbla*, tömd på elektroner, som följer laserpulsen i sin framfart med en hastighet mycket nära ljusets hastighet i vakuum.

Merparten av experimenten som beskrivs i denna avhandling handlar om att på ett kontrollerat sätt placera ett litet antal elektroner inne i bubblan bakom laserpulsen. Då dessa elektroner placeras i den bakre delen av bubblan kommer de att utsättas för en kraft riktad mot centrum av bubblan på grund av den positiva laddningen. Dessa elektroner kommer snabbt upp i hastigheter nära ljusets, men eftersom bubblan hela tiden rör sig framåt med en nästan lika hög hastighet kan denna kraft verka på elektronerna över flera millimeter trots att bubblan endast är ca 10 mikrometer lång. På så vis kan en stor mängd energi överföras från laserpulsen, via plasmat, till rörelseenergi hos elektronerna.

I experimenten studeras olika metoder för att fånga elektroner i bubblan bakom en laserpuls. Ett sätt att göra detta går ut på att modulera plasmats densitet, så att laserpulsen först går genom ett tätare plasma för att sedan nå ett tunnare plasma. I denna övergång ändrar bubblan sin form och växer bakåt. Elektroner som befinner sig precis vid bubblans bakkant faller då in i den växande bubblan och påbörjar sin acceleration framåt mot högre rörelseenergi.

I andra experiment fångas elektroner genom att en liten mängd gas av ett atomslag med högre atomnummer blandas in i den annars rena vätgasen. Elektronerna i de inre skalen är då fortfarande bundna till atomkärnan då partikeln nås av laserpulsens topp. Styrkan på laserpulsens topp är dock så hög att även elektronerna från de inre skalen kan frigöras. Eftersom framkanten av laserpulsen redan trängt undan en stor mängd elektroner och på så vis skapat ett utrymme tomt från elektroner vid laserpulsens topp, kommer de elektroner som frisläpps där lättare att kunna fångas i bubblan.

Även protoner och andra positivt laddade joner kan accelereras till höga energier med hjälp av laserpulser och plasmor. En stor skillnad ligger dock i massan för protonen som är ca 2000 gånger högre än massan för elektronen. Detta medför en betydligt större tröghet vid acceleration av protoner och de fält som används för att accelerera

protoner måste därför vara över längre tid. En metod för att accelerera protoner med hjälp av plasmor går ut på att belysa framsidan av en metallfolie med en tjocklek av endast några få mikrometer med en kort och intensiv laserpuls. Plasmat som bildas på framsidan av folien är för tätt för att laserpulsen ska kunna gå igenom, men elektronerna i plasmat hettas upp av de elektromagnetiska fälten från laserpulsen och en ström av elektroner riktad mot baksidan av folien skapas. Elektronerna når baksidan med en hög hastighet och försvinner ut från folien som då blir positivt elektriskt laddad och ett starkt elektriskt fält bildas riktat mot elektronerna. Detta fält är tillräckligt starkt för att jonisera partiklar, av bland annat vattenmolekyler och kolväten, som finns på foliens baksida. De positiva jonerna och då framför allt vätejonerna från vattnet, d.v.s. protoner, accelereras sedan i de starka elektriska fälten och färdas ifrån folien med hög rörelseenergi i fältens riktning.

I de experiment som beskrivs i appendix till denna avhandling studeras hur fälten på foliens baksida kan formas genom att styra storleken av laserpulsen som belyser framsidan. Genom att belysa en större yta så minskar styrkan av fälten på baksidan men medför också att en de accelererade partiklarna sprids över en mindre vinkel. I experimenten skapas även två åtskilda laserpulser som används för att belysa folien. Då de två pulserna träffar folien samtidigt, men vertikalt separerade med några få mikrometer, formas fälten på foliens baksida så att partikelstrålen får en mindre utbredning vertikalt än horisontellt.

List of Publications

This dissertation is based on Papers I-X. Papers XI-XII belong to the work described in the Appendix. The papers are appended at the end of the dissertation.

I **Enhanced stability of laser wakefield acceleration using dielectric capillary tubes**
M. Hansson, L. Senje, A. Persson, O. Lundh, C.-G. Wahlström, F. G. Desforges, J. Ju, T. L. Audet, B. Cros, S. Dobosz Dufrénoy, and P. Monot.
Physical Review Special Topics - Accelerators and Beams **17**, 031303 (2014).

II **Reproducibility of electron beams from laser wakefield acceleration in capillary tubes**
F. G. Desforges, M. Hansson, J. Ju, L. Senje, T. L. Audet, S. Dobosz Dufrénoy, A. Persson, O. Lundh, C.-G. Wahlström, and B. Cros.
Nuclear Instruments and Methods in Physics Research A **740**, 54 (2014).

III **Supersonic jets of hydrogen and helium for laser wakefield acceleration**
K. Svensson, M. Hansson, F. Wojda, L. Senje, M. Burza, B. Aurand, G. Genoud, A. Persson, C.-G. Wahlström, and O. Lundh.
Physical Review Accelerators and Beams **19**, 051301 (2016).

IV **Laser wakefield acceleration using wire produced double density ramps**
M. Burza, A. Gonoskov, K. Svensson, F. Wojda, A. Persson, M. Hansson, G. Genoud, M. Marklund, C.-G. Wahlström and O. Lundh.
Physical Review Special Topics - Accelerators and Beams **16**, 011301 (2013).

V **Down-ramp injection and independently controlled acceleration of electrons in a tailored laser wakefield accelerator**
M. Hansson, B. Aurand, X. Davoine, H. Ekerfelt, K. Svensson, A. Persson, C.-G. Wahlström, and O. Lundh.
Physical Review Special Topics - Accelerators and Beams **18**, 071303 (2015).

VI **Dynamics of ionization-induced electron injection in the high density regime of laser wakefield acceleration**
F. G. Desforges, B. S. Paradkar, M. Hansson, J. Ju, L. Senje, T. L. Audet, A. Persson, S. Dobosz Dufrénoy, O. Lundh, G. Maynard, P. Monot, J.-L. Vay, C.-G. Wahlström, and B. Cros.
Physics of Plasmas **21**, 120703 (2014).

VII **Investigation of ionization-induced electron injection in a wakefield driven by laser inside a gas cell**
T. L. Audet, M. Hansson, P. Lee, F. G. Desforges, G. Maynard, S. Dobosz Dufrénoy, R. Lehe, J.-L. Vay, B. Aurand, A. Persson, I. Gallardo González, A. Maitrallain, P. Monot, C.-G. Wahlström, O. Lundh, and B. Cros.
Physics of Plasmas **23**, 023110 (2016).

VIII **Localization of ionization-induced trapping in a laser wakefield accelerator using a density down-ramp**
M. Hansson, T. L. Audet, H. Ekerfelt, B. Aurand, I. Gallardo González, F. G. Desforges, X. Davoine, A. Maitrallain, S. Reymond, P. Monot, A. Persson, S. Dobosz Dufrénoy, C.-G. Wahlström, B. Cros, and O. Lundh.
Plasma Physics and Controlled Fusion **58**, 055009 (2016).

IX **Shock assisted ionization injection in laser-plasma accelerators**
C. Thaury, E. Guillaume, A. Lifschitz, K. Ta Phuoc, M. Hansson, G. Grittani, J. Gautier, J.-P. Goddet, A. Tafzi, O. Lundh, and V. Malka.
Scientific Reports **5**, 16310 (2015).

X **Injection of electrons by colliding laser pulses in a laser wakefield accelerator**
M. Hansson, B. Aurand, H. Ekerfelt, A. Persson, and O. Lundh.
In press: *Nuclear Instruments and Methods in Physics Research A (2016) DOI:10.1016/j.nima.2016.02.070.*

XI **A setup for studies of laser-driven proton acceleration at the Lund Laser Centre**
B. Aurand, M. Hansson, L. Senje, K. Svensson, A. Persson, D. Neely, O. Lundh, and C.-G. Wahlström.
Laser and Particle Beams **33**, 59 (2015).

XII **Manipulation of the spatial distribution of laser-accelerated proton beams by varying the laser intensity distribution**
B. Aurand, L. Senje, K. Svensson, M. Hansson, A. Higginson, A. Gonoskov, M. Marklund, A. Persson, O. Lundh, D. Neely, P. McKenna, and C.-G. Wahlström.
Physics of Plasmas **23**, 023113 (2016).

Symbols

$\mathbf{A}$	Electromagnetic vector potential
$\mathbf{a} = \frac{e\mathbf{A}}{m_e c}$	Normalized electromagnetic vector potential
$\mathbf{B}$	Magnetic flux density
$c = 299792458\,\mathrm{m/s}$	Speed of light in vacuum
$e \approx 1.602 \times 10^{-19}\,\mathrm{C}$	Elementary charge
$1\,\mathrm{eV} = 1.602 \times 10^{-19}\,\mathrm{J}$	Electronvolt – unit of energy
E	Energy
$\mathbf{E}$	Electric field
$\mathbf{F}$	Force
f	Frequency
$h \approx 6.625 \times 10^{-34}\,\mathrm{Js}$	Planck's constant
I	Intensity or irradiance
i	Imaginary unit
$\mathbf{j}$	Current density
$\mathbf{k}$	Wave vector
$k_B = 1.381 \times 10^{-23}\,\mathrm{J/K}$	The Boltzmann constant
$m_e \approx 9.109 \times 10^{-31}\,\mathrm{kg}$	Electron rest mass
n_e	Electron number density
P	Power
$\mathbf{p}$	Momentum
p	Pressure
q	Charge
$\mathbf{r}$	Position

s	Optical path length
T	Temperature
t	Time
$\mathbf{v}$	Velocity
v_g	Group velocity
v_p	Phase velocity
γ	Lorentz factor
$\epsilon_0 = 8.854 \times 10^{-12}\,\mathrm{F/m}$	Vacuum permittivity
η	Refractive index
λ	Wavelength
λ_{De}	Electron Debye length
λ_p	Plasma wavelength
$\mu_0 = 4\pi \times 10^{-7}\,\mathrm{N/A^2}$	Vacuum permeability
ρ	Charge density
τ	Pulse duration
Φ	Electrostatic potential
$\phi = \frac{e}{m_e c^2}\Phi$	Normalized electrostatic potential
φ	Phase
$\omega = 2\pi f$	Angular frequency

Contents

Papers

Chapter 1

Introduction

The work presented in this dissertation involves the interaction between femtosecond laser pulses and matter at peak intensities above 10^{18} W/cm^2. The laser pulses are so intense that the electromagnetic fields even far away from the peak are sufficiently strong to ionize the atoms in the target material. Thus, the main part of a pulse interacts with the electrons and ions of the plasma that is formed. The physics of laser-plasma interactions is a broad area of research, and includes several branches, such as harmonic generation, X-ray generation, and inertial confinement fusion. The focus in this dissertation, however, is on the physics involved in the acceleration of particles to high energies in the interaction between laser pulses and plasmas. In the oscillating fields of a laser pulse with intensities of 10^{18} W/cm^2 and above, free electrons oscillate at speeds approaching the speed of light in vacuum, c, and with corresponding kinetic energies on the order of the energy associated with the electron rest mass, $E = m_e c^2$. Thus, the motion of these electrons is affected by relativistic effects, and the intensity of such laser pulses is often referred to as *relativistic*. Although the instantaneous kinetic energy of the electrons in the fields of a laser pulse may be high, the direction of the fields changes rapidly. The energy gained by an electron in the electromagnetic fields of a linearly polarized laser pulse, averaged over one oscillation, is zero.

In order to achieve a net energy gain, the fields of a laser pulse must be rectified or transformed into directed, quasi-static fields in the reference frame of the accelerating particles. The collective behavior of a plasma can be utilized to do just that. For electron acceleration, the fields following a short, focused high-power laser pulse propagating in a plasma are used in a scheme called *laser wakefield acceleration* (LWFA). Although they are oscillating, these fields form a fast-moving wave in which electrons with sufficiently high initial energy can be *trapped* and further accelerated.

Due to their large mass, protons and heavier ions remain essentially stationary in the direct interaction with the electromagnetic fields of the laser pulses used in the work presented here. To accelerate such particles, fields that are quasi-static on much longer time scales are needed. In a mechanism called *target-normal sheath acceleration* (TNSA), energy is first transferred from a laser pulse to the electrons in a plasma formed on the surface of a micrometer-thick solid foil. The heated electrons propagate through the foil and exit through the rear, where they set up large-magnitude quasi-static sheath fields. Protons and other positive ions at the rear surface of the foil are

rapidly accelerated in these quasi-static fields.

Particle accelerators have been important historically, and in many cases necessary tools in several areas of research, industry and medicine. In high-energy particle physics, large-scale accelerator facilities provide beams of particles for studies on the fundamental laws of physics at energies far beyond the particle energies achieved using the accelerators described in this dissertation. Beams of particles at more moderate energies are used to probe physical and chemical processes, as well as material properties. In medicine, accelerators are used to provide particle beams that are used, e.g., for radiation therapy and for radioisotope production, as well as for the production of X-rays used for medical imaging.

Beams of high-energy electrons are also used to generate high-brightness X-ray radiation in third-generation synchrotron light sources, such as the newly built MAX IV laboratory in Lund. In such synchrotron light sources, highly relativistic electrons are forced to wiggle transversely by arrays of magnetic fields with alternating direction. As they wiggle, the electrons emit electromagnetic radiation with wavelengths in the X-ray region, and the properties of the generated radiation can be tuned by the properties of the magnetic field array. Beams of relativistic electrons propagating through arrays of alternating magnetic fields are also a fundamental part of free-electron lasers. In this case, modulation in the longitudinal electron density distribution leads to coherent generation of radiation.

Conventional accelerators have proven successful in providing high reproducibility and control of the resulting beams. In these accelerators, charged particles are accelerated in either static or alternating electric fields inside metallic structures. However, the magnitude of the applied electric field is limited by electrical breakdown at the surfaces of the metallic walls. Increasing the magnitude of the electric field above a certain threshold results in sparks due to electrical breakdown which not only destroys the accelerating field, but can also damage the equipment. In modern accelerators, the fields are applied at radio frequencies, which helps increase the breakdown voltage, although it is still limited to about 100 MV/m. The *plasma* accelerators described in this dissertation do not suffer from a such limitation, and accelerating fields at least three orders of magnitude higher can be sustained in a plasma. This implies that the distance needed for acceleration is decreased by the same factor. An electron energy on the order of 100 MeV, achieved by acceleration over 1 mm is typical for the experiments described in this dissertation.

The typical size of the accelerating structure of the plasma accelerators described in this dissertation is also several orders of magnitude smaller than the structures used in conventional accelerators. Furthermore, the physics involved in plasma accelerators is typically of nonlinear nature. These two features have meant that the plasma accelerators developed so far suffer from a lack of reproducibility and control compared to the conventional accelerators. One significant source of fluctuations in the first generation of laser wakefield accelerators is a lack of control of the starting point of acceleration. In the first experiments with this type of accelerator, electrons were injected and *trapped* in the plasma waves by, so-called, self-trapping. This mechanism is extremely difficult to control, and even minor variations in the laser pulse or plasma may lead to large variations in the position at which trapping occurs. This dissertation describes work carried out on alternative mechanisms to trap electrons in the plasma waves, allowing the starting point of acceleration of these electrons to be controlled.

In the following chapter (Chapter 2), the physics of laser wakefield acceleration

of electrons in plasmas is described together with the mechanism of simultaneous generation of X-ray radiation. The methods of investigations used in this dissertation work is presented in Chapter 3. Studies of various methods of controlled trapping of electrons for acceleration in the wakefields is then described in Chapter 4 and summarized in Chapter 5. Finally, the physics of target-normal sheath acceleration of protons and the corresponding studies performed within the scope of this dissertation are presented in the Appendix.

The fundamental concepts of high-power lasers and models of short, intense laser pulses are presented in the next section of this chapter. In later sections, the general properties of plasmas and the models used to describe them are introduced, and fundamental laser-plasma interaction is described.

1.1 High-power lasers

The invention of lasers in 1960 provided researchers with a tool that has been used widely in experimental physics. In a laser, light originating from spontaneous emission is amplified by stimulated emission in a *gain medium* inside an optical resonator. The energy is provided by *pumping* the gain medium to reach population inversion using, for example, excitation by electrical discharges, or optical excitation by flash lamps or other lasers. The resulting laser light is coherent, has well-defined wavelengths, and is bright. Over the years, research on and the development of lasers has constantly improved the characteristics of the light produced and provided increased control over the emitted radiation. Lasers are available for various applications, ranging from continuous-wave lasers with narrow, stabilized spectral bands, to ultrashort (< 6 fs) pulses and peak powers on the order of petawatts (1 PW $= 10^{15}$ W).

At the front end of a high-power pulsed laser system there is typically a laser oscillator in which seed pulses are generated. These seed pulses are further amplified in one or several optical amplification stages. A physical limitation of each amplification stage is determined by laser-induced damage to the gain medium or to other optical components in the stage. By successively expanding the pulses transversely between the amplification stages, such that the intensity is decreased, the pulses can be further amplified and the maximum achievable power can be increased. Although the beams can theoretically be expanded to any arbitrary size, the transverse size of the beams is limited in practice due to difficulties in producing large optical components with sufficient quality at a reasonable cost.

The invention of the *chirped pulse amplification* (CPA) technique [1] reported in 1985 constituted a major leap towards higher pulse power. This technique relies on controlled temporal stretching of short, bandwidth-limited laser pulses from a mode-locked laser oscillator. This allows the pulses to be expanded, not only transversely, but also in the direction of propagation, which further reduces their intensity. The laser pulses can thus be amplified to high energies with small-diameter laser components, before the temporal stretching is finally reversed and the laser pulses are re-compressed to reach very high peak powers.

The CPA technique can be used to produce laser pulses with peak powers up to a few hundred TW (1 TW $= 10^{12}$ W) using so-called table-top laser systems in research laboratories. The technique is also used in large scale laser facilities to produce pulses with peak powers in excess of 1 PW. By focusing such pulses to transverse sizes on

the order of 10 μm, peak intensities ranging from 10^{18} to above 10^{22} W/cm^2 [2] can be achieved. These laser pulses allow researchers to study matter under the influence of extreme electromagnetic fields. The intensities generated by focused high-power femtosecond laser pulses can be compared with the intensity at the surface of the Sun, which is on the order of 10^4 W/cm^2.

Most of the experiments described in this dissertation, were performed using the multi-terawatt laser system at the high-power laser facility at the Lund Laser Centre. This laser system is based on CPA, using titanium-doped sapphire (Ti:Al_2O_3 or Ti:sapphire) as the gain medium in 4 amplification stages after the oscillator. The amplification bandwidth of Ti:sapphire is extraordinarily large, ranging from 650 nm to 1100 nm, peaking around 800 nm [3]. Because of its high damage threshold, together with its large amplification bandwidth, Ti:sapphire has become the standard gain medium in table-top, high-power CPA laser systems. This laser system was used in the experiments to produce pulses with energies up to 1.6 J before re-compression of the pulses. The pulses after final amplification can be re-compressed to a duration below 40 fs (FWHM). With an efficiency of approximately 50 % for beam compression and transport to the target, this yielded peak powers of up to 20 TW at the target. Depending on the choice of focusing optics, peak intensities ranging from 10^{18} W/cm^2 to approximately 5×10^{19} W/cm^2 were achieved. The characteristics and operation of this laser system are described in more detail in Chapter 3. A general description of laser beams and pulses is given below.

The propagation of light is governed by Maxwell's equations,

$$\begin{cases} \nabla \cdot \mathbf{E} &= \frac{1}{\epsilon_0}\rho \\ \nabla \cdot \mathbf{B} &= 0 \\ \nabla \times \mathbf{E} &= -\frac{\partial \mathbf{B}}{\partial t} \\ \nabla \times \mathbf{B} &= \mu_0 \left(\mathbf{j} + \epsilon_0 \frac{\partial \mathbf{E}}{\partial t}\right). \end{cases} \tag{1.1}$$

It can be shown that this system of equations supports solutions in the form of electromagnetic waves. In a linear, non-magnetic material, the most typical example is the linearly polarized monochromatic plane wave with angular frequency ω and wavevector $\mathbf{k}$, [4]

$$\begin{cases} \mathbf{E} &= E_0 \exp\left(i\omega t - \mathbf{k}\cdot\mathbf{r}\right)\hat{\mathbf{e}}_{\perp,\mathbf{1}}\,. \\ \mathbf{B} &= B_0 \exp\left(i\omega t - \mathbf{k}\cdot\mathbf{r}\right)\hat{\mathbf{e}}_{\perp,\mathbf{2}}\,. \end{cases}$$

The unit vectors $\hat{\mathbf{e}}_{\perp,\mathbf{1}}$ and $\hat{\mathbf{e}}_{\perp,\mathbf{2}}$ are perpendicular to each other and both are also perpendicular to $\mathbf{k}$ in order to comply with Eqs 1.1. The magnitude of the wave vector is related to the wavelength and frequency through $|k| = 2\pi/\lambda = \omega\eta/c$, where η is the refractive index of the medium. The intensity of such waves can be expressed as

$$I = \frac{c\eta\epsilon_0}{2}\left|E\right|^2\,.$$

In the interaction with matter, the laser pulses are often more conveniently described in terms of a vector potential, $\mathbf{A}$. The electric and magnetic fields are related to this vector potential through

$$\begin{cases} \mathbf{E} = -\frac{\partial \mathbf{A}}{\partial t} \\ \mathbf{B} = \nabla \times \mathbf{A}\,. \end{cases}$$

The mathematical descriptions of laser-plasma interaction are simplified by normalizing the vector potential according to

$$\mathbf{a} = \frac{e\mathbf{A}}{m_e c}\,.$$

The absolute value of the normalized vector potential can be related to the intensity of a linearly polarized wave through

$$a = \sqrt{\frac{e^2}{2\pi^2\epsilon_0 m_e^2 c^5}\lambda^2 I} \approx 0.85\frac{\lambda}{1\,\mu\mathrm{m}}\sqrt{\frac{I}{10^{18}\,\mathrm{W/cm^2}}}\,. \tag{1.2}$$

It can be shown that the normalized vector potential (approximately) describes the transverse normalized momentum of an electron in a laser field, i.e., $\mathbf{p}_\perp = m_e c\mathbf{a}$. Thus, the transverse motion of the electron becomes relativistic as the amplitude of $\mathbf{a}$ approaches 1.

1.1.1 Femtosecond pulses

For optical pulses of femtosecond duration, the electromagnetic fields cannot be described as monochromatic waves, i.e., waves with a single frequency and wavelength. Instead, such pulses are formed by the superposition of several waves with a broad range of angular frequencies, centered around an angular carrier frequency, ω_0, corresponding to the central wavelength of the optical pulse. The frequency content is revealed by a Fourier transform. For example, a pulse with a complex Gaussian envelope in the temporal domain at a fixed location in space,

$$\mathbf{E}\,(t) = \mathbf{E_0}\cdot\exp\left(-\,(1-\mathrm{i}\kappa)\,\frac{t^2}{2\tau^2}\right)\cdot\exp\left(i\omega_0 t\right)\,,$$

with a pulse duration of $\tau_{\mathrm{FWHM}} = 2\sqrt{\log 2}\tau$ FWHM of the intensity, corresponds to a Gaussian shape also in the spectral domain [4] given by

$$\widetilde{\mathbf{E}}\,(f) = \mathbf{E_0}\frac{\tau}{2\sqrt{\pi}}\exp\left(-\frac{\pi^2\tau^2\,(f-f_0)^2}{1-\mathrm{i}\kappa}\right)\,.$$

The variable κ is called the *chirp parameter*, and results in a time-varying instantaneous frequency. It can be shown that the spectral bandwidth (FWHM), Δf, is related to the pulse duration and chirp parameter through the expression

$$\Delta f = \frac{0.44}{\tau_{\mathrm{FWHM}}}\sqrt{1+\kappa^2}\,. \tag{1.3}$$

In order to generate optical pulses with a duration of a few femtoseconds, the gain medium must support amplification of all frequencies in the optical pulse spectrum.

1.1.2 Laser beams

The light inside and emerging from lasers also has a finite size and divergence (convergence), and cannot be described as plane waves. It is customary to describe ideal

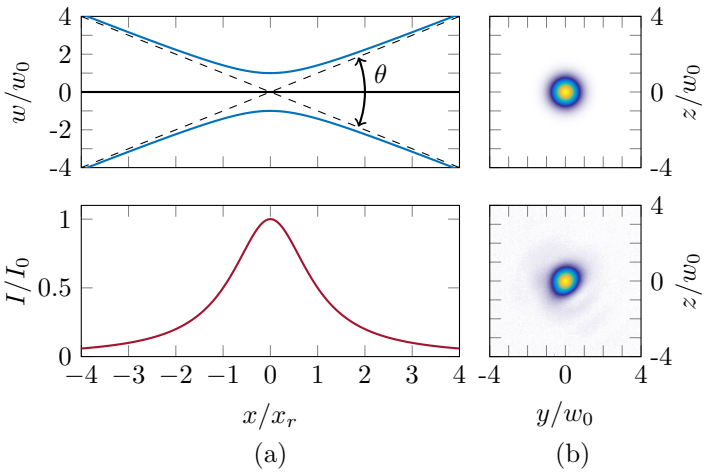

Figure 1.1: (a) The width, $w(x)$ (above) and on-axis intensity, $I(x)$ (below) of a focused Gaussian beam. The intensity peaks sharply at the waist and the asymptotic divergence is θ. (b) The transverse intensity distribution at the waist according to the Gaussian model (above) and for the actual pulse of the Lund multi-terawatt laser (below).

laser light as a Gaussian beam, i.e., a solution to the slowly varying envelope approximation of the Helmholtz equation, which applies to monochromatic electromagnetic waves. In terms of the radial and longitudinal coordinates (r, x), the electric field of a Gaussian beam, polarized in the y-direction, with its waist in the plane $x = 0$, can be expressed as [4]

$$\begin{cases} \mathbf{E}\,(r,x) &= E_0 \frac{w_0}{w(x)} \exp\left(-\frac{r^2}{w(x)^2}\right) \exp\left(-i\left(kx + k\frac{r^2}{2R(z)} - \psi(x)\right)\right)\left(\mathbf{e}_y + \frac{y}{x+ix_0}\mathbf{e}_x\right) \\ w(x) &= w_0\sqrt{1+\left(\frac{x}{x_r}\right)^2} \\ x_r &= \frac{\pi w_0^2}{\lambda} \\ R(x) &= x\left(1+\left(\frac{x}{x_r}\right)^2\right) \\ \psi &= \arctan\left(\frac{x}{x_r}\right). \end{cases} \tag{1.4}$$

In accordance with Maxwell's equations, a similar expression applies to the magnetic component of the wave. In the expressions above (Eqs 1.4) $w(x)$ denotes the radius of the beam at $1/\exp(2)$ of the on-axis intensity, and depends on the distance, x, from the focal plane. The radius at the waist is denoted w_0 and, together with the wavelength λ, determines the Rayleigh length x_r, which is a measure of the beam expansion close to the waist.

The width of a Gaussian beam is shown, as a function of longitudinal position, x, together with the on-axis intensity in Figure 1.1(a). The dashed lines indicate the asymptotic divergence of a Gaussian beam far away from the focal plane, which is approximately $\theta = \frac{4\lambda}{2\pi w_0}$. The intensity peaks sharply at the waist, where the radius is smallest, and is above half the maximum value in a region of length x_r on either side of the peak. The transverse intensity distribution of a Gaussian beam at the waist is illustrated in Figure 1.1(b), together with an acquired image of the focused pulse from the Lund multi-terawatt laser.

In practice, the actual laser beams deviate somewhat from the Gaussian model.

The laser amplifiers are often intentionally designed to provide a transverse beam profile closer to a top-hat profile, to increase the efficiency of each amplification stage. However, after focusing, the central part of the beam can often be approximated by a Gaussian in the close vicinity of the waist, and the model is therefore still useful for describing and understanding the results of experiments. More refined models of the transverse beam distribution and propagation of the beams are based on decomposition into transverse modes, as in the Fourier optics model, for example.

1.1.3 Ionization of atoms

With the development of lasers and the increasing power available for experiments, a series of new regimes of photoionization of atoms has been realized. The original picture of photoionization, occurring when the energy of a single photon, $E_{ph} = hf$, exceeds the binding energy of an electron, must be modified at higher interaction intensities in order to understand multi-photon ionization. According to a perturbational approach to quantum-mechanical calculations, several photons, with a *total* energy exceeding the binding energy, may also be absorbed to release an electron. At low intensity, the rate of ionization due to the absorption of multiple photons is low, but increases as I^n, where n is the number of absorbed photons. The first experimental observations of multi-photon ionization were made using laser intensities on the order of 10^{11} W/cm^2, and showed good agreement with the perturbational model [5, 6]. It was further found experimentally [7] that at even higher intensities ($\sim 10^{13}$ W/cm^2), more photons could be absorbed during the ionization process than were necessary to release an electron from the remaining ion. In this, so-called, above-threshold ionization process the distribution of the energy of the released electrons contains peaks separated by an energy corresponding to one photon, and the experimental findings at these intensities suggest that this process cannot be described by a perturbational model [8].

At the intensities achievable with focused femtosecond terawatt laser pulses, the electric field is so strong that it significantly modifies the atomic binding potential of the electrons. A potential barrier is formed (see Figure 1.2(a)), through which the electron wave packet can tunnel with increased probability as the barrier becomes narrower and weaker. At even higher intensities, the barrier is suppressed below the binding energy of the electron, and the originally bound electron is free to escape from the atom, as shown in Figure 1.2(b). The intensity at which this occurs, and a new species of ion is formed, is called the appearance intensity, I_{app}, and can be approximated by considering a bound electron in a Coulomb potential modified by the electric field of the laser pulse. The potential along the polarization axis, y, can be expressed as,

$$V(y) = -\frac{1}{4\pi\epsilon_0}\frac{Ze^2}{|y|} - eEy\,. \tag{1.5}$$

Here, the electric field, E, of the laser pulse is treated quasi-statically since the electromagnetic oscillations at optical frequencies are slow on an atomic scale. The position of the peak of the barrier, y_b, is found at the stationary point of this function, and can be expressed as

$$y_b = \sqrt{\frac{Ze}{4\pi\epsilon_0 E}}\,.$$

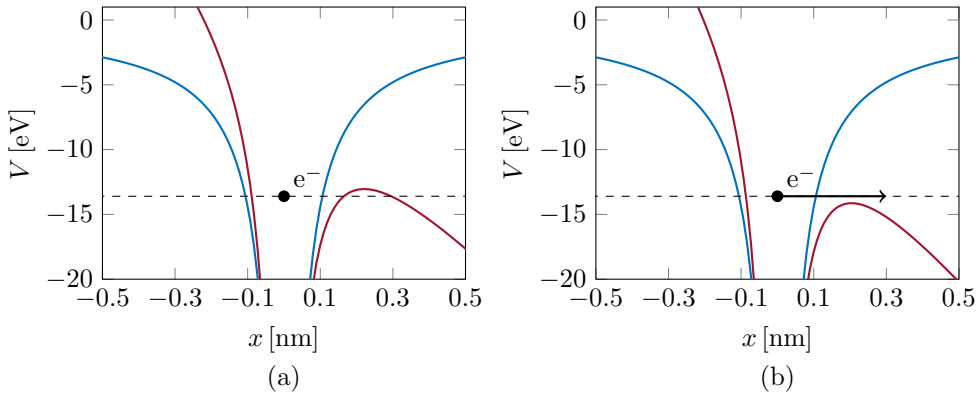

Figure 1.2: Illustration of the over-the-barrier ionization mechanism in hydrogen. The Coulomb potential of the atom (blue) is modified by the instantaneous electric field of the laser pulse to yield a total potential affecting the electron. (a) The probability of ionization increases when the formed potential barrier becomes weak and narrow. (b) For a sufficiently high light intensity, the barrier is suppressed below the binding energy of the electron, which is then free to escape.

Inserting this expression into Eq. 1.5 gives the expression for the potential energy at the peak of the barrier as

$$V_b = -\sqrt{\frac{Ze^3E}{4\pi\epsilon_0}}\,.$$

The electric field and the corresponding intensity required to suppress the barrier below the energy level of the bound electron, $-E_{\text{ion}}$, are then given by

$$E = \frac{E_{\text{ion}}^2 \pi \epsilon_0}{Ze^3} \Rightarrow I_{app} = \frac{c\epsilon_0^3 \pi^2 E_{\text{ion}}^4}{2Z^2 e^6}\,. \tag{1.6}$$

The appearance intensities have been calculated for some selected species of ions relevant for the work on laser wakefield acceleration presented in this dissertation and are given in Table 1.1. Although the calculations were performed using a crude estimate of the shape of the atomic binding potential, the calculated appearance intensities agrees well with the results of experiments and simulations using more advanced models. In the experiments on laser wakefield acceleration presented in the following chapters, the focused laser pulses from the Lund multi-terawatt laser reached intensities on the order of 10^{18} W/cm^2. In fields of this strength, nitrogen will be ionized up to the N^{5+} state, and thus release all but the two most tightly bound electrons. In order to reach higher ionization states, additional focusing of the laser pulse is needed.

1.2 Plasmas

At the laser pulse intensities described in this dissertation, neutral matter is ionized long before and far away from the peak of the pulse. Thus, the peak of the pulse does not interact with neutral atoms or molecules, but with matter in a state that can be described as a mixture of unbound electrons and ions, which constitutes a plasma.

Species	E_{ion} [eV]	I_{app} [W/cm^2]	a
H^+	13.6	1.4×10^{14}	0.008
He^+	24.6	1.5×10^{15}	0.026
He^{2+}	54.4	8.8×10^{15}	0.064
N^+	14.5	1.8×10^{14}	0.009
N^{2+}	29.6	7.7×10^{14}	0.019
N^{3+}	47.4	2.3×10^{15}	0.032
N^{4+}	77.5	9.0×10^{15}	0.065
N^{5+}	97.9	1.5×10^{16}	0.083
N^{6+}	552.1	1.0×10^{19}	2.197
N^{7+}	667.0	1.6×10^{19}	2.750

Table 1.1: Calculated appearance intensities and corresponding normalized vector potentials for some ion species that are relevant to the work presented in this dissertation.

The fundamental features of plasmas are described in this section and various models that can be used to describe plasmas are introduced. The sections below summarize the fundamentals of plasma physics that can be found in textbooks (e.g. [9]), in which more detailed descriptions are given.

1.2.1 Definition

For an ionized gas to be called a plasma, further criteria must be satisfied. It is generally said that a plasma is quasi-neutral, and exhibits collective behavior. It can be shown that a plasma shields out local charge accumulations, through so-called Debye shielding, by rapid rearrangement of the plasma electrons. The typical length scale for this shielding is the electron Debye length, λ_{De}, which can be expressed as,

$$\lambda_{De} = \sqrt{\frac{\epsilon_0 k_B T_e}{e^2 n_e}}\,. \tag{1.7}$$

Thus, the electron Debye length increases with increasing temperature of the electrons, T_e, due to their thermal motion, which tends to lead to them spreading out. The electron Debye length decreases with increasing electron number density, n_e, due to the fact that more electrons are then available for shielding. The condition that a plasma should be quasi-neutral can then be related to the electron Debye length and quasi-neutrality is assumed for plasmas with length scales $l \gg \lambda_{De}$.

Furthermore, Debye shielding requires that a large number of electrons collectively shield a local charge accumulation, which is another condition for an ionized medium to be treated as a plasma. The number of electrons within a sphere of radius λ_{De} is called the plasma parameter, and can be written as

$$N_{De} = \left(\frac{4}{3}\pi\lambda_{De}^3\right) n_e\,. \tag{1.8}$$

For Debye shielding to be effective, this parameter must be large, i.e., $N_{De} \gg 1$.

The criterion that a plasma should exhibit collective effects is related to the typical time scale of collective effects in a plasma. As will be shown in the following chapters, collective effects of particular interest are the plasma oscillations with angular frequency,

$$\omega_{pe} = \sqrt{e^2 n_e/\epsilon_0 m_e}\,. \tag{1.9}$$

This frequency should be compared to the typical time scale for the interactions between particles, i.e., collisions, which tend to destroy the collective behavior of plasma. It can be shown that the condition $\omega_{pe}/\omega_{\text{coll}} \gg 1$ is fulfilled when $N_{De} \gg 1$.

For example, the laser-produced plasmas used for wakefield acceleration of electrons in the experiments presented in this dissertation have a typical electron number density of $n_e = 1 \times 10^{19}$ cm^{-3}. At this density, the plasma frequency is approximately 1.8×10^{14} s^{-1}. The plasma parameter is 100 at a temperature of $k_b T_e = 30$ eV, a temperature which is by far exceeded in the laser-produced plasmas considered in this dissertation. At this temperature, the Debye length is only approximately 13 nm.

1.2.2 Plasma models

The most complete way to model a plasma is, quite obviously, to treat each particle separately, according to the equations of motion, and calculate the contributions to the electric and magnetic fields from each of these particles. This is, of course, an impossible task in practice. The second most complete way of modeling a plasma is to use the so-called kinetic description based on a statistical approach. In this model, the plasma is fully described by a single distribution function for each particle species in phase space and time, $f_s(\mathbf{r}, \mathbf{v}, t)$, such that $f_s(\mathbf{r}, \mathbf{v}, t)\mathrm{d}\mathbf{r}\mathrm{d}\mathbf{v}$ represents the number of particles of species s at time t in the infinitesimal phase space volume $\mathrm{d}\mathbf{r}\mathrm{d}\mathbf{v}$ centered at $(\mathbf{r}, \mathbf{v})$. From the conservation of particles,

$$\frac{\partial f_s}{\partial t} = -\nabla_{6D} \cdot (\mathbf{v} f_s) \,,$$

an equation can be derived that describes the evolution of the phase space distribution function, and which can be expressed as

$$\frac{\partial f_s}{\partial t} + \mathbf{v} \cdot \frac{\partial f_s}{\partial \mathbf{r}} + \frac{q_s}{m_s} (\mathbf{E} + \mathbf{v} \times \mathbf{B}) \cdot \frac{\partial f_s}{\partial \mathbf{v}} = \left(\frac{\partial f_s}{\partial t} \right)_c \,.$$

Here, m_s and q_s are the particle mass and charge. This equation is called the Boltzmann equation and, together with Maxwell's equations, describes self-consistently the evolution of the distribution functions. The term on the right-hand side of this equation is due to collisions. Based on the discussion in the previous section, this term can be neglected for plasmas with large values of the plasma parameter, and the equation is then commonly known as the Vlasov equation,

$$\frac{\partial f_s}{\partial t} + \mathbf{v} \cdot \frac{\partial f_s}{\partial \mathbf{r}} + \frac{q_s}{m_s} (\mathbf{E} + \mathbf{v} \times \mathbf{B}) \cdot \frac{\partial f_s}{\partial \mathbf{v}} = 0 \,. \tag{1.10}$$

The kinetic model can be used in situations where simple models are inadequate. However, the equation is complex, and considerable effort is required to find solutions. The less complex fluid dynamic model can be derived from the Vlasov equation. The quantities in the fluid dynamic model depend only on position and time, and represent averages of the corresponding quantities in the kinetic model over velocity space. The most important fluid quantities are:

$n_s = \int f_s(\mathbf{r}, \mathbf{v}, t)\, d\mathbf{v}$	Number density of species s
$\mathbf{u}_s = \frac{1}{n_s} \int \mathbf{v} f_s(\mathbf{r}, \mathbf{v}, t)\, d\mathbf{v}$	Average fluid velocity
$w_s = \frac{1}{n_s} \int \frac{1}{2} m_s v^2 f_s(\mathbf{r}, \mathbf{v}, t)\, d\mathbf{v}$	Average kinetic energy
$P = \int m_s (\mathbf{v} - \mathbf{u}_s)(\mathbf{v} - \mathbf{u}_s) f_s(\mathbf{r}, \mathbf{v}, t)\, d\mathbf{v}$	Pressure tensor

Equations that describe the evolution of the fluid quantities can be found by taking different moments of the Vlasov equation [10]. Taking the first moment of the Vlasov equation results in the fluid continuity equation

$$\frac{\partial n_s}{\partial t} + \frac{\partial}{\partial \mathbf{r}} \cdot (n_s \mathbf{u}_s) = 0\,. \tag{1.11}$$

In the next step, an equation of momentum is found by taking the second moment of the Vlasov equation,

$$m_s n_s \frac{d\mathbf{u}_s}{dt} = q_s n_s \left(\mathbf{E} + \mathbf{u}_s \times \mathbf{B}\right) - \frac{\partial}{\partial \mathbf{r}} \cdot \mathbf{P}_s\,. \tag{1.12}$$

Here, $\frac{d\mathbf{u}_s}{dt} = \frac{\partial \mathbf{u}_s}{\partial t} + \mathbf{u}_s \cdot \nabla$ represents the full convective derivative.

Clearly, each equation here requires solving also for the next higher moment. This sequence is infinite, and the system of equations is thus not closed. However, the sequence can be truncated at any point by making an assumption for the next higher moment. A common choice is to truncate the sequence by assuming thermal equilibrium. In the interaction between focused femtosecond high-power laser pulses and plasmas, the approximation of a cold plasma is suitable, since in this case the forces due to thermal pressure can be neglected in comparison to the forces due to the fields of the laser pulse. Under this approximation, the equation for the momentum is simplified to the fluid equivalent of the Lorentz force,

$$m_s \frac{d\mathbf{u}_s}{dt} = q_s \left(\mathbf{E} + \mathbf{u}_s \times \mathbf{B}\right)\,. \tag{1.13}$$

In the case of laser wakefield acceleration, the main interaction occurs on time scales on which the ions can be assumed to be stationary due to their high charge-to-mass ratio. Thus, it is customary to treat the ions as a fixed, homogeneous, positively charged background and to consider only the motion of the plasma electrons.

1.3 Laser pulse propagation in plasmas

The fundamental properties of light wave propagation in a plasma can be derived by considering plane electromagnetic waves, i.e., $\mathbf{E} = \mathbf{E}_{\mathbf{k},\omega} \exp\left(i\left(\mathbf{k}\cdot\mathbf{r} - \omega t\right)\right)$ and $\mathbf{B} = \mathbf{B}_{\mathbf{k},\omega} \exp\left(i\left(\mathbf{k}\cdot\mathbf{r} - \omega t\right)\right)$. Maxwell's equations then yield

$$\begin{cases} \mathbf{k} \times \mathbf{E} = \omega \mathbf{B} \\ i\mathbf{k} \times \mathbf{B} = \mu_0 \mathbf{j} - i\omega\mu_0\epsilon_0 \mathbf{E}\,. \end{cases} \tag{1.14}$$

Furthermore, the current density, $\mathbf{j} = -en_e\mathbf{u_e}$, is due to the response of the plasma electrons to the fields, as described by Eq. (1.13). At low light intensities only the linear response is considered, and the second term of the Lorentz force can be neglected. The current density can then be expressed as

$$\mathbf{j} = \frac{in_e e^2}{\omega m_e}\mathbf{E}\,.$$

Inserting this expression into Eq. (1.14) gives

$$\begin{cases} \mathbf{k} \times \mathbf{E} = \omega \mathbf{B} \\ \mathbf{k} \times \mathbf{B} = \frac{\mu_0 n_e e^2}{\omega m_e}\mathbf{E} - \omega\mu_0\epsilon_0 \mathbf{E}\,. \end{cases} \tag{1.15}$$

This system of equations has very different solutions depending on the direction of the wave vector **k** with respect to the direction of the electric field. When **k** is parallel to **E**, the first of these equations reduces to $\mathbf{B} = 0$, and the second has non-trivial solutions only for

$$\omega^2 = \omega_{pe}^2 \equiv \frac{n_e e^2}{m_e \epsilon_0}\,. \tag{1.16}$$

These waves represent collective plasma oscillations at the plasma frequency that was introduced, without derivation, already in the section defining a plasma, and which is independent of the magnitude of the wave vector k. Due to the fact that there is no magnetic field associated with these waves, they are commonly referred to as *electrostatic* plasma waves, or *Langmuir* waves. These waves will be described in greater detail in Chapter 2, as they are fundamental to laser wakefield acceleration.

When **k** is instead perpendicular to **E**, Eqs (1.15) can be reduced to a single equation for **E**,

$$-k^2\mathbf{E} = \frac{\mu_0 n_e e^2}{m_e}\mathbf{E} - \omega^2 \mu_0 \epsilon_0 \mathbf{E}\,.$$

The non-trivial solutions of this equation give the dispersion relation for light waves in plasmas

$$\omega^2 = k^2 c^2 + \omega_{pe}^2\,. \tag{1.17}$$

Clearly, the dispersion relation reveals two different regimes of behavior of the electromagnetic fields in the plasma. For frequencies lower than the plasma frequency, the wave vector will be fully imaginary. Instead of propagating wave solutions, this corresponds to non-propagating waves with amplitudes that decay exponentially with distance in the direction of **k**, so-called evanescent waves. Correspondingly, for a fixed frequency, the wave vector becomes imaginary at electron number densities above the *critical density*,

$$n_c = \frac{\omega^2 m_e \epsilon_0}{e^2}.$$

Thus, light cannot propagate in plasmas with a density higher than n_c, and the plasma is then called *overdense*. Due to the large difference in refractive index between the plasma and vacuum, light incident on an overdense plasma will be reflected, and only a small fraction of the fields will enter the plasma. This effect is used, for example, to form mirrors for laser pulses at intensities far above the ionization threshold for dielectric or metallic mirrors. The interaction between laser pulses and overdense plasma and the connection to TNSA of ions is further described in the Appendix.

For frequencies above the plasma frequency, or for electron densities below the critical density, the dispersion relation (Eq. 1.17) results in real-valued wave vectors and, thus, electromagnetic waves at these frequencies can propagate through the plasma. In this case, the plasma is referred to as *underdense*. Furthermore, the phase velocity and group velocity of the waves are given by

$$\begin{aligned} v_p &= \tfrac{c}{\eta} = \tfrac{\omega}{k} = \sqrt{c^2 + \tfrac{\omega_{pe}^2}{k^2}} = \tfrac{c}{\sqrt{1-\omega_{pe}^2/\omega^2}}\,, \text{ and} \\ v_g &= \tfrac{d\omega}{dk} = \tfrac{c^2}{v_{ph}} = c\sqrt{1-\omega_{pe}^2/\omega^2}\,. \end{aligned} \tag{1.18}$$

This shows the well-known, but quite remarkable feature that light propagates with phase velocities higher than c in plasmas. However, this does not violate the theory

of special relativity, since nothing can be transported at this phase velocity. Instead, the group velocity, which is the velocity at which a laser pulse propagates through a plasma, is lower than c.

In the case of laser pulses with a center wavelength of $\lambda = 800$ nm, as used in the experiments on which this dissertation is based, the critical density is $n_c = 1.74 \times 10^{21}$ cm^{-3}. At $n_e = 10^{19}$ cm^{-3}, which is representative for the experiments on laser wakefield acceleration of electrons, the phase velocity is $1.00288c$, and the laser pulses propagate through the plasma with a group velocity of $0.9971c$.

Chapter 2

Laser wakefield acceleration

The process of laser wakefield acceleration can be described in a simplified, yet instructive, picture in which the laser pulse expels electrons from its path through an underdense plasma, leaving an electron void in its wake. This leads to the separation of positive and negative charge behind the laser pulse, since the more inert ions do not respond as quickly to the forces exerted by the laser pulse and can be regarded as stationary. The force resulting from this charge separation pulls the electrons back, initiating oscillations. The initial electron density is restored after an approximate time of $2\pi/\omega_{pe}$ after the laser pulse has passed a particular point. The positively charged electron void, or *bubble*, is thus formed behind the laser pulse and co-propagates with the pulse at a speed of v_g, with a longitudinal size of approximately $2\pi v_g/\omega_{pe}$.

Some of the plasma electrons may deviate from the collective motion that forms the electron void due to thermal motion or other effects, and some electrons may occasionally become located inside the electron void, in which case they are accelerated towards the center. These electrons can co-propagate with the electron void and the laser pulse for several millimeters, gaining significant amounts of energy.

In this chapter, the theoretical foundation of plasma waves and the excitation of such waves by laser pulses is first introduced. The effects of electron density modulations, i.e., the plasma waves, on the evolution of the co-propagating laser pulses are then described. Finally, the longitudinal and transverse dynamics of electrons in the acceleration phase of a laser wakefield accelerator are described, which introduces certain tuning parameters for the accelerator and results in the generation of X-rays.

2.1 Plasma waves

When displaced by an external force, the electrons in a plasma will oscillate collectively at the plasma frequency depending only on the electron number density. These oscillations take the form of moving waves, as the exciting force moves through the plasma. A plasma wave represents a modulation in the electron number density, which implies that there is also an associated electric field wave.

In Chapter 1, plasma waves were found to be a solution to the cold fluid equations, and it was shown that the wavenumber is independent of frequency. Thus, these waves

do not propagate in the regular sense. Instead, the phase velocity is determined by the exciting force which, for laser wakefield acceleration, is due to a laser pulse moving through the plasma at the speed v_g. Generalizing the derivation to include thermal effects [9], leads to plasma waves with finite propagation velocities. However, for laser wakefield acceleration, only the first few plasma periods following the laser pulse are of interest. The wave structure far away from the laser pulse is of minor importance, and the cold fluid model therefore provides an adequate approximation in this case.

Plasma waves used for particle acceleration are either driven by beams of relativistic charged particles, which is outside the scope of this dissertation, or by tightly focused femtosecond laser pulses. Before describing the theoretical models of the excited plasma waves, the force responsible for the excitation of plasma waves by laser pulses will be described.

2.1.1 The ponderomotive force

An electron interacting with an electromagnetic wave with a constant, small amplitude will move primarily in response to the force of the electric field. Thus, an electron will oscillate back and forth at the optical frequency of the pulse, but will on average remain at its initial position. This motion can be described by the Lorentz force

$$m_e \frac{\partial \mathbf{v}}{\partial t} \approx -e\mathbf{E} = -e\frac{\partial \mathbf{A}}{\partial t}\,, \tag{2.1}$$

which yields that the velocity of an electron at rest before the arrival of the laser pulse, is

$$\mathbf{v} = -e/m\mathbf{A} = -c\mathbf{a}\,. \tag{2.2}$$

When the amplitude of the electric field wave is modulated over the path of the oscillating electron, as is the case in a focused laser pulse, the total momentum gained in one direction of the oscillation, will not be exactly equal to the total momentum gained during motion in the opposite direction. Thus, after having performed one oscillation, the electron will not return to its initial position. Instead, the electron starts to drift towards regions of lower electric field amplitude. This intuitive and simple picture describes the physical background of the ponderomotive force, which is responsible for the excitation of plasma waves.

Following more rigorous derivations, in which the motion of a charged particle is expanded in orders of the amplitude of the electromagnetic waves, the nonlinear ponderomotive force in the non-relativistic regime can be written [10–13]

$$\mathbf{F_p} = -\frac{q^2}{2\omega^2 m}\nabla\langle\mathbf{E}\rangle^2\,. \tag{2.3}$$

Here, and below, $\langle\cdot\rangle$ denotes the time average of the corresponding quantity over one optical cycle. A number of observations can be made regarding this expression. (1) The force is independent of the sign of the electric charge, and pushes both electrons and ions in the same direction. (2) The force is inversely proportional to the mass of the particle. The force on a proton is thus approximately 2000 times weaker than the force on an electron. (3) The force pushes the particles along the negative gradient of the square of the electric field, towards regions of lower intensity. This means that

the force is, quite remarkably, independent of the polarization of the electromagnetic wave.

The derivation of the ponderomotive force, generalized to the relativistic case, is much more complicated, and has been the subject of theoretical studies for many years. General expressions for the ponderomotive force in the relativistic case can be found, for example, in [11] as

$$\mathbf{F_p} = -\frac{q^2}{2m\langle\gamma\rangle}\nabla\langle A^2\rangle \ .$$

Although the expression in the generalized case is different, the general features of the ponderomotive force are the same as in the non-relativistic case: the force is independent of the sign of the electric charge, inversely proportional to the mass of the particle, and pushes particles along the gradient towards regions of lower intensity.

The ponderomotive force implies that a tightly focused femtosecond laser pulse propagating through a plasma will push electrons away from its peak, both longitudinally and transversely. This makes it ideal for exciting plasma waves with phase velocities close to c.

2.1.2 Linear plasma waves

It can be shown that the plasma response to a short laser pulse with low amplitude, $a \ll 1$, remains linear, and the following equation can be derived for the electric field of the excited plasma wave [14, 15]:

$$\left(\frac{\partial^2}{\partial\xi^2} + k_p^2\right)\mathbf{E}(\mathbf{r},\xi) = -k_p^2\frac{m_0c^2}{2e}\nabla a^2(\mathbf{r},\xi) \tag{2.4}$$

where $\xi = x - v_g t$ is the longitudinal coordinate in a frame moving with the laser pulse, and $\mathbf{r}$ is the position vector in the plane normal to the direction of propagation. This equation can be solved analytically both formally and for certain pulse shapes, as described in [14, 15]. However, the general features of the equation can be identified without solving it. The equation takes the well-known form of a simple harmonic oscillator in the variable ξ, with a period of $2\pi/k_p$, where $k_p = 2\pi/\lambda_p$ is the wavenumber and $\lambda_p = 2\pi c/\omega_{pe}$ is the linear plasma wavelength. The oscillator is driven by the term on the right-hand side of the equation, which is proportional to the ponderomotive force.

As an illustration, the equation is numerically integrated for a Gaussian pulse with a 35 fs duration (FWHM) and a Gaussian transverse shape with a diameter of 20 μm (FWHM) in a plasma with electron number density $n_e = 5\times10^{18}$ cm^{-3}. The resulting longitudinal, E_x, and radial, E_r, electric fields are shown in Figure 2.1. In this figure, the laser pulse intensity envelope is shown as a solid black line. As expected, the longitudinal component of the electric field behind the laser pulse is sinusoidal, with a period corresponding to the plasma wavelength. The amplitude of the longitudinal field component is maximum on the optical axis and decreases with increasing radial distance. The radial electric field component is also sinusoidal in the variable ξ, but the amplitude is zero on the optical axis. The two field components are out of phase by $\pi/2$ with respect to each other, as indicated by the pairs of dashed lines in the figure. The electric field both longitudinally accelerates and radially focuses electrons located in the region between the pair of dashed lines.

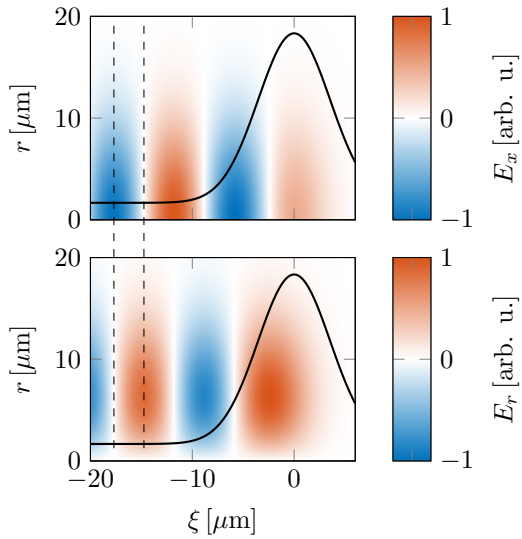

Figure 2.1: Longitudinal (upper) and radial (lower) electric field components of a linear plasma wave excited by a laser pulse (black solid line) centered at $\xi = 0$. Both components are sinusoidal with respect to ξ with a period of λ_p, but shifted by a quarter of a wavelength with respect to each other. In the region between the pairs of dashed lines, separated by a distance of $\lambda_p/4$, the fields both accelerate and focus the negatively charged electrons. The magnitude of the longitudinal field is greatest at $r = 0$, whereas the radial field is zero here.

2.1.3 Nonlinear plasma waves

As the amplitude of the driving electromagnetic pulse is increased, such that the condition $a \ll 1$ no longer holds, the response of the plasma becomes nonlinear. In a one-dimensional model, an equation governing the excitation of a plasma wave by a laser pulse can be written as [16–19]

$$\frac{\partial^2 \phi}{\partial \xi^2} = \frac{k_p^2}{2}\left(\frac{1+a^2}{(1+\phi)^2} - 1\right). \tag{2.5}$$

Here, ϕ, is the electrostatic potential, normalized to $m_e c^2/e$, associated with the plasma wave, and is related to the density modulation through

$$\delta n/n_0 = 1/2\left(\frac{1+a^2}{(1+\phi)^2} - 1\right). \tag{2.6}$$

Solutions of this equation are only found for specific pulse shapes. However, the nonlinear features of the plasma waves can be identified by numerically solving the equation for laser pulses with different parameter values. The resulting electron density modulations and electrostatic fields are shown for a number of pulse durations and pulse amplitudes in Figure 2.2.

Two key features of the nonlinear plasma waves can be observed in this figure. (1) A large fraction of the plasma electrons is located at positions separated by approximately one plasma wavelength, giving rise to a steep transition in the electric field. Between these positions the electron number density is approximately constant, corresponding to a constant slope of the electric field. Thus, the sinusoidal shape of the electric field for low-amplitude plasma waves transforms into a sawtooth shape at higher amplitudes. (2) Due to the relativistic mass increase of the electrons contributing to the wake, the period of the plasma oscillations increases, and thus also the plasma period. When deviating from the one-dimensional model, by using laser

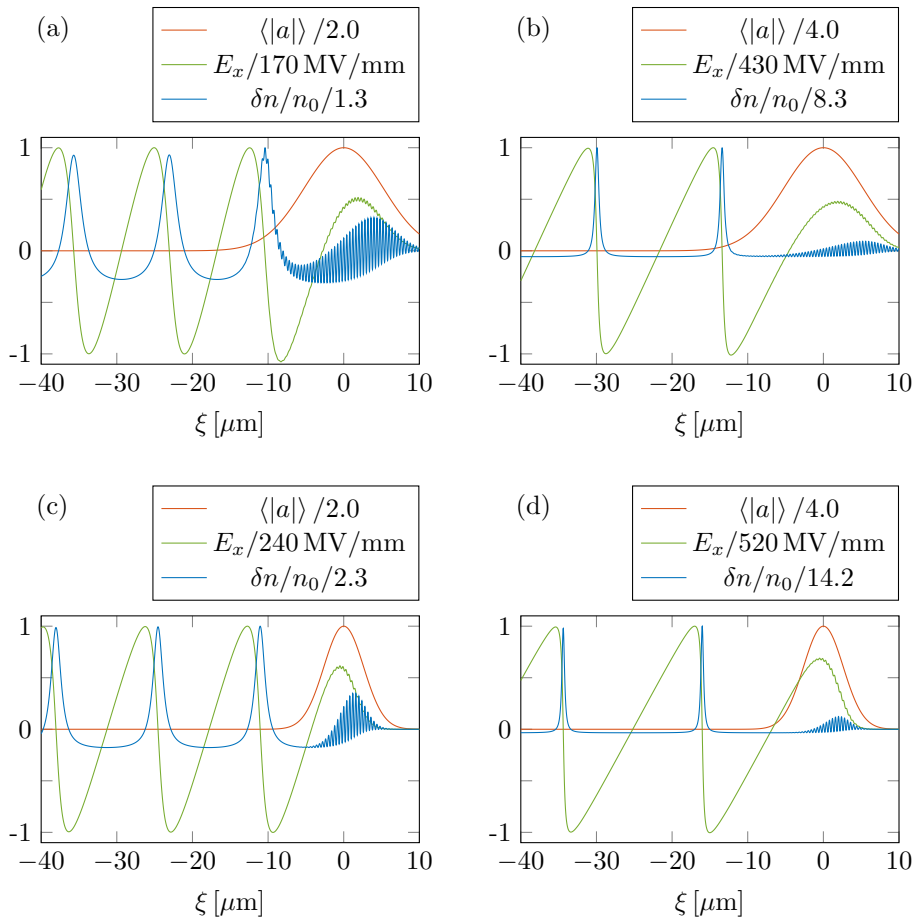

Figure 2.2: Electron density oscillations (blue) and corresponding electric fields (green) of nonlinear wakefields excited by laser pulses (red) of different amplitudes and durations, as described using a one-dimensional model, in a plasma with an initial electron number density of 8×10^{18} cm^{-3}. The amplitude of the excited waves increases with a_0 (a-b). Furthermore, the waves are excited more efficiently when the laser pulse duration is decreased from $0.75\lambda_p/c$ (a-b) to $0.37\lambda_p/c$ (c-d), which corresponds to the resonance condition. As the amplitude of the wave grows, the nonlinear features become more pronounced. The shape of the electric field is no longer sinusoidal, but has a more sawtooth shape. Also, the wavelength of the nonlinear waves becomes greater than the linear plasma wavelength λ_p. Note also that the local electron number density is sharply peaked at values several times the unperturbed density.

pulses of finite transverse size, the amplitude of the plasma wave is no longer constant in the transverse plane. Thus, it is expected that the nonlinear plasma wavelength will depend on the distance from the optical axis, resulting in curved phase fronts.

By keeping the amplitude fixed, while varying the pulse duration (FWHM) of a Gaussian pulse, an optimum can be found at approximately $0.4\lambda_p/c$. This is a resonance condition due to the timing between the ponderomotive kicks in the forward

and backward directions. The front of the laser pulse pushes the plasma electrons forward, but will eventually overtake them. For an optimally chosen pulse duration, the laser pulse then continues to push the electrons backwards, just as the electrons have turned around due to the forces of the associated charge separation. The wakefield is excited most efficiently with such a pulse duration.

2.1.4 Blow-out/bubble regime

The excitation of highly nonlinear plasma waves has been theoretically studied and described in three dimensions in e.g. [20–22]. In a three-dimensional plasma wave excited by a laser pulse the electrons not only oscillate longitudinally, but also stream in the direction orthogonal to the direction of propagation. Due to the more complicated behavior of these waves, the theoretical models are often accompanied by numerical calculations or simulations. Furthermore, a phenomenological description of the physics involved in highly nonlinear plasma waves is provided by Lu *et al.* [23]. This picture is used to provide scaling laws, which agree well with the results from simulations and experiments.

If a sufficiently strong laser pulse is used, the plasma electrons will be completely expelled, or *blown out*, by the ponderomotive force, leaving a complete void in the wake of the laser pulse. Thus, the plasma wave forms a *bubble* in the electron density distribution. For laser pulses with a transverse size approximately equal to the diameter of the bubble, the condition on the peak normalized vector potential for full cavitation is $a_0 > 2$ [23]. Under these conditions, the radius, R, of the bubble can be expressed as

$$R = \frac{2}{k_p}\sqrt{a_0}\,. \tag{2.7}$$

Since, in this regime, the end of the laser pulse is located inside the bubble where there are no electrons, the ponderomotive force from this side of the pulse has no effect. Thus, the resonance condition on the pulse length found in the linear case and the one-dimensional nonlinear case, no longer applies.

A frame from a three-dimensional so-called Particle-in-Cell simulation, using the code *CALDER-CIRC* (see Chapter 3), is shown in Figure 2.3. This figure shows a cross section of the electron density distribution, together with the on-axis longitudinal electric field component and the laser pulse intensity. The longitudinal electric field component has a shape similar to that shown in the one-dimensional nonlinear case. The large accumulation of electrons around the edges of the bubble, which generates the steep transitions in the electric field, is clearly visible. The electric field inside the bubble is directed toward the center. Thus, an electron located in the back of the bubble is accelerated towards positive ξ and, at the same time, restored radially towards the optical axis.

2.2 Nonlinear electromagnetic wave propagation

Due to the large difference in charge-to-mass ratio of electrons and ions, the propagation of high-frequency electromagnetic waves of a laser pulse depends mainly on the response of the electrons in a plasma. A high-amplitude laser pulse in a plasma modulates the electron density distribution as described in the previous section, and

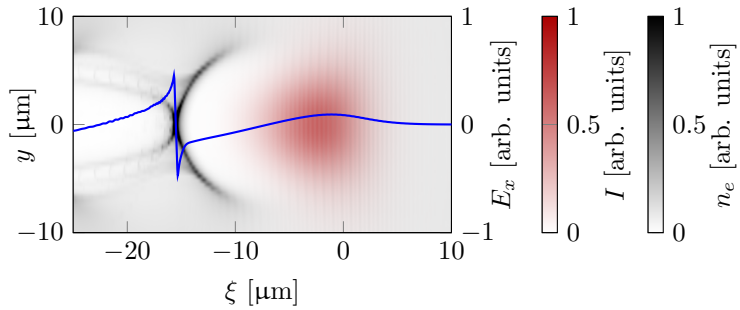

Figure 2.3: A snapshot from a Particle-in-Cell simulation showing the cross section of the electron density distribution (gray shading). An electron void following the laser pulse (red shading) is formed with an associated high-magnitude nonlinear electric field (blue curve). Inside the bubble, the electric field is directed towards the center, and is approximately linearly dependent on the distance from the center. Thus, if an electron would be placed in this field, then it would oscillate both transversely and longitudinally.

will therefore affect the propagation of the laser pulse itself. Additionally, at high electromagnetic wave amplitudes, the electrons oscillating in the laser field are subject to a relativistic mass increase, which in turn alters the response of the plasma. These modulations in electron density and mass result in several interesting effects, which are also important in the design of laser wakefield accelerators.

The modulations in electron density and mass can be expressed in terms of the refractive index, η, of the plasma. In the limit of weakly relativistic laser pulses, $a_0 < 1$, and low-amplitude plasma waves, $\frac{\Delta n}{n_0} < 1$ the refractive index can be expressed as [23–25]

$$\eta = 1 - \frac{1}{2}\frac{\omega_{pe}^2}{\omega_0^2}\left(1 + \frac{\Delta n_e}{n_0} - \frac{\langle a^2 \rangle}{2}\right). \tag{2.8}$$

The first term inside the parentheses is the linear plasma response, while the second term corresponds to the variations in electron density variations in the excited plasma wave. The effect of relativistic mass increase is described by the last term in this equation. The modulation of the refractive index results in both transverse and longitudinal effects on the propagation, which are described separately below.

2.2.1 Transverse pulse evolution

The two final terms in Eq. 2.8 represent the so-called ponderomotive and relativistic modulations of the refractive index. At the location of the laser pulse in the excited plasma wave, the relative electron density difference is on the order of 1. Thus, for amplitudes of a of about 1, the two effects are equally strong.

Relativistic self-focusing

The relativistic mass increase depends on the local intensity, and the refractive index will therefore also vary radially. The relativistic mass increase is greatest on the optical axis, and gives rise to a higher refractive index than further away from the

axis. The phase fronts therefore propagate more slowly on the optical axis than radially further out, resulting in a focusing effect of the laser pulse. When considering only the relativistic contribution to the refractive index, the spot radius, r, evolves according to [13, 26, 27]

$$\frac{d^2r}{dx^2} = \frac{r_0^4}{z_r^2 r^3}\left(1 - \frac{P}{P_c}\right), \tag{2.9}$$

where

$$P_c = 2c\frac{m_e^2c^4}{e^2}\frac{\omega^2}{\omega_{pe}^2} \approx 17.4\frac{\omega^2}{\omega_{pe}^2}\text{GW}$$

and r_0 is the minimum spot radius in vacuum. The first term on the right-hand side of Eq. 2.9 describes the diffraction of the laser pulse, while the second term corresponds to the focusing effect due to the relativistic mass increase. When these two terms are equal in magnitude, diffraction is counteracted, and the laser pulse propagates with a constant transverse size. Hence, relativistic self-focusing occurs when $P > P_c$, and P_c is therefore referred to as the critical power for self-focusing. Relativistic self-focusing can thus be used to guide laser pulses over several Rayleigh lengths in a plasma, over which plasma waves may be excited.

For short laser pulses ($L_p < \lambda_p$), however, the ponderomotive force induces a local accumulation of electrons at the front of the pulse with a density that decreases radially. This density modulation effectively counteracts the self-focusing resulting from the relativistic mass increase [23], and relativistic self-focusing is therefore not efficient in guiding laser pulses that are matched for driving a plasma density wave.

Ionization defocusing

When the plasma is formed by photoionization of gas species with multiple ionization stages, the electron number density depends on the local stage of ionization. The electron will be released earlier close to the optical axis than further away. Locally, this leads to a lower refractive index on the optical axis than radially further away, and contributes to defocusing of the laser pulse. Note that this effect is always present at some point along the laser pulse envelope when photoionization is used to produce the plasma. When tuned properly, ionization defocusing occurs far in front of the peak of the laser pulse, and the main part of the pulse propagates through a homogeneous plasma. The ionization front of one or several ionization stages may be located close to the peak of the pulse for unfortunate combinations of peak laser pulse intensity and gas species. This leads to defocusing of a large fraction of the energy content of the pulse.

Self-guiding and local pump depletion

As described above, relativistic self-focusing is not efficient in combination with excitation of high-amplitude wakefields using short pulses. Thus, without external guiding structures, wakefield excitation is only efficient over a distance of the order of the Rayleigh length. However, it is found that in the three-dimensional blow-out/bubble regime, another effect will effectively lead to self-guiding of the laser pulse, until the contained laser pulse energy is transferred to the plasma wave.

In the blow-out/bubble regime, the rear part of the laser pulse propagates in an electron void created by the leading part of the laser pulse. The steep radial density

transition at the edges of the void efficiently refocuses the diffracting light from the rear part, thereby guiding this part of the pulse. The leading part of the pulse, however, will not be subject to any refocusing transverse modulations of the refractive index, and this part is therefore free to diffract. Simultaneously, the leading part of the laser pulse excites a wakefield and deposits energy in the plasma wave and the laser pulse becomes locally depleted. In this way, the laser pulse will be etched from the front while exciting a wakefield, and the length of the pulse will decrease while the rear part is still guided.

The speed with which the laser pulse is etched can be expressed as [28]

$$v_{\text{etch}} = c\frac{\omega_{pe}^2}{\omega^2}\,. \tag{2.10}$$

The leading edge of the pulse propagates at the group velocity (Eq. 1.18) minus the etching velocity. In a highly underdense plasma, i.e., $\omega_{pe}^2/\omega^2 \ll 1$, the phase velocity of the plasma wave, v_p, or, equivalently, the velocity of the bubble, can then be approximated by

$$\frac{v_p}{c} = 1 - \frac{3\omega_{pe}^2}{2\omega^2}\,. \tag{2.11}$$

2.2.2 Longitudinal modulation

The density modulations driven by the laser pulse will affect the longitudinal evolution of the laser pulse itself during its propagation through the plasma. The refractive index of the plasma decreases with increasing electron number density. In regions of electron accumulation, this leads to a higher phase velocity on one hand, and a lower group velocity on the other.

When a laser pulse is temporally matched to excite a nonlinear plasma wave, the length of the pulse is approximately half of the plasma wavelength. Therefore, the peak of the pulse, and also the main part of the energy contained in it, is located on the upward density slope towards the leading part of the pulse. This is illustrated in the upper part of Figure 2.4, while the corresponding modulations in phase velocity and group velocity are shown in the lower part of the same figure. To a first-order approximation, the longitudinal modulation of the local phase velocity around the peak of the pulse is a linear slope, with higher phase velocity in the front of the pulse than in the back. Thus, while the laser pulse moves through the plasma, the distance between the phase fronts of the carrier wave increases, corresponding to an increase in wavelength, typically called a red shift. Measurements of the electromagnetic spectrum before and after the interaction to determine the amount of redshift have been used extensively, as described in the literature [29–31], as a diagnostic of the strength of the excited plasma waves.

The group velocity at the back of the laser pulse simultaneously becomes higher than at the front. During propagation through the plasma, the back of the pulse will therefore move forward relative to the front of the pulse, effectively compressing the pulse longitudinally [32]. Compression of the pulse has been studied both experimentally [33, 34] and using simulations [35]. This mechanism was used to some extent in all experiments presented in this dissertation to self-compress the laser pulse in order to reach higher peak intensities.

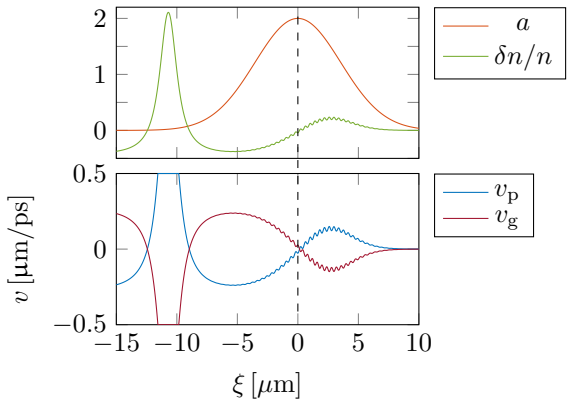

Figure 2.4: The plasma density wave excited by the laser pulse, shown in the upper figure, results in variation of the refractive index. The corresponding deviations in phase velocity and group velocity are shown in the lower figure. The main part of the laser pulse overlaps the increasing density ramp, and the phase and group velocity will therefore depend on the longitudinal position. This leads to red shifting of the laser pulse spectrum together with compression of the pulse.

The self-modulated laser wakefield acceleration scheme (SM-LWFA) relies completely on the modulation of the group velocity over the length of the pulse, which acts as a feedback mechanism to increase the amplitude of the wakefield [36–39]. The SM-LWFA scheme was used frequently in early experiments on laser acceleration as access to pulses with durations matched to the plasma was limited. In SM-LWFA, the laser pulse entering the plasma is much longer than the plasma wavelength, and will initially only drive a plasma wave of low amplitude. The variations in longitudinal group velocity will start to modulate the envelope of the laser pulse, with the same periodicity as the plasma wave. The modulated laser envelope in turn excites the plasma wave more efficiently which increases the feedback.

2.3 Acceleration of electrons

So far, the excitation of collective electron oscillations in plasmas have been described primarily using the cold fluid model. In this model, all the electrons are well behaved and move collectively to form plasma waves. The excited plasma waves can only be used for the acceleration of electrons belonging to a population that is not described by the average fluid motion. The acceleration phase of laser wakefield acceleration is instead typically described using *test* electrons, inserted or injected into the excited plasma wave in one or another way. In this section, the motion of electrons already trapped in a plasma wave will be described. However, a description of a fundamental mechanism that can be used to direct some electrons into orbits in the electric potential formed by the plasma wave is given first.

2.3.1 Wave-breaking and self-trapping

The plasma waves described by the fluid model cannot grow infinitely large, but are instead limited to a certain amplitude. Above this limit, the waves lose coherence and start to break. Various mechanisms are responsible for the breaking of the waves, such as transverse [40] and longitudinal [41] wave-breaking. In a simple, one-dimensional picture, the wave starts to break when the fluid velocity of plasma electrons approaches and exceeds the phase velocity of the wave itself. In the cold non-relativistic one-dimensional case, wave-breaking limits the maximum amplitude of the plasma waves

to [42]

$$E_0 = cm_e\omega_{pe}/e\,, \tag{2.12}$$

in terms of the maximum electric field. The field can become substantially larger in the cold relativistic case, where the maximum electric field is given by [41, 43]

$$E_{\mathrm{wb}} = \sqrt{2\,(\gamma_p - 1)}E_0\,. \tag{2.13}$$

Here, γ_p is the Lorentz factor associated with the phase velocity of the wave. For an electron number density of 1×10^{19} cm^{-3}, which is representative of the experiments presented in this dissertation, the wave-breaking field is approximately 300 MV/mm in the non-relativistic case and 1500 MV/mm in the relativistic case, with $\gamma_p \approx 13$ for a plasma wave driven by a 800 nm laser pulse.

The wave structure is not immediately destroyed by wave-breaking. Some of the electrons still produce a wave-like structure, although it is limited and deformed. In this case, electrons contributing to the break may enter the potential well formed by the plasma wave and become trapped there. If the wave can be sustained over a significant length after the point at which trapping occurs, the electrons can be accelerated to high energies. This mechanism is referred to as self-injection or self-trapping of electrons.

In the three-dimensional blow-out/bubble regime, the condition for wave-breaking and self-trapping can be expressed in terms of the radius of the bubble [44]

$$\omega_{pe}r_b \geq 2c\sqrt{\ln\left(2\gamma_p^2\right) - 1}\,. \tag{2.14}$$

The condition for self-trapping has been validated experimentally in an extensive study reported in literature [45], in which the parameters of the laser pulse were varied to explore the threshold for self-trapping. In this study, it was found that the threshold for self-trapping could be expressed in terms of a scaled laser pulse energy,

$$\alpha E n_e/n_c \gtrsim 2, \tag{2.15}$$

where αE is the energy contained within the central part (FWHM) of the transverse profile. The fraction of energy outside the central part of the laser pulse is not efficiently self-focused during initial propagation through the plasma, and therefore does not contribute much to the excitation of the plasma wave.

As shown in several experimental and numerical studies, self-trapping is intrinsically difficult to control, due to both the nonlinear nature of laser pulse propagation and evolution in the plasma, and the nonlinear nature of the high-amplitude plasma waves. The self-trapping mechanism was first tamed experimentally in 2004, when three groups of scientists independently generated quasi-monoenergetic beams of laser-wakefield-accelerated electrons [46–48]. However, experiments on laser wakefield acceleration of electrons based of self-trapping still suffer from considerable fluctuation in the energy of the electrons and the amount of charge in the beams of accelerated electrons. Research on minimizing these fluctuations is, to a large extent, focused on different schemes for controlled trapping of electrons, for example, by tailoring the longitudinal electron number density distribution, the release of electrons tightly bound to a nucleus by photoionization close to or inside the bubble, and by localized stochastic heating of the plasma electrons in the beating between two laser pulses.

2.3.2 Single-particle dynamics in a plasma wakefield

The acceleration of trapped electrons can be analyzed by considering the motion of single test particles in the field of a plasma wave. In one dimension, the evolution of the longitudinal momentum and position of an electron, i.e., the electron's position in phase space, in the absence of the electromagnetic field from a laser pulse, can be written

$$\begin{cases} \frac{du_x}{dt} = -\frac{e}{m_e c} E_x = -c\frac{\partial \phi}{\partial \xi} \\ \frac{d\xi}{dt} = c\left(\frac{u_x}{\sqrt{1+u_x^2}-\beta_p}\right), \end{cases} \tag{2.16}$$

where $u_x = p_x/(m_e c)$ is the normalized longitudinal momentum of the electron, and ϕ is the electrostatic potential normalized to $m_e c^2/e$. These equations can be solved numerically, although advanced methods are required due to the numerical stiffness introduced by the relativistic mass increase. An alternative method is to study longitudinal phase space orbits by first constructing a constant of motion, H, through (cf. Hamiltonian dynamics)

$$\begin{cases} \frac{du_x}{dt} = -\frac{\partial H}{\partial \xi} \\ \frac{d\xi}{dt} = \frac{\partial H}{\partial u_x}. \end{cases} \tag{2.17}$$

Step-wise integration of Eqs 2.17, using the expressions for each derivative from Eqs 2.16, results in the constant of motion being expressed as

$$H = c\sqrt{1+u_x^2} - c\phi - c\beta_p u_x \,. \tag{2.18}$$

Furthermore, the equation can be solved for u_x, which can then be expressed in terms of the constant of motion and the potential as [49]

$$u_x = \beta_p \gamma_p^2 \left(\frac{H}{c} + \phi(\xi)\right) \pm \gamma_p \sqrt{\gamma_p^2 \left(\frac{H}{c} + \phi(\xi)\right)^2 - 1} \,. \tag{2.19}$$

Several orbits, for different values of H, are plotted in Figure 2.5 using the nonlinear wakefield shown in Figure 2.2(c). It can be seen from Figure 2.5 that for certain values of H, the electrons are trapped within one period of the plasma wave, shown as closed orbits. An electron with initially low momentum in the bottom of a closed orbit, injected by some means into the plasma wave, will first slip back in the plasma period, while simultaneously gaining energy from the electric field of the wave. The electron will eventually catch up with the phase velocity of the wave, and thus turn around and instead move forwards in the reference frame of the plasma wave. As the electron passes the phase where the electric field crosses the axis $E_x = 0$ it will start to decelerate instead. Upon decelerating until its velocity is lower than the phase velocity, the electron will again turn around. Thus, the trapped electrons will perform longitudinal oscillations in the frame moving with the plasma wave, periodically gaining energy from the wave and losing energy to the wave.

In order to use the plasma wave for a net energy gain, an electron injected into a plasma wave must be extracted at a point of higher energy than the initial electron energy, and preferably at the top of the orbit before it has performed a full revolution. Maximum energy gain is achieved when the electron is injected at the very bottom of the orbit, and extracted exactly as it reaches the top. When an electron passes the

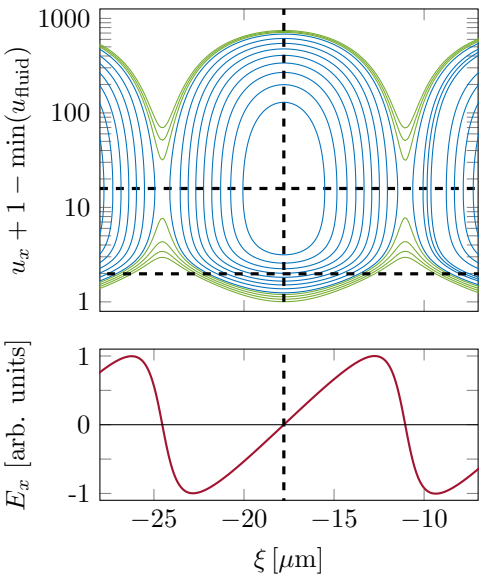

Figure 2.5: Possible (rescaled) longitudinal phase space orbits (above) for electrons in the fields of a nonlinear plasma wave (below). The lowest green curve represents the fluid orbit, i.e., the orbit of electrons with zero momentum before the arrival of the laser pulse. These electrons do not become trapped in the plasma wave. The upper green curves represent the hypothetical orbits of electrons with too large forward momenta to become trapped. The blue curves describe the orbits of trapped electrons. The vertical dashed lines indicate the zero crossing of the electric field. The lower horizontal dashed line in the upper panel marks zero longitudinal momentum and the upper dashed line the longitudinal momentum corresponding to the phase velocity of the plasma wave.

peak of the orbit and starts to decelerate, it dephases, and the acceleration distance that takes an electron from rest to dephasing is called the *dephasing length*, L_d. In the three-dimensional blow-out/bubble regime, the dephasing length can be expressed as [23]

$$L_d = \frac{4}{3k_p}\frac{\omega_0^2}{\omega_{pe}^2}\sqrt{a_0}\,. \tag{2.20}$$

The corresponding limit on the energy gain in a laser wakefield accelerator is

$$\Delta E_{\mathrm{e}^-} = \frac{2}{3}\frac{\omega_0^2}{\omega_{pe}^2} a_0 m_e c^2. \tag{2.21}$$

The physical background of the dephasing limit on energy gain is the group velocity of the laser pulse, which is close to, but smaller than, c. After gaining energy in the plasma wave, the accelerated electrons can therefore reach a higher velocity than the laser pulse, and thus outrun the wave and end up in a decelerating phase. Correspondingly, in order to increase the maximum energy gain, the electron number density should be reduced in order to increase the laser pulse group velocity.

In the case of plasma wakefield accelerators driven by beams of relativistic charged particles (typically electrons or protons), a similar mechanism limits the acceleration distance by dephasing. However, in this case it is the velocity of the particles in the driving beam that sets the limitation, and this is typically much closer to c than the group velocity in laser wakefield accelerators. Thus, dephasing is typically not considered a limiting factor for beam-driven plasma wakefield accelerators.

Electron dephasing can be prevented using an increasing density gradient along the axis of laser pulse propagation. In an increasing density gradient, the laser pulse group velocity decreases. However, the plasma wavelength also decreases and the gradient can be designed such that the back of the plasma bubble follows the electron bunch [50]. When the density gradient is properly tuned, the phase of the electrons

may even be locked relative to the plasma wave [51, 52]. It has been experimentally demonstrated that trapped electrons can be rephased with respect to the electric field wave by a step-wise increase in electron number density [53]. In this way, electrons that are starting to dephase after acceleration in the first part of the plasma become relocated in a phase of higher electric field after traversing a steep increase in electron number density such that the plasma period decreases.

2.3.3 Electron bunches in plasma wakefields

In the previous section, the acceleration of single test electrons in the wakefield was described. In all practical implementations, electrons are instead trapped in bunches containing of the order of at least 1 pC of charge or, correspondingly, at least 10^7 electrons. All these electrons will have slightly different orbits in the plasma wave, and the resulting beam of electrons must therefore be described in terms of distributions in energy, longitudinal space (or time) and angular space.

Electron energy spectrum

In most applications, quasi-monoenergetic beams of electrons are preferred. In order to generate quasi-monoenergetic bunches of electrons accelerated in a laser wakefield, several criteria must be fulfilled.

First of all, the injection and trapping of electrons into the plasma wave must be well-localized in the longitudinal extent of the accelerator, otherwise, the acceleration distance will not be the same for all electrons, and the final energy spectrum will be wide and/or contain several peaked features. This is typically the case when using self-trapping, unless the laser and plasma parameters are perfectly tuned.

When injection and trapping are appropriately controlled, the electrons are initially located longitudinally over a small fraction of the length of the bubble. However, since the accelerating electric field is larger at the back of the bubble than at the front, the electrons in a bunch will be accelerated differently. If all the trapped electrons initially have the same energy, this will lead to an energy spread that increases monotonically with acceleration distance. However, the fact that the electric field varies over the length of the bubble may also be used to reduce an initially large energy spread, as illustrated in Figure 2.6 (a). Here, the electrons at the back of the bunch have lower energy than those at the front, but after acceleration the energy difference is decreased. This effect is referred to as *phase space rotation* of a distribution of electrons.

In the case of bunches of trapped electrons with an initial small energy spread, phase space rotation is undesirable as it leads to an increase in energy spread. The effect of a varying electric field over the length of the bunch of trapped electrons may, in that case, be reduced by trapping a sufficiently large number of electrons. The electric fields of these trapped relativistic electrons will then push the lighter plasma electrons and thus excite a wakefield [54–56]. This effect is called *beam loading* and, for a sufficient number of trapped electrons in the accelerating phase of a nonlinear wakefield, it will lead to a flattened electric field at the location of the trapped electrons. Beam loading is illustrated in Figure 2.6(b), where the fields of a nonlinear plasma wave, driven by a laser pulse and loaded by a significant amount of trapped charge, are shown.

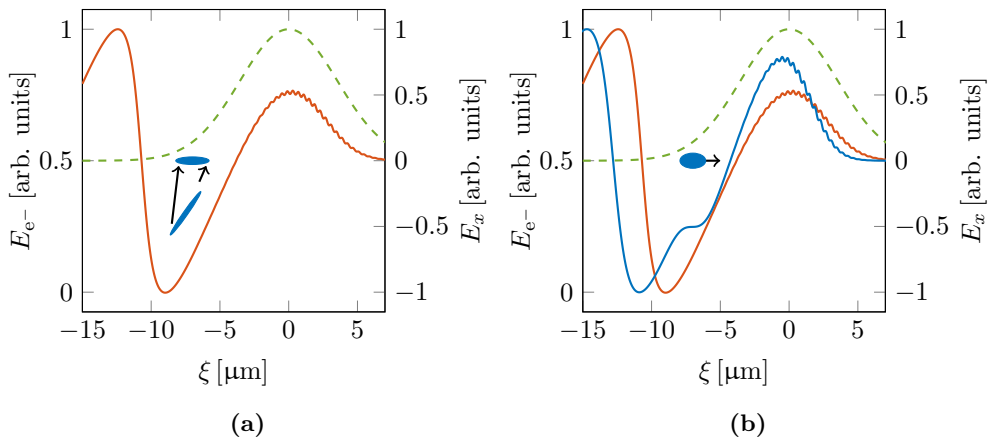

Figure 2.6: Illustration of phase space rotation of an electron bunch with an energy spread correlated to the phase coordinate (a). The electrons at the back of the bunch gain more energy than those at the front. After a certain distance, all the electrons have the same energy. Beam loading of the plasma wave is illustrated in (b). The fields generated in the plasma by the electron bunch modify the unloaded electric field (red) of the plasma wave to generate the effective electric field (blue) acting on the electrons in the bunch. The green dashed curve indicates the intensity envelope of the laser pulse.

Furthermore, in order to generate electron beams with small energy spread, the initial energy spread of the trapped electrons should preferably be small. During acceleration, electrons with different initial energy take slightly different paths in longitudinal phase space and the original energy distribution will thus be deformed. Therefore, unless care is taken to tune the parameters of the plasma wakefield accelerator, the initial energy spread may become large by the time the bunch exits the accelerator. In particular, the acceleration distance required for an injected electron to dephase with the wave depends on the initial energy of an electron. Thus, the time required to perform one longitudinal oscillation is not the same for electrons in different orbits. If the total length of the plasma wakefield accelerator is long compared to the dephasing length, the electrons in a bunch will oscillate several times and spread out in longitudinal phase space.

Electron beam divergence

Electrons trapped in a three-dimensional plasma wave, have a transverse spread. All the electrons must have to be located inside the three-dimensional bubble structure in order to be accelerated, and this results in a transverse electron beam source size smaller than the size of the bubble. Furthermore, the trapped electrons typically start with a finite transverse momentum, and refocusing forces are thus needed to keep the electrons in the accelerating field. Luckily, in addition to the longitudinal electric fields used to accelerate the electrons, transverse electric fields of the same order of magnitude are present in the bubble. This was briefly mentioned in the description of linear three-dimensional wakefields, for which there exist a region with a length of $\lambda_p/4$ in each period where the electric fields are both accelerating and focusing the

electrons. In the three-dimensional blow-out/bubble regime, the phase region in which the electric fields are focusing the electrons is significantly larger. Inside the bubble, the electric field points away from the center of the bubble, and the fields are therefore focusing the electrons anywhere inside the bubble.

The radial electric field, together with the initial transverse distribution, leads to a non-zero divergence of the emerging electron beams. Heuristically, the beam divergence increases both with the transverse size of the source and with the strength of the focusing forces. While inside the plasma accelerator, the radial field of the bubble keeps the electrons of the bunch together. As the electrons leave the plasma, the focusing forces vanish and the electrons are free to expand transversely [57]. The reported divergence of the electron beams in experiments are in the range of a few milliradians up to a few tens of milliradians, depending on the experimental parameters. The various mechanisms of trapping of electrons, investigated in this work, resulted in different characteristic beam divergences. This is discussed in Chapter 4 for the mechanisms for controlled trapping used in the reported experiments.

Transverse oscillations and X-ray generation

The radially focusing forces in the bubble of a laser wakefield accelerator force the electrons to perform transverse oscillations, referred to as *betatron* oscillations. In the three-dimensional blow-out/bubble regime, it can be shown [58] that an electron with a relativistic factor γ, corresponding to the longitudinal motion, will oscillate at an angular frequency of

$$\omega_\beta = \frac{\omega_{pe}}{\sqrt{2\gamma}} .$$

One betatron oscillation is performed while the electron has propagated over a distance $\lambda_u \approx \sqrt{2\gamma}\lambda_p$, called the undulator period.

Just as relativistic electrons are forced to oscillate in the insertion devices of synchrotron light sources, the electrons oscillating inside the bubble radiate electromagnetic energy. The frequency of the radiated emission is a factor γ^2 higher than the transverse oscillation frequency in the laboratory frame. Thus, electrons with energies on the order of 100 MeV accelerated in plasma waves with wavelengths on the order of 10 µm predominantly emit XUV and X-ray photons. Furthermore, due to relativistic field transformation, the X-rays are emitted predominantly within a narrow cone with an opening angle of approximately $1/\gamma$.

It has been shown that the energy spectrum of the radiation emitted by a bunch of electrons being simultaneously accelerated is synchrotron-like [59, 60]. The energy spectrum of the emitted X-rays along the optical axis can, in this case, be well described by the expression [59]

$$\frac{dI}{dE} \propto \left(\frac{E}{E_c}\right)^2 \kappa_{2/3}^2 \left(\frac{E}{2E_c}\right) , \tag{2.22}$$

where $\kappa_{2/3}$ is the modified Bessel function of the second kind of order 2/3. The critical energy, E_c, has been found in experiments to be on the order of a few keV.

The laser wakefield accelerator thus acts as a source of X-rays with a synchrotron-like spectrum, and this radiation can be directly used for applications such as X-ray imaging and spectroscopy. The emitted X-rays have also been found to be a useful tool

for diagnostics of the acceleration process, as discussed in Paper VI. For example, the transverse size of the oscillations can be estimated by experimental characterization of the critical energy [61], and assuming that the spectrum is similar to that emitted by a single electron. In this case, the critical energy can be expressed as [59]

$$E_c = \frac{3}{4c}\hbar\gamma^2\omega_{pe}^2 r_\beta,$$

where r_β is the amplitude of the oscillations. Furthermore, the cone of emitted X-rays was cropped by the exit of the dielectric capillary tube used in the experiment to confine the gas, and the resulting transverse X-ray distribution could be used to determine the position of the X-ray source, and therefore also to determine the position of trapping and acceleration of the electrons. This will be discussed in further detail in Chapter 4.

Transverse beam emittance

The quantity transverse beam emittance [62] is a measure of the quality of the beam, and is related to the transverse beam size and divergence. The normalized beam emittance, in each transverse direction y and z, is defined as $\epsilon_n^{y,z} = A^{y,z}/(\pi m_e c)$, where $A^{y,z}$ is the area (root-mean-square) in phase space, (y, p_y) and (z, p_z), respectively, occupied by the electrons in the beam [63]. Values as small as possible of the transverse beam emittance are usually desirable for applications such as synchrotron light sources and free-electron lasers in order to produce radiation with high brightness. The transverse emittance of laser wakefield accelerated electrons has been measured using different methods, resulting in beam emittances in the range from $1\,\pi$ mm mrad to $3\,\pi$ mm mrad [64–66] which is comparable to conventional high quality electron sources. Transverse normalized emittances even below $0.5\,\pi$ mm mrad [63, 67] has recently been measured of the beams generated by laser wakefield acceleration.

Chapter 3

Tools and methods

The studies on laser wakefield acceleration and controlled trapping of electrons in the plasma waves presented in this dissertation are, to a large extent, based on experiments. Although the experiments involve the interaction between real laser pulses and plasmas, the measurements are typically related only to the end result after the interaction has occurred, and conclusions about the interaction itself are drawn from these measurements. Therefore, the studies are supported by computer simulations of the interactions. In contrast to the experiments, simulations can provide information about the electromagnetic fields and the distribution of the plasma at any chosen time during the interaction, limited only by computational and storage capacity. However, the results of the simulations are based on models and calculations with intrinsic limitations, and it is therefore important to compare them with experiments.

This chapter describes the tools used for the studies on laser wakefield acceleration together with the methods used in the investigations.

3.1 Experimental methods

The essential components in a typical setup for the experimental studies on laser wakefield acceleration are illustrated in Figure 3.1. A laser pulse is focused on the front edge of a gas target, which is immediately ionized by the leading edge of the pulse, forming a plasma. Under certain conditions, electrons are accelerated in the interaction between the laser pulse and the plasma, and these electrons leave the plasma along the optical axis of the laser pulse. A screen intersecting the beam, which scintillates upon the impact of electrons, is used to detect and characterize the beams of electrons. The screen is imaged onto a charge-coupled device (CCD) camera, and the image is acquired by a computer for further analysis. Before impacting on the scintillating screen, the electrons pass through a dipole magnetic field, which disperses the electrons according to energy. This enables the electron energy spectrum to be determined. In order to characterize the electron beam profile instead, the dipole magnet is retracted from the electron beam path, allowing the electrons to propagate undeflected towards the scintillating screen.

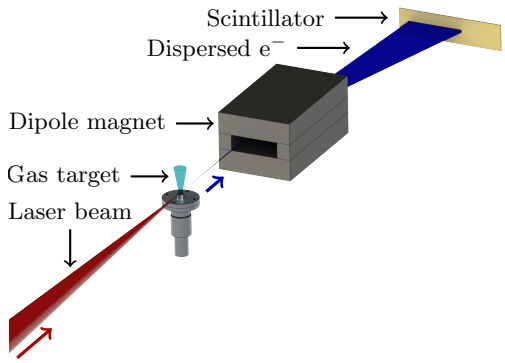

Figure 3.1: Illustration of the essential components of a typical experiment on laser wakefield acceleration. A high-power laser pulse is focused onto a gas target, in this case shown as a gas jet supplied by a nozzle. Electrons accelerated in the interaction co-propagate with the laser pulse towards a dipole magnet which disperses the electrons according to energy before impacting on a scintillating screen. The scintillating screen is imaged from the back using a CCD camera. The dipole magnet may be retracted from the optical axis to instead image the electron beam profile of the undeflected electrons.

3.1.1 Lund multi-terawatt laser

The experiments reported in the papers on which this dissertation is based, apart from Paper IX, were all conducted at the Lund High-Power Laser facility using the multi-terawatt laser. The laser system is based on CPA [1] and was inaugurated in its original form in 1992. Since then it has been developed, improved and upgraded. During the course of the work leading to this dissertation, the laser system was dynamically modified to best suit each experiment. The aim in this section is to describe the laser system in its default configuration. The system, which is illustrated schematically in Figure 3.2, generates amplified high-power laser pulses in two arms allowing separate experiments to be performed independently. The amplifying medium throughout the system is Ti:sapphire in crystals of different shapes and sizes, and the laser beam size is expanded transversely between the amplification stages. The amplifying media are pumped in all stages except for the first, using laser pulses at a wavelength of 532 nm produced by frequency doubling the light pulses from flash-lamp-pumped neodymium-doped YAG lasers.

The first main component in the laser system is an oscillator based on Kerr lens mode locking [68], which generates an 80 MHz train of pulses, each with a bandwidth of approximately 50 nm at a central wavelength of 800 nm, corresponding to a bandwidth-limited pulse duration below 20 fs. Using a Pockels cell pulse-picker, 10 pulses per second are sent for further amplification in a pre-amplifier stage which increases the pulse energy from approximately 5 nJ to a few μJ. In certain configurations of the laser system, the laser pulses are temporally and spatially cleaned after this stage using crossed-polarized wave generation (XPW) in a barium fluoride (BaF_2) crystal [69]. This helps to increase the contrast between the peak of the laser pulse and the undesired amplified spontaneous emission (ASE).

The laser pulses are then temporally expanded in a grating stretcher to 9 ps per nm bandwidth. The pulse duration in the following stages thus depends on the width of the spectrum at each stage. Assuming that the spectral width from the oscillator is preserved, the pulse duration after the stretcher is approximately 450 ps. This corresponds to an increase in the length of the pulse by a factor of more than 20,000

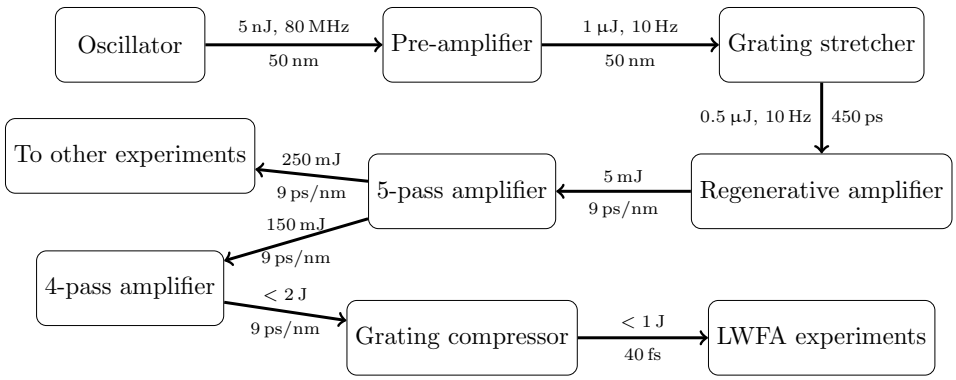

Figure 3.2: Block diagram of the Lund multi-terawatt laser system. All values given in this figure are approximate. The amplifying medium in all stages is Ti:sapphire in crystals of different sizes. The laser system produces high-power laser pulses in two separate arms, allowing for two experiments to be performed simultaneously and independently.

from 6 µm to 14 cm. The stretched pulses are further amplified in a regenerative amplifier by switching the pulses into an optical resonator using a Pockels cell. The pulses are here amplified to a few mJ after 10-15 round trips in the resonator, and are then switched out. The beam is expanded to a diameter of 8 mm and the pulse energy is increased in a 5-pass amplifier to approximately 400 mJ. Two separate Pockels cells are mounted between the stages, which temporally clean the pulses and suppress any pre-pulses that are generated intrinsically in the regenerative amplifier.

The laser pulses are split after this amplification stage and approximately 250 mJ leaves the laser system for compression and use in experiments unrelated to this dissertation. The remaining part of the pulses pass through a spatial filter, to clean the beam profile, before further amplification in a 4-pass stage. The beam is transversely expanded to a diameter of 16 mm before entering this amplification stage. The amplifying Ti:sapphire crystal in this stage is pumped with 5 Nd:YAG lasers, producing in total up to 7 J per pulse. To decrease the effects of thermal lensing, the crystal is mounted in a cryostat and can be cooled to a temperature of approximately 70 K. At this temperature, the thermal conductivity of sapphire is high, which leads to lower thermal gradients in the crystal [70]. This stage is able to amplify the pulses up to 2 J, although for the experiment presented in this dissertation the gain was lowered to give pulse energies of below 1.6 J to ensure that the laser system could be operated safely and to avoid damage to the optical components.

Finally, the pulses are expanded to a beam diameter of approximately 50 mm before entering a grating compressor. The bandwidth of the amplified pulses is just below 40 nm, which supports compression to a pulse duration of approximately 35 fs. From this point on, the pulses are propagated in vacuum ($\sim 10^{-4}$ mbar) to prevent filamentation and other nonlinear effects in air at ambient pressure. The pulses are compressed using a grating compressor to reverse the effect of the grating stretcher. The pulse compression is fine-tuned using an acousto-optic programmable dispersive filter (Fastlite Dazzler [71]) located in the beam before the stretcher. The acousto-optic modulator is used to compensate for higher-order spectral phase variations which cannot be compensated for by the grating compressor. The modulator is also used to

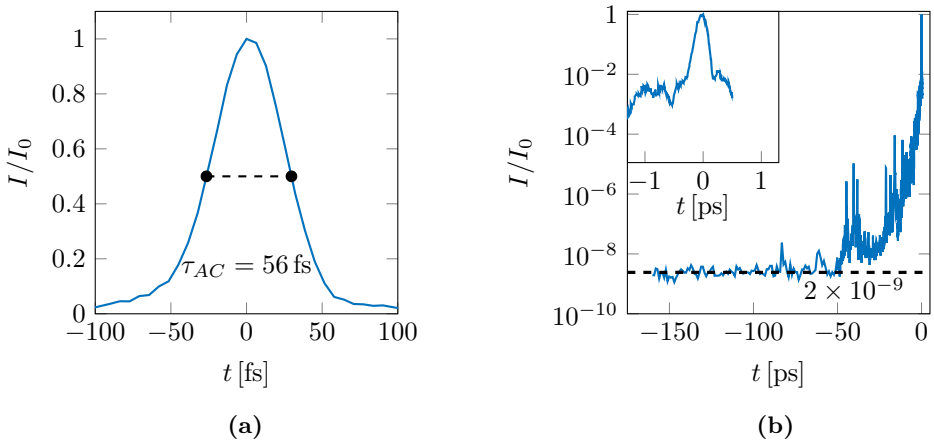

Figure 3.3: (a) A typical trace from the intensity autocorrelator. The duration of the peak is 56 fs (FWHM), corresponding to an approximate laser pulse duration of 39 fs (FWHM) assuming a Gaussian pulse shape. (b) A typical trace from the third-order autocorrelator while scanning the delay stage over approximately 5 cm. The contrast ratio of the peak of the pulse to the intensity 150 ps before the peak is $1:(2\times10^{-9})$. The inset shows an enlargement of the region around the peak.

adjust the amplitude envelope of the spectrum to pre-compensate for gain narrowing during amplification of the pulses.

The beam position is monitored at several locations within the laser system. The beam position at these locations is actively aligned and kept fixed after start-up using piezo-electrically actuated mirror mounts and control software implementing feedback loops. This system not only prevents drifting of the beam position and direction, but also reduces the drift in performance, such as gain, spectral shape and contrast.

After being temporally compressed, the laser pulses are reflected from an electronically actuated deformable mirror consisting of 32 separate actuators. The wave fronts of the laser pulses are optimized to yield an almost diffraction-limited spot after final focusing using a wave front sensor (Phasics SID4) and software implementing an iterative feedback loop. The deformable mirror is also used to fine-tune the longitudinal position of the beam waist in experiments in cases when it was not possible to move the gas target.

Furthermore, before reaching the focusing mirror used in the experiment, the pulses are reflected from a 100 mm diameter piezo-electrically actuated steering mirror which allows the implementation of active pointing stabilization or alignment. By monitoring the position of a co-propagating reference beam using a fast position-sensitive device (PSD) and a fast feedback loop, it is possible to reduce beam-pointing drift and fluctuations at frequencies up to a few hundred hertz [72]. This advanced system was implemented and used in the experiments reported in Papers I-II and Paper VI. In a simpler setup, the transverse focus position of the co-propagating reference beam is monitored using a camera. This limits the speed of the feedback system to only a few hertz, but allows drifts in the beam pointing to be minimized. This configuration was used in the experiments reported in Papers VII-VIII.

The laser pulses are characterized on a daily basis after the grating compressor

using an intensity autocorrelator to estimate the pulse duration and a third-order autocorrelator (Amplitude SEQUOIA) to measure the contrast ratio between the peak of the pulse and the ASE pedestal. A typical trace from the intensity autocorrelator is shown in Figure 3.3(a), where the signal has a FWHM of 56 fs. Estimation of the laser pulse duration requires an assumption of the shape of the pulse envelope. Typically, the central part of the pulse envelope can be estimated as Gaussian, which yields a pulse duration of $\tau_{\text{pulse}} = \tau_{\text{AC}}/1.44$, and results in a pulse duration of 39 fs (FWHM) in the example shown above. The daily estimates of the pulse duration are compared the results obtained with to more elaborate measurements using the technique of *spectral phase interferometry for direct electric field reconstruction* (Avesta SPIDER SP-120). These measurements have been found to agree well with the estimates of the pulse duration using the intensity autocorrelator.

A typical trace acquired using the third-order autocorrelator is shown in Figure 3.3(b). In this configuration, the average intensity contrast ratio 150 ps before the peak is $1:(2 \times 10^{-9})$, which is at the limit of the dynamic range of the measurement instrument. The acquired trace shows how the laser pulse intensity increases rapidly approximately 50 ps before the main peak of the pulse.

Amplified spontaneous emission builds up in the laser system primarily in the regenerative amplifier. In order to keep the ASE contrast ratio to a minimum, it is crucial that the cavity of the regenerative amplifier and the coupling of the seed pulses to this cavity are optimally aligned. This ensures that the maximum amplification of the seed pulses is achieved for a certain pump power in relation to the amplification of spontaneous emission.

3.1.2 Gas targets

In the experiments on laser wakefield acceleration described in this dissertation, the plasma was formed by ionization of a neutral gas by the leading part of the laser pulse itself. Gas was supplied to the interaction zone in the vicinity of the laser beam waist either in the form of a jet provided by a nozzle, or confined in a gas cell or a dielectric capillary tube (see Figure 3.4). These methods of supplying the gas and the characterization of the corresponding gas target are described in more detail below.

Since the laser pulses cannot propagate in air at ambient pressure after recompression, the experiments are performed in vacuum chambers. Therefore, gas can only be supplied immediately before each laser pulse arrives at the interaction zone, and the gas supply must therefore be pulsed with as short an opening time as possible while still allowing the gas flow to build up sufficiently. Between the laser pulses are triggered, the gas supplied to the vacuum chambers must be pumped out. With the available vacuum pumps, the amount of gas injected into the vacuum chamber for each shot limits the repetition rate of the experiments to one shot approximately every ten seconds.

Gas jets

In the experiments reported in Papers III-V and IX, the gas was supplied to the interaction region in the form of pulsed jets using nozzles similar to those described by Schmid *et al.* [73]. The orifice of the nozzle is usually located close to the optical axis, and the jet is directed toward the optical axis. The nozzle is conical with a

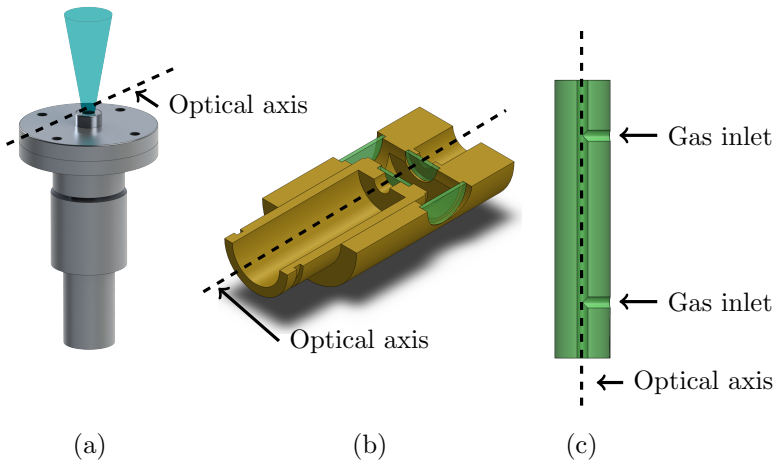

Figure 3.4: Illustrations of three different gas targets used in the experiments. (a) A jet of gas is directed towards the optical axis of the focused laser pulses using a nozzle approximately 1 mm away. (b) A cell with variable length is used the confine the gas. The gas is supplied through holes not shown in this figure. After the transient density increase upon opening the gas valve, the gas density is constant within the cell compartment. The entrance and exit gradients are characterized using computational fluid dynamics. (c) A dielectric capillary tube is used to confine gas supplied through two slits close to the ends of the tube. The density is approximately constant between the slits and the gradients are characterized using computational fluid dynamics.

cylindrical cross section and the jet therefore expands in the form of a cone. The angle of expansion depends on the shape of the nozzle and the exit velocity. For the experiments reported in Papers III and V, the gas distribution was characterized using the setup shown in Figure 3.5(a). In this case, a helium-neon (HeNe) laser beam propagates through the jet of gas and picks up an additional optical path length due to the refractive index of the gas. For a ray, with transverse coordinates y and z, the additional optical path length can be written as

$$\Delta s\,(y,z) = \int (\eta\,(x,y,z) - 1)\,dx = \int \alpha\,\rho\,(x,y,z)\,dx\,, \tag{3.1}$$

where $\rho\,(x,y,z)$ is the local molecular number density of the gas. The value of the constant α was calculated from tabulated values of refractive index for the specific gas species at ambient pressure and temperature.

The transverse variations in additional optical path length were measured using a wave front sensor (Phasics SID4). A typical measured wave front passing through a jet of gas is shown in Figure 3.5(b). In this experiment, a jet of hydrogen gas was supplied using a 2 mm diameter nozzle with a backing pressure of 10 bar. The local molecular number density is determined from such measurements assuming cylindrical symmetry in each plane normal to the direction of the jet, either by using an inverse Abel transform or by fitting the density profile of certain shape to agree with the measured additional path length. For the results shown in Figure 3.5(c), a flat-top profile with linear gradients was assumed, and the plateau molecular number density

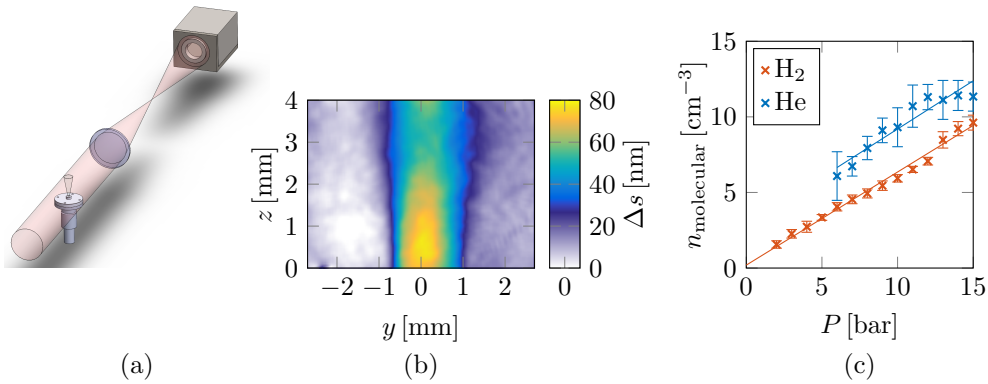

Figure 3.5: (a) Setup used for the characterization of gas jet density by measuring the additional optical path length of a HeNe laser probe passing through the jet, using a wave front sensor. (b) A typical map of the additional path length over the transverse profile of the laser beam. In this case, a jet of hydrogen gas was supplied from a 2 mm diameter nozzle at a backing pressure of 10 bar. (c) Determined plateau molecular number density of hydrogen and helium gas jets supplied by the same nozzle as a function of backing pressure.

is shown as a function of backing pressure for molecular hydrogen and helium. The fit of the flat-top profile shows a plateau length of 0.8 mm and gradient lengths of 0.7 mm.

In the measurements described above, the exposure time of the wave front sensor was set below 0.1 ms, which allows for time-resolved measurements of the pulsed jet flow. In laser wakefield experiments, it is of certain interest to determine the shortest possible length of the gas pulse in order to minimize the gas load on the vacuum pumps. By following the evolution of the maps of the additional optical path length, it was found that a steady state was reached after approximately 2 ms. Thus, the gas supply is triggered so as to reach a steady state flow just before the laser pulse arrives, and it is closed as soon as possible after the laser pulse has passed.

Gas cells

In the experiments reported in Papers VII-VIII, the gas was confined in variable-length gas cells. Two different models of gas cell were used in these experiments, which are equivalent for the laser wakefield experiments. The focused laser pulse enters the gas cells through a hole in a 0.5 mm thick plate, made of either steel or sapphire. The accelerated electrons exit the cell, together with the remaining laser pulse, through a similar hole in a plate on the opposite side. The diameter of the holes is initially in the range 100 µm and 200 µm, but they grow slowly as a result of laser machining due to the energy in the wings of each laser pulse.

The one cell that was designed and assembled by co-workers in Lund is illustrated in Figure 3.6. Here, the entrance plate is mounted on a piston inside an outer cylinder, in which the exit plate is mounted. This design allows the inner surfaces of the entrance and exit windows to be in contact, i.e., the inner length of the cell can, in principle, be 0 mm. The maximum length of the gas cell is determined by the length of the cylinder, and is approximately 30 mm. Leakage between the piston surface and inner

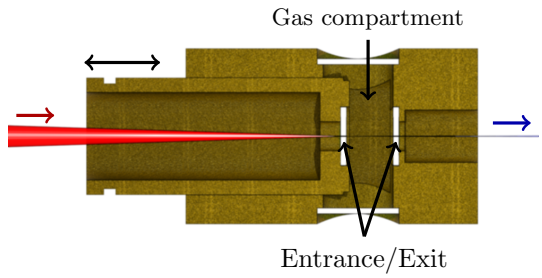

Figure 3.6: Illustration of one of the gas cells used. The laser pulse (red) enters the gas compartment from the left through a 100 µm diameter hole in a 0.5 mm thick sapphire window. Electrons (blue) accelerated in the interaction exit the cell on the right through a similar hole. The cell compartment is formed by an outer cylinder and a piston, allowing the length of the cell to be varied.

surface of the cylinder is avoided by a combination of precision machining, a long contact surface, and a small amount of vacuum grease. This cell has three optical windows, two of which can be seen in the figure, and the third, which is located on the top of the cell. These windows allow for both optical diagnostics and probing the laser wakefield, and for characterization of the gas density inside the cell. The density in this cell was determined by time-resolved optical interferometry, using a Mach-Zehnder interferometer, as shown in Figure 3.7(a). The additional optical path length was determined from interferograms acquired while filling the cell with gas. Again, the additional optical path length is related to the molecular number density through Eq. 3.1. By assuming constant density over the known width of the cell, the steady-state molecular number density was determined to be 90% of the molecular number density in the reservoir from which the cell is filled. Furthermore, the filling time was determined to approximately be 50 ms, and the trigger to the valve was set accordingly in the laser wakefield experiments.

The density gradients at the entrance and exit of both of the used cells are difficult to measure with optical probes. These gradients were therefore estimated by computational fluid dynamics using COMSOL Multiphysics for one of the cells and OpenFOAM for the other. Both computational models are based on turbulent gas flow and the results from these computations are thus only valid at densities for which the mean free path of the gas molecules, given by the expression $\bar{l} = \frac{k_B T}{\sqrt{2}\pi d_m^2 p}$ where d_m is the effective molecular diameter, is significantly smaller than the typical size of the confining geometry. For example in hydrogen, at a pressure of 10 mbar and a temperature of 20 °C, the mean free path is approximately 12 µm, and is thus much smaller than the diameter of the holes in the entrance and exit plates [74, 75]. At this pressure and temperature the electron number density of the fully ionized gas is 5×10^{17} cm^{-3}, which is much too low to significantly influence the acceleration process. The normalized density distribution in a cell with a length of 1 mm between the inner surfaces of the entrance and exit plates is shown in Figure 3.7(b). The total length of the gradients between 10% and 90% of the plateau density is approximately 0.6 mm.

Dielectric capillary tubes

In the experiments reported in Papers I, II and VI, the gas was confined in narrow-channel glass tubes, referred to as *dielectric capillary tubes* (see Figure 3.4(c)). The length of the glass tubes ranged from 5 mm to 30 mm, and the diameter of the

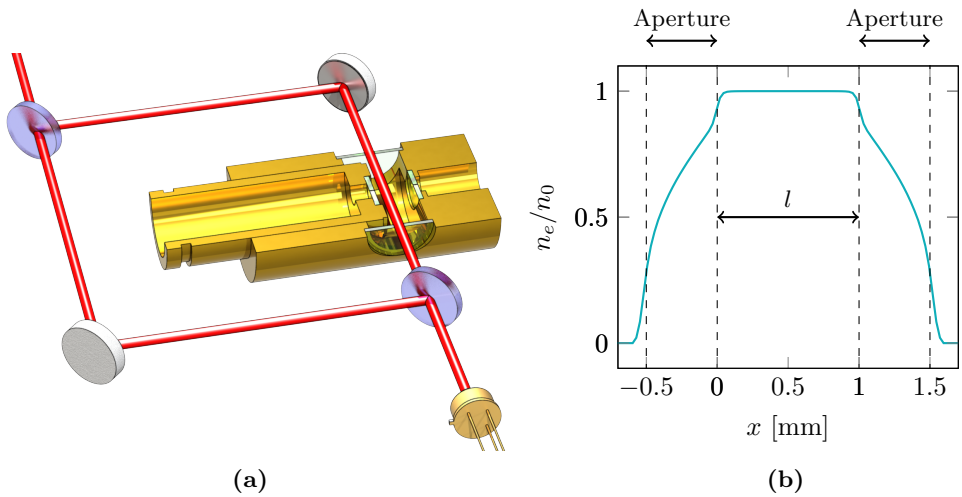

Figure 3.7: The gas density inside the cell was characterized interferometrically using the setup illustrated in (a). The HeNe-laser beams from the two arms interfere on the detector. The detector signal was acquired while the cell was filled and the final gas density was retrieved from the interferogram. Furthermore, the gradients at the entrance and exit of the cell were estimated through computational fluid dynamics, and the resulting density profile is shown in (b).

capillaries was 75 µm to 250 µm. Gas is injected through two lateral slits in the channel, approximately 2.5 mm from each end. The molecular number density is almost constant between the slits, and the gradient at the entrance and exit of the capillary is about 2.5 mm long, determined from computational fluid dynamics.

In addition to providing a gas target with a flat density profile and low turbulence, the inner walls of the capillary refocus the diffracting parts of the laser pulse, thus extending the interaction length in cases when this is limited by diffraction. Dielectric capillaries with small diameters can even act as waveguides, and this has been used previously to drive nonlinear plasma waves over lengths of several centimeters [30, 76].

3.1.3 Electron diagnostics

The beams of electrons accelerated in all experiments reported in this dissertation were detected and characterized as illustrated in Figure 3.1, using screens (Kodak Lanex Regular) which scintillate upon impact by electrons. The amount of charge in the beams was determined by calibrating the values of the pixels in the acquired images using a known source of light, and using published calibration factors for the scintillation efficiency of the screens [77, 78]. The divergence of the beams was determined by spatial calibration of these images and measurement of the distance between the interaction point and the scintillating screen.

In order to evaluate the energy of the accelerated electrons, a dipole magnetic field is used to disperse the electrons before impacting on the screen. In the experiments reported in Papers I-VIII and X, the magnet had a physical length of 100 mm and a peak magnetic field of approximately 0.7 T, and the scintillating screen was mounted

normal to the optical axis. In the approximately constant magnetic field, the electrons follow circular orbits with radii defined by $R = \gamma c m_e / eB$. For example, an electron with an energy of 100 MeV follows a path with a radius of curvature of 0.5 m, yielding an angular deviation on the order of 250 mrad after propagating through the magnetic field, whereas an electron with an energy of 75 MeV is deflected by an angle of 340 mrad.

The dispersion of electrons was determined more accurately, by numerically tracing electrons with different energies through a measured map of local magnetic field, from the gas target to the scintillating screen. The curve describing the dispersion of electrons at a scintillating screen placed 0.4 m from the interaction point, after propagation through the magnetic field used in the experiments, is shown in Figure 3.8.

An example of an image of the scintillating screen when impacted by an electron beam from one of the experiments is shown in false colors in the upper panel of Figure 3.9. By first summing the image along the non-dispersed direction, the energy spectrum may be determined. If dC denotes the total value of the signal in the acquired image due to the charge dQ impacting within a small region dz along the direction of dispersion, then

$$\begin{aligned} dC = k\,\mathrm{d}Q = g\,\frac{dQ}{dE}\,\frac{dE}{dz}\,dz \\ \Rightarrow \frac{dQ}{dE} = \frac{1}{g\,\frac{dE}{dz}}\,\frac{dC}{dz}\,, \end{aligned} \tag{3.2}$$

where $\frac{dQ}{dE}$ is the spectrum of electron energies to be determined and $\frac{dE}{dz}$ is the derivative of the dispersion curve shown in Figure 3.8. In this expression, g contains the calibration factor for the camera image response to the emitted photons for the specific configuration used (including the optical components and camera objective aperture). This factor also describes the scintillation efficiency, which is constant for electrons above approximately 3 MeV. Furthermore, electrons of different energies propagate through the scintillator at different angles; the largest impact angle corresponding to the lowest energy. Thus, the effective propagation distance of an electron within the scintillator, which is proportional to the number emitted photons, depends on the electron energy and is included in the calibration factor $g = g(\theta)$. The electron energy spectrum determined in this example is shown in the lower panel of Figure 3.9.

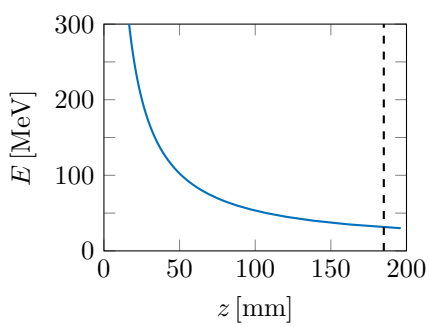

Figure 3.8: The dipole magnetic field disperses the electrons as described above before they impact on the scintillator. This dispersion curve was generated by numerically tracing electrons through the magnetic field until they impact on the scintillating screen using a geometry typically used in the experiments reported in the papers. Together with the beam divergence, the dispersion curve also determines the energy resolution of the spectrometer, which varies with energy. The dashed line indicates the greatest distance from the optical axis at which electrons are detected, due to geometrical constraints, thus defining the smallest detectable energy.

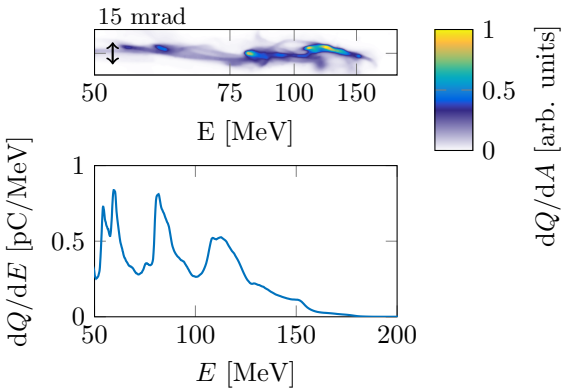

Figure 3.9: The upper figure shows an example of the image obtained with a scintillating screen (in false color) when impacted by an electron beam dispersed by the dipole magnetic field. A dispersion curve, generated by numerically tracing electrons of different energies through a map of measured magnetic field, provides a conversion from the position on the screen to electron energy. The corresponding electron energy spectrum is shown in the lower panel.

When this method is used, the energy resolution is determined by the divergence of the beam in combination with the dispersion by the magnet. After dispersion by the magnet, a perfectly monoenergetic beam will occupy an angle corresponding to the divergence of the beam, thus corresponding to an apparent energy spread. This effect is smaller at low energies, where the dispersion is large, than at high energies where the dispersion is small.

3.1.4 X-ray detection and diagnostics

In the experiments reported in Paper VI, the beams of X-rays generated by the electrons during laser wakefield acceleration were used as diagnostics of the accelerator itself and of the trapping of electrons. The critical energy of the synchrotron-like X-ray spectrum is determined by inserting a so-called Ross filter array [60, 79] into the X-ray beam and acquiring the intensity distributions using a 16-bit X-ray-sensitive CCD camera (Princeton SXTE/CCD-512TKB1). This method is similar to the way in which the three kinds of cone cells in the human eye, which are sensitive to different parts of the optical spectrum, are used to determine color. A Ross filter array consists of a number of thin metallic foils, each with a specific transmission function $G_i\,(E)$ placed at different locations in front of the CCD camera. The average pixel value behind each of these foils, N_i, is a measure of the X-ray beam filtered by the specific metallic foil,

$$N_i = \int \frac{dN_\gamma}{dE}\,(E)\; G_i\,(E)\, S\,(E)\, dE\,. \tag{3.3}$$

Here, $S\,(E)$ denotes the camera sensitivity, which is energy dependent, and also includes a calibration factor used to convert between pixel value and photon flux, $N_\gamma\,(E)$. The metallic filters are chosen such that the k-edge is within the typical energy range of the X-rays. By using an array of different filtering metals, such as vanadium, iron, copper and zirconium, the detected intensities in the different parts of the beam provide samples that can be used to numerically fit parameters of a desired spectral shape. Based on the discussion in Chapter 2, the X-ray spectrum is assumed to be synchrotron-like, and the parameters fitted are the critical energy and the amplitude. The method is illustrated in Figure 3.10, in which an assumed X-ray spectrum is shown together with the transmission curves for four different metal foils, each with a thickness of 5 μm.

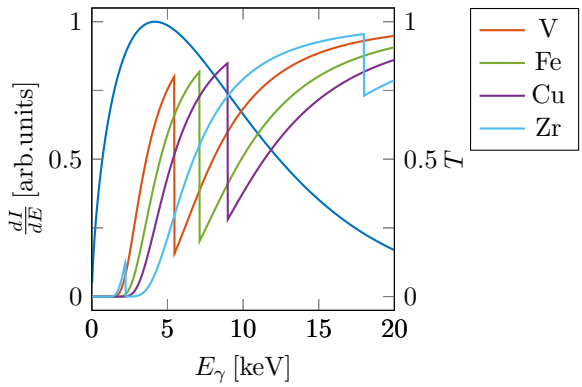

Figure 3.10: An example of a synchrotron-like spectrum with a critical energy of 5 keV, assumed for the X-rays generated in a laser wakefield accelerator. The transmission function is also plotted for a number of metallic foils, each with a thickness of 5 µm. The signal measured after the filters provides independent samples of the spectrum, which are used to determine the critical energy.

The transverse shape of the X-ray beam, measured using the CCD camera, is also used to determine the longitudinal position of the source. The generated X-ray beam has a full-cone angle of approximately $1/\gamma$, where γ is the Lorentz factor for the electrons. When the beam is generated inside a dielectric capillary tube, the tube itself will act as an aperture obstructing the X-rays. Thus, in the case of a fixed point source, the measured beam profile will have a sharp edge, corresponding to the shadow of the capillary exit aperture. For an extended source, longitudinal variations in source intensity, $\frac{dI}{dx}$, translate into radial variations of the intensity profile according to [80, 81]

$$N_\gamma(r) = \int_{-r_c L/r}^{0} \frac{dI}{dx} dx\,, \tag{3.4}$$

where r_c is the radius of the capillary tube, $x = 0$ defines the exit plane of the capillary tube, and L is the distance from the capillary exit plane to the detector plane. This method was used in the experiment presented in Paper VI to compare the location of trapping of electrons due to self-trapping and ionization-induced trapping.

3.1.5 Experiments on self-trapping

The aim of the studies on laser wakefield acceleration using self-trapping of electrons described in this dissertation was to improve the stability of the generated beams, and

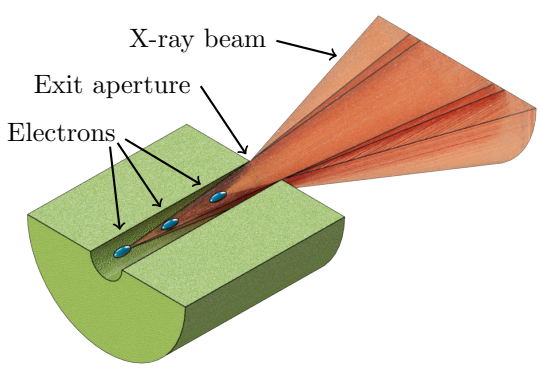

Figure 3.11: Schematic illustration of the cropping of the X-ray beam depending on the source position. The X-rays generated at a greater distance from the exit aperture will be cropped at a small angle, and will only contribute to the total flux close to the center of the profile. Each position in the X-ray beam is associated with a maximum distance from the contributing sources to the exit aperture.

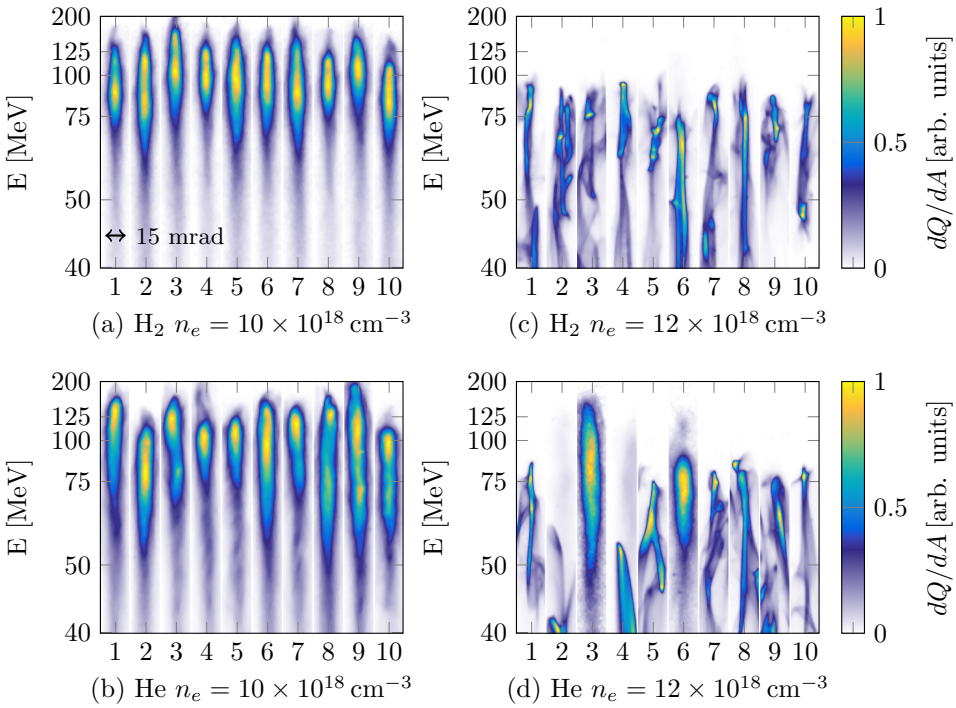

Figure 3.12: Comparison of stability of electron beams accelerated in plasmas formed from jets of hydrogen and helium supplied at different electron number densities. The reproducibility of the beams is similar for hydrogen and helium when using the same electron number densities. It was found that the beams were most reproducible at an electron number density of approximately 10×10^{18} cm^{-3}.

to minimize shot-to-shot fluctuations. The two most common choices of gas species in experiments on laser wakefield acceleration are hydrogen and helium, primarily because of their low number of ionization stages which minimizes the effect of ionization defocusing. Working only with helium would be preferable for safety reasons. Although the topic was discussed within the research community, no systematic comparison of the properties of the electron beams generated using these two gas species could be found in the literature. The experimental study on laser wakefield acceleration in jets of these two gases, reported in Paper III, was therefore performed in an attempt to fill this gap. The dispersed beams of electrons generated in plasmas formed from jets of hydrogen and helium are shown in Figure 3.12. It was found that there was no significant difference in the quality or the reproducibility of the beams generated using the two gas species, provided the electron number densities of the fully ionized gases were the same. However, the electron number density achieved using the same backing pressure is different for the two gases, due to the different flow properties of molecular hydrogen gas and atomic helium gas in a nozzle, and may result in an apparent difference in beam quality and reproducibility.

In the studies reported in Papers I and II, the reproducibility of electron beams generated using dielectric capillary tubes is compared to the typical stability of the

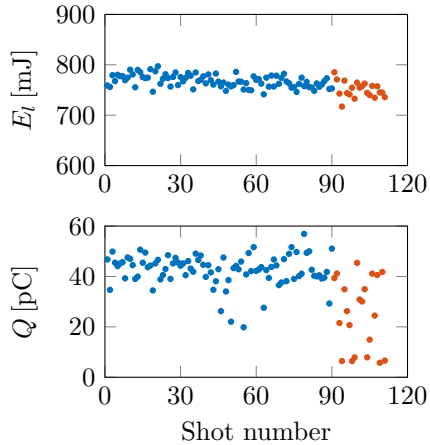

Figure 3.13: (a) The variation in laser pulse energy in a sequence of over 120 shots and (b) the corresponding detected charge for each shot. The laser pulse energy decreased slowly during the whole series of shots, while the detected charge remained constant within the shot-to-shot fluctuations for the first 90 shots. The active pointing stabilization system was turned off after these shots. After this, the detected charge fluctuates significantly and after a few tens of shots the capillary tube was damaged and became blocked.

beams generated in gas jets. It was found that the shot-to-shot variation in the amount of charge detected was reduced from approximately 50% when using gas jets, to 14% when using capillary tubes to confine the gas. The drawback of using capillary tubes in these experiments is the higher demand on laser beam pointing stability, since even the slightest misalignment may damage the capillary tubes. Therefore, the fast active pointing stabilization system was implemented in this experiment, and proved to be a necessary component of the experiment, as shown in Figure 3.13. This figure shows the laser pulse energy and the charge detected in a sequence of over 120 laser pulses. The laser pulse energy drifts only slightly during the whole series of shots. The charge shows only small shot-to-shot variations for the first 90 pulses. After this, the active beam pointing stabilization system was turned off, and the variations become significantly larger. After a few tens of laser pulses, the capillary tube became so damaged that the channel was blocked.

3.2 Particle-in-Cell simulations

Although this dissertation is primarily based on experiments, numerical methods are useful in supporting the experimental findings and in providing complementary data that would be difficult to obtain experimentally. The difficulty in the experiments lies in performing reliable measurements that allow the correct conclusions to be drawn from the results. Furthermore, the experimental methods used in the experiments of this dissertation measure the result of a physical interaction *after* it has taken place and, thus, do not directly probe the dynamics of the interaction. A complementary tool, used to support the experimental studies presented in this dissertation, is numerical calculation of the interaction of the laser pulses and plasmas in the corresponding experiments, using so-called *Particle-in-Cell* (PIC) simulations. A significant advantage of such numerical calculations is that they provide information on the electromagnetic fields and plasma phase space distributions resolved in space *and* time. Thus, numerical calculations provide snapshots of the interaction between a laser pulse and plasma. The drawback is that the reliability and accuracy of the results depend on the choice of numerical method and the parameters such as time and space resolution.

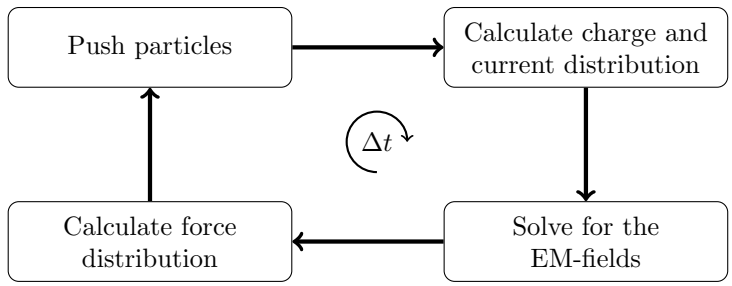

Figure 3.14: The principle of PIC simulation. Each round trip represents the progression in one time step.

PIC simulations are used to numerically solve the Vlasov equation (Eq. 1.10), using the iterative scheme illustrated in Figure 3.14. The six-dimensional distribution is represented in the PIC simulations using a finite set of macro-particles that represent the average properties of a bunch of particles. The charge distribution and current distribution are calculated on a grid using the position and velocity of these macro-particles. These distributions are then used to solve Maxwell's equations for the electric and magnetic fields at these grid points. In the next step, the fields are interpolated to calculate the Lorentz force applied to the macro-particles, which are then pushed accordingly in space over a distance corresponding to a finite time step.

When applying the PIC simulations to laser-plasma interactions, the distance between two grid points and the size of each time step must be sufficiently small to resolve the rapid oscillations of the laser pulse. The spatial dimension of the simulation is determined by the extent of the interaction being studied. The transverse dimension of the simulation geometry is usually set to a few times the diameter of the laser beam or the plasma wavelength, whichever is the largest. In the case of laser wakefield acceleration, the laser pulse typically propagates over a distance of millimeters in the plasma, which determines the longitudinal dimension of the simulation geometry. A moving window is then often employed to decrease the size of the simulated geometry. In this way, only the macro-particles and fields within a box surrounding and co-propagating with the laser pulse are considered, which reduces the computational demands considerably.

There are several numerical codes for PIC simulations, including, OSIRIS [82], VLPL [83], CALDER [84] and ELMIS [85]. These codes implement the PIC method slightly differently, which affects the resolution, accuracy and the time required for the simulations. In other codes, such as WAKE [86], the rapid oscillations of the laser pulse are not considered at all. Only the envelope of the laser pulse is considered, and the interaction between the laser pulse and the plasma is modeled by the ponderomotive force. In this model, the sizes of the time step and spatial scale are not limited by the laser frequency and wavelength, but instead by the time scale of the dynamics of the plasma, i.e., ω_{pe}^{-1}. Thus, the computational demands for simulations in underdense plasmas are much lower using such models. The drawback is, however, that many features, such as laser beam propagation and self-trapping, cannot be reliably reproduced.

The simulations reported in Papers V,VIII and IX were performed using the code CALDER-CIRC [87]. In this code, the geometry is defined in radial coordinates

around the optical axis of a propagating laser pulse. The mesh is defined by equally sized steps in the azimuthal angle, yielding a coarser mesh size at greater radii. The macro-particles are distributed over the grid with equal probability, leading to fewer macro-particles, but with a higher weight, at greater radii. Therefore, the resolution is poorer further away from the optical axis, thus also reducing the computational load while pushing particles. Furthermore, the electric and magnetic fields are described in azimuthal Fourier modes. In the case of laser wakefield acceleration, the interaction is almost cylindrically symmetric, and the fields can therefore usually be well-described using a small number of modes. This further reduces the computational load.

Simulations are performed on large computer clusters, where the computational load can be shared by several processor cores. Most simulations performed for the studies included in this dissertation were performed on the Alarik cluster at Lunarc, at Lund University. A typical simulation of wakefield acceleration in the geometries described in the papers requires on the order of 10,000 core hours, and the work load is divided between 400 cores, giving a total simulation time of 25 hours. In these simulations, the separation between grid points was about 20 nm in the longitudinal direction, and the time step was chosen to be 50 attoseconds in order to resolve the laser pulse oscillations. The distance between grid points may be larger in the radial direction and is often set to on the order of 100 nm.

Chapter 4

Controlled trapping in laser wakefield accelerators

In Chapter 2, the physics of plasma waves driven by laser pulses was discussed. It was described how electrons may be trapped in a plasma wave when the fluid velocity of the electrons forming the wave approaches and exceeds the phase velocity of the wave itself. In the case of self-trapping, this condition is reached simply by increasing the amplitude of the laser pulse in relation to the electron number density to drive the wave to the breaking limit. Achieving beams of accelerated electrons with single peaked energy spectra in experiments using this method of trapping electrons is difficult, and relies on a localized increase in the peak intensity of the laser pulse, for example, by self-focusing and/or self-compression of the laser pulse. In this way, the amplitude of the plasma wave is increased locally, and may lead to trapping of electrons if the wave reaches a sufficiently high amplitude. However, the shot-to-shot variations in the resulting beams of electrons should be as small as possible. This means that localized trapping must occur at the same place for every shot, and that the conditions for acceleration after this point are the same for every shot. When relying on nonlinear effects for self-focusing and pulse compression in the plasma, even the slightest variation in laser pulse parameters or plasma density distribution may alter both these conditions.

In this chapter, methods for controlled trapping of electrons in plasma waves are described. The aims in applying these methods are to find externally controlled parameters to enable tuning of the properties of the generated beams of electrons, such as beam charge, electron energy and energy spread, and to keep these externally controlled parameters constant in order to achieve small shot-to-shot fluctuations.

4.1 Trapping in density gradients and transitions

In contrast to the self-trapping mechanism, in which the amplitude of the wave is increased until the fluid velocity exceeds the phase velocity of the wave and the wave thereby breaks, trapping can be achieved by instead decreasing the phase velocity of the wave with respect to the electron fluid velocity. One way of doing this is by

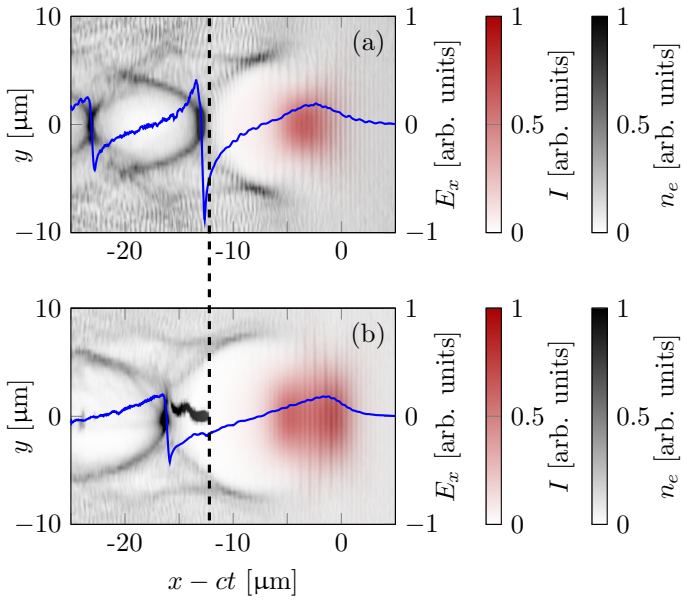

Figure 4.1: Results from a PIC simulation showing an electron plasma wave (black) and a corresponding on-axis electric field (blue) driven by a laser pulse (red) moving in the positive x-direction before (a) and after (b) a density down-ramp. Electrons injected in the first plasma period from the back are trapped and accelerated. The front of the trapped electron bunch corresponds to the back of the first plasma period before the density down-ramp (dashed line).

introducing a designed density modulation along the direction of propagation of the laser pulse. As the laser pulse propagates through a density down-ramp, the plasma frequency decreases as $\sqrt{n_e}$. The laser pulse group velocity increases correspondingly, according to Eqs 1.18, but the increase is negligible when considering a highly underdense plasma, for which $v_g \approx c$, and the net effect is an increasing plasma wavelength. The phase velocity of the plasma wave is equal to the group velocity of the laser pulse both before and after the density down-ramp. However, the *local* phase velocity is reduced within the down-ramp in order for the plasma wavelength to grow. Assuming that the density down-ramp is formed over a length l, the difference in the phase velocity at the end of the first period can be written as $\Delta v_p/c = (\lambda_{\mathrm{p},1} - \lambda_{\mathrm{p},2})/l$, where $\lambda_{\mathrm{p},1}$ and $\lambda_{\mathrm{p},2}$ are the plasma wavelengths before and after the density down-ramp. Thus, the reduction in phase velocity in relation to the peak fluid velocity may trigger trapping in a density down-ramp of sufficient steepness. This mechanism of trapping was proposed already in 1998 by Bulanov *et al.* [88] to localize and control trapping of electrons. The concept has been further studied and refined, and simulations have been described in several papers [89–91].

Snapshots from a PIC simulation of a plasma wave before and after a density down-ramp from $n_e = 12 \times 10^{18}$ cm^{-3} to $n_e = 6 \times 10^{18}$ cm^{-3} are shown in Figure 4.1. Here, the cross section of the electron density distribution in the plane of the laser polarization shows a clear bubble, free from electrons, being formed behind the laser pulse already before the density down-ramp (a). The electron void expands backwards in the ramp, and electrons are trapped over a length corresponding to the difference in plasma wavelength, in this case approximately 4 µm.

The original concept is based on long density gradients ($l \gg \lambda_{\mathrm{p}}$), which result in beams with large spreads in electron energy, since trapping then occurs over an extended distance. Short, sharp density transitions were first considered in the context of beam-driven plasma wakefield accelerators [92]. Trapping in short density transi-

tions usually results in beams of electrons with a small energy spread. In this case, there is a sudden change in the plasma wavelength, which cannot be followed by all the plasma electrons. Equivalently, the three-dimensional bubble structure following the laser pulse makes a sudden change in shape. Consequently, electrons located at the back of the bubble suddenly become located inside the bubble.

Controlled trapping has been achieved experimentally in laser wakefield accelerators using both these regimes of density modulations. Short density transitions have been formed, for example, using a second laser pulse to pre-form a transverse plasma channel [93] which expands to yield a local density depression at the time of arrival of the main laser pulse. Also, razor blades or plates with sharply cut edges have been used to obstruct jets of gas to form shock waves, which constitute sharp density transitions [94–96]. Longer density ramps have been formed using a gas jet inside a capillary tube [97].

Studies on trapping using both short and long density modulations were performed in two different experiments within the scope of this dissertation. Sharp density transitions were formed to trigger trapping of electrons by inserting a thin stainless steel wire (50 µm or 25 µm) into the gas flow from a 3 mm diameter nozzle, as illustrated in Figure 4.2(a), and as described in detail in Paper IV. The wire obstructing the jet generates shock waves which propagate outwards perpendicular to the length of the wire and at an angle relative to the gas flow determined by the Mach number. The density profile at the height of the axis of the laser pulse was characterized by interferometric measurements of the neutral gas distribution. The spatial resolution of the interferometric measurements is much poorer than what is needed to resolve the sharp density transitions of the shock waves. Thus, the measurements cannot be used directly to quantify the amplitude and length of the density transitions of the shock. Therefore, the results of the interferometric measurements were fitted to a piece-wise linear distribution, as shown in Figure 4.3(a), based on an extrapolated model of shock waves in a gas jet [98]. The sharp density transitions at ±0.5 mm are the outward moving shock waves, and the inner density ramps are due to the expansion waves that follow.

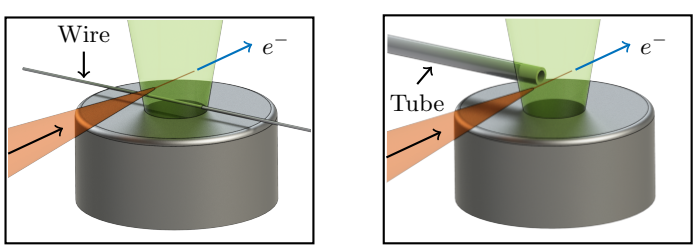

(a) (b)

Figure 4.2: Illustration of two methods used to manipulate the density profile along the optical axis of the laser pulse. In (a) a thin metallic wire is obstructing a gas jet flow to generate shock waves propagating towards the optical axis and forwards and backwards along the optical axis. In (b) a narrow tube is inserted into a jet of gas. An additional amount of gas is provided through this tube which is located right next to the optical axis of the laser pulse and results in a local increase in electron number density.

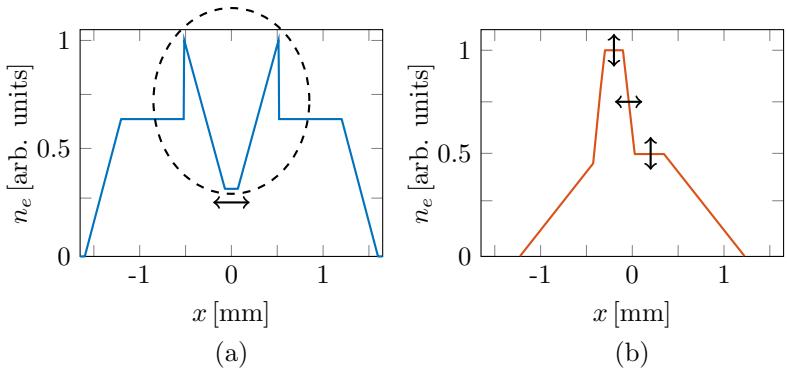

Figure 4.3: Piece-wise linear approximations of the density profile along the optical axis (x) of the laser pulse for the two ways to manipulate the density distribution of a gas jet. In (a) the shock waves generated by a wire are represented by the steep slopes propagating out from the center. At the location of the wire ($x = 0$) is a local density depression and the shock waves are accompanied with two expansion waves with density gradients with smaller slope. By moving the wire in the direction of the optical axis, the positions of the gradients can be shifted. In (b) an additional amount of gas is supplied through a narrow tube and generates a peak located at $x = -0.2$ mm. The density at the peak and the plateau are set individually using the backing pressure of the two nozzles. Furthermore, the length of the plateau is determined by the relative position of the narrow tube with respect to the larger gas jet. The arrows show how the density distributions are tunable as described above.

High-quality beams of accelerated electrons were generated in the experiment when using this setup to achieve controlled trapping. The electron energy spectra are quasi-monoenergetic with an energy spread of only approximately 4%. PIC simulations revealed that trapping of electrons is triggered already in the long density down-ramp, which is reached first by the laser pulse. However, as the plasma wavelength and the size of the bubble decrease in the following up-ramp, these electrons enter decelerating phases or even defocusing phases of the plasma wave. Thus, these electrons do not contribute to the final beam. Electrons are again trapped as the laser pulse and plasma wave reach the sharp density transition. These electrons are well localized within the plasma wave, and become accelerated in the following density plateau to an energy on the order of 100 MeV. Interferometric measurements show that the shape of the density modulation is unaltered by moving the wire along the optical axis of the laser pulse, provided that the longitudinal position of the wire is no more than 0.5 mm from the center of the nozzle. The position of trapping along the laser wakefield accelerator could be controlled in this way, and thereby also the length of the plasma remaining after the point of trapping. The experimental results showed that the peak energy of the electrons trapped using the wire could be tuned in this way.

The beams generated using this method of trapping were found to have approximately 25% smaller divergence than corresponding beams generated using self-trapping at the same electron number density. Furthermore, the beams generated using self-trapping were slightly elliptical in the plane of laser pulse polarization, in contrast to the beams generated using the wire in the jet (see Figure 4.4). This ellipticity indicates that the self-trapped electrons are influenced by the fields of the laser

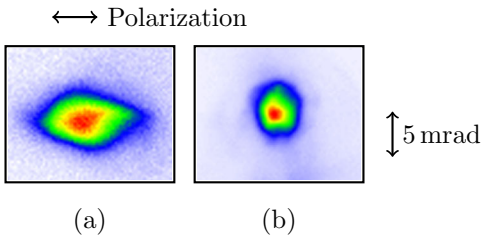

Figure 4.4: Comparison of the profiles of beams generated by self-trapping (a) and trapping in a density transition generated using a wire in a gas jet (b). The beams generated by self-trapping show evidence of interaction with the fields of the laser pulse.

pulse [99]. The electrons trapped in the density transition were not influenced by the fields of the laser pulse to the same degree, which results in circularly symmetric beams. This is probably due to the difference in plasma wavelength, which is lower when trapping is triggered by the density transition. In that case, the laser pulse occupies a smaller fraction of the first plasma period, and the electrons injected from the back therefore experience a smaller overlap with the laser pulse.

Long density ramps were produced in the experiment described in Paper V by inserting a narrow tube into the flow from a 2 mm diameter jet nozzle close to, and at the same height as, the optical axis of the laser pulse. The inner diameter was only 400 μm, and a separate flow of gas was supplied through the tube. The setup is illustrated in Figure 4.2(b), and the density distribution along the optical axis was characterized using the method described in Section 3.1.2. The additional optical path length of a probe beam was measured with and without the flow through the narrow tube, and the difference between the two measurements reveals the contribution to the density from the narrow tube. The density distribution along the optical axis of the laser pulse driving the plasma wave was determined from these measurements, and is sketched in Figure 4.3(b). Independently supplying gas from these two separate nozzles enables the density distribution to be tailored using three different parameters. The backing pressure of the gas supplied to the narrow tube is used to vary the density in the peak of the density distribution, while the backing pressure of the gas supplied to the jet nozzle is used to define the density in the following plateau. A gradient with a length of approximately 230 μm is formed between these two regions, which is unaffected by variations in the backing pressures within the range used in the experiment. The position of the narrow tube along the optical axis of the main laser beam determines the position of the density gradient in which electron trapping occurs.

Good control was achieved over the amount of trapped charge using this double gas source, and the amount of trapped charge scaled essentially linearly with the electron number density in the peak of the density distribution in the range from $7 \times 10^{18}\mathrm{cm}^{-3}$ to $10 \times 10^{18}\mathrm{cm}^{-3}$ (see Figure 4.5(b)). In this range, the shot-to-shot variation in the amount of detected charge from the fitted linear dependence was only 0.1 pC. For electron number densities in the peak above approximately $10 \times 10^{18}\mathrm{cm}^{-3}$, the amount of trapped charge fluctuated considerably from shot to shot. It is remarkable, however, that there is not a single data point below the fitted line extrapolated to higher electron number densities. This led to the conclusion that there is an additional set of electrons, self-trapped in the density peak, in some, but not all of the shots. This is further supported by the shape of the dispersed electron beams, which typically reveal two separate features for the shots containing higher amounts of charge. One

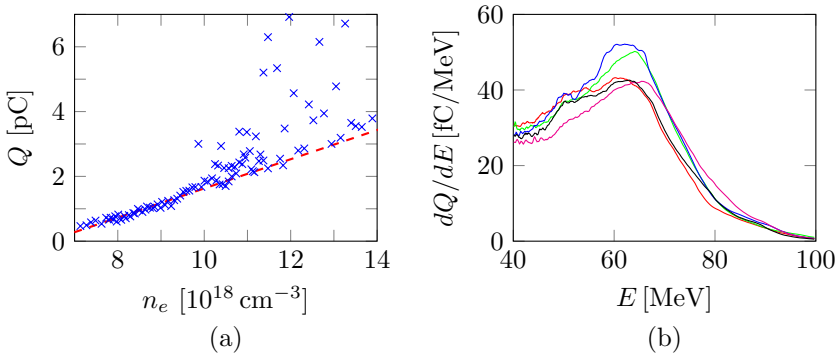

Figure 4.5: The amount of charge in the beams is controlled using the density in the peak of the density distribution (a) while keeping the density in the plateau fixed. At densities up to approximately 10×10^{18} cm^{-3} the amount of charge scales linearly with the density in the peak and the electron energy spectra (b) contain a single wide peak. At higher densities, the amount of charge fluctuates a lot, but never falls below the extrapolated line (dashed red).

of these components is very similar to the only component present at lower densities, while the other is similar to beams of self-trapped electrons achieved in experiments with a single gas source. The observation that the electron number density at the onset of these features fits perfectly with the threshold for self-trapping in the unmodulated 2 mm gas jet further supports this conclusion.

Trapping was achieved in both density modulation experiments, resulting in an increased level of control of the resulting electron beams. Although electron beams of high quality were generated when using the wire to modulate the density distribution, this setup is more experimentally demanding to use. The wire must be located close to the optical axis of the laser pulses, where it is ablated by the laser energy far out in the wings of the laser pulses. Therefore, the wire must be replaced after a finite number of shots, and the setup must be realigned, since trapping occurs only in a narrow parameter range using this setup. The setup using a second supply of gas through a narrow tube was therefore found to be more robust, and was used to produce electron beams with stable and peaked energy spectra in a sequence of over 100 shots.

Phase space rotation

When using the setup discussed above to introduce an additional amount of gas through a narrow tube, the relative energy spread of the beams of accelerated electrons was greater than when using a sharp density transition. This was expected, since trapping most likely occurs over the full length of the 230 μm long density ramp, thus filling up a large fraction of the first plasma period. The electrons trapped at the very beginning of the ramp are already significantly accelerated by the end of the ramp, where the last electrons are trapped with an initially low energy. Therefore, the bunch of trapped electrons has a large energy spread (≈100%) immediately after the density ramp. However, since the plasma wave period increases while the electrons are trapped in the density ramp, the electrons are also distributed longitudinally, with a clear correlation between their position in the plasma period (or phase) and their

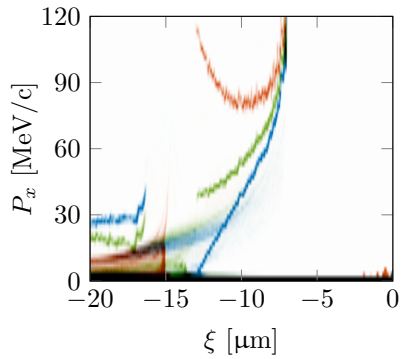

Figure 4.6: Longitudinal phase space distribution of electrons shown in a frame moving with the laser pulse located at $\xi = 0$ at three different locations along the accelerator. The distribution immediately after the density ramp is shown in blue. The distributions in green and red correspond to the times at which the back of the bubble has reached 75 μm and 300 μm after the density ramp, respectively. The average electron energy increases and the absolute energy spread decreases with acceleration distance.

energy after the density ramp. Thus, the slice energy spread, i.e., the energy spread of electrons located within a small longitudinal region, is expected to be much smaller.

This was confirmed in PIC simulations performed using the density distribution generated with the narrow tube inside the 2 mm gas jet. Figure 4.6 shows the longitudinal phase space distribution of electrons trapped in the first period of the plasma wave at three different positions along the accelerator. The distribution shown in blue (lowest curve) describes the electrons immediately after the density down-ramp. This distribution shows an almost linear correlation between position and forward momentum, corresponding to a large total energy spread, but with a significantly smaller slice energy spread.

The electrons are further accelerated in the density plateau by the electric field of the plasma wave, which increases towards the end of the first period. Thus, the energy of the electrons at the back of the plasma bubble increases more rapidly than that of the electrons at the front of the plasma bubble, thus decreasing the difference in energy. The distributions in green and red describe the distribution of the electrons at positions where the back of the plasma bubble has propagated 75 μm and 300 μm, respectively, after the density down-ramp, and clearly show an increase in average electron energy. At the same time, the absolute energy spread decreases, resulting in a peaked electron energy spectrum.

This effect, commonly known as phase space rotation, thus acts to decrease the energy spread of the trapped electrons, and explains why peaked electron energy spectra can also be observed in the case of long density ramps.

4.2 Ionization-induced trapping

The mechanisms of self-trapping and trapping in density down-ramps are both based on that part of the plasma electron population deviates from the motion of plasma oscillation, and ends up in an accelerating phase of a plasma wave with sufficiently large forward momentum to become trapped. The orbits shown in Figure 2.5 indicate the possibility of trapping electrons in a way that is completely different from the two methods described above. In this figure, the electrons described using the cold fluid model are all bound to the orbits that starts with $u_x \approx 0$ in front of the laser pulse. It is clear that, for this wave amplitude, no electrons will be self-trapped nor accelerated in the plasma wave. If another population of electrons could somehow be injected into,

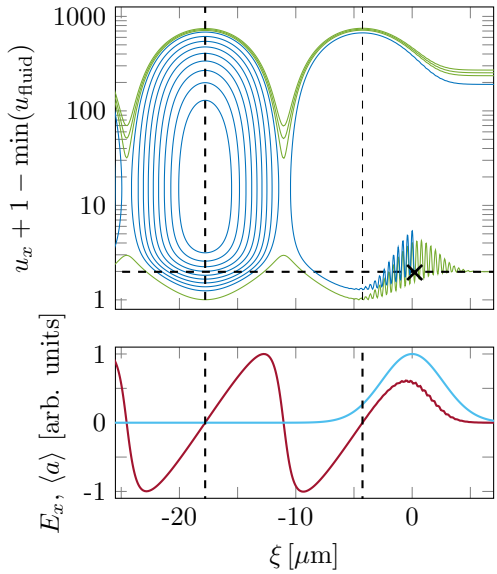

Figure 4.7: Longitudinal phase space orbits in the first plasma wave period are affected by the combined fields of a nonlinear plasma wave and the driving laser pulse shown in the lower panel. These orbits exhibit longitudinal oscillations, and when averaged over the fast oscillations, these orbits show a local increase in momenta due to the ponderomotive force. An electron released by ionization with zero forward momentum at the peak of the pulse (marked by a black cross) finds itself in an orbit in which it is accelerated in the field of the plasma wave. The orbits of electrons trapped in the second plasma period are unaffected by the laser pulse. However, these orbits are purely hypothetical, since no electrons are trapped there.

or created inside, the wake following the laser pulse, the forward momentum required for trapping would be significantly reduced.

This is the idea behind ionization-induced trapping, in which a separate population of electrons is generated by the release of more tightly bound electrons by ionization in the already formed plasma wave. In the original concept [100], a laser pulse was used to drive a wave in a plasma formed by the ionization of a high-Z gas up to a certain level, without self-trapping any electrons. A second intense laser pulse is then used to further ionize the remaining ions to the next ionization stage, thereby releasing new electrons with low initial momenta, that are independent of the electrons currently performing plasma oscillations according to the cold fluid model. Ionization-induced trapping has been achieved experimentally in a simplified setup [101–104], in which the second electron population is released by photoionization by the peak of the main laser pulse itself, and the mechanism of trapping has been studied analytically and by using PIC simulations [105]. The mechanism is illustrated in Figure 4.7, which shows orbits both in the first and second period of a nonlinear plasma wave. The electrons in the vicinity of the laser pulse are affected by the fields of the pulse, and it can be shown that electrons follow phase space orbits defined by the constant of motion, H, which can be written as [49]

$$u_x = \beta_p \gamma_p^2 \left(\frac{H}{c} + \phi(\xi) \right) \pm \gamma_p \sqrt{\gamma_p^2 \left(\frac{H}{c} + \phi(\xi) \right)^2 - 1 - \left(a(\xi) - a_{ion} \right)^2}, \qquad (4.1)$$

where a_{ion} is the value of the normalized vector potential at the occasion of ionization. For the background plasma electrons, $a_{ion} \approx 0$ since ionization occurs already at low intensity. This relation is still valid for electrons released closer to the peak of a linearly polarized laser pulse, since ionization occurs preferentially when the electric field peaks during the optical oscillations at which $a \approx 0$. The longitudinal momentum of the fluid electrons, shown by the lower green curve, exhibits oscillations in the vicinity of the

laser pulse. When averaged over these fast oscillations, the effect of the ponderomotive force is first a push forwards and then backwards, leading to the initial modulation in forward momentum. An electron released with zero momentum close to the peak of the laser pulse (indicated by a cross in Figure 4.7) finds itself in an orbit in which it will gain sufficient energy to slip backwards no further than to the position where the electric field changes sign. Following this orbit the electron is accelerated and will eventually catch up with the laser pulse and even overtake it.

Ionization-induced trapping was studied, within the scope of this dissertation, with the aim to determine the onset of trapping in dielectric capillary tubes filled with hydrogen gas with an additive of 1% nitrogen gas, as described in detail in Paper VI. Nitrogen gas was chosen as an additive since the appearance intensities of the two last ionization stages are appropriate for the laser parameters used in this experiment. In fact, the peak normalized vector potential of the laser pulse, when focused in vacuum, is $a_0 \approx 1.3$, and is too low to ionize the gas to these stages. However, after self-compression and self-focusing in the plasma, the intensity required to ionize these stages is reached.

In this study, the electron number density of the pre-formed plasma was set well above the threshold for both ionization-induced trapping and self-trapping. Therefore, the electron energy spectra are wide, and decrease with energy in both cases. Ionization-induced trapping in this configuration is essentially not localized, and occurs all along the plasma column as long as the intensity of the laser pulse is above the ionization thresholds for the final stages, and as long as a plasma wave is efficiently excited. When the nitrogen gas additive is used, the total amount of charge detected is about 100 pC, which is approximately twice that when using pure hydrogen gas.

Measurements of the beam profiles of the X-rays generated in the acceleration process show that the flux is approximately twice as high when using the gas mixture, than when using pure hydrogen gas. This is a direct result of the larger number of electrons trapped by ionization, compared to with self-trapping. The profiles of the X-ray beams, cropped by the dielectric capillary tube, are used to evaluate the longitudinal position of trapping of electrons, as described in Section 3.1.4. In this case, the exit aperture of the capillary tube makes an angle of 3.7 mrad as seen from the entrance aperture, which is much smaller than the divergence of the X-ray beam. Typical radial profiles of the X-ray beams generated during acceleration in the capillary tube, with and without the nitrogen gas additive, are shown in Figure 4.8(a). Two observations can be made upon comparing these profiles. Firstly, the X-ray beam profile obtained when using the gas mixture starts to decay rapidly at a smaller radius than in the case of pure hydrogen gas. Since X-rays are radiated by electrons almost immediately after being trapped, this indicates that trapping occurs at an earlier location within the capillary tube. Secondly, the slope is longer when the nitrogen is added, indicating that the transverse oscillations, and thus also the acceleration process, occur over a longer distance. The longitudinal X-ray emission profile was mapped from the radial distribution of X-rays, as described in Paper VI. The results are shown in Figure 4.8(b), where it can be seen that ionization-induced trapping starts approximately 1.5 mm before the position at which self-trapping starts. Furthermore, the electrons already trapped by ionization affect the wake by beam loading, and are believed to decrease the amount of self-trapped electrons when the gas mixture is used. At the position of the onset of self-trapping when using pure hydrogen gas, there is an increase in the rate of X-ray generation also when using the gas mixture. However,

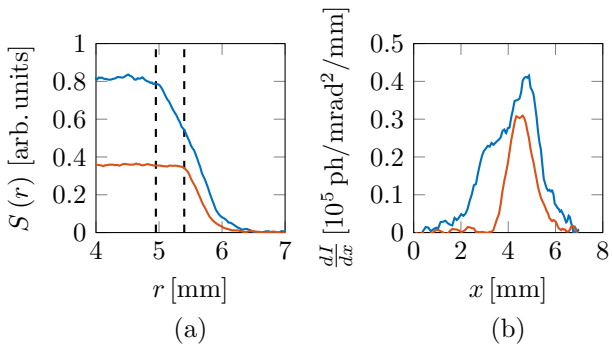

Figure 4.8: The radial profiles of the X-ray flux shown in (a) are used to determine the source position within the capillary tube shown in (b). Red curves correspond to a self-trapped electron beam, and blue curves corresponds to a beam of electrons trapped by ionization. The source position reveals that ionization-induced trapping occurs earlier in the plasma than self-trapping.

this increase is much smaller when the gas mixture is used, and thus electrons are already trapped by ionization.

Several benefits of using ionization-induced trapping were identified from these studies. (1) The amount of charge in the beams increases. (2) The increased charge leads to a higher X-ray flux being available for applications. (3) The shot-to-shot fluctuations in charge are reduced. The drawback, however, is that using ionization-induced trapping clearly produces electron beams with wide energy spectra, and is therefore not suitable for applications that require quasi-monoenergetic beams of electrons.

Ionization-induced trapping in a density down-ramp

Ionization-induced trapping was also studied using a variable-length gas cell, as presented in Paper VII. In this study, it was observed that the amount of trapped charge and the shape of the electron energy spectrum depend strongly on the longitudinal position of the focus with respect the gas cell. This therefore constitutes an experimental parameter that can be used to control the properties of the beams of accelerated electrons. The main effect of changing the longitudinal position of the focus position with respect to the gas cell is that the position at which the laser pulse intensity reaches the threshold for ionization of the final stages of nitrogen changes. This directly affects the length over which the electrons are accelerated after trapping, and thus the electron energy distribution. The amount of trapped charge can also be controlled using this method, since the length over which the electrons are trapped can be varied.

A major benefit of using ionization-induced trapping in laser wakefield accelerators is the increased amount of trapped charge that can be accelerated, as this improves the efficiency of the accelerator. However, the experimental electron energy spectra are typically wide and without peaked features. In order to use these beams in applications requiring peaked electron energy spectra, an energy filter must be employed. However, this leads to most of the accelerated electrons being wasted, which reduces the efficiency of the accelerator.

Ionization-induced trapping was combined with density down-ramps in the search for peaked electron energy spectra. In the study presented in Paper VIII, the density down-ramp at the exit of a gas cell (see Section 3.1.2), with an inner length of 0.7 mm, was used to localize ionization-induced trapping and to produce peaked electron energy

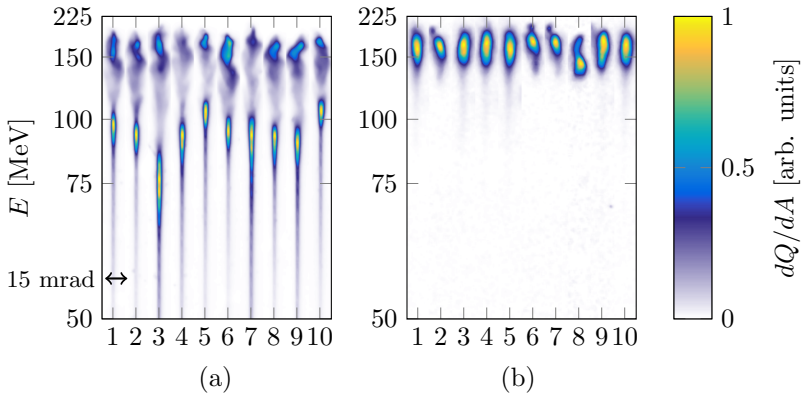

Figure 4.9: Dispersed beams of electrons trapped and accelerated in the density down-ramp at the exit of a gas cell filled with a mixture of hydrogen and 1% nitrogen (a) and pure hydrogen (b). In both cases the component at approximately 150 MeV is present whereas the component at lower energy only emerges when using the gas mixture.

spectra. Two separated energy peaks were observed in the experimental spectra, as shown in Figure 4.9(a) when using a gas mixture of hydrogen with 1% nitrogen. It was found that these two peaks corresponded to trapping of background electrons and electrons released by the ionization of N^{5+} and N^{6+}; in both cases trapped in the density down-ramp at the exit of the cell. These experimental results were supported by PIC simulations which revealed that an increased amount of electrons were trapped in the density down-ramp at the exit of the cell. Electrons from the background plasma were also trapped in this density down-ramp. However, these two components were clearly separated in longitudinal phase space; the electrons from the background plasma being located behind the electrons from the ionization of N^{5+} and N^{6+}. This leads to a separation of the two components in final electron energy, in agreement with the experimental observations. When pure hydrogen was used in the gas cell, but otherwise identical experimental parameters, only one of the peaks was observed, corresponding to regular trapping in the density down-ramp.

In another experiment, ionization-induced trapping was combined with a sharp density transition, as described in Paper IX. Here, the short density transition was formed by a shock wave emerging from the sharp straight edge of a silicon plate inserted at the front of a gas jet of helium with the addition of 1% nitrogen. This shock wave produced a sharp density transition towards lower electron density in the otherwise increasing density ramp at the front of the gas jet. The plasma wavelength decreases in the density up-ramp, which prevents trapping of both electrons from the background plasma and electrons released by ionization close to be peak of the laser pulse. At the position of the density transition, the threshold for trapping is locally reduced, and electrons released by ionization are thus trapped only in a very limited region.

The silicon plate with a straight edge was mounted on a motorized linear stage to allow scanning of the position of the shock wave. The peak electron energy was shown to be tunable between 70 MeV and 120 MeV and the mean electron energy spread of these beams was only 14 MeV.

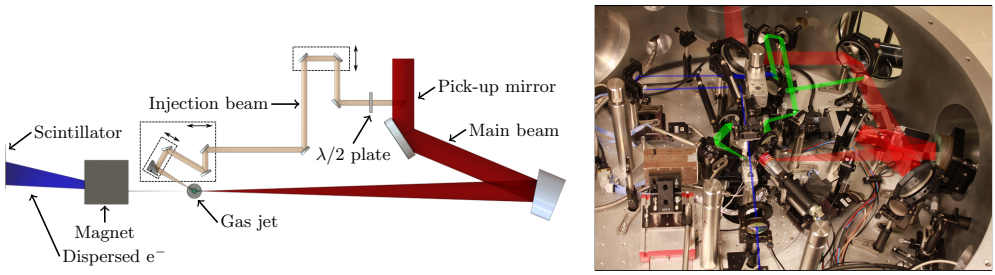

(a) (b)

Figure 4.10: (a) Overview of the compact experimental setup for trapping using colliding pulses, showing the pick-up mirror used to extract a fraction of the laser pulses. The two focusing mirrors are shown which generate two foci in the gas jet. The beams of accelerated electrons follow the optical axis of the main pulse until the electrons are dispersed by the dipole magnetic field and later impact on a scintillating screen imaged onto a CCD camera. (b) A photograph showing the experimental setup mounted inside the vacuum chamber. The red and green overlays show the beam paths of the main and injection pulses, respectively.

The two experiments reported in Papers VIII and IX show clearly that ionization-induced trapping can be combined with density modulations to localize electron trapping and in this way generate electron beams with peaked energy spectra. The method of using a separately mounted object to obstruct the gas jet provides the benefit of introducing a degree of freedom that can be used to control the position of trapping and thus the final energy of the electrons.

4.3 Trapping by colliding laser pulses

In the experiments presented in Paper X, a method of optically controlling the trapping of electrons was used. The original ideas to use additional laser pulses to trigger trapping of electrons were described in literature already in 1996. The first method proposed [106] was to use a second tightly focused laser pulse propagating transversely to, and intersecting, the optical axis of a laser pulse exciting a plasma wave. When timed such that the second pulse reaches the end of the first plasma period as it intersects the main optical axis, the ponderomotive force of the second laser pulse provides enough additional forward momentum to a few electrons for them to be trapped in the plasma wave. Later, in 1997, a mechanism was suggested for pre-accelerating electrons in the beat wave formed by the interference between two counter-propagating laser pulses [107]. In the most simplified setup, the main laser pulse, which drives the plasma wave, interferes with a second, weaker, pulse and thus only two laser pulses are required to be spatially and temporally overlapped [108]. A time-independent ponderomotive force due to the beat wave is present during the short collision of the pulses, and pre-accelerates electrons which are then trapped in the plasma wave driven by the main laser pulse. In the case of linearly polarized colliding pulses, the motion of the electrons in the interfering electromagnetic fields may become chaotic, and pre-acceleration is then rather due to stochastic heating [109–112]. A threshold for the onset of stochastic heating in terms of the normalized

vector potentials of the main and second pulse, a_0 and a_1, respectively, is $a_0 a_1 \gtrsim 0.5$ [110].

During the collision of two pulses with parallel polarization, the electric potential of the beat wave prevents motion of the plasma electrons over distances longer than the wavelength of the beat wave. Thus, the electrons cannot contribute to the plasma oscillations that form the wave in which the electrons should be trapped. This mechanism is called *plasma wake inhibition*, and results in a lower amount of trapped charge [113].

The results of the first experiments reported in the literature using the technique of two colliding laser pulses to trap electrons in a wakefield accelerator showed improved beam quality, compared to electron beams generated by self-trapping, with small energy spread and divergence [114]. Furthermore, the shot-to-shot fluctuations were significantly reduced. This technique of trapping has also been used in experimental studies of the pulse duration of the bunches of accelerated electrons [115] and in studies demonstrating beam-loading effects that lower the effective accelerating field [56]. Further theoretical work has shown that it is possible to generate beams with even smaller electron energy spread by decreasing the temperature (i.e., the energy spread) of the trapped electrons [116].

In the experiment presented in Paper X, a simplified, compact experimental setup was implemented and used to achieve controlled trapping by colliding the main laser pulse driving a plasma wave with a second weaker pulse. The experimental setup is illustrated schematically in Figure 4.10. The second pulse was generated by intersecting the main beam, before the focusing optics, with a small (13 mm diameter) mirror to reflect out the central part of the main beam, corresponding to approximately 8% of the total laser pulse energy. Both pulses were focused close to the center of a 2 mm hydrogen jet, and the two optical axes make an angle of 150°. The photograph in Figure 4.10 shows the inside of the vacuum chamber in which acceleration takes place.

The method of trapping electrons using two colliding laser pulses is experimentally demanding, as it requires spatial and temporal overlap of two femtosecond laser pulses focused to spots of a few tens of micrometers. A prism edge cut at an angle to vertically reflect both the main and injection pulses was introduced at the desired position of collision, and the edge was imaged using a microscope objective and a camera inside the vacuum chamber. The spatial overlap could then be achieved by steering both foci to this position, and the correct focusing of the two pulses found. A typical

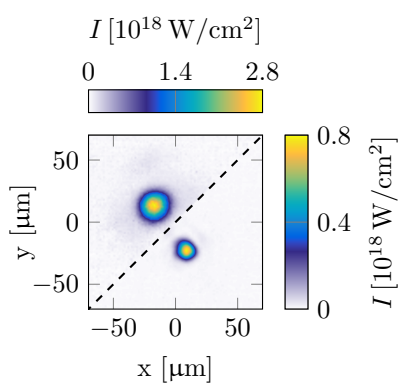

Figure 4.11: A microscope is used to image the focus of the main laser pulse (upper left) and the second pulse (lower right), simultaneously, at the point of collision by introducing a prism edge there to reflect both beams vertically. The dashed line marks the edge of the prism, and each of the two parts of the image is normalized to the corresponding peak intensity.

image of the two foci after spatial overlap is achieved is shown in Figure 4.11. Note that the color scales of the two parts of the image are different and that each color scale is normalized to the peak intensity in the corresponding part of the image in order to improve visibility. The peak intensity of the main pulse was found to be 2.8×10^{18} W/cm^{-2} and that of the injection pulse 0.8×10^{18} W/cm^{-2}.

Temporal overlap was achieved using a combination of two methods. First, an additional short laser probe pulse was used to backlight the interaction region, which is imaged using a lens. This allows time-resolved shadowgrams to be acquired with a camera. The ionization front of each laser pulse can readily be observed in these shadowgrams, and the timing of the two pulses can be set such that the ionization fronts overlap at the desired position and time. The spatio-temporal resolution of this method is on the order of 100 fs, and thus not sufficient to overlap the two 40 fs laser pulses accurately. In the second step, the microscope imaging the two foci on the prism edge was defocused such that the intensity distributions of the two pulses overlap on the camera chip. The optical path difference between the two pulses was then scanned in small steps (20 µm) until an interference pattern was observed, indicating that the two pulses have arrived simultaneously. The method is illustrated in Figure 4.12, where no interference pattern is observed in (a) but is clearly visible in (d).

Using this experimental setup high-quality beams of accelerated electrons were achieved. An example of such a beam is shown in Figure 4.13. The divergence was approximately 3 mrad, and the spectra were peaked with energy spread below 5 MeV, with peak energies up to 120 MeV. It was experimentally confirmed that trapping was triggered by the interference of the fields of the two laser pulses by introducing a half-wave plate to rotate the polarization of the injection beam with respect to the main beam. The maximum number of amount of accelerated electrons was found when the polarization of both pulses was in the same plane, and decreased as the polarization of the injection pulse was rotated. No beams of accelerated electrons were observed when the polarization of the two pulses was crossed.

The shot-to-shot fluctuations of the beams in this experiment were large in comparison to other experiments reported in the literature, in which trapping was triggered

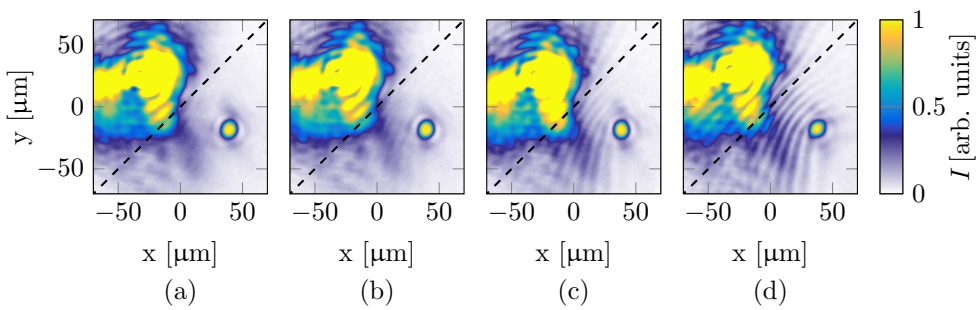

Figure 4.12: The microscope imaging the two foci is defocused such that the intensity distributions of the two pulses overlap on the camera detector. When scanning the optical path difference from 60 µm (a) in steps of 20 µm to 0 µm (d), an interference pattern appears, indicating that the two pulses have arrived simultaneously. The dashed lines marks the edge of the prism used to reflect the two pulses towards the imaging system.

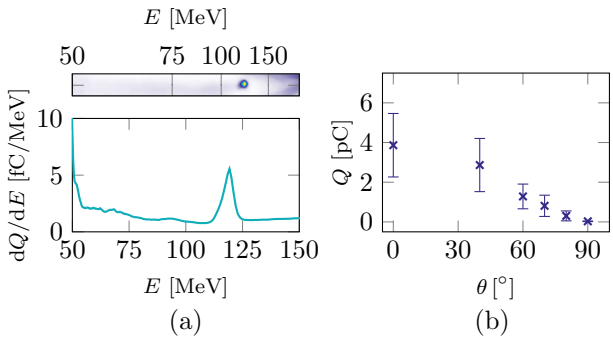

Figure 4.13: High-quality beam of accelerated electrons (a) obtained using the colliding pulse trapping technique. (b) The amount of charge in the beams of accelerated electrons was controlled by rotating the polarization of the two pulses, providing clear evidence that the interference of the two pulses is responsible for triggering the injection of the electrons. The full length of the error bars indicates one standard deviation.

by colliding laser pulses. These shot-to-shot fluctuations are probably due to small fluctuations in the pointing of the two laser pulses, which must be stable on a scale of a few micrometers.

In addition to demonstrating that interference triggers the trapping of electrons, rotation of the polarization of the injection beam provides a simple method of controlling the amount of charge in the beams of accelerated electrons. Furthermore, control over the peak electron energy was achieved by tuning the acceleration length after the collision point.

Chapter 5

Summary

This dissertation describes the underlying physics of laser wakefield acceleration of electrons. Experimental studies of the acceleration mechanism and different methods of trapping electrons in the accelerating structure are presented. One of the most important advantages of this kind of accelerator is its ability to produce large accelerating fields in small plasma waves, which in the experiments have wavelengths on the order of 10 μm. Based on the results of several experiments presented in this dissertation, the average effective strength of the accelerating fields was estimated to range from 30 MV/mm to 250 MV/mm, depending on the plasma parameters and the trapping mechanism. The characteristics of the beams are, to a large extent, influenced by the size of the accelerating structure, i.e., the plasma wave. For example, the bunches of accelerated electrons are intrinsically short since the electrons must be located within a fraction of a plasma period. Furthermore, the transverse source size of the X-rays generated in the acceleration process is small as the transverse deviation of the wiggling electrons is smaller than the transverse size of the plasma wave.

However, the small size of the accelerating structure also results in difficulties in operating laser wakefield accelerators as stable and robust sources of beams of accelerated electrons. Very small variations in the position of the electron bunch in relation to the plasma wave lead to large variations in the strength of the accelerating force, and thus also large variation in the final electron energy. Consequently, even a small longitudinal spread in the electrons in the plasma wave may lead to a large spread in the final energy distribution of the electrons. In addition, the excitation of the plasma waves using focused femtosecond laser pulses is highly nonlinear, and the accelerating fields are thus highly sensitive to variations in longitudinal waist position, laser beam pointing, pulse duration and energy. Thus, the laser wakefield accelerators used in the experiments presented here rely, to a large extent, on the mechanical stability of the optics mounted in the laser beamline and the target holders. Other sources of fluctuation affecting the experiments are the intrinsic fluctuations in the laser pulse parameters and gas distribution.

Improved shot-to-shot stability was achieved in the experiments presented in Papers I and II using dielectric capillary tubes to confine the gas to be ionized to a plasma, compared to the use of gas jets. In addition to increasing the fraction of useful laser energy for driving the plasma waves, the dielectric capillary tubes provided

Table 5.1: Comparison of the electron beams generated using different methods of controlled trapping. The values given are typical values obtained in the experiments described in this dissertation.

	Energy spectrum	Charge	Divergence	Robustness
Density down-ramp	Peaked	1 pC	10 mrad	Good
Density transition	Quasi-monoenergetic	10 pC	5 mrad	Good
Ionization	Wide	30 pC	15 mrad	Good
Colliding pulses	Quasi-monoenergetic	2 pC	3 mrad	Poor

stable and homogeneous distribution of gas which improves stability of the accelerator. The performance of laser wakefield accelerators based on jets of hydrogen and helium gas are compared in Paper III. Although ionization occurs differently for the two gases, no significant differences were found in the quality and stability of the beams generated in the parameter range used in this study, provided that the pressure of the gas supplied to the nozzle was set such that the electron number density in the plasmas formed were the same for both gas species.

Experimental studies are presented in which several different methods were used in order to control the characteristics of the electron beams generated. These methods have in common that they are used to externally control the process of trapping of electrons in the plasma wave. The different methods are summarized in Table 5.1 based on the experiments described in this dissertation.

Papers IV and V describe experiments in which the trapping of electrons was achieved by electron density modulations, which lead to modulation of the plasma wavelength and thus also the local phase velocity of the wave. Using a second gas source to generate a density modulation to trigger injection was shown to be robust, and the fluctuations in peak electron energy were small. Furthermore, this method is relatively simple to implement experimentally, and does not require high-precision alignment.

In contrast, trapping using colliding pulses, as described in Paper X, which may be used to generate beams of electrons of superior quality, requires an experimental setup of much higher complexity. Furthermore, significant effort is required to align the two pulses so that they overlap both spatially and temporally. In comparison to experiments based on density modulations, trapping using colliding pulses is not very robust, and the stability is partly limited by the mechanical stability of the optical mounts in the two beamlines.

Experiments on the trapping of electrons released by inner-shell ionization close to the peak of the laser pulse are described in Papers VI-IX. This method may be used when beams containing high charge are required. However, the electron spectra are usually wide if the method is not combined with other techniques, such as trapping by density modulation.

5.1 Outlook

Laser-driven acceleration of electrons is certainly a promising technique for future small-scale accelerators. The characteristics of the beams generated using the tech-

niques described in this dissertation are complementary to conventional techniques for particle acceleration. It is anticipated that future applications of particles accelerated using laser wakefield acceleration will take advantage of the unique features of these particle beams, such as the short pulse duration. However, efforts to reduce the fluctuations in the bunches of electrons generated must be continued, and future research should be devoted to developing methods of controlling the trapping of electrons.

Appendix

Target-normal sheath acceleration of protons

Laser acceleration of protons and positive ions is also possible using laser pulses provided by the Lund multi-terawatt laser, in a scheme called target-normal sheath acceleration (TNSA). Studies were also performed on TNSA of protons with the aim of tailoring and controlling the resulting beams of energetic ions. This chapter introduces the concept of TNSA and describes the experimental methods used in these studies. The results of the studies are also briefly discussed, and a future outlook is given.

A.1 Acceleration mechanism

Target-normal sheath acceleration [117] is based on the interaction between the fields of a laser pulse and the plasma formed from a solid target, typically a micrometer-thick metallic foil. Conceptually, TNSA can be regarded as a mechanism to rectify the oscillating electromagnetic field of a laser pulse to form a quasi-static electric field with constant direction determined by the target geometry. The mechanism is illustrated as a step-wise process in Figure A.1. In the first step (a), well before the peak of the laser pulse arrives, the target is ionized by the strong electric field in the pedestal of the pulse. The plasma immediately starts to expand into the surrounding vacuum, leading to a gradient in electron number density, from zero outside the expansion front to overcritical densities at the plasma–solid interface.

In the interaction between the main part of the laser pulse and the dense plasma, the electrons are heated and a fraction of the laser pulse energy is thus absorbed. The remainder of the laser pulse is reflected as it cannot propagate through the overcritical plasma. Several mechanisms for efficient heating of electrons in various regimes have been described in the literature, including relativistic $\mathbf{v} \times \mathbf{B}$ heating [118], resonant absorption, and Brunel heating [119]. In $\mathbf{v} \times \mathbf{B}$ heating , electrons are accelerated along the direction of propagation of the laser pulse in the interaction between the magnetic field of the laser pulse and the transverse velocity component of the electron due to the interaction with the electric field of the laser pulse. Resonant absorption occurs when the laser pulse approaches the surface of critical density. Here, the optical oscillations

resonantly drive an electron plasma wave, and the energy is dissipated as heat into the foil. The Brunel heating mechanism is used to describe the heating of electrons by a laser pulse with an oblique angle of incidence on a steep vacuum–plasma interface. In this case, the laser pulse is reflected close to the surface of critical density. The incident and reflected beams form an electric field component normal to the surface, which pulls electrons out of the plasma during half an optical cycle. When the field changes direction, these electrons are re-accelerated back into the plasma, where they are shielded from the fields. During each optical oscillation, a fraction of the plasma electrons gains energy from the electromagnetic fields of the laser pulse over half the optical cycle, and this energy is then delivered to the plasma in the other half of the optical cycle. This process dominates over $\mathbf{v} \times \mathbf{B}$ heating when the interface between the vacuum and the plasma is steep.

The heated electrons propagate through the foil towards the back where they leave the foil. The separation distance is on the order of the Debye length. These electrons form a sheath of negative charge in relation to the foil, which becomes positively charged. The quasi-static electric fields that are formed between the sheath and the foil are on the order of TV/m, and act to attract the electrons back to the foil, but may also accelerate any positively charged particles at the back the target. In practice, the surfaces of the target are covered with contaminants such as water molecules and hydrocarbon compounds. These are ionized by the strong electric fields resulting from the sheath of electrons, leaving a significant number free protons and other positive ions at the back of the foil. Finally, the accelerated protons and other light positively charged ions form a quasi-neutral beam of particles by combination with an equal number of negatively charged electrons. Due to the large charge-to-mass ratio in comparison to all other positive ions, the accelerated beam consists primarily of protons. Since the accelerating field peaks at the center of the electron distribution on the back of the foil, the most energetic protons will be directed close to the normal, with a smaller divergence than protons with lower energy.

Target-normal sheath acceleration of protons was first demonstrated at the beginning of the 2000s [120]. The beams emerging from the back of the target usually have considerable divergence, on the order of 0.1 rad. Furthermore, the energy spectra of the accelerated protons are approximately Maxwellian up to a certain cut-off energy, which was found to be approximately 5 MeV in these experiments.

A.2 Tools and methods

The studies were performed using the multi-terawatt laser at the Lund Laser Centre, described in Chapter 3, using focusing optics to provide a laser beam waist with a diameter of approximately 5 μm. The pulses were focused onto the front of flat aluminum foils with thickness of only a few micrometers. Absorption of the laser energy is increased by using an oblique angle of incidence, and was chosen to be 45° in these experiments.

After each shot, the foil at the position of the focus is evaporated, and the next shot must be aligned on a new spot on the foil. A system consisting of a three-axis motorized target foil holder and an optical imaging system was used for this, as described in Paper XI. The target holder is mounted inside the vacuum chamber, and allows for quick and accurate manipulation of the foil position with respect to

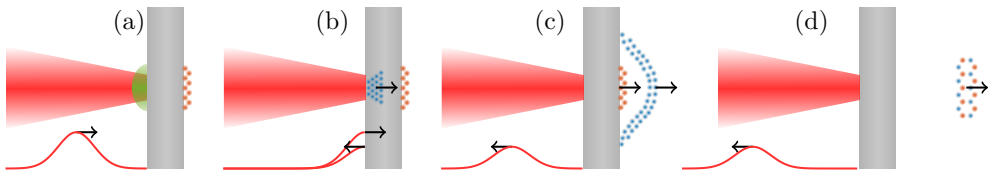

Figure A.1: Principle of target-normal sheath acceleration. (a) The electromagnetic fields in the ASE pedestal have ionized the front surface of a thin metallic foil forming a plasma at overcritical density (green shaded area). (b) The interaction between the main part of the laser pulse and the plasma heats electrons (blue), setting up a large flow of electrons towards the back of the foil. The unabsorbed part of the laser pulse is reflected. (c) The hot electrons leave the back of the foil and form a quasi-static electric field directed along the normal to the target surface. Contaminants, such as water and hydrocarbons, on the rear surface of the target are ionized, and the protons (red) and other positively charged ions are accelerated to high energies. (d) A beam of accelerated positive ions leaves the foil together with an equal number of electrons.

the laser beam waist. The optical imaging system is based on relay imaging using an infinity corrected microscope objective with a numerical aperture of 0.28 on the object side. The microscope is mounted such that when the target is retracted, the focus of the laser pulse is imaged onto the camera, and the reference position of the focus is stored in the software. The target can then be re-positioned with a new flat spot at the location of the laser pulse focus. Owing to the large numerical aperture of the imaging system, the depth of focus is short (approximately 4 μm) allowing positioning of the target to a precision much better than the Rayleigh length of the main laser pulse which, is approximately 70 μm.

A.2.1 Detection of protons

The accelerated protons were detected primarily using a polyvinyl toluene plastic scintillator that scintillates when impacted by protons and other positive ions (St. Gobain BC-408). The scintillator is imaged from the back, and images synchronized with the laser pulses are acquired using CCD cameras. A thin metallic foil covering the front of the scintillator prevents any stray light from the laser pulse being detected by the camera. This metallic foil also prevents heavier ions with low energies from impacting on the scintillator and, thus, only accelerated protons are detected in these experiments.

In order to determine the energy distribution of the protons, a 6 cm long dipole magnet, with a peak magnetic field of 0.7 T, was used to disperse the protons. The paths of protons of different energies are determined by numerically tracing them through a map of the magnetic field, similar to the experiments on laser wakefield acceleration. Since the beam divergence is significant in relation to the angular dispersion, a slit with a 1 mm opening is used to decrease the divergence in the direction of dispersion.

The scintillation efficiency, i.e., the number of photons emitted per impact, is energy dependent. Therefore, cross-calibration was performed with a CR-39 nuclear track detector [121]. A sheet of CR-39 is inserted so as to intersect half the beam at the location of the scintillator, such that the dispersed protons impacts both de-

tectors. After etching the CR-39, the impact positions are readily observable using a microscope, providing an absolutely calibrated proton energy spectrum to which the signal from the scintillator is calibrated.

The profiles of the beams of accelerated protons are characterized by inserting another scintillator into the beam before the dispersing dipole magnet. The scintillation efficiency is dependent on proton energy, and the signal detected in this case represents the areal density of deposited energy.

A.2.2 Two-pulse generation

A specially designed mirror and mount were placed in the beamline close to, but before, the focusing mirror. This consists of two separate flat mirrors with straight edges, and the substrate is cut at an angle to allow the reflecting surfaces to be placed very close to each other (see Figure A.2(a)). The incident laser beam was centered on the combined mirror such that one half of the beam was reflected from each mirror. Motorized tip and tilt of one of the mirrors allows for angular separation of the beams resulting in two separate foci at the surface of the target foil, as shown in Figure A.2(b). When the two reflecting surfaces are in the same plane, the two halves of the beam are combined after focusing, generating a single focal spot on the target.

Furthermore, one of the mirrors is mounted so as to allow translation along the normal to the mirror surface, allowing the relative time of arrival of the two pulses to be controlled. A motorized translation stage also allows the mount to be moved parallel to the surface of the mirrors, allowing the energy ratio between the two parts to be varied. In future studies of TNSA these features will be utilized to study the acceleration mechanism while altering the energy ratio between the two parts of the laser beam and the relative time of arrival of the two pulses.

Aligning the two mirror surfaces to form a single focus after introducing the mirror mount in the beam is technically challenging. While observing images of the two foci at the repetition rate of the laser, the separation is decreased until only one spot

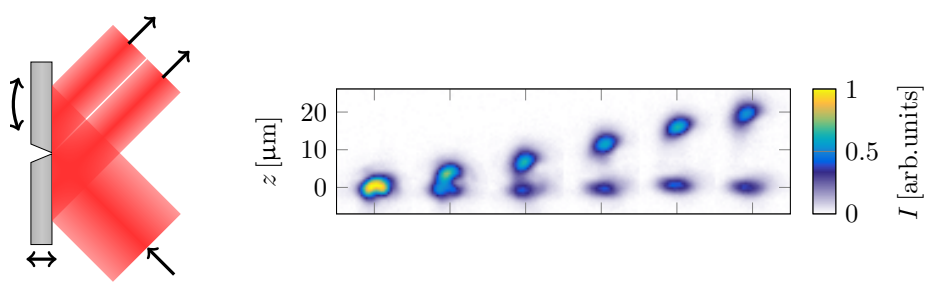

Figure A.2: (a) Schematic illustration of the mount of two flat mirrors to generate two separate pulses to arrive at the target foil. Motorized alignment screws allow control of the relative separation of the two foci (b). Furthermore, one of the mirrors may be translated normal to the reflecting surface to adjust the relative time of arrival of the two pulses. The full mirror mount may also be translated parallel to the reflecting surface to vary the relative energy in the two pulses.

is observed, indicating that the two mirror surfaces are parallel. However, the two surfaces may not yet be in a common plane, resulting in the two separate pulses arriving at the target at different times. The position of one of the mirrors along the surface normal is then scanned until an interference pattern is observed in the focal plane. This interference pattern appears only when the two pulses arrive in the focal plane simultaneously. The position is then optimized to maximize the visibility of the fringes in the interference pattern.

When the angular separation of the two beams is small, two to three clear fringes are usually observed. The precision of the motorized tip, tilt and translation is not sufficient to perfectly overlap the two pulses to form a single, symmetric focal spot. Therefore, the deformable mirror and wave front sensor described in Chapter 3 are used in a feedback loop to remove residual wave front deformations resulting from imperfect alignment of the two mirrors.

A.3 Proton beam collimation

The sketch of the process of TNSA in Figure A.1 indicates that the divergence of the proton beams depends on the shape of the sheath field formed on the back of the target. This suggests on the possibility of controlling the beam divergence by manipulating the shape of the sheath.

Using a tightly focused laser pulse to irradiate the front of the target allows a large fraction of the laser pulse energy to heat electrons. Although the electrons spread out as they propagate through the target, with an opening angle of approximately 30°, the sheath formed is still small in the transverse direction, and corresponds to a small radius of curvature of the overall shape of the sheath. In order to increase the radius of curvature, the spot size of the laser pulse irradiating a 3 µm aluminum foil was increased in one experiment by defocusing the target as described in Paper XII. This increases the transverse size of the sheath and thus the radius of curvature. The experimental results from the first part of the study presented in Paper XII clearly show a decrease in the size of the proton beams. Examples of the beam profiles observed for different locations of the foil with respect to the position of the beam waist are shown in Figure A.3. The Rayleigh length of the beam in this configuration was approximately 120 µm. The diameter of the spot irradiating the foil is thus increased

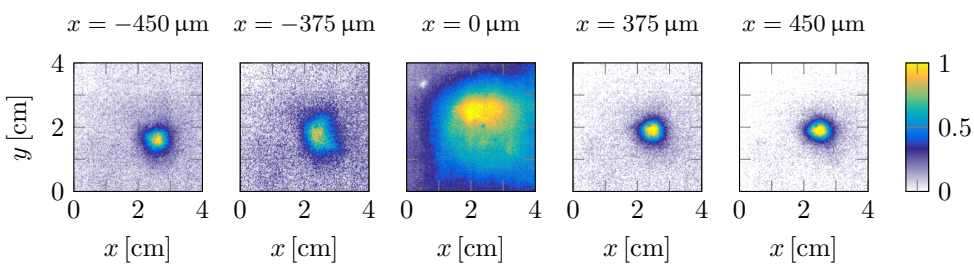

Figure A.3: Examples of observed proton beam profiles with the foil at different positions along the optical axis. $x = 0$ corresponds to the foil being positioned at the waist of the beam. When the foil is placed a few hundred micrometers from the waist, corresponding to $3 - 4$ Rayleigh lengths, the size of the proton beam decreases.

by a factor of approximately 4 at a distance of 450 µm from the waist. Increasing the laser spot size by this amount, drastically reduces the beam divergence, as can be seen in the figure.

The strength of the sheath field is expected to decrease as the size of the of irradiated spot increases, since the electrons propagating through the foil are spread out over a larger area. This was confirmed in the experiments. However, although the maximum proton energy in these beams decreases, the number of protons at lower energy increases.

A.4 Two-pulse TNSA

In the second part of the experiment reported in Paper XII, the mirror mount described above was used to generate two separate foci on the target foil. The aim of this setup was to manipulate the distribution of electrons on the back of the foil and thus tailor the shape of the sheath. The principle is illustrated schematically in Figure A.4. Without any separation (a), a large number of electrons leave the back of the foil and form a high-amplitude sheath field, but with transversely small size. The protons are thus accelerated to high energies, with a large divergence. As the two foci are slightly separated (b), the flows of electrons resulting from the interaction of each laser pulse form a common sheath. The amplitude of this field is smaller, but covers a larger area. The sheath field is almost flat in a large fraction of this area, in the region between the two foci, and the protons are thus accelerated in the same direction. Therefore, a collimation effect can be expected in the direction of separation of the two foci, while in the other direction, the sheath field is expected to be similar to that when using only one pulse.

Upon increasing the separation even more, Figure A.4(c), the flows of electrons resulting from each laser pulse form separate sheaths as they leave the back of the target. The shape of each sheath is similar to the shape when a single laser pulse is used, and the radius of curvature of these sheaths is expected to be equal to that when using only one pulse. The beam divergence should therefore be similar to the divergence of the beam generated with a single pulse. However, due to the decreased

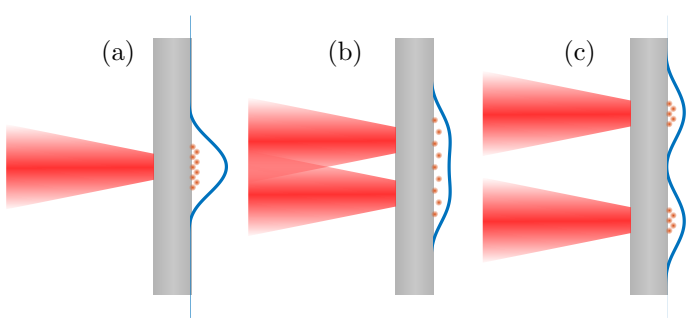

Figure A.4: Illustration of sheath field formation using a single pulse (a) and two pulses, containing the same total energy, at a small separation (b) and at a large separation (c). When the flow of electrons from the two pulses combine to form a single sheath, the distribution in the center is flattened, leading to a decrease in divergence.

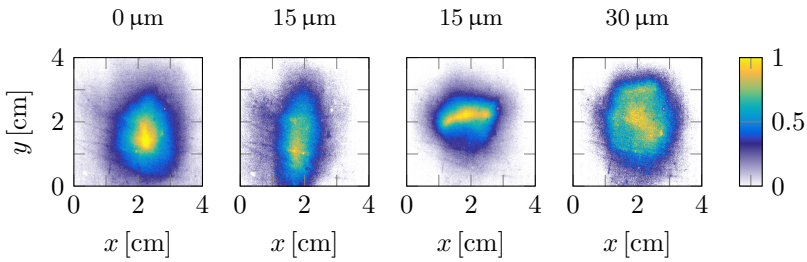

Figure A.5: Examples of observed proton beam profiles for different separations of the two foci. When the two foci overlap the beam profile is circularly symmetric. For separations of approximately 15 µm, either horizontally or vertically, the beam profiles show a decrease in divergence in the perpendicular direction. Increasing the separation further yields a circularly symmetric beam profile, indicating that the sheath fields do not overlap on the back of the target.

sheath field amplitude, the maximum proton energy in these beams in this case is smaller.

Figure A.5 shows proton beam profiles for four different separations of the two foci. In the left panel the two pulses overlap leading to a beam with large divergence. When the foci are separated by 15 µm (two central panels) the beam profiles are no longer circularly symmetric. These beams have a smaller divergence in the direction of separation of the two foci. Finally, when the separation is further increased, the proton beam profile again becomes circularly symmetric, with a size approximately equal to the case when the two foci overlap.

A.5 Outlook

It was shown in these experiments that the shape of the laser pulse irradiating the front of the target side plays a crucial role in controlling the shape and divergence of the beams of protons accelerated in the process. In further experiments, TNSA will be studied by varying both the time of arrival of the two pulses, and the splitting ratio of the energy.

The author's contribution

The experiments reported in all the papers except Paper IX were performed using the Lund multi-terawatt laser. In these experiments, the author took an active part in the operation of the laser system and work in the laboratory.

I **Enhanced stability of laser wakefield acceleration using dielectric capillary tubes**
The author took an active part in the planning of the experiments and was largely responsible for the major part of the experimental setup, including laser beam focusing and stabilization, and electron and X-ray diagnostics. The experimental data were recorded by the author in collaboration with the co-authors. The author analyzed the data, wrote the manuscript with input from the co-authors, and was the corresponding author in the submission and review process.

II **Reproducibility of electron beams from laser wakefield acceleration in capillary tubes**
The author took an active part in the planning of the experiments and was largely responsible for the major part of the experimental setup, including laser beam focusing and stabilization, and electron and X-ray diagnostics. The experimental data were recorded by the author in collaboration with the co-authors. The author contributed to the analysis of the data and to the preparation of the manuscript.

III **Supersonic jets of hydrogen and helium for laser wakefield acceleration**
The author took an active part in the planning of the experiments and was largely responsible for the major part of the experimental setup, including laser beam focusing and stabilization, and electron and X-ray diagnostics. The experimental data were recorded by the author in collaboration with the co-authors. Furthermore, the author arranged the setup for target characterization and performed the corresponding data analysis. The author contributed to the analysis of the data and to the preparation of the manuscript.

IV **Laser wakefield acceleration using wire produced double density ramps**
The author took part in the experimental work during the recording of the data and in scientific discussions during the analysis of the experimental results. The author gave feedback on the manuscript.

V **Down-ramp injection and independently controlled acceleration of electrons in a tailored laser wakefield accelerator**
The author proposed and designed the experiment, including the target design, and arranged the experimental setup. The author recorded and analyzed the data on electron acceleration, and developed and implemented the novel technique for target characterization. The author took a leading role in designing the cases for Particle-in-Cell simulations. The author wrote the manuscript with input from the co-authors, and was the corresponding author in the submission and review process.

VI **Dynamics of ionization-induced electron injection in the high density regime of laser wakefield acceleration**
The author took an active part in the planning of the experiments and was largely responsible for the major part of the experimental setup, including laser beam focusing and stabilization, and electron and X-ray diagnostics. The experimental data were recorded by the author in collaboration with the co-authors. The author contributed to the analysis of the data and to the preparation of the manuscript.

VII **Investigation of ionization-induced electron injection in a wakefield driven by laser inside a gas cell**
The author took an active part in the planning of the experiments and was largely responsible for the major part of the experimental setup, including laser beam focusing and stabilization, and electron and X-ray diagnostics. The experimental data were recorded by the author in collaboration with the co-authors. The author contributed to the analysis of the data and to the preparation of the manuscript.

VIII **Localization of ionization-induced trapping in a laser wakefield accelerator using a density down-ramp**
The author took an active part in the planning of the experiments and was largely responsible for the major part of the experimental setup, including laser beam focusing and stabilization, and electron and X-ray diagnostics. The experimental data were recorded by the author in collaboration with the co-authors. The author analyzed the data, wrote the manuscript with input from the co-authors, and was the corresponding author in the submission and review process.

IX **Shock assisted ionization injection in laser-plasma accelerators**
The author took part in the design and performance of the experiment, and in the scientific discussions that followed. The author gave feedback on the manuscript.

X **Injection of electrons by colliding laser pulses in a laser wakefield accelerator**
The author took a major role in the experiment, including designing the laser focusing and collision geometry. The author arranged the experimental setup and had an active part in recording the data on electron acceleration. The author analyzed the data, wrote the manuscript with input from the co-authors, and was the corresponding author in the submission and review process.

Papers belonging to the Appendix

XI **A setup for studies of laser-driven proton acceleration at the Lund Laser Centre**
The author took part in designing and performing the experiment, and in the scientific discussions that followed. The author contributed to the analysis of the data and to the preparation of the manuscript.

XII **Manipulation of the spatial distribution of laser-accelerated proton beams by varying the laser intensity distribution**
The author took part in designing and performing the experiment and in the scientific discussions that followed. The author contributed to the analysis of the data and to the preparation of the manuscript.

Acknowledgements

The work with and completion of this dissertation would not have been possible without the help, assistance and support of such a large number of people that all of them cannot be named here. Their support is however deeply appreciated. In particular, I would like to thank all the co-authors of the papers included in this dissertation.

I wish to express my sincere gratitude toward my supervisors Claes-Göran Wahlström and Olle Lundh. You have provided me with much valuable support and guidance over the years that I have worked with you. In addition, I much appreciate the atmosphere that you provide within the research group, which allowed me to gain confidence and independence when beginning my work on experimental physics.

I have had the great pleasure to work closely with Anders Persson in the daily work in the laboratory, and in particular with the multi-terawatt laser system. I have learned so much just by observing you work in the laboratory and even more by listening to your explanations. I deeply appreciate how you are willing to share your knowledge and experience with me.

Much of the practical experimental work was carried out in collaboration with my dear friend Bastian Aurand. Your practical skills together with your attitude towards the experimental work was much valuable for the work presented in this dissertation. Also, your company in the laboratory helped me keep up the pace and never give up whenever I felt discouraged.

The simulations used in this dissertation were performed by Xavier Davoine together with Henrik Ekerfelt. I want to thank you both for all inspiring discussions we have had, which always led to better understanding of our experiments.

During the work for this dissertation I have been part of a research group all working on topics related to the interaction between matter and femtosecond laser pulses of high intensity. I want to thank all, past and present, members of this group, with whom I have had the pleasure to work, both for your direct contribution to the work described in this dissertation, but also for the good company you have provided; Jonas Björklund Svensson, Matthias Burza, Isabel Gallardo González, Guillaume Genoud, Malay Dalui, Solveig Reymond, Lovisa Senje, Philip Siederer, Jack Strand Berg, Kristoffer Svensson, Franck Wojda, and Elnaz Yazdani.

I want to thank my international collaborators with whom I have had the opportunity to work. In particular, I want to thank Brigitte Cros, Sandrine Dobosz Dufrénoy, Frédéric Desforges, Thomas Audet, and Jinchuan Ju. I greatly appreciated working with you and your attitude towards the research and studies we have performed. You provided an open environment which allowed for detailed discussions to be held about our experiments and I am convinced that this have led to a better understanding of the physics and paved the way for efficiently performing the experiments.

In addition, over the years I have had the pleasure to get acquainted with a large number of past and present members of the division of Atomic Physics. You all contribute to the positive, friendly, and inspiring work environment; For this I want to thank you all. In particular, I want to acknowledge the support from Bertil Hermansson, Åke Johansson, Harriet Lindahl, Camilla Nilsson, Anne Petterson-Jungbeck and Jakob Testad.

Finally, I want to express my deepest appreciation toward my family; Hans Axel, Carina, Andreas and Fredrik, as well as Sophia and Aina. Over the years you have always supported me, trusted my choices and provided me with helpful advice both personally and technically.

References

1. D. Strickland and G. Mourou. *Compression of amplified chirped optical pulses.* Opt. Commun. **56**, 219 (1985).

2. S.-W. Bahk, P. Rousseau, T. A. Planchon, V. Chvykov, G. Kalintchenko, A. Maksimchuk, G. A. Mourou and V. Yanovsky. *Generation and characterization of the highest laser intensities (10^{22} W/cm^2).* Opt. Lett. **29**, 2837 (2004).

3. P. F. Moulton. *Spectroscopic and laser characteristics of Ti:Al_2O_3.* J. Opt. Soc. Am. B **3**, 125 (1986).

4. B. E. A. Saleh and M. C. Teich. *Fundamentals of photonics, 2nd Edition.* Wiley (2007).

5. G. S. Vornov and N. B. Delone. *Ionization of the xenon atom by the electric field of ruby laser emission.* J. Exp. Theor. Phys. Lett. **1**, 66 (1965).

6. G. S. Vornov and N. B. Delone. *Many-photon ionization of the xenon atom by ruby laser radiation.* J. Exp. Theor. Phys. **23**, 54 (1966).

7. P. Agostini, F. Fabre, G. Mainfray, G. Petite and N. K. Rahman. *Free-free transitions following six-photon ionization of xenon atoms.* Phys. Rev. Lett. **42**, 1127 (1979).

8. P. Kruit, J. Kimman, H. G. Muller and M. J. van der Wiel. *Electron spectra from multiphoton ionization of xenon at 1064, 532, and 355 nm.* Phys. Rev. A **28**, 248 (1983).

9. F. F. Chen. *Introduction to plasma physics and controlled fusion.* Plenum Press (1984).

10. W. L. Kruer. *The physics of laser plasma interactions.* Westview Press (2003).

11. B. Quesnel and P. Mora. *Theory and simulation of the interaction of ultraintense laser pulses with electrons in vacuum.* Phys. Rev. E **58**, 3719 (1998).

12. P. Gibbon. *Short pulse laser interactions with matter.* Imperial College Press (2005).

13. E. Esarey, C. B. Schroeder and W. P. Leemans. *Physics of laser-driven plasma-based electron accelerators.* Rev. Mod. Phys. **81**, 1229 (2009).

14. L. M. Gorbunov and V. I. Kirsanov. *Excitation of plasma waves by an electromagnetic wave packet.* J. Exp. Theor. Phys. **66**, 290 (1987).

15. P. Sprangle, E. Esarey, A. Ting and G. Joyce. *Laser wakefield acceleration and relativistic optical guiding.* Appl. Phys. Lett. **53**, 2146 (1988).

16. P. Sprangle, E. Esarey and A. Ting. *Nonlinear interaction of intense laser pulses in plasmas.* Phys. Rev. A **41**, 4463 (1990).

17. P. Sprangle, E. Esarey and A. Ting. *Nonlinear theory of intense laser-plasma interactions.* Phys. Rev. Lett. **64**, 2011 (1990).

18. E. Esarey, P. Sprangle, J. Krall, A. Ting and G. Joyce. *Optically guided laser wake-field acceleration.* Phys. Fluids B **5**, 2690 (1993).

19. C. B. Schroeder, E. Esarey, B. A. Shadwick and W. P. Leemans. *Trapping, dark current, and wave breaking in nonlinear plasma waves.* Phys. Plasmas **13**, 033103 (2006).

20. A. Pukhov and J. Meyer-ter Vehn. *Laser wake field acceleration: the highly non-linear broken-wave regime.* Appl. Phys. B **74**, 355 (2002).

21. W. Lu, C. Huang, M. Zhou, W. B. Mori and T. Katsouleas. *Nonlinear theory for relativistic plasma wakefields in the blowout regime.* Phys. Rev. Lett. **96**, 165002 (2006).

22. W. Lu, C. Huang, M. Zhou, M. Tzoufras, F. S. Tsung, W. B. Mori and T. Katsouleas. *A nonlinear theory for multidimensional relativistic plasma wave wakefields.* Phys. Plasmas **13**, 056709 (2006).

23. W. Lu, M. Tzoufras, C. Joshi, F. S. Tsung, W. B. Mori, J. Vieira, R. A. Fonseca and L. O. Silva. *Generating multi-GeV electron bunches using single stage laser wakefield acceleration in a 3D nonlinear regime.* Phys. Rev. ST Accel. Beams **10**, 061301 (2007).

24. W. B. Mori. *The physics of the nonlinear optics of plasmas at relativistic intensities for short-pulse lasers.* IEEE J. Quant. Electron. **33**, 1942 (1997).

25. E. Esarey, P. Sprangle, J. Krall and A. Ting. *Overview of plasma-based accelerator concepts.* IEEE Trans. Plasma Sci. **24**, 252 (1996).

26. G.-Z Sun, E. Ott, Y. C. Lee and P. Guzdar. *Self-focusing of short intense pulses in plasmas.* Phys. Fluids **30**, 526 (1987).

27. P. Sprangle, C.-M. Tang and E. Esarey. *Relativistic self-focusing of short-pulse radiation beams in plasmas.* IEEE Trans. Plasma Sci. **15**, 145 (1987).

28. C. D. Decker, W. B. Mori, K.-C. Tzeng and T. Katsouleas. *The evolution of ultra-intense, short-pulse lasers in underdense plasmas.* Phys. Plasmas **3**, 2047 (1996).

29. N. E. Andreev and M. V. Chegotov. *Wakefield generation as the mechanism behind spectral shift of a short laser pulse.* J. Exp. Theor. Phys. **101**, 56 (2005).

30. F. Wojda, K. Cassou, G. Genoud, M. Burza, Y. Glinec, O. Lundh, A. Persson, G. Vieux, E. Brunetti, R. P. Shanks, D. Jaroszynski, N. E. Andreev, C.-G. Wahlström and B. Cros. *Laser-driven plasma waves in capillary tubes.* Phys. Rev. E **80**, 066403 (2009).

31. N. E. Andreev, K. Cassou, F. Wojda, G. Genoud, M. Burza, O. Lundh, A. Persson, B. Cros, V. E. Fortov and C.-G. Wahlström. *Analysis of laser wakefield dynamics in capillary tubes.* New J. Phys. **12**, 045024 (2010).

32. E. Esarey, C. B. Schroeder, B. A. Shadwick, J. S. Wurtele and W. P. Leemans. *Nonlinear theory of nonparaxial laser pulse propagation in plasma channels.* Phys. Rev. Lett. **84**, 3081 (2000).

33. J. Faure, Y. Glinec, J. J. Santos, F. Ewald, J.-P. Rousseau, S. Kiselev, A. Pukhov, T. Hosokai and V. Malka. *Observation of laser-pulse shortening in nonlinear plasma waves.* Phys. Rev. Lett. **95**, 205003 (2005).

34. J. Schreiber, C. Bellei, S. P. D. Mangles, C. Kamperidis, S. Kneip, S. R. Nagel, C. A. J. Palmer, P. P. Rajeev, M. J. V. Streeter and Z. Najmudin. *Complete temporal characterization of asymmetric pulse compression in a laser wakefield.* Phys. Rev. Lett. **105**, 235003 (2010).

35. D. F. Gordon, B. Hafizi, R. F. Hubbard, J. R. Peñano, P. Sprangle and A. Ting. *Asymmetric self-phase modulation and compression of short laser pulses in plasma channels.* Phys. Rev. Lett. **90**, 215001 (2003).

36. C. Joshi, T. Tajima, J. M. Dawson, H. A. Baldis and N. A. Ebrahim. *Forward Raman instability and electron acceleration.* Phys. Rev. Lett. **47**, 1285 (1981).

37. N. E. Andreev, L. M. Gorbunov, V. I. Kirsanov, A. A. Pogosova and R. R. Ramazashvili. *Resonant excitation of wakefields by a laser pulse in a plasma.* Pis'ma Zh. Eksp. Teor. Fiz **55**, 551 (1992).

38. T. M. Antonsen and P. Mora. *Self-focusing and Raman scattering of laser pulses in tenuous plasmas.* Phys. Rev. Lett. **69**, 2204 (1992).

39. P. Sprangle, E. Esarey, J. Krall and G. Joyce. *Propagation and guiding of intense laser pulses in plasmas.* Phys. Rev. Lett. **69**, 2200 (1992).

40. S. V. Bulanov, F. Pegoraro, A. M. Pukhov and A. S. Sakharov. *Transverse-wake wave breaking.* Phys. Rev. Lett. **78**, 4205 (1997).

41. E. Esarey and M. Pilloff. *Trapping and acceleration in nonlinear plasma waves.* Phys. Plasmas **2**, 1432 (1995).

42. J. M. Dawson. *Nonlinear electron oscillations in a cold plasma.* Phys. Rev. **113**, 383 (1959).

43. A. I. Akhiezer and R. V. Polovin. *Theory of wave motion of an electron plasma.* J. Exp. Theor. Phys. **3**, 696 (1956).

44. A. G. R. Thomas. *Scalings for radiation from plasma bubbles.* Phys. Plasmas **17**, 056708 (2010).

45. S. P. D. Mangles, G. Genoud, M. S. Bloom, M. Burza, Z. Najmudin, A. Persson, K. Svensson, A. G. R. Thomas and C.-G. Wahlström. *Self-injection threshold in self-guided laser wakefield accelerators.* Phys. Rev. ST Accel. Beams **15**, 011302 (2012).

46. S. P. D. Mangles, C. D. Murphy, Z. Najmudin, A. G. R. Thomas, J. L. Collier, A. E. Dangor, E. J. Divall, P. S. Foster, J. G. Gallacher, C. J. Hooker, D. A. Jaroszynski, A. J. Langley, W. B. Mori, P. A. Norreys, F. S. Tsung, R. Viskup, B. R. Walton and K. Krushelnick. *Monoenergetic beams of relativistic electrons from intense laser-plasma interactions.* Nature **431**, 535 (2004).

47. C. G. R. Geddes, Cs. Toth, J. van Tilborg, E. Esarey, C. B. Schroeder, D. Bruhwiler, C. Nieter, J. Cary and W. P. Leemans. *High-quality electron beams from a laser wakefield accelerator using plasma-channel guiding.* Nature **431**, 538 (2004).

48. J. Faure, Y. Glinec, A. Pukhov, S. Kiselev, S. Gordienko, E. Lefebvre, J.-P. Rousseau, F. Burgy and V. Malka. *A laser-plasma accelerator producing monoenergetic electron beams.* Nature **431**, 541 (2004).

49. J. Faure. *Plasma injection schemes for laser-plasma accelerators.* CERN Yellow Reports **1**, 143 (2016).

50. H. Suk, C. Kim, G. H. Kim, J. U. Kim, I. S. Ko and H. J. Lee. *Energy enhancement in the self-injected laser wakefield acceleration using tapered plasma densities.* Phys. Lett. A **316**, 233 (2003).

51. P. Sprangle, B. Hafizi, J. R. Peñano, R. F. Hubbard, A. Ting, C. I. Moore, D. F. Gordon, A. Zigler, D. Kaganovich and T. M. Antonsen. *Wakefield generation and GeV acceleration in tapered plasma channels.* Phys. Rev. E **63**, 056405 (2001).

52. W. Rittershofer, C. B. Schroeder, E. Esarey, F. J. Grüner and W. P. Leemans. *Tapered plasma channels to phase-lock accelerating and focusing forces in laser-plasma accelerators.* Phys. Plasmas **17**, 063104 (2010).

53. E. Guillaume, A. Döpp, C. Thaury, K. Ta Phuoc, A. Lifschitz, G. Grittani, J.-P. Goddet, A. Tafzi, S. W. Chou, L. Veisz and V. Malka. *Electron rephasing in a laser-wakefield accelerator.* Phys. Rev. Lett. **115**, 155002 (2015).

54. S. Wilks, T. Katsouleas, J. M. Dawson, P. Chen and J. J. Su. *Beam loading in plasma waves.* IEEE Trans. Plasma Sci. **15**, 210 (1987).

55. M. Tzoufras, W. Lu, F. S. Tsung, C. Huang, W. B. Mori, T. Katsouleas, J. Vieira, R. A. Fonseca and L. O. Silva. *Beam loading in the nonlinear regime of plasma-based acceleration.* Phys. Rev. Lett. **101**, 145002 (2008).

56. C. Rechatin, X. Davoine, A. Lifschitz, A. Ben Ismail, J. Lim, E. Lefebvre, J. Faure and V. Malka. *Observation of beam loading in a laser-plasma accelerator.* Phys. Rev. Lett. **103**, 194804 (2009).

57. M. Migliorati, A. Bacci, C. Benedetti, E. Chiadroni, M. Ferrario, A. Mostacci, L. Palumbo, A. R. Rossi, L. Serafini and P. Antici. *Intrinsic normalized emittance growth in laser-driven electron accelerators.* Phys. Rev. ST Accel. Beams **16**, 011302 (2013).

58. S. Corde, K. Ta Phuoc, G. Lambert, R. Fitour, V. Malka, A. Rousse, A. Beck and E. Lefebvre. *Femtosecond x rays from laser-plasma accelerators.* Rev. Mod. Phys. **85**, 1 (2013).

59. E. Esarey, B. A. Shadwick, P. Catravas and W. P. Leemans. *Synchrotron radiation from electron beams in plasma-focusing channels.* Phys. Rev. E **65**, 056505 (2002).

60. S. Fourmaux, S. Corde, K. Ta Phuoc, P. M. Leguay, S. Payeur, P. Lassonde, S. Gnedyuk, G. Lebrun, C. Fourment, V. Malka, S. Sebban, A. Rousse and J. C. Kieffer. *Demonstration of the synchrotron-type spectrum of laser-produced Betatron radiation.* New J. Phys. **13**, 033017 (2011).

61. M. Schnell, A. Sävert, B. Landgraf, M. Reuter, Mm Nicolai, O. Jäckel, C. Peth, T. Thiele, O. Jansen, A. Pukhov, O. Willi, M. C. Kaluza and C. Spielmann. *Deducing the electron-beam diameter in a laser-plasma accelerator using X-ray betatron radiation.* Phys. Rev. Lett. **108**, 075001 (2012).

62. K. Wille. *The physics of particle accelerators.* Oxford University Press (2000).

63. S. Kneip, C. McGuffey, J. L. Martins, M. S. Bloom, V. Chvykov, F. Dollar, R. Fonseca, S. Jolly, G. Kalintchenko, K. Krushelnick, A. Maksimchuk, S. P. D. Mangles, Z. Najmudin, C. A. J. Palmer, K. Ta Phuoc, W. Schumaker, L. O. Silva, J. Vieira, V. Yanovsky and A. G. R. Thomas. *Characterization of transverse beam emittance of electrons from a laser-plasma wakefield accelerator in the bubble regime using betatron x-ray radiation.* Phys. Rev. ST Accel. Beams **15**, 021302 (2012).

64. S. Fritzler, E. Lefebvre, V. Malka, F. Burgy, A. E. Dangor, K. Krushelnick, S. P. D. Mangles, Z. Najmudin, J.-P. Rousseau and B. Walton. *Emittance measurements of a laser-wakefield-accelerated electron beam.* Phys. Rev. Lett. **92**, 165006 (2004).

65. C. M. S. Sears, A. Buck, K. Schmid, J. Mikhailova, F. Krausz and L. Veisz. *Emittance and divergence of laser wakefield accelerated electrons.* Phys. Rev. ST Accel. Beams **13**, 092803 (2010).

66. E. Brunetti, R. P. Shanks, G. G. Manahan, M. R. Islam, B. Ersfeld, M. P. Anania, S. Cipiccia, R. C. Issac, G. Raj, G. Vieux, G. H. Welsh, S. M. Wiggins and D. A. Jaroszynski. *Low emittance, high brilliance relativistic electron beams from a laser-plasma accelerator.* Phys. Rev. Lett. **105**, 215007 (2010).

67. R. Weingartner, S. Raith, A. Popp, S. Chou, J. Wenz, K. Khrennikov, M. Heigoldt, A. R. Maier, N. Kajumba, M. Fuchs, B. Zeitler, F. Krausz, S. Karsch and F. Grüner. *Ultralow emittance electron beams from a laser-wakefield accelerator.* Phys. Rev. ST Accel. Beams **15**, 111302 (2012).

68. D. E. Spence, P. N. Kean and W. Sibbett. *60-fsec pulse generation from a self-mode-locked Ti:sapphire laser.* Opt. Lett. **16**, 42 (1991).

69. A. Jullien, O. Albert, F. Burgy, G. Hamoniaux, J.-P. Rousseau, J.-P. Chambaret, F. Augé-Rochereau, G. Chériaux, J. Etchepare, N. Minkovski and S. M. Saltiel. 10^{-10} *temporal contrast for femtosecond ultraintense lasers by cross-polarized wave generation.* Opt. Lett. **30**, 920 (2005).

70. E. R. Dobrovinskaya, L. A. Lytvynov and V. Pishchik. *Sapphire.* Springer (2009).

71. P. Tournois. *Acousto-optic programmable dispersive filter for adaptive compensation of group delay time dispersion in laser systems.* Opt. Commun. **140**, 245 (1997).

72. G. Genoud, F. Wojda, M. Burza, A. Persson and C.-G. Wahlström. *Active control of the pointing of a multi-terawatt laser.* Rev. Sci. Instrum. **82**, 033102 (2011).

73. K. Schmid and L. Veisz. *Supersonic gas jets for laser-plasma experiments.* Rev. Sci. Instrum. **83**, 053304 (2012).

74. J. Yarwood. *High vacuum technique : theory, practice, industrial applications and properties of materials.* Chapman & Hall (1955).

75. G. Lewin. *Fundamentals of vacuum science and technology.* McGraw-Hill (1965).

76. D. P. Umstadter. *Laser-wakefield accelerators: Glass-guiding benefits.* Nat. Photon. **5**, 576 (2011).

77. Y. Glinec, J. Faure, A. Guemnie-Tafo, V. Malka, H. Monard, J. P. Larbre, V. De Waele, J. L. Marignier and M. Mostafavi. *Absolute calibration for a broad range single shot electron spectrometer.* Rev. Sci. Instrum. **77**, 103301 (2006).

78. A. Buck, K. Zeil, A. Popp, K. Schmid, A. Jochmann, S. D. Kraft, B. Hidding, T. Kudyakov, C. M. S. Sears, L. Veisz, S. Karsch, J. Pawelke, R. Sauerbrey, T. Cowan, F. Krausz and U. Schramm. *Absolute charge calibration of scintillating screens for relativistic electron detection.* Rev. Sci. Instrum. **81**, 033301 (2010).

79. P. Kirkpatrick. *On the theory and use of Ross filters.* Rev. Sci. Instrum. **10**, 186 (1939).

80. S. Corde, C. Thaury, K. Ta Phuoc, A. Lifschitz, G. Lambert, J. Faure, O. Lundh, E. Benveniste, A. Ben-Ismail, L. Arantchuk, A. Marciniak, A. Stordeur, P. Brijesh, A. Rousse, A. Specka and V. Malka. *Mapping the x-ray emission region in a laser-plasma accelerator.* Phys. Rev. Lett. **107**, 215004 (2011).

81. G. Genoud, K. Cassou, F. Wojda, H. E. Ferrari, C. Kamperidis, M. Burza, A. Persson, J. Uhlig, S. Kneip, S. P. D. Mangles, A. Lifschitz, B. Cros and C.-G. Wahlström. *Laser-plasma electron acceleration in dielectric capillary tubes.* Appl. Phys. B **105**, 309 (2011).

82. R. A. Fonseca, L. O. Silva, F. S. Tsung, V. K. Decyk, W. Lu, C. Ren, W. B. Mori, S. Deng, S. Lee, T. Katsouleas and J. C. Adam. *OSIRIS: A three-dimensional, fully relativistic particle in cell code for modeling plasma based accelerators.* In P.M.A. Sloot et al (Ed.) ICCS 2002 Proceedings, LNCS **2331**, 342 (2002).

83. A. Pukhov. *Three-dimensional electromagnetic relativistic particle-in-cell code VLPL (Virtual Laser Plasma Lab).* J. Plasma Phys. **61**, 425 (1999).

84. E. Lefebvre, N. Cochet, S. Fritzler, V. Malka, M.-M. Aléonard, J.-F. Chemin, S. Darbon, L. Disdier, J. Faure, A. Fedotoff, O. Landoas, G. Malka, V. Méot, P. Morel, M. Rabec Le Gloahec, A. Rouyer, Ch. Rubbelynck, V. Tikhonchuk, R. Wrobel, P. Audebert and C. Rousseaux. *Electron and photon production from relativistic laser-plasma interactions.* Nucl. Fusion **43**, 629 (2003).

85. A. Gonoskov, S. Bastrakov, E. Efimenko, A. Ilderton, M. Marklund, I. Meyerov, A. Muraviev, A. Sergeev, I. Surmin and E. Wallin. *Extended particle-in-cell schemes for physics in ultrastrong laser fields: Review and developments.* Phys. Rev. E **92**, 023305 (2015).

86. P. Mora and T. M. Antonsen. *Kinetic modeling of intense, short laser pulses propagating in tenuous plasmas.* Phys. Plasmas **4**, 217 (1997).

87. A. F. Lifschitz, X. Davoine, E. Lefebvre, J. Faure, C. Rechatin and V. Malka. *Particle-in-Cell modelling of laser-plasma interaction using Fourier decomposition.* J. Comput. Phys. **228**, 1803 (2009).

88. S. Bulanov, N. Naumova, F. Pegoraro and J. Sakai. *Particle injection into the wave acceleration phase due to nonlinear wake wave breaking.* Phys. Rev. E **58**, R5257 (1998).

89. P. Tomassini, M. Galimberti, A. Giulietti, D. Giulietti, L. A. Gizzi, L. Labate and F. Pegoraro. *Production of high-quality electron beams in numerical experiments of laser wakefield acceleration with longitudinal wave breaking.* Phys. Rev. ST Accel. Beams **6**, 121301 (2003).

90. J. U. Kim, N. Hafz and H. Suk. *Electron trapping and acceleration across a parabolic plasma density profile.* Phys. Rev. E **69**, 026409 (2004).

91. A. V. Brantov, T. Zh. Esirkepov, M. Kando, H. Kotaki, V. Yu. Bychenkov and S. V. Bulanov. *Controlled electron injection into the wake wave using plasma density inhomogeneity.* Phys. Plasmas **15**, 073111 (2008).

92. H. Suk, N. Barov, J. B. Rosenzweig and E. Esarey. *Plasma electron trapping and acceleration in a plasma wake field using a density transition.* Phys. Rev. Lett. **86**, 1011 (2001).

93. J. Faure, C. Rechatin, O. Lundh, L. Ammoura and V. Malka. *Injection and acceleration of quasimonoenergetic relativistic electron beams using density gradients at the edges of a plasma channel.* Phys. Plasmas **17**, 083107 (2010).

94. C. G. R. Geddes, K. Nakamura, G. R. Plateau, Cs. Toth, E. Cormier-Michel, E. Esarey, C. B. Schroeder, J. R. Cary and W. P. Leemans. *Plasma-density-gradient injection of low absolute-momentum-spread electron bunches.* Phys. Rev. Lett. **100**, 215004 (2008).

95. K. Schmid, A. Buck, C. M. S. Sears, J. M. Mikhailova, R. Tautz, D. Herrmann, M. Geissler, F. Krausz and L. Veisz. *Density-transition based electron injector for laser driven wakefield accelerators.* Phys. Rev. ST Accel. Beams **13**, 091301 (2010).

96. A. Buck, J. Wenz, J. Xu, K. Khrennikov, K. Schmid, M. Heigoldt, J. M. Mikhailova, M. Geissler, B. Shen, F. Krausz, S. Karsch and L. Veisz. *Shock-front injector for high-quality laser-plasma acceleration.* Phys. Rev. Lett. **110**, 185006 (2013).

97. A. J. Gonsalves, K. Nakamura, C. Lin, D. Panasenko, S. Shiraishi, T. Sokollik, C. Benedetti, C. B. Schroeder, C. G. R. Geddes, J. van Tilborg, J. Osterhoff, E. Esarey, C. Toth and W. P. Leemans. *Tunable laser plasma accelerator based on longitudinal density tailoring.* Nat. Phys. **7**, 862 (2011).

98. C. Wang, J. Li, J. Sun and X. Luo. *Shock-wave-based density down ramp for electron injection.* Phys. Rev. ST Accel. Beams **15**, 020401 (2012).

99. S. P. D. Mangles, A. G. R. Thomas, M. C. Kaluza, O. Lundh, F. Lindau, A. Persson, F. S. Tsung, Z. Najmudin, W. B. Mori, C.-G. Wahlström and K. Krushelnick. *Laser-wakefield acceleration of monoenergetic electron beams in the first plasma-wave period.* Phys. Rev. Lett. **96**, 215001 (2006).

100. M. Chen, Z.-M. Sheng, Y.-Y. Ma and J. Zhang. *Electron injection and trapping in a laser wakefield by field ionization to high-charge states of gases.* J. Appl. Phys. **99**, 056109 (2006).

101. E. Oz, S. Deng, T. Katsouleas, P. Muggli, C. D. Barnes, I. Blumenfeld, F. J. Decker, P. Emma, M. J. Hogan, R. Ischebeck, R. H. Iverson, N. Kirby, P. Krejcik, C. O'Connell, R. H. Siemann, D. Walz, D. Auerbach, C. E. Clayton, C. Huang, D. K. Johnson, C. Joshi, W. Lu, K. A. Marsh, W. B. Mori and M. Zhou. *Ionization-induced electron trapping in ultrarelativistic plasma wakes.* Phys. Rev. Lett. **98**, 084801 (2007).

102. T. P. Rowlands-Rees, C. Kamperidis, S. Kneip, A. J. Gonsalves, S. P. D. Mangles, J. G. Gallacher, E. Brunetti, T. Ibbotson, C. D. Murphy, P. S. Foster, M. J. V. Streeter, F. Budde, P. A. Norreys, D. A. Jaroszynski, K. Krushelnick, Z. Najmudin and S. M. Hooker. *Laser-driven acceleration of electrons in a partially ionized plasma channel.* Phys. Rev. Lett. **100**, 105005 (2008).

103. A. Pak, K. A. Marsh, S. F. Martins, W. Lu, W. B. Mori and C. Joshi. *Injection and trapping of tunnel-ionized electrons into laser-produced wakes.* Phys. Rev. Lett. **104**, 025003 (2010).

104. C. McGuffey, A. G. R. Thomas, W. Schumaker, T. Matsuoka, V. Chvykov, F. J. Dollar, G. Kalintchenko, V. Yanovsky, A. Maksimchuk, K. Krushelnick, V. Yu. Bychenkov, I. V. Glazyrin and A. V. Karpeev. *Ionization induced trapping in a laser wakefield accelerator.* Phys. Rev. Lett. **104**, 025004 (2010).

105. M. Chen, E. Esarey, C. B. Schroeder, C. G. R. Geddes and W. P. Leemans. *Theory of ionization-induced trapping in laser-plasma accelerators.* Phys. Plasmas **19**, 033101 (2012).

106. D. Umstadter, J. K. Kim and E. Dodd. *Laser injection of ultrashort electron pulses into wakefield plasma waves.* Phys. Rev. Lett. **76**, 2073 (1996).

107. E. Esarey, R. F. Hubbard, W. P. Leemans, A. Ting and P. Sprangle. *Electron injection into plasma wakefields by colliding laser pulses.* Phys. Rev. Lett. **79**, 2682 (1997).

108. G. Fubiani, E. Esarey, C. B. Schroeder and W. P. Leemans. *Beat wave injection of electrons into plasma waves using two interfering laser pulses.* Phys. Rev. E **70**, 016402 (2004).

109. J. T. Mendonça. *Threshold for electron heating by two electromagnetic waves.* Phys. Rev. A **28**, 3592 (1983).

110. Z.-M. Sheng, K. Mima, Y. Sentoku, M. S. Jovanović, T. Taguchi, J. Zhang and J. Meyer-ter Vehn. *Stochastic heating and acceleration of electrons in colliding laser fields in plasma.* Phys. Rev. Lett. **88**, 055004 (2002).

111. A. Bourdier, D. Patin and E. Lefebvre. *Stochastic heating in ultra high intensity laser-plasma interaction.* Physica D **206**, 1 (2005).

112. X. Davoine, E. Lefebvre, J. Faure, C. Rechatin, A. Lifschitz and V. Malka. *Simulation of quasimonoenergetic electron beams produced by colliding pulse wakefield acceleration.* Phys. Plasmas **15**, 113102 (2008).

113. C. Rechatin, J. Faure, A. Lifschitz, V. Malka and E. Lefebvre. *Plasma wake inhibition at the collision of two laser pulses in an underdense plasma.* Phys. Plasmas **14**, 060702 (2007).

114. J. Faure, C. Rechatin, A. Norlin, A. Lifschitz, Y. Glinec and V. Malka. *Controlled injection and acceleration of electrons in plasma wakefields by colliding laser pulses.* Nature **444**, 737 (2006).

115. O. Lundh, J. Lim, C. Rechatin, L. Ammoura, A. Ben-Ismail, X. Davoine, G. Gallot, J-P. Goddet, E. Lefebvre, V. Malka and J. Faure. *Few femtosecond, few kiloampere electron bunch produced by a laser-plasma accelerator.* Nat Phys **7**, 219 (2011).

116. X. Davoine, E. Lefebvre, C. Rechatin, J. Faure and V. Malka. *Cold optical injection producing monoenergetic, multi-GeV electron bunches.* Phys. Rev. Lett. **102**, 065001 (2009).

117. S. C. Wilks, A. B. Langdon, T. E. Cowan, M. Roth, M. Singh, S. Hatchett, M. H. Key, D. Pennington, A. MacKinnon and R. A. Snavely. *Energetic proton generation in ultra-intense laser-solid interactions.* Phys. Plasmas **8**, 542 (2001).

118. S. C. Wilks, W. L. Kruer, M. Tabak and A. B. Langdon. *Absorption of ultra-intense laser pulses.* Phys. Rev. Lett. **69**, 1383 (1992).

119. F. Brunel. *Not-so-resonant, resonant absorption.* Phys. Rev. Lett. **59**, 52 (1987).

120. R. A. Snavely, M. H. Key, S. P. Hatchett, T. E. Cowan, M. Roth, T. W. Phillips, M. A. Stoyer, E. A. Henry, T. C. Sangster, M. S. Singh, S. C. Wilks, A. MacKinnon, A. Offenberger, D. M. Pennington, K. Yasuike, A. B. Langdon, B. F. Lasinski, J. Johnson, M. D. Perry and E. M. Campbell. *Intense high-energy proton beams from petawatt-laser irradiation of solids.* Phys. Rev. Lett. **85**, 2945 (2000).

121. B.G. Cartwright, E.K. Shirk and P.B. Price. *A nuclear-track-recording polymer of unique sensitivity and resolution.* Nucl. Instr. Meth. **153**, 457 (1978).

Papers

Paper I

Enhanced stability of laser wakefield acceleration using dielectric capillary tubes

M. Hansson, L. Senje, A. Persson, O. Lundh, C.-G. Wahlström, F. G. Desforges, J. Ju, T. L. Audet, B. Cros, S. Dobosz Dufrénoy, and P. Monot.

Physical Review Special Topics - Accelerators and Beams **17**, 031303 (2014).

PHYSICAL REVIEW SPECIAL TOPICS - ACCELERATORS AND BEAMS **17,** 031303 (2014)

Enhanced stability of laser wakefield acceleration using dielectric capillary tubes

M. Hansson,* L. Senje, A. Persson, O. Lundh, and C.-G. Wahlström
Department of Physics, Lund University, P.O. Box 118, S-22100 Lund, Sweden

F. G. Desforges, J. Ju, T. L. Audet, and B. Cros
Laboratoire de Physique des Gaz et des Plasmas, CNRS-Université Paris-Sud 11, 91405 Orsay, France

S. Dobosz Dufrénoy, and P. Monot
Service des Photons, Atomes et Molécules, CEA Saclay, 91191 Gif-sur-Yvette, France
(Received 25 October 2013; published 17 March 2014)

The stability of beams of laser wakefield accelerated electrons in dielectric capillary tubes is experimentally investigated. These beams are found to be more stable in charge and pointing than the corresponding beams of electrons accelerated in a gas jet. Electron beams with an average charge of 43 pC and a standard deviation of 14% are generated. The fluctuations in charge are partly correlated to fluctuations in laser pulse energy. The pointing scatter of the electron beams is measured to be as low as 0.8 mrad (rms). High laser beam pointing stability improved the stability of the electron beams.

DOI: 10.1103/PhysRevSTAB.17.031303 PACS numbers: 41.75.Jv, 52.35.-g, 52.38.-r, 52.50.Jm

Laser wakefield accelerators, first proposed in 1979 [1], appear promising as sources of highly relativistic electrons and associated X-ray radiation, in particular since experiments have demonstrated the possibility of generating high-quality quasimonoenergetic pulses of electrons [2–4].

Laser wakefield accelerators benefit from the much higher electric field that can be sustained in electron plasma waves compared to conventional accelerators, and thus hold promise for size and cost reduction. The beams of laser wakefield accelerated electrons have properties that are complementary to those of conventional accelerators, and thus open doors to novel applications. These sources therefore attract worldwide interest from many different areas of science, technology, and medicine, e.g., X-ray free-electron lasers, high-energy particle physics, and oncology. However, laser-plasma accelerators are still at their early stage of development and are hampered by, in particular, limited reproducibility and stability, restricting their use in applications.

Much current research in this field is focused on increasing the maximum energy of the electrons, for example by extending the acceleration length through the use of different laser waveguiding structures [5,6], or by using multiple accelerator stages [7]. Large efforts are also made to control the injection of electrons into the accelerating structure to increase the quality of the electron pulses and to gain better control of the mechanism.

In this paper we report on a study of the stability of beams of laser-plasma accelerated electrons using dielectric capillary tubes as laser waveguides. This type of waveguide [8] has three main advantages: (i) The plasma density inside the tubes can be arbitrarily low, as the laser beam is then guided purely by reflection from the tube walls [6]. The absence of a minimum density requirement for guiding [9] makes the capillary tube relevant for laser wakefield acceleration over long distance since the maximum achievable electron energy scales with the inverse electron density assuming the process is limited by dephasing [1]. (ii) When the laser focal spot is smaller than the matched focal spot for coupling to the capillary tube, and for laser power larger than the critical power for self-focusing, the laser energy outside the main peak of the focal spot can be reflected from the tube wall back to the laser axis, which helps to sustain relativistic self-focusing and laser guiding over a longer distance than in a gas jet or in a gas cell with similar plasma density [9,10]. (iii) the capillary tube provides a shock-free gas medium [11]. In this study electrons from the background plasma are trapped and accelerated in the so-called bubble regime of laser plasma acceleration. This mechanism is simple to achieve experimentally, and has been observed by numerous groups in gas jet, gas cell, or waveguides. Using hydrogen filled capillary tubes, we have performed a statistical analysis of the stability of the parameters of the electrons accelerated by a laser beam which pointing position is stabilized in the focal plane.

The experiments were conducted at the Lund Laser Centre, using a Ti:Sapphire based multi-terawatt laser

*martin.hansson@fysik.lth.se

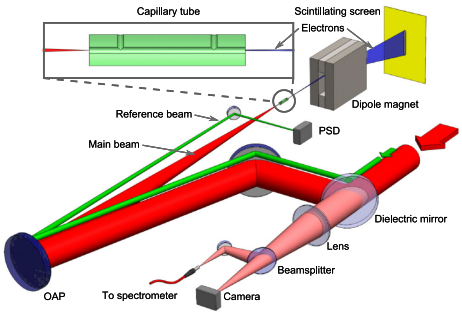

FIG. 1. Sketch of the experimental setup. The main laser pulse (red) is focused by an off-axis parabolic mirror (OAP) into a dielectric capillary tube (or a gas jet) filled with hydrogen gas. The accelerated electrons are dispersed by a dipole magnet before reaching a scintillating screen. The leakage from a dielectric mirror in the beam path is used to record spatial and spectral intensity distributions of every laser pulse. A continuous reference beam (marked in green for clarity, but in reality of the same wavelength as the main beam) is used in combination with a position sensitive detector (PSD) for feedback to a system for active pointing stabilization.

system. A sketch of the experimental setup is shown in Fig. 1. Typically, the laser was set to deliver pulses with energy of 750 mJ on target with a pulse duration of 40 fs at a center wavelength of 800 nm, giving a peak power of 18 TW. The laser beam was focused by an $f = 76$ cm off-axis parabolic mirror. Using a closed looped optimization system, consisting of a wavefront sensor and a deformable mirror in the beam path, a focal spot with a FWHM of 19 μm, close to the diffraction limit (Strehl ratio ≥ 0.95), was achieved. An estimated peak intensity of 4.4×10^{18} W/cm^2 was thus achieved in the focus of the beam, corresponding to a peak normalized vector potential of $a_0 = 1.4$.

An active system for stabilization of the transverse position of the focus [12] was used to minimize laser pointing errors. This system uses an analog position sensitive device to measure the position of the focus from a reference beam, and a large (100 mm) piezoelectric actuated mirror in the beam path to steer the beam. With this system a short-term scatter of the focal spot position with a rms distance from the average position of ≈ 4 μrad was achieved, while any long-term drift of the transverse focal position was essentially eliminated.

The laser pulses were focused one millimeter inside different glass capillary tubes, with diameters in the range 76 to 254 μm and lengths in the range 8 to 20 mm, carefully aligned to the laser beam axis [9]. The capillaries were filled with hydrogen gas from a reservoir with variable backing pressure, 35 ms before each laser pulse. The resulting molecular density of the gas inside each capillary was deducted from interferometric studies [13] performed off-line. The gas inside the capillary tubes became fully ionized into a plasma by the leading edge of the laser pulse. Alternatively, a gas nozzle could be moved under vacuum to replace the capillary tube to create a cylindrical jet of hydrogen gas with a diameter of 3 mm at the laser focus for comparison with capillary tubes.

The accelerated electrons were observed on a scintillating screen (Kodak Lanex Regular), using a 16-bit CCD camera. This way the electron beam profile and pointing could be studied. In addition, a 120 mm long rectangular dipole magnet with a peak magnetic field of 0.7 T could be inserted into the electron beam path to disperse the electrons according to energy and thus allow the energy spectrum of the electrons to be determined. The energy axis of the spectra was absolutely calibrated by numerically tracing electrons through a map of the measured magnetic field. The physical boundaries of the dipole magnet set a lower limit on the energy of the electrons that could be observed to ≈ 40 MeV taking into account the electron beam divergence. The energy resolution of the spectrometer is decreasing with increasing energy. For the divergence of the electron beams observed in this experiment, the energy resolution is $\approx 8\%$ at 80 MeV. The total amount of charge impacting the scintillating screen was determined by integrating the images and using published calibration factors [14] for the scintillating screen.

Furthermore, the laser pulses were sampled, using the leakage through a dielectric mirror in the laser beam path, and focused using an achromatic lens (see Fig. 1). An image of this focus was acquired at each shot, which provided an absolutely calibrated measurement of the laser pulse energy on target and also an estimate of the scatter of the laser focus position and size. In addition, the spectral intensity distribution of each laser pulse was acquired using an optical spectrometer. Neglecting shot-to-shot fluctuations in spectral phase, these spectral intensity variations allow an estimate of shot-to-shot variations in pulse duration to be made through an inverse Fourier transform.

The data presented in Fig. 2 were acquired during a sequence of 130 consecutive pulses with identical settings. The delay between pulses was 30 s in order to allow the pumps to evacuate the target vacuum chamber from the gas load. Thus, these data points were acquired over 65 min. The measured pulse energy, shown in Fig. 2(a) as a function of the shot number, indicates a slight drift toward lower energy during the sequence of shots. However, the standard deviation of the laser pulse energy is only 1.9%. The estimated laser pulse duration showed similar stability, with a standard deviation of 1.9%, but without any drift. After the first 90 pulses, marked in red in the figures, the active pointing stabilization system was turned off, marked in blue in the figures. As expected, no change in stability of laser energy or pulse duration was observed when turning off the active pointing stabilization system.

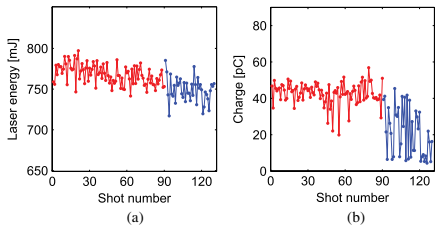

FIG. 2. Laser pulse energy delivered to the entrance of a 20 mm long, 152 μm diameter capillary tube (a) and the corresponding accelerated charge with an energy above 40 MeV (b) as a function of shot number. The active stabilization system is on during the first 90 pulses, and thereafter off. The stability of the electron bunch charge is significantly decreased by turning this system off.

During this sequence, the laser pulses were focused into a 20 mm long dielectric capillary tube with a diameter of 152 μm filled with hydrogen gas at a backing pressure of 340 mbar, resulting in a fully ionized plasma density of 1.3×10^{19} cm^{-3}. At this plasma electron density and the given peak power, the ratio between the peak power and the critical power for relativistic self-focusing [15,16] is $P/P_c \approx 7$. Under these experimental conditions, the laser pulse is expected to self-focus soon after entering the plasma, resulting in an increased peak intensity. The laser pulse expels electrons from regions of high intensity, leading to a bubble structure following the laser pulse, in which electrons are self-injected at multiple locations along the propagation through the plasma [10,17]. The density threshold for injection of electrons into the accelerating structure was experimentally determined to be $\approx 0.85 \times 10^{19}$ cm^{-3}.

The amount of charge in the resulting electron beams, with energy above 40 MeV, is shown in Fig. 2(b) as a function of the shot number. The electron beam parameters show larger fluctuations than the laser pulse parameters. Immediately after the active pointing system is turned off, the quality and stability of the electron beams degrade significantly and after ~25 shots the capillary tube is damaged beyond being operational. This shows that controlling the scatter and drift of the laser focal spot is crucially important when accelerating electrons in dielectric capillary tubes using laser pulses of high intensity and energy. The active stabilization system employed in the present study enabled long sequences of data collection and an enhanced endurance of the capillaries.

The average charge for the first 90 shots in the sequence was determined to 43 pC with a standard deviation of only 14%. This small spread in charge was found to be typical also for dielectric capillary tubes of different dimension after similar optimization. For example, in another sequence the charge of electrons, with energy above 40 MeV, accelerated inside a capillary tube with a larger diameter, 254 μm, and a shorter length, 10 mm, was measured to be higher, 107 pC, while the standard deviation was still only 18%. We did not observe any significant correlation between the amount of accelerated charge and the dimensions of the capillary tube. The difference in amount of accelerated charge between the different series of data reported here can instead be attributed to small differences in experimental parameters, such as laser energy and plasma density, that affect the amount of accelerated charge [17,18]. The experimental parameters were optimized for best stability before acquiring each series of data, which resulted in slightly different values of these parameters.

The stability in charge using the capillary tube is very good compared to the results achieved when, in the same setup and with identical laser parameters, the capillary tube is replaced with a 3 mm gas jet as a target, which showed a standard deviation in charge of 55%, with an average value of 68 pC. The charge stability of beams accelerated in capillary tubes is very good also when compared to published studies on laser wakefield acceleration in gas jets and gas cells showing stable beams [11,19,20]. The average value and stability of measured parameters of the beams of electrons accelerated in dielectric capillary tubes of different sizes, and in a gas jet, are summarized in Table I.

The energy stability of the accelerated electron beams is shown in Fig. 3. False color images of traces of the dispersed electrons on the scintillating screen, from 15 consecutive laser shots (number 25 to 39 in Fig. 2), are shown in Fig. 3(a) using the same color scale for all images. The electron energy spectra in this study show continuous energy distribution, as shown in Fig. 3(b), rather than

TABLE I. Summary of electron beam stability parameters acquired in three series using capillaries of different diameter (ø) and lengths (l) (A–C) in comparison with one series of data acquired using gas jet. The stabilities of the electron beams were studied using the same regime of acceleration. Before acquiring each series of data, the experimental conditions were optimized for best stability, yielding slightly different values of, e.g., backing pressure and laser intensity. The average and standard deviation of charge (Q) corresponds to electrons with an energy above 40 MeV measured with the dispersing dipole magnet in the electron beam path. The divergence (θ) and the RMS pointing stability (ϕ) was measured without the dispersing dipole in the electron beam path.

Parameter	A	B	C	Gas jet
ø [μm]	152	178	254	···
l [mm]	20	10	10	3
$\langle Q \rangle$ [pC]	43	88	107	68
std (Q) [%]	14	14	18	55
$\langle \theta \rangle$ [mrad]	11	10	10	14
std (θ) [%]	13	14	11	64
$\langle \phi \rangle$ [mrad]	1.2	···	0.8	4.4

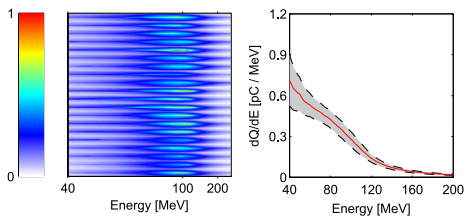

FIG. 3. False color images of the dispersed electrons on the scintillating screen from 15 consecutive shots are shown in (a), all using the same color scale. The average electron spectrum of all shots in the sequence is plotted as a solid red line in (b). The shaded area, bounded by dashed lines, shows the corresponding standard deviation from the average spectrum. Over the full energy range, the maximum standard deviation from the average spectrum is 27%.

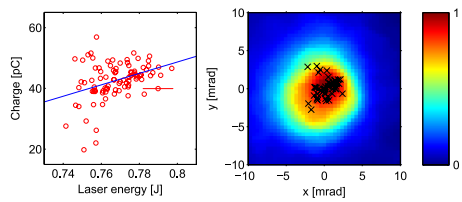

FIG. 4. In (a), the charge of the electrons in the beam, with energy above ~40 MeV, is plotted as a function of laser pulse energy for the first 90 shots in Fig. 2, with the active pointing stabilization system on. The estimated measurement error in laser energy of 1% is marked as a solid red line only in one data point for clarity. This figure shows a clear correlation to laser energy. In (b), a typical beam profile is shown together with a scatter map of the centroids of a sequence of 30 shots with the pointing stabilization system on.

features of peaks, indicating that the acceleration process is dominated by injection at multiple locations in space and time [10,17]. Previous studies [9] report on electron beams from dielectric capillary tubes with quasimonoenergetic energy spectra, but with lower charge, when experimental parameters were instead optimized in order to achieve self-injection in a well-localized phase-space volume and to avoid dephasing. The parameters of the present study were selected for their capability to produce, on every shot, an accelerated beam with a significant amount of charge, interesting for example for the study of X-ray generation or other applications.

The energy spectrum of the beams of accelerated electrons in dielectric capillary tubes are reproducible, as indicated by Fig. 3. The standard deviation from the average spectrum is less than 27% over the full measured energy range. This standard deviation is below 15% for energies between 65 and 80 MeV and has a minimum of 14% at 72 MeV.

The dependence of the amount of accelerated charge, with an energy above 40 MeV, on the laser pulse energy on target is shown in Fig. 4(a). This figure shows a clear dependence between the charge and laser pulse energy. This behavior is expected since higher laser energy for the same pulse parameters implies a higher probability of self-injection due to the higher amplitude of the plasma wave [18]. The data points are scattered along the solid line, which is fitted from the experimental data, and indicates that the stability in charge can be improved by a better stability in laser pulse energy. Although a certain amount of fluctuations in beam charge is clearly due to variations in laser pulse energy, these variations account only for part of the total charge fluctuations within a given series. However, the figure shows that small variations in laser energy can explain the observed difference in accelerated charge between different series.

We could not find any significant correlation between the electron beam parameters and intrinsic variations in focal spot size or width of the laser pulse spectrum. Although this might be due to insufficient accuracy of the measurement, it can also be due to the nonlinear laser pulse evolution in the plasma, such as self-phase modulation and relativistic self-focusing. Thus, fluctuations in laser pulse duration and spot size after propagation in plasma are not necessarily the same as the measured initial values.

A typical electron beam charge distribution in the transverse plane is shown in Fig. 4(b) acquired during a sequence of 30 shots using the same setup as above, but without the dispersing dipole magnet in the electron beam path. The average divergence (FWHM) for these shots was measured to 11 mrad with a standard deviation of 13%. This divergence is larger than the opening angle of the capillary tube as viewed from the entrance plane, which is 7.6 mrad. Similar divergence of the electron beam was measured on electron beams accelerated inside capillaries tubes of other dimensions as shown in Table I, which suggests that the beam is not limited by the aperture of the capillary tube. The divergence of the beams of electrons accelerated inside the capillary tubes is also similar to divergence of the beams accelerated inside a gas jet (see Table I).

The pointing scatter of the electron beams accelerated inside the capillary with diameter 152 μm and length of 10 mm is also shown in Fig. 4(b), where the center of each beam profile is marked by a cross. The rms distance from the average beam position is only 1.2 mrad for this sequence. This is significantly less than the corresponding value of 4.4 mrad measured for the beams of electrons accelerated inside a gas jet during this experiment. Small pointing scatter was observed also using capillaries of other dimensions. For example, during a sequence of 100 pulses in a capillary with a diameter of 254 μm and a length of

10 mm, the rms pointing scatter was as low as 0.8 mrad and no shot deviated more than 2.7 mrad from the average beam position.

The beams of electrons accelerated during this experiment have been shown to be very stable in charge, divergence, and pointing. The stable and uniform gas density distribution, which is also shockfree, that can be achieved in a dielectric capillary tube, or a gas cell of similar dimensions, is expected to contribute to this stability of the resulting electron beams.

In conclusion, we have shown an enhanced stability of beams of electrons accelerated in dielectric capillary tubes compared to electrons accelerated using a gas jet as target. Very good laser beam pointing stability has been shown to be necessary in order to carry out the studies reported in this paper. In the present study, such stability was achieved using an active beam pointing stabilization system. The measured beam charge variations are shown to be partly due to laser pulse energy fluctuations. The stability of the electron beam parameters appears to be similar for the different sizes of capillary tubes used in this experiment. The enhanced stability of laser wakefield acceleration using dielectric capillary tubes indicates a path toward applications of these electron beams.

We acknowledge the support of the Swedish Research Council, the Knut and Alice Wallenberg Foundation, the Swedish Foundation for Strategic Research, the Lund University X-ray Centre (LUXC), Laserlab-Europe/CHARPAC (Grant Agreement No. 284464, EC's 7th Framework Programme) and EuCARD2/ANAC2 (Grant Agreement No. 312453, EC's 7th Framework Programme). J. Ju acknowledges financial support from the Chinese Scholarship Council (CSC). This project has benefited from financial support from ARC.

[1] T. Tajima and J. M. Dawson, Phys. Rev. Lett. **43**, 267 (1979).
[2] C. G. R. Geddes, C. Toth, J. van Tilborg, E. Esarey, C. B. Schroeder, D. Bruhwiler, C. Nieter, J. Cary, and W. P. Leemans, Nature (London) **431**, 538 (2004).
[3] J. Faure, Y. Glinec, A. Pukhov, S. Kiselev, S. Gordienko, E. Lefebvre, J.-P. Rousseau, F. Burgy, and V. Malka, Nature (London) **431**, 541 (2004).
[4] S. P. D. Mangles, C. D. Murphy, Z. Najmudin, A. G. R. Thomas, J. L. Collier, A. E. Dangor, E. J. Divall, P. S. Foster, J. G. Gallacher, C. J. Hooker, D. A. Jaroszynski, A. J. Langley, W. B. Mori, P. A. Norreys, F. S. Tsung, R. Viskup, B. R. Walton, and K. Krushelnick, Nature (London) **431**, 535 (2004).
[5] D. J. Spence, A. Butler, and S. M. Hooker, J. Phys. B **34**, 4103 (2001).
[6] B. Cros, C. Courtois, G. Matthieussent, A. Di Bernardo, D. Batani, N. Andreev, and S. Kuznetsov, Phys. Rev. E **65**, 026405 (2002).
[7] C. B. Schroeder, E. Esarey, C. G. R. Geddes, C. Benedetti, and W. P. Leemans, Phys. Rev. ST Accel. Beams **13**, 101301 (2010).
[8] F. Wojda, K. Cassou, G. Genoud, M. Burza, Y. Glinec, O. Lundh, A. Persson, G. Vieux, E. Brunetti, R. P. Shanks, D. Jaroszynski, N. E. Andreev, C.-G. Wahlström, and B. Cros, Phys. Rev. E **80**, 066403 (2009).
[9] G. Genoud, K. Cassou, F. Wojda, H. Ferrari, C. Kamperidis, M. Burza, A. Persson, J. Uhlig, S. Kneip, S. Mangles, A. Lifschitz, B. Cros, and C.-G. Wahlström, Appl. Phys. B **105**, 309 (2011).
[10] H. E. Ferrari, A. F. Lifschitz, and B. Cros, Plasma Phys. Controlled Fusion **53**, 014005 (2011).
[11] J. Osterhoff, A. Popp, Z. Major, B. Marx, T. P. Rowlands-Rees, M. Fuchs, M. Geissler, R. Hörlein, B. Hidding, S. Becker, E. A. Peralta, U. Schramm, F. Grüner, D. Habs, F. Krausz, S. M. Hooker, and S. Karsch, Phys. Rev. Lett. **101**, 085002 (2008).
[12] G. Genoud, F. Wojda, M. Burza, A. Persson, and C.-G. Wahlstrom, Rev. Sci. Instrum. **82**, 033102 (2011).
[13] J. Ju and B. Cros, J. Appl. Phys. **112**, 113102 (2012).
[14] A. Buck, K. Zeil, A. Popp, K. Schmid, A. Jochmann, S. D. Kraft, B. Hidding, T. Kudyakov, C. M. S. Sears, L. Veisz, S. Karsch, J. Pawelke, R. Sauerbrey, T. Cowan, F. Krausz, and U. Schramm, Rev. Sci. Instrum. **81**, 033301 (2010).
[15] P. Sprangle, C.-M. Tang, and E. Esarey, IEEE Trans. Plasma Sci. **15**, 145 (1987).
[16] G.-Z. Sun, E. Ott, Y. C. Lee, and P. Guzdar, Phys. Fluids **30**, 526 (1987).
[17] J. Ju, K. Svensson, H. Ferrari, A. Dopp, G. Genoud, F. Wojda, M. Burza, A. Persson, O. Lundh, C.-G. Wahlstrom, and B. Cros, Phys. Plasmas **20**, 083106 (2013).
[18] S. P. D. Mangles, G. Genoud, M. S. Bloom, M. Burza, Z. Najmudin, A. Persson, K. Svensson, A. G. R. Thomas, and C.-G. Wahlström, Phys. Rev. ST Accel. Beams **15**, 011302 (2012).
[19] S. Corde, C. Thaury, A. Lifschitz, G. Lambert, K. Ta Phuoc, X. Davoine, R. Lehe, D. Douillet, A. Rousse, and V. Malka, Nat. Commun. **4**, 1501 (2013).
[20] S. Banerjee, S. Y. Kalmykov, N. D. Powers, G. Golovin, V. Ramanathan, N. J. Cunningham, K. J. Brown, S. Chen, I. Ghebregziabher, B. A. Shadwick, D. P. Umstadter, B. M. Cowan, D. L. Bruhwiler, A. Beck, and E. Lefebvre, Phys. Rev. ST Accel. Beams **16**, 031302 (2013).

Paper II

Reproducibility of electron beams from laser wakefield acceleration in capillary tubes

F. G. Desforges, M. Hansson, J. Ju, L. Senje, T. L. Audet,
S. Dobosz Dufrénoy, A. Persson, O. Lundh, C.-G. Wahlström, and B. Cros.

Nuclear Instruments and Methods in Physics Research A **740**, 54 (2014).

Nuclear Instruments and Methods in Physics Research A 740 (2014) 54–59

Contents lists available at ScienceDirect

Nuclear Instruments and Methods in Physics Research A

journal homepage: www.elsevier.com/locate/nima

Reproducibility of electron beams from laser wakefield acceleration in capillary tubes

F.G. Desforges [a], M. Hansson [b], J. Ju [a], L. Senje [b], T.L. Audet [a], S. Dobosz-Dufrénoy [c], A. Persson [b], O. Lundh [b], C.-G. Wahlström [b], B. Cros [a,*]

[a] Laboratoire de Physique des Gaz et des Plasmas, CNRS-Université Paris-Sud, 91405 Orsay, France
[b] Department of Physics, Lund University, P.O. Box 118, S-22100 Lund, Sweden
[c] Service des Photons, Atomes et Molécules, CEA Saclay, 91191 Gif-sur-Yvette, France

ARTICLE INFO

Available online 5 November 2013

Keywords:
Laser wakefield
Laser plasma accelerator
Electron acceleration
Capillary tube
Electron beam stability

ABSTRACT

The stability of accelerated electron beams produced by self-injection of plasma electrons into the wakefield driven by a laser pulse guided inside capillary tubes is analyzed statistically in relation to laser and plasma parameters, and compared to results obtained in a gas jet. The analysis shows that reproducible electron beams are achieved with a charge of 66 pC ± 11%, a FWHM beam divergence of 9 mrad ± 14%, a maximum energy of 120 MeV ± 10% and pointing fluctuations of 2.3 mrad using 10 mm long, 178 μm diameter capillary tubes at an electron density of $(10.0 \pm 1.5) \times 10^{18}$ cm^{-3}. Active stabilization of the laser pointing was used and laser parameters were recorded on each shot. Although the shot-to-shot laser energy fluctuations can account for a fraction of the electrons fluctuations, gas density fluctuations are suspected to be a more important source of instability.

1. Introduction

The development of conventional, linear electron accelerators composed of evacuated radio-frequency cavities has reached a technological limit with accelerating gradients of the order of 50 MV/m. Alternative ways of accelerating electrons in plasmas are being investigated since the proposition of laser plasma wakefield acceleration (LPA) [1]. The plasma wave created in the wake of an intense and short laser pulse is associated with large amplitude electric fields, typically in the range 10–100 GV/m with state-of-the-art laser systems. For high enough intensity (typically above 10^{18} W/cm^2), plasma electrons are blown out from the high intensity region close to the laser axis, and a moving cavity, or bubble, is created behind the driving pulse. A fraction of the plasma electrons can become self-trapped in this ion cavity and be accelerated to high energies. This mechanism provides with relative ease a source of accelerated electrons, with properties that depend on several laser and plasma parameters and competing nonlinear mechanisms. Electron acceleration has been observed experimentally by numerous groups (see for example Esarey et al. for a review [2]) in various plasma targets such as gas jets, gas cells, capillary discharge waveguides and dielectric capillary tubes [3].

The produced electron beams, with an energy ranging from 50 MeV to a few GeV with the most powerful laser drivers [4,5], have an interest for various applications, including the generation of radiation [6] in the X-ray range in the plasma, as drivers for free electron lasers, or the development of injectors for multi-stage laser plasma accelerators [7].

Development of these novel sources of electrons will depend on their reliability and the stability of their properties. In order to get some insight on the performance of an electron source produced by self-injection of plasma electrons, we have studied the stability of electron parameters against laser and plasma parameters.

The properties of electron beams reported in this paper were achieved in capillary tubes and gas jet targets with plasma densities suitable for a comparison of results. Previous studies [8,3] have shown, for example, that similar electron energy and charge can be achieved with these two types of targets for specific plasma densities.

The paper is organized as follows: the experimental setup is presented in Section 2; the properties of electron beams generated inside capillary tubes are shown in Section 3; the effect of the gas distribution on electron properties is reported in Section 4; and finally, in Section 5, a conclusion is given.

2. Experimental setup

The reproducibility of electron beams from laser wakefield acceleration in capillary tubes has been studied at the Lund Laser Centre (LLC) in Sweden with a multi-terawatt laser. The laser is a

* Corresponding author.
E-mail addresses: frederic.desforges@u-psud.fr (F.G. Desforges), brigitte.cros@u-psud.fr (B. Cros).

0168-9002/$ - see front matter © 2013 Elsevier B.V. All rights reserved.
http://dx.doi.org/10.1016/j.nima.2013.10.062

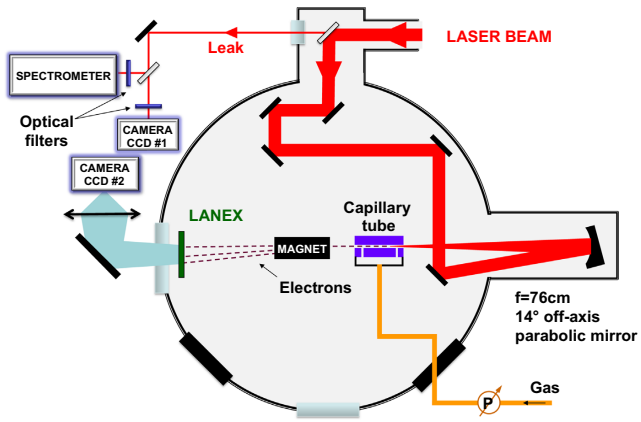

Fig. 1. Schematic diagram of the experimental setup.

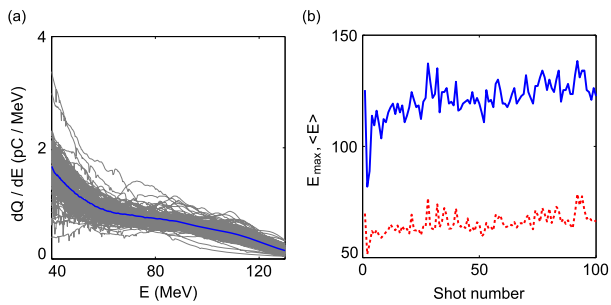

Fig. 2. Data from a series of 100 shots in a 10 mm long, 178 μm diameter capillary tube containing H_2 at an electronic density of $(10.0 \pm 1.5) \times 10^{18}$ cm^{-3}: (a) electron spectra (gray lines) and the corresponding mean curve (blue line) and (b) average energy (red dashed line) and maximum energy (blue solid line) of the electron spectra shown in (a); the mean values of $\langle E \rangle$ and E_{max} are 65 and 120 MeV with a standard deviation of 9 and 10%, respectively. (For interpretation of the references to color in this figure caption, the reader is referred to the web version of this paper.)

titanium-doped sapphire (Ti:Sa) laser using chirped pulse amplification (CPA), and delivers pulses with FWHM duration of 40 fs and a wavelength of 800 nm. The experimental setup is schematically shown in Fig. 1.

The laser beam with an energy on target of (800 ± 20) mJ was focused using a $f=76$ cm off-axis parabola. The laser spot on target inside the chamber was optimized by tuning a deformable mirror. A Gaussian waist of 17 μm (radius at e^{-2}) was computed by fitting the laser radial profile with a Gaussian function. 88% of the laser energy was contained within a circle having a radius equal to 17 μm. The laser peak intensity is thus estimated to be $I_0 \approx 3.6 \times 10^{18}$ W/cm^2 and the normalized laser vector potential $a_0 \approx 1.3$. An active system for stabilizing the laser pointing developed at LLC [9] was used in this experimental campaign, giving a standard deviation of the laser pointing of ≈ 4 μrad and improving the electron properties as well as extending the lifetime of capillary tubes [10]. Input laser parameters were recorded on every shot using a small fraction of the incident laser beam leaking through a dielectric mirror. This fraction was further divided and sent to a fiber spectrometer and focused on a charge-coupled device (CCD) camera. The relative shot-to-shot fluctuations of the laser energy were computed from the signal recorded by this camera. The relative fluctuations of laser pulse duration were approximately estimated by applying an inverse Fourier transform on the laser spectra, assuming a flat phase.

Capillary tubes were mounted, one at a time, in a motorized holder allowing the capillary tubes to be accurately aligned on the laser axis. The capillary tubes could be removed from the laser axis and a 3 mm nozzle of a gas jet inserted instead. Therefore, it was possible to switch from one gas target to the other without opening the vacuum chamber, thus avoiding significant drifts of laser parameters. Capillary tubes with inner diameter of 178 μm and a length varying from 8 mm to 20 mm were used for the data presented here. They are made of glass and are optically smooth at the laser wavelength. Gas was let in through two slits cut in the capillary wall, providing a spatially uniform gas density profile between the two slits. The molecular density inside the capillary tubes was adjusted by a gas regulator controlling the upstream reservoir pressure. The resulting molecular density for different reservoir pressure had been characterized by interferometric studies [11]. The gas density was shown to fluctuate about 15% in space and in time due to the propagation of sound waves in the gas plateau during the gas filling process. The laser pulses were focused 1 mm inside the capillary tubes.

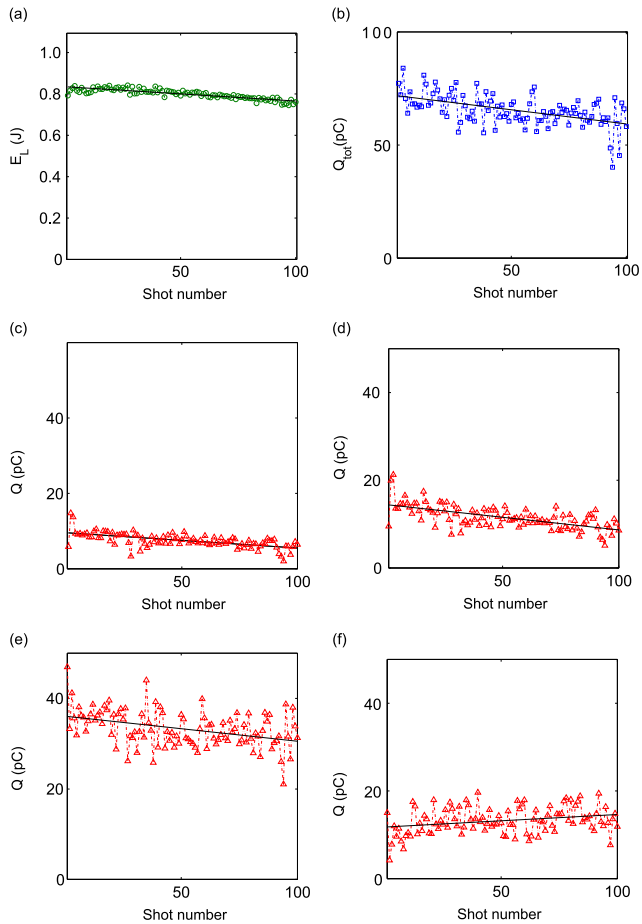

Fig. 3. (a) Laser energy as a function of shot number (green curve with circles) for the data of Fig. 2. (b) Charge as a function of shot number for the whole spectrum (blue curve with squares) and for electrons (red curves with triangles) with an energy between 40 and 45 MeV (c), 45 and 55 MeV (d), 55 and 100 MeV (e), above 100 MeV (f). (For interpretation of the references to color in this figure caption, the reader is referred to the web version of this paper.)

Spectra of accelerated electron beams were studied using a 12 cm long dipole magnet with a peak field of 0.7 T, located 13 cm after the capillary entrance. After an additional drift of 16 cm, the electron beams impinged on a scintillating screen (Kodak Lanex Regular) which was imaged by a 16-bit CCD camera located outside of the vacuum chamber. The spectra of electrons were obtained from the distribution of electrons impinging on the lanex screen after being deflected. The lowest energy that could be measured was about 40 MeV. The divergence of electron beam is the limiting factor on energy resolution. It was numerically estimated as follows. First, the magnetic field has been experimentally mapped. Then, the trajectory of electrons with an incidence angle has been computed taking into account the realistic magnetic field and the incidence angle of the electron beams. The incidence angle is taken as the FWHM beam divergence which is measured when the magnet is removed. It yields to a resolution of 6% at 50 MeV and 16% at 120 MeV for a FWHM beam divergence of 10 mrad. The charge was calculated from the image of the scintillating screen using published calibration factors [12].

3. Electron properties

The properties of electrons self-injected and accelerated inside capillary tubes, such as spectrum, charge and divergence, were measured during a series of 100 laser shots on a H_2 gas contained in a 10 mm long, 178 μm diameter capillary tube. Root-Mean-Square (RMS) fluctuations of electron pointing were estimated from a different series of 30 laser shots with the same gas and

Table 1
Average charge and standard deviation of the whole spectrum and the energy windows for the data in Fig. 2.

Energy range (MeV)	⟨Q⟩ (pC)	std(Q) (%)
> 40	66	11
40–45	8	25
45–55	12	23
55–100	33	12
> 100	13	23

laser parameters. For the laser parameters given in Section 2, the electron density was scanned in order to optimize the amount of accelerated electron charge and its reproducibility; the optimum electron density was found to be $(10.0 \pm 1.5) \times 10^{18}$ cm^{-3} and was used for the studies on stability.

The electron spectra plotted in Fig. 2a were obtained during a series of 100 laser shots with laser energy and pulse duration fluctuations both equal to 2%.

They can be characterized by their average energy, *i.e.* a mean value weighted with respect to the charge contained in each energy bin, as well as by their maximum energy, considered as the highest energy for which the charge contained in its bin is at least equal to 10% of the maximum charge contained in each energy bin. These parameters are plotted in Fig. 2b. The mean value of $\langle E \rangle$ and E_{max} are 65 and 120 MeV with a standard deviation of 9 and 10%, respectively.

The laser energy and the beam charge for different energies are shown in Fig. 3. The laser energy is represented by the green curve with circles in Fig. 3a and the total charge as a function of shot number by the blue curve with squares in Fig. 3b. The red curves with triangles represent the amount of charge in the ranges 40–45 MeV, 45–55 MeV, 55–100 MeV and above 100 MeV as a function of shot number in Fig. 3(c), (d), (e) and (f), respectively. They are linearly fitted in order to highlight the tendency over the series of shots.

The mean total amount of charge above 40 MeV is 66 pC with a standard deviation of 11%, the stability of each energy window is reported in Table 1.

The charge is found to be fairly stable. Despite this stability, a drift in charge distribution can be observed over the series of shots. The amount of low energy electrons ($E \in$ [40 MeV;100 MeV]) decreases as a function of the shot number whereas the number of high energy electrons ($E >$ 100 MeV) increases slightly. As shown in Fig. 3a, a drift of ~80 mJ of the laser energy occurred progressively during the 42 min of data acquisition. It corresponds to a drop of laser energy of 10% whereas the total amount of charge decreases by 27% so the laser fluctuations cannot completely account for this drift.

In a previous study of the self-injection threshold in a gas jet by Mangles et al. [13] for a range of parameters similar to those in our experiment, the accelerated electron charge was found to depend mainly on the scaled pulse energy, defined as $\alpha E n_e n_c^{-1}$, where α is the fraction of laser energy within the FWHM intensity of the focal spot, E the laser energy, n_e the electronic density of the plasma and n_c the critical density. This study shows that the energy distribution and the electron density are key parameters for the control of the self-injected and accelerated charge. Gas density fluctuations are estimated to be of the order of 15% and can also contribute to the charge fluctuation as will be discussed in Section 4. In the case of the data of Fig. 3, the scaled pulse energy, using $\alpha \approx 0.5$ for a Gaussian pulse, is calculated to be approximately 2.2 mJ, and corresponds to a region where the charge was observed in Ref. [13] to exhibit a fluctuation of roughly 33%. The better stability observed in the present study, with a fluctuation of 11%, suggests that the scaled pulse energy is larger than the one estimated from

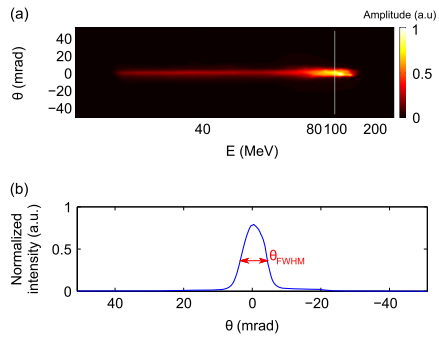

Fig. 4. Example of electron spectrum for a single shot inside a 10 mm long, 178 μm diameter capillary tube containing pure H_2 at an electronic density of $(10.0 \pm 1.5) \times 10^{18}$ cm^{-3}. (a) Image of the scintillating screen and (b) transverse profile plotted for the electron energy indicated by the white line in (a).

the input experimental parameters. This can be attributed to an increase of α caused by the use of capillary tubes. Indeed, the energy contained in the wings of the focal spot, when a capillary tube is employed, can be collected by the walls and refocused onto the laser axis, increasing the energy used for the nonlinear laser plasma interaction [3]. This increase of the scaled pulse energy can bring the charge injection to a more stable region.

A one dimension divergence can be determined from images of electron spectra on the scintillating screen in the direction perpendicular to the dispersion axis. The charge and transverse FWHM divergence can be calculated for each energy bin. An example is shown in Fig. 4.

Fig. 4a is a typical image of the scintillating screen; the transverse profile of the charge distribution at 100 MeV, indicated by a white line in Fig. 4a, is plotted in Fig. 4b. The FWHM beam divergence is estimated as

$$\theta_{FWHM} = \frac{\sum_E Q(E) \times \theta_{FWHM}(E)}{\sum_E Q(E)} \quad (1)$$

which sums all the FWHM divergences weighted by their corresponding charge. This method allows to compute both the spectrum and the transverse beam divergence for the same data.

This method was used to analyze the experimental data of Fig. 2 producing the beam divergence plotted in Fig. 5a as a function of the shot number.

The mean FWHM beam divergence is estimated to be ≈ 9 mrad with a standard deviation of 14% and undergoes two types of fluctuations. On one hand, the divergence fluctuates from shot to shot with a standard deviation of about 10%, which is of the order of gas density fluctuations inside the capillary tube as explained in Section 4. On the other hand, the divergence slowly decreases from 10 mrad to 7.5 mrad over the series of 100 shots. This drift can be explained by the significant change in charge distribution shown in Fig. 3. The divergence as a function of the electron energy is plotted in Fig. 5b; it shows that the lower the electron energy is the larger the corresponding divergence is so a drift of the charge distribution toward higher energies causes a decrease of the beam divergence.

The beam pointing fluctuations and the associated beam divergence were determined from a different series of 30 shots for the same experimental parameters. The beam divergence in this case was measured from the profile of the electron beam on the scintillating screen when the magnet was removed, so that electrons are not deflected. An example of electron beam image is

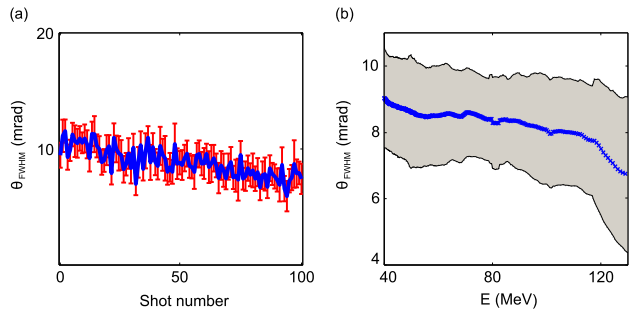

Fig. 5. (a) FWHM divergence of the electron beam as a function of shot number for the data in Fig. 2; vertical error bars correspond to the standard deviation of the divergence distribution of the bunch. The mean divergence is about 9 mrad with a standard fluctuation of 14%. (b) Mean FWHM divergence as a function of electron energy (blue curve) and corresponding standard deviation (gray area). (For interpretation of the references to color in this figure caption, the reader is referred to the web version of this paper.)

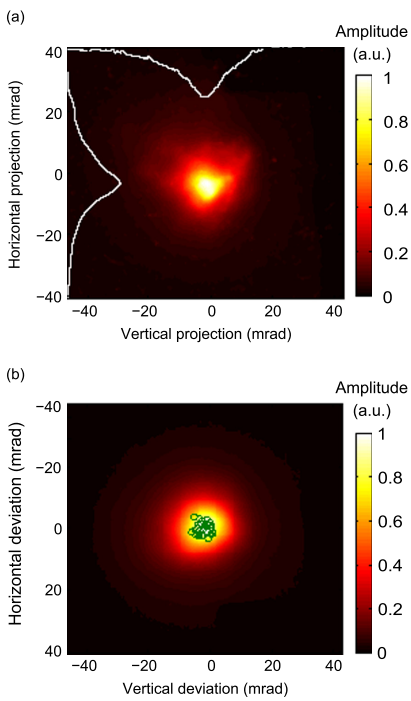

Fig. 6. Electron beam spatial distribution on the scintillating screen, 41 cm away from a 10 mm long, 178 μm diameter capillary tube containing H_2 at an electron density of $(10.0 \pm 1.5) \times 10^{18}$ cm^{-3}. (a) Single shot image of the scintillating screen. (b) Sum of 30 images; green circles indicate the center of each electron beam. (For interpretation of the references to color in this figure caption, the reader is referred to the web version of this paper.)

given by Fig. 6a, the FWHM beam divergence is estimated from the projected profiles, *i.e.* cumulated signal for each row and column of pixels of the CCD chip, which are plotted in the same figure. Despite an appropriate noise processing, the FWHM beam divergence of 14 mrad determined by this method is 35% larger than the previous value obtained from the spectra of Fig. 2a. This discrepancy is quite significant and can be explained as follows. Removing the magnet significantly changes the amount of charge reaching the scintillating screen, increasing it from 66 to 112 pC. It means that about half of the electrons have an energy below 40 MeV. When the magnet is used the electrons below detection level do not contribute to the determination of beam divergence. The electron beams which are detected are different, thus these two methods of measurement provide complementary information on the beam properties.

The beam pointing fluctuations are estimated as

$$\langle \phi \rangle = \frac{1}{ND} \sum_{i}^{N} \sqrt{(\langle X_c \rangle - X_c^i)^2 + (\langle Y_c \rangle - Y_c^i)^2} \quad (2)$$

where (X_c^i, Y_c^i) are the coordinates of the electron beam center for shot i, $(\langle X_c \rangle, \langle Y_c \rangle)$ is the mean position of beam centers, N is the number of shots and $D \approx 41$ cm is the distance between the scintillating screen and the electron source. The coordinates of a beam center are taken as the position of maxima for each projected beam profile. The data of the series are presented in Fig. 6b, the color map represents the sum of 30 electron beam images of the scintillating screen and the green circles are the centers of electron beams. Pointing fluctuations of the electron beam centers are estimated to be 2.3 mrad, that is only 17% of the FWHM beam divergence.

4. Importance of gas confinement on electron properties

Several gas targets are currently investigated for optimizing the properties of electron beams self-injected and accelerated by laser plasma wakefields. Here we compare the properties of electron beams generated from self-injection in a gas jet and in 178 μm diameter, 8 mm, 10 mm, and 20 mm long capillary tubes. H_2 gas was used and the electron density inside the capillary tubes was $(10.0 \pm 1.5) \times 10^{18}$ cm^{-3}, whereas it was $(7 \pm 2) \times 10^{18}$ cm^{-3} for the gas jet. These values of density correspond to the optimum values in terms of charge and reproducibility for the capillary tubes and the gas jet for this experiment. The experimental results are summarized in Table 2. The values reported for the 10 mm long diameter capillary tube are discussed in Section 3.

Experiments with the gas jet as well as other capillary tubes were performed with the same laser settings for a series of

Table 2
Properties of electron beams generated by self-injection in a H_2 gas. The mean beam charge and mean beam divergence were calculated for a series of 30 shots either on a gas jet or 178 μm diameter capillary tube of length 8, 10 and 20 mm. The electron density within the capillary tube was $(10.0 \pm 1.5) \times 10^{18}$ cm^{-3} whereas it was $(7 \pm 2) \times 10^{18}$ cm^{-3} for the gas jet.

Target	Gas length (mm)	$Q_{E>40\ \mathrm{MeV}}$ (pC)	$E_{\max}$	θ_{FWHM} (mrad)	ϕ_{RMS} (mrad)
Gas jet	3	60 ± 60%	75 ± 32%	12 ± 80%	8.1
Capillary tubes	8	77 ± 47%	114 ± 15%	10 ± 19%	1.5
	10	66 ± 11%	120 ± 10%	9 ± 14%	2.3
	20	58 ± 18%	139 ± 6%	6 ± 16%	1.5

30 shots. The length of the gas plateau, where electron self-injection occurs, was 3 mm for the gas jet whereas it was 4 mm for 8 mm long capillary tubes, 5 mm for 10 mm long capillary tubes and 15 mm for 20 mm long capillary tubes. This could explain the comparable amount of charge produced in the gas jet and the capillary tubes. In the cases of the 10 and 20 mm long capillary tubes, electron beams with similar maximum energies were generated. As the electronic density and the laser energy were the same in both cases, the comparison with the 10 mm tubes case shows that the 20 mm long capillary tubes are longer than the effective acceleration length, defined here as the sum of the self-focusing and dephasing length. Finally, the 10 mm long capillary generates the most stable beam charge. Higher energy is reached with the capillary tubes compared to the gas jet. It can be explained by the length of gas medium which is longer in the case of capillary tubes. Fluctuations of maximum energy, beam divergence and pointing are found to be much smaller in capillary tubes than in the gas jet used in this experiment. Differences in the gas distributions of these different targets can contribute to these observations. The gas distribution within a capillary tube is composed of a plateau between the two gas inlets and two steep gradients between the gas inlets and the exits of the capillary tube. The plateau is established in less than 1 ms; the stationary state is a laminar, and shock-free, flow. It lasts for several tens of milliseconds during which the molecular density fluctuations, *i.e.* density fluctuations due to mechanical vibrations induced by the gas feed system and its environment, are estimated to be of the order of 15% and induce an uncertainty on the electron density from shot to shot. The profile of the gas jet is composed of first a steep up-ramp of 0.5 mm then a 3 mm long plateau and ends with a steep down-ramp of 0.5 mm. Both the fluid and PIC simulations need to be performed in order to improve our understanding of the impact of the gas distribution and its dynamics on the properties of electron beams.

5. Conclusion

The properties of electron beams generated by self-injection inside capillary tubes and in a gas jet were analyzed statistically. The results show that reproducible electron beams are produced with a charge above 40 MeV of 66 pC ± 11%, a FWHM beam divergence of 9 mrad ± 14%, a maximum energy of 120 MeV ± 10% and pointing fluctuations of 2.3 mrad in 10 mm long, 178 μm diameter capillary tubes at a density of $(10.0 \pm 1.5) \times 10^{18}$ cm^{-3}. An improved charge stability for electrons above 40 MeV was observed using capillary tubes compared to the case with a gas jet. This can in part be attributed to an increase of the effectively used laser energy when a capillary tube is employed.

Gas distribution fluctuations are suspected to be a significant source of instability. A gas jet and several capillary tubes were compared in order to determine if the gas distribution was modifying the stability of electron beams. A better reproducibility of electron properties is achieved when a capillary tube is used. The laminar, and shock-free, flow established in capillary tubes might be a more reproducible medium than a supersonic gas flow for producing stable electrons beams. Gas density fluctuations, as a source of instability for laser plasma generated electron beams, will be further investigated in future works. Fluid and PIC simulations will be performed in order to enhance our understanding of the impact of the gas distribution and its dynamics on the properties of electron beams.

Acknowledgments

The authors acknowledge the support of the Swedish Research Council, the Knut and Alice Wallenberg Foundation, the Swedish Foundation for Strategic Research, the Lund University X-ray Centre (LUXC), Laserlab-Europe/CHARPAC (Grant agreement 284464, ECs 7th Framework Programme) and EuCARD2/ANAC2 (Grant agreement 312453, ECs 7th Framework Programme). J. Ju acknowledges financial support from the Chinese Scholarship Council (CSC). This project has benefited from financial support from ARC.

References

[1] T. Tajima, J.M. Dawson, Phys. Rev. Lett. 43 (1979) 267, http://dx.doi.org/10.1103/PhysRevLett.43.267, URL: ⟨http://link.aps.org/doi/10.1103/PhysRevLett.43.267⟩.
[2] E. Esarey, C.B. Schroeder, W.P. Leemans, Rev. Mod. Phys. 81 (2009) 1229, http://dx.doi.org/10.1103/RevModPhys.81.1229, URL: ⟨http://link.aps.org/doi/10.1103/RevModPhys.81.1229⟩.
[3] J. Ju, K. Svensson, H. Ferrari, A. Dopp, G. Genoud, F. Wojda, M. Burza, A. Persson, O. Lundh, C.-G. Wahlström, B. Cros, Phys. Plasmas 20 (8) (2013) 083106, http://dx.doi.org/10.1063/1.4817747, URL: ⟨http://link.aip.org/link/?PHP/20/083106/1⟩.
[4] W.P. Leemans, B. Nagler, A.J. Gonsalves, C. Toth, K. Nakamura, C.G.R. Geddes, E. Esarey, C.B. Schroeder, S.M. Hooker, Nat. Phys. 2 (10) (2006) 696, URL: http://dx.doi.org/10.1038/nphys418.
[5] X. Wang, R. Zgadzaj, N. Fazel, Z. Li, S.A. Yi, X. Zhang, W. Henderson, Y.-Y. Chang, R. Korzekwa, H.-E. Tsai, C.-H. Pai, H. Quevedo, G. Dyer, E. Gaul, M. Martinez, A. C. Bernstein, T. Borger, M. Spinks, M. Donovan, V. Khudik, G. Shvets, T. Ditmire, M.C. Downer, Nat. Commun. 4 (2013) 1, URL: http://dx.doi.org/10.1038/ncomms2988.
[6] S. Corde, K. Ta Phuoc, G. Lambert, R. Fitour, V. Malka, A. Rousse, A. Beck, E. Lefebvre, Rev. Mod. Phys. 85 (2013) 1, http://dx.doi.org/10.1103/RevModPhys.85.1, URL: http://link.aps.org/doi/10.1103/RevModPhys.85.1.
[7] C.B. Schroeder, E. Esarey, C.G.R. Geddes, C. Benedetti, W.P. Leemans, Phys. Rev. Spl. Top. Accel. Beams 13 (2010) 101301, http://dx.doi.org/10.1103/PhysRevSTAB.13.101301, URL: http://link.aps.org/doi/10.1103/PhysRevSTAB.13.101301.
[8] J. Ju, K. Svensson, A. Dopp, H.E. Ferrari, K. Cassou, O. Neveu, G. Genoud, F. Wojda, M. Burza, A. Persson, O. Lundh, C.-G. Wahlström, B. Cros, Appl. Phys. Lett. 100 (19) (2012) 191106, http://dx.doi.org/10.1063/1.4712594, URL: ⟨http://link.aip.org/link/?APL/100/191106/1⟩.
[9] G. Genoud, F. Wojda, M. Burza, A. Persson, C.-G. Wahlström, Rev. Sci. Instrum. 82 (3) (2011) 033102, http://dx.doi.org/10.1063/1.3556438, URL: ⟨http://link.aip.org/link/?RSI/82/033102/1⟩.
[10] M. Hansson, F.G. Desforges, J. Ju, L. Senje, S. Dobosz-Dufrénoy, A. Persson, O. Lundh, T.L. Audet, C.-G. Wahlström, B. Cros, Enhanced stability of laser wakefield acceleration using dieletric capillary tubes, Appl. Phys. Lett., submitted for publication.
[11] J. Ju, B. Cros, J. Appl. Phys. 112 (11) (2012) 113102, http://dx.doi.org/10.1063/1.4768209, URL: ⟨http://link.aip.org/link/?JAP/112/113102/1⟩.
[12] A. Buck, K. Zeil, A. Popp, K. Schmid, A. Jochmann, S.D. Kraft, B. Hidding, T. Kudyakov, C.M.S. Sears, L. Veisz, S. Karsch, J. Pawelke, R. Sauerbrey, T. Cowan, F. Krausz, U. Schramm, Rev. Sci. Instrum. 81 (3) (2010) 033301, http://dx.doi.org/10.1063/1.3310275, URL: ⟨http://link.aip.org/link/?RSI/81/033301/1⟩.
[13] S.P.D. Mangles, G. Genoud, M.S. Bloom, M. Burza, Z. Najmudin, A. Persson, K. Svensson, A.G.R. Thomas, C.-G. Wahlström, Phys. Rev. Spl. Top. Accel. Beams 15 (2012) 011302, http://dx.doi.org/10.1103/PhysRevSTAB.15.011302, URL: ⟨http://link.aps.org/doi/10.1103/PhysRevSTAB.15.011302⟩.

Paper III

Supersonic jets of hydrogen and helium for laser wakefield acceleration

K. Svensson, M. Hansson, F. Wojda, L. Senje, M. Burza, B. Aurand, G. Genoud, A. Persson, C.-G. Wahlström, and O. Lundh.

Physical Review Accelerators and Beams **19**, 051301 (2016).

PHYSICAL REVIEW ACCELERATORS AND BEAMS **19,** 051301 (2016)

Supersonic jets of hydrogen and helium for laser wakefield acceleration

K. Svensson,[*] M. Hansson, F. Wojda, L. Senje, M. Burza, B. Aurand, G. Genoud, A. Persson, C.-G. Wahlström, and O. Lundh[†]

Department of Physics, Lund University, P.O. Box 118, SE-221 00 Lund, Sweden

(Received 1 December 2015; published 2 May 2016)

The properties of laser wakefield accelerated electrons in supersonic gas flows of hydrogen and helium are investigated. At identical backing pressure, we find that electron beams emerging from helium show large variations in their spectral and spatial distributions, whereas electron beams accelerated in hydrogen plasmas show a higher degree of reproducibility. In an experimental investigation of the relation between neutral gas density and backing pressure, it is found that the resulting number density for helium is ∼30% higher than for hydrogen at the same backing pressure. The observed differences in electron beam properties between the two gases can thus be explained by differences in plasma electron density. This interpretation is verified by repeating the laser wakefield acceleration experiment using similar plasma electron densities for the two gases, which then yielded electron beams with similar properties.

DOI: 10.1103/PhysRevAccelBeams.19.051301

The development of bright and ultrashort sources of particles and x rays is an important area of research. Such sources are of interest in many domains, including materials science, chemistry, biology, and medicine. Currently, emerging sources based on laser-plasma acceleration [1] are attracting significant attention. The accelerator can be very compact, and the particle beams have several unique characteristics. Recent achievements include the generation of electron beams with high energies (few GeV) [2], short pulse duration (few femtoseconds) [3], high peak current (few kA) [4], low energy spread ($< 1.5\%$) [5], and low emittance (few mm × mrad) [6]. For most demanding applications, however, the stability of the source is also very important. A critical issue for laser wakefield accelerator (LWFA) research is to find ways to decrease shot-to-shot fluctuations.

In a typical LWFA, an intense laser pulse is focused in a neutral gas medium and atoms, or molecules, are rapidly ionized by the leading edge of the laser pulse. The main part of the pulse interacts with a plasma, and free electrons are displaced by the laser ponderomotive force which leads to a significant charge separation and a copropagating plasma wave. Strong accelerating electric fields (∼100 GV/m) are present in the plasma wave, and copropagating electrons can be accelerated to high energies if they have sufficient initial kinetic energy and are located in an appropriate phase of the plasma wave. In the so-called bubble regime [7], the injection of electrons can be achieved by driving the plasma wave to such a high amplitude that the wave breaks. This occurs as the velocity of the electrons exceeds the phase velocity of the plasma wave and results in self-injection of electrons from the background plasma into the accelerating phase of the plasma wave.

The threshold for wave breaking can be described as a laser power threshold [8] as well as a laser energy threshold [9] for a given plasma electron density n_e. Thus, for a given set of laser parameters, the self-injection threshold can be found by adjusting n_e. Assuming ideal gas behavior, the neutral gas number density n in a supersonic jet is proportional to the pressure p_0 supplied to the nozzle and for a fully ionized gas $n_e = N_e n$, where N_e is the number of electrons per atom, or molecule, depending on the gas species. Thus, for fully ionized gases, $n_e \propto p_0$. In this article, we present, to our knowledge, the first comparative study of electron beams emerging from supersonic jets of H_2 and He. These gases were chosen since they will be fully ionized for the present experimental conditions.

The experimental investigations were conducted using the multiterawatt laser at the Lund Laser Centre. This Ti:sapphire-based system produced 37 fs duration laser pulses with 650 mJ of energy on target during the present study. An $f/15$ parabolic mirror focused the laser pulse to a 16 μm (FWHM) spot measured in vacuum, which yielded a peak intensity of 5.7×10^{18} W/cm^2. The beam waist was positioned, within one Rayleigh length, at the front edge of a supersonic gas flow released from a 2 mm diameter nozzle. Behind the interaction medium, along the laser propagation axis, a permanent dipole magnet dispersed the accelerated electrons according to energy. The dispersed electron beams impacted on a scintillating screen, imaged using a 16-bit digital camera. The integrated charge above

[*]kristoffer.svensson@fysik.lth.se
[†]olle.lundh@fysik.lth.se

the spectrometer threshold energy (40 MeV) was also estimated using the measured response of the scintillator screen [10,11].

In Fig. 1, two five-image sequences of electron beams accelerated in 2 mm gas jets of H_2 and He operated at $p_0 = 9.5$ bar are presented. It is apparent that electron beams originating from H_2 [Fig. 1(a)] were, compared to those accelerated in He plasmas [Fig. 1(b)], more stable in terms of maximum electron energy, position, and spatial divergence, as well as integrated beam charge. Most electron energy spectra contained a single peak with a relatively large energy spread, corresponding to the dispersed electron beams shown in Fig. 1(a). Also, the individual images shown in Fig. 1(a) are similar to the average of the full sequence, consisting of ten images, which is shown in Fig. 1(c). However, the electron beams emerging from He [Fig. 1(b)] fluctuated significantly and suffered from filamentation, which was not the case for beams from H_2. Most of the energy spectra of the beams originating in He had multiple peaks, each often having very small energy spreads. It is also apparent that the sequence average [see Fig. 1(d)] is not similar to any of the individual images shown in Fig. 1(b). When comparing the two series, it can also be deduced that the integrated charge of beams accelerated in He is significantly larger than those accelerated in H_2.

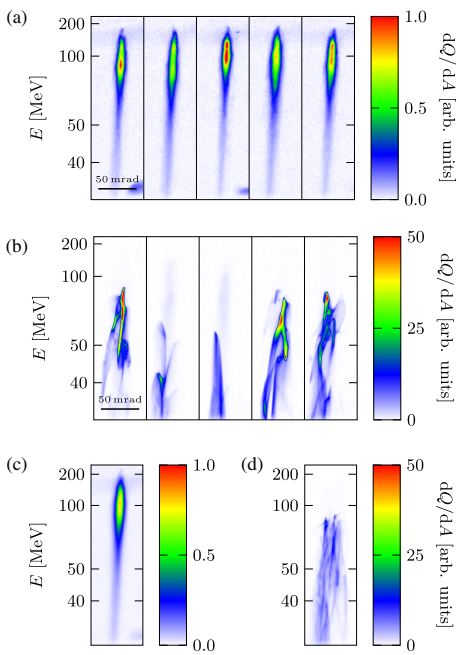

FIG. 1. False-color images of five electron beams emerging from (a) H_2 and (b) He dispersed by a permanent dipole magnet. In both cases, a 2 mm nozzle was used at a fixed backing pressure of 9.5 bar. The reproducibility of the data is shown by the average of ten individual images of electron spectra for beams emerging from (c) H_2 and (d) He. All color scales are normalized to the maximum signal in (a).

The integrated beam charge was measured in a sequence of pulses while varying the pressure in the range 3–15 bar, and the results are shown in Fig. 2. As can be seen, the threshold for self-injection, which is the point where beam charge increases rapidly, is at 9 bar for He but occurs at 11 bar for H_2, indicating differences between the two media.

We have evaluated several phenomena in order to explain our observations, such as differences in the neutral gas ionization and the corresponding ionization-induced defocusing [12]. However, the intensity needed [13] for $He \rightarrow He^+$ is 1.4×10^{15} W/cm^2, and for $He^+ \rightarrow He^{2+}$ is 8.8×10^{15} W/cm^2, which are at least 2 orders of magnitude below the peak laser intensity used in this experiment. Thus, this effect should have been noticeable only at the front of the laser pulse and in the wings. Simulations of the laser-pulse evolution performed using the code WAKE [14], which included ionization of neutral gases, did not show any significant differences in pulse characteristics when propagating through H_2 compared to He at identical n_e.

Another possible cause for the behavior in Fig. 2 could be weaker accelerating fields for H_2 than for He. Since H_2 is a molecular gas, the background of positively charged ions in the bubble behind the laser pulse might not be homogenous, as is expected for monatomic gases such as He. Assuming that the protons of the fully ionized H_2 ions

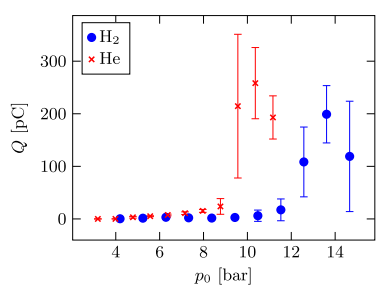

FIG. 2. Measured charge Q in the electron beams accelerated in a 2 mm gas jet over the scanned pressure range 3–15 bar in H_2 (blue circles) and He (red crosses) plotted as functions of the backing pressure. Each point represents the average of ten individual measurements with error bars indicating one standard deviation in each direction. Note that only electrons with an energy exceeding the cutoff (40 MeV) contributes to Q in this figure.

are separated by their molecular bond distance (0.074 nm), Coulomb repulsion will cause an explosion. However, in a H_2 plasma, the initial ion speed (~4.5 nm/fs) is too small to have a noticeable effect on the ion density in the bubble.

Finally, the differences between the gases seen in Figs. 1 and 2 can be due to fluid mechanical differences between the gases. To determine the magnitude of such an influence on the resulting n_e, a simple model of a converging-diverging nozzle was investigated. The relation between the nozzle throat sizes and flow Mach number M is [15]

$$\left(\frac{r_0}{r^*}\right)^2 = \frac{1}{\mathrm{M}}\left[\frac{2+(\kappa-1)\mathrm{M}^2}{(\kappa+1)}\right]^{\frac{\kappa+1}{2(\kappa-1)}}, \quad (1)$$

where r_0 is the nozzle exit radius, r^* is the critical radius where the flow reaches sonic speeds inside the nozzle, and κ is the ratio of specific heats of the gas with numerical values 1.41 for H_2 and 1.66 for He [16]. For the specified $r^* = 0.39$ mm of the 2.0 mm diameter nozzle used in the experiments, Eq. (1) yields $\mathrm{M} = 3.5$ and $\mathrm{M} = 4.2$, for H_2 and He, respectively. Assuming that the gas can be described as an ideal gas, it is also possible to express the density at the nozzle exit, n_{exit}, as [17]

$$n_{\mathrm{exit}} = \frac{p_0}{k_B T_0}\left[1+\frac{\kappa-1}{2}\mathrm{M}^2\right]^{\frac{1}{\kappa-1}}, \quad (2)$$

where k_B is Boltzmann's constant and $T_0 = 293$ K the temperature. As the flow exits the nozzle, it will diverge with half-angle φ given by $\varphi = \alpha + \theta$, where $\alpha = \arcsin \mathrm{M}^{-1}$ is the Mach cone half-angle and θ the nozzle expansion angle. This means that, using cylindrical symmetry, the radius of the gas flow can be written as $r = r_0 + h\tan\varphi$, where h is the vertical distance from the nozzle exit. Assuming that φ remains constant, the gas density at a specific h close to the nozzle exit can be estimated as $n = n_{\mathrm{exit}}(r_0/r)^2$.

As is seen from Eqs. (1) and (2), there is a nontrivial relation between n_{exit} and the gas-species-dependent κ. Therefore, characterizing the relation between p_0 and n for both gases released from the nozzle was necessary and performed experimentally. The phase shift introduced by He at $n = 5\times10^{18}$ cm^{-3} over 2 mm for 633 nm light is 0.14 rad (corresponding to a 14 nm optical path length difference), which is difficult to measure with an ordinary interferometer. Therefore, n was measured as a function of p_0 with a setup consisting of an expanded HeNe-laser beam and a wave-front sensor [18], which is sensitive enough to determine the phase shift introduced by He. By assuming full ionization, n_e is then plotted as a function of p_0 for the two gases in Fig. 3, which clearly shows that they resulted in different n_e at all p_0. Using r^* as a fitting parameter in Eq. (1) to simultaneously fit the theoretical model to experimental results obtained for both H_2 and He yielded $r^* \approx 0.35$ mm, which is close to the specified critical radius

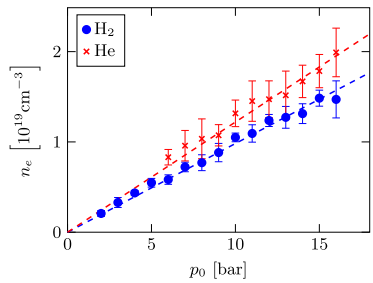

FIG. 3. The plasma electron number density n_e, 1 mm from the nozzle orifice (2 mm diameter) as a function of the applied backing pressure (p_0) for H_2 (blue circles) and He (red crosses). Assuming full ionization, the plateau electron number density n_e along the center axis in the laser propagation direction is determined from measurements of the neutral gas number density (n) using a setup consisting of an expanded HeNe beam and a wave-front sensor. Each point represents the average of 10–20 individual measurements, and the error bars indicate one standard deviation in each direction. The dashed lines are the theoretical results fitted with regards to r^*.

of the nozzle. The fitted results, shown as dashed lines in Fig. 3, are in excellent agreement with the experimental data.

From the theoretical model, it was found that $n_{\mathrm{He}} \approx 1.3 n_{\mathrm{H_2}}$. Thus, n_e in He is ~30% higher than for H_2 at any specific p_0. Compensating for this difference and plotting the data in Fig. 2 as a function of n_e instead of p_0 results in Fig. 4(a). Now it can be seen that the rapid increase in Q occurs at the same n_e for both gas species. The effect observed in Fig. 1 is therefore not significantly due to any of the previously discussed differences between the two gas species but can be explained by the relation between n_e and p_0 in Fig. 3. In Fig. 1, the electrons were accelerated in gas jets with $p_0 = 9.5$ bar which corresponds to $n_e = 9.3\times10^{18}$ cm^{-3} for H_2 and $n_e = 1.2\times10^{19}$ cm^{-3} for He. Using a similar n_e for He as for H_2 in Fig. 1(a) results in Fig. 4(b). Now, the accelerated electron beams emerging from He are very similar to the ones from H_2, which is also seen when comparing the averages of ten individual images in Figs. 1(c) (H_2) and 4(c) (He). Laser self-focusing inside the plasma becomes stronger with increasing n_e, resulting in a smaller spot size w_0 and a higher normalized vector potential a_0 for He than for H_2. For small w_0 and high a_0, it is expected that self-injection LWFA results in unstable, high charge electron beams, since transversal injection dominates over longitudinal injection [19]. When longitudinal injection is the dominant injection mechanism (large w_0 and small a_0), the accelerated electron beams becomes very stable, but with low charge. Thus, the differences seen in Fig. 1 can be explained by the differences in n_e between H_2 and He at

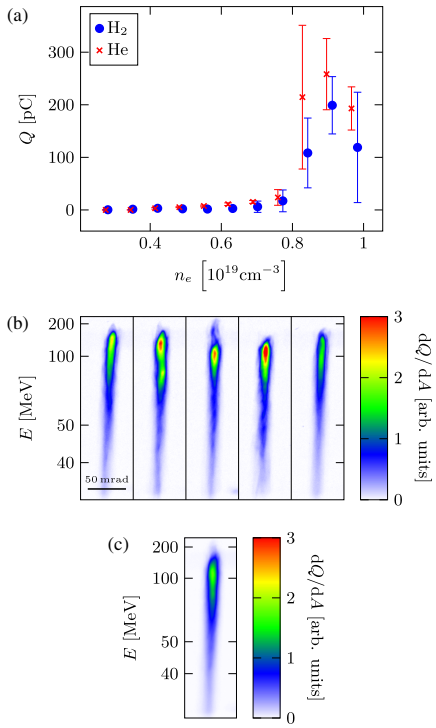

FIG. 4. (a) Measured charge Q from Fig. 2 plotted against plasma electron density n_e (assuming full ionization) instead of backing pressure p_0, by using the results of Fig. 3. Again, only electrons with energies exceeding the cutoff energy of the spectrometer setup contribute to Q. Each point represents the average of ten individual measurements with error bars indicating one standard deviation. (b) False-color images of five electron beams emerging from He at $n_e = 9.8 \times 10^{18}$ cm^{-3} dispersed by a permanent dipole magnet, showing a high resemblance to electron beams accelerated in H_2 at similar n_e. (c) Average of the full ten-image sequence which is partly shown in (b). The color scales are normalized to the maximum signal in Fig. 1(a).

identical p_0, since the two series have different injection mechanisms.

In this study, we have shown that electron beams emerging from H_2 and He at identical nozzle backing pressures have different properties. This is found to be primarily a result of the supersonic gas jet number density dependence on a specific heat ratio which, generally, differs between gas species. Repeating the experiment using similar n_e for both gases confirms these findings, since the resulting beams of accelerated electrons then showed similar properties regardless of gas species. Thus, both gases resulted in stable, low charge electron beams for $n_e < 8 \times 10^{18}$ cm^{-3}, which can be deduced from Fig. 4. It is also believed that this effect can have implications when using gas mixtures as an acceleration medium and should be studied further.

We acknowledge the support of the Swedish Research Council, the Knut and Alice Wallenberg Foundation, the Swedish Foundation for Strategic Research, Laserlab-Europe/CHARPAC (Grant Agreement No. 284464, EC's 7th Framework Programme) and EuCARD2/ANAC2 (Grant Agreement No. 312453, EC's 7th Framework Programme).

[1] T. Tajima and J. M. Dawson, Laser Electron Accelerator, Phys. Rev. Lett. **43**, 267 (1979).

[2] W. P. Leemans, A. J. Gonsalves, H. S. Mao, K. Nakamura, C. Benedetti, C. B. Schroeder, C. Toth, J. Daniels, D. E. Mittelberger, S. S. Bulanov, J. L. Vay, C. G. R. Geddes, and E. Esarey, Multi-GeV Electron Beams from Capillary-Discharge-Guided Subpetawatt Laser Pulses in the Self-Trapping Regime, Phys. Rev. Lett. **113**, 245002 (2014).

[3] A. Buck, M. Nicolai, K. Schmid, C. M. S. Sears, A. Sävert, J. M. Mikhailova, F. Krausz, M. C. Kaluza, and L. Veisz, Real-time observation of laser-driven electron acceleration, Nat. Phys. **7**, 543 (2011).

[4] O. Lundh, J. Lim, C. Rechatin, L. Ammoura, A. Ben-Ismaïl, X. Davoine, G. Gallot, J.-P. Goddet, E. Lefebvre, V. Malka, and J. Faure, Few femtosecond, few kiloampere electron bunch produced by a laser–plasma accelerator, Nat. Phys. **7**, 219 (2011).

[5] C. Rechatin, J. Faure, A. Ben-Ismaïl, J. Lim, R. Fitour, A. Specka, H. Videau, A. Tafzi, F. Burgy, and V. Malka, Controlling the Phase-Space Volume of Injected Electrons in a Laser-Plasma Accelerator, Phys. Rev. Lett. **102**, 164801 (2009).

[6] R. Weingartner, S. Raith, A. Popp, S. Chou, J. Wenz, K. Khrennikov, M. Heigoldt, A. R. Maier, N. Kajumba, M. Fuchs, B. Zeitler, F. Krausz, S. Karsch, and F. Grüner, Ultralow emittance electron beams from a laser-wakefield accelerator, Phys. Rev. Accel. Beams **15**, 111302 (2012).

[7] A. Pukhov and J. Meyer-ter-Vehn, Laser wake field acceleration: The highly non-linear broken-wave regime, Appl. Phys. B **74**, 355 (2002).

[8] D. H. Froula, C. E. Clayton, T. Döppner, K. A. Marsh, C. P. J. Barty, L. Divol, R. A. Fonseca, S. H. Glenzer, C. Joshi, W. Lu, S. F. Martins, P. Michel, W. B. Mori, J. P. Palastro, B. B. Pollock, A. Pak, J. E. Ralph, J. S. Ross, C. W. Siders, L. O. Silva, and T. Wang, Measurements of the Critical Power for Self-Injection of Electrons in a Laser Wakefield Accelerator, Phys. Rev. Lett. **103**, 215006 (2009).

[9] S. P. D. Mangles, G. Genoud, M. S. Bloom, M. Burza, Z. Najmudin, A. Persson, K. Svensson, A. G. R. Thomas, and C.-G. Wahlström, Self-injection threshold in self-guided laser wakefield accelerators, Phys. Rev. Accel. Beams **15**, 011302 (2012).

[10] Y. Glinec, J. Faure, A. Guemnie-Tafo, V. Malka, H. Monard, J. P. Larbre, V. De Waele, J. L. Marignier, and M. Mostafavi, Absolute calibration for a broad range single shot electron spectrometer, Rev. Sci. Instrum. **77**, 103301 (2006).

[11] A. Buck, K. Zeil, A. Popp, K. Schmid, A. Jochmann, S. D. Kraft, B. Hidding, T. Kudyakov, C. M. S. Sears, L. Veisz, S. Karsch, J. Pawelke, R. Sauerbrey, T. Cowan, F. Krausz, and U. Schramm, Absolute charge calibration of scintillating screens for relativistic electron detection, Rev. Sci. Instrum. **81**, 033301 (2010).

[12] T. Auguste, P. Monot, L.-A. Lompré, G. Mainfray, and C. Manus, Defocusing effects of a picosecond terawatt laser pulse in an underdense plasma, Opt. Commun. **89**, 145 (1992).

[13] P. Gibbon, *Short Pulse Laser Interactions with Matter, An Introduction* (Imperial College Press, London, 2005).

[14] P. Mora and J. Thomas M. Antonsen, Kinetic modeling of intense, short laser pulses propagating in tenuous plasmas, Phys. Plasmas **4**, 217 (1997).

[15] S. Semushin and V. Malka, High density gas jet nozzle design for laser target production, Rev. Sci. Instrum. **72**, 2961 (2001).

[16] C. Nordling and J. Österman, *Physics Handbook*, 7th ed. (Studentlitteratur, Lund, 2004).

[17] K. Schmid and L. Veisz, Supersonic gas jets for laser-plasma experiments, Rev. Sci. Instrum. **83**, 053304 (2012).

[18] G. R. Plateau, N. H. Matlis, C. G. R. Geddes, A. J. Gonsalves, S. Shiraishi, C. Lin, R. A. van Mourik, and W. P. Leemans, Wavefront-sensor-based electron density measurements for laser-plasma accelerators, Rev. Sci. Instrum. **81**, 033108 (2010).

[19] S. Corde, C. Thaury, A. Lifschitz, G. Lambert, K. Ta Phuoc, X. Davoine, R. Lehe, D. Douillet, A. Rousse, and V. Malka, Observation of longitudinal and transverse self-injections in laser-plasma accelerators, Nat. Commun. **4**, 1501 (2013).

Paper IV

Laser wakefield acceleration using wire produced double density ramps

M. Burza, A. Gonoskov, K. Svensson, F. Wojda, A. Persson, M. Hansson, G. Genoud, M. Marklund, C.-G. Wahlström and O. Lundh.

Physical Review Special Topics - Accelerators and Beams **16**, 011301 (2013).

PHYSICAL REVIEW SPECIAL TOPICS - ACCELERATORS AND BEAMS **16**, 011301 (2013)

Laser wakefield acceleration using wire produced double density ramps

M. Burza,[1] A. Gonoskov,[2,3] K. Svensson,[1] F. Wojda,[1] A. Persson,[1] M. Hansson,[1] G. Genoud,[1] M. Marklund,[2] C.-G. Wahlström,[1] and O. Lundh[1]

[1]*Department of Physics, Lund University, P.O. Box 118, SE-221 00 Lund, Sweden*
[2]*Department of Physics, Umeå University, SE-901 87 Umeå, Sweden*
[3]*Institute of Applied Physics, Russian Academy of Sciences, 46 Ulyanov Street, Nizhny Novgorod 603950, Russia*

(Received 22 May 2012; published 8 January 2013)

A novel approach to implement and control electron injection into the accelerating phase of a laser wakefield accelerator is presented. It utilizes a wire, which is introduced into the flow of a supersonic gas jet creating shock waves and three regions of differing plasma electron density. If tailored appropriately, the laser plasma interaction takes place in three stages: Laser self-compression, electron injection, and acceleration in the second plasma wave period. Compared to self-injection by wave breaking of a nonlinear plasma wave in a constant density plasma, this scheme increases beam charge by up to 1 order of magnitude in the quasimonoenergetic regime. Electron acceleration in the second plasma wave period reduces electron beam divergence by $\approx 25\%$, and the localized injection at the density downramps results in spectra with less than a few percent relative spread.

DOI: 10.1103/PhysRevSTAB.16.011301 PACS numbers: 41.75.Jv, 52.35.Tc, 52.38.−r, 52.50.Jm

Plasma-based laser-driven electron accelerators can produce strong longitudinal fields, $\sim$100 GV/m, in the collective electron oscillations in the wake of an intense laser pulse [1]. This gives an advantage over conventional accelerators using rf cavities regarding the relatively compact high-power tabletop laser systems readily available [2].

In most experiments, injection of electrons into the accelerating structure relies on breaking of the plasma wave, which can thus self-inject electrons. This scheme is rather simple and quasimonoenergetic beams have been produced [3–5]. Electron beams of low spectral spread and divergence are necessary for these accelerators to be attractive for applications [6–8]. However, the wave breaking process is highly nonlinear, and in order to achieve higher quality beams, means to control the injection process are required. Both the amount of charge and the time of electron injection from the background plasma into the accelerating and focusing phase of the wakefield are crucial [9–11]. Here, self-injection [12–14] is inferior to most schemes with external injection control, such as colliding pulse techniques [15–18], ionization injection [19,20], or gradients in plasma electron density [21–24], which are used in this experiment. At the downwards gradient the plasma wavelength increases rapidly, the plasma wave breaks and electrons are trapped.

Shock waves resulting in very abrupt density transitions have been produced previously with a knife edge introduced into a supersonic gas flow [25]. By this, a well-defined shock wave and a density downwards gradient is provided on the laser axis. Alternatively, an auxiliary pulse produced an electron depleted region by formation of an ionization channel followed by hydrodynamic expansion [26,27]. Our experiment relates to these, as plasma densities are modulated on the laser axis to control injection externally.

We present a novel, staged, three step, laser wakefield accelerator that utilizes a thin wire crossing the supersonic flow of a gas jet. In this scheme, extremely sharp density transitions and shock waves facilitate gradient injection. These transitions may be of only some microns length [28]. In the first stage, comprised of a constant plasma density prior to reaching the first shock front, the pulse propagates and may thus match itself to the plasma conditions by relativistic self-focusing, self-modulation and temporal compression, with only a negligible amount of charge being trapped. After a variable length, adjustable by the wire position along the optical axis, the laser pulse reaches the second stage, where the first shock front, originating from the wire, in combination with the subsequent expansion fan produces gradients that enable injection. During the transition to the third stage, the plasma density increases from the density-diluted region right above the wire to the final constant density region. The plasma wavelength shrinks rapidly, which under certain circumstances enables a controlled charge transfer of the previously injected electrons from the first into the second plasma wave period. This mechanism, which is driven by inertia, may in addition have a filtering effect on the previously injected charges. The dominant process, however, is a new injection at the second shock front. The proceeding constant density plasma is finally utilized for electron acceleration driven by the already matched laser pulse.

The experiment was conducted at the Lund Laser Centre, Sweden, where a Ti:Sa CPA laser system provided pulses at 800 nm central wavelength with 42 fs duration and 1 J energy. The laser field is horizontally polarized. A deformable mirror and an $f = 75$ cm off-axis parabolic mirror facilitated a nearly diffraction limited focal spot, 0.7 mm above the orifice of a 3 mm diameter supersonic gas nozzle. The laser was focused at the boundary of the gas jet producing a spot with 15 μm diameter (intensity FWHM). A motorized holder positioned a wire above the nozzle but below the laser optical axis (z axis). This produced three distinct plasma density regions for the laser interaction as schematized by the white broken line function in Fig. 6. To tailor and model plasma electron densities for simulations, interferometric measurements were carried out using hydrogen at 9 bar backing pressure. It was found that the laser pulse initially encounters a region of approximately constant electron density (region I), which was determined to 6×10^{18} cm^{-3}. After ≈ 1 mm it encounters the first shock wave and a downwards gradient, followed by region II, where the plasma density is reduced to 3×10^{18} cm^{-3} over ≈ 300 μm. After a second shock wave transition, region III is reached. Here the density is approximately the same as in region I and it is here the main acceleration takes place. Plasma densities scale linearly with backing pressure. Adjustments of wire position, thickness, Mach number, and backing pressure tailor gradients, lengths, and density ratios between region I and region II to match the requirements for electron injection and laser guiding. Shock wave divergence angle and density ramps were found to be symmetric as long as the wire is $<$0.5 mm off the nozzle center. Without wire, the plasma density is almost constant and comparable to that at the plateau regions I and III.

As diagnostics served a top view camera and a permanent magnet electron spectrometer equipped with a Lanex screen (Kodak Lanex Regular), whose emission was recorded by a 16 bit CCD camera. Based on previous work [29,30], the electron spectrometer is calibrated in absolute charge. The setup is depicted in Fig. 1.

Stainless steel wires with 300, 200, 50, and 25 μm diameter were tested, but only the latter two were found to trigger injection, with the clearly best performance with the 25 μm wire. Thicker wires inevitably increase the length and depth of the density-diluted region II, promoting diffraction and making it difficult to maintain a sufficiently focused laser pulse for region III.

Hydrogen and helium were both tested as target gas together with the wire but while hydrogen could deliver electron beams in more than 90% of the shots; helium was much less reliable with an optimized injection probability of less than 20%. This is in line with parallel studies investigating the influence of the target gas on beam quality and reliability in a constant density gas jet [31]. Thus, in the following, results obtained with hydrogen are presented.

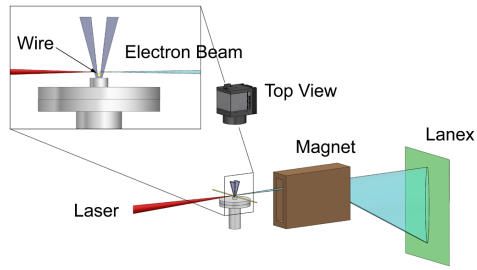

FIG. 1. Experimental setup: The laser pulse enters from the left and impinges on the gas jet 0.7 mm above the nozzle. The wire is positioned ≈ 0.2 mm above the orifice. Top view and a permanent magnet Lanex electron spectrometer serve as primary diagnostics. The position $z = 0$ along the laser axis is centered above the nozzle.

A wire height scan revealed that the probability for the production of electron beams increases with reduced distance to the optical axis. However, when closer than 0.65 mm the lifetime of the wire is reduced. As no improved performance on the production of electron beams could be observed in the range between 0.35 and 0.50 mm, the latter position was chosen. Here, the 25 μm wire survived about 60 to 100 shots.

A z scan conducted with the 25 μm wire, 0.50 mm below the laser optical axis, and with a backing pressure below but close to the threshold for self-injection, revealed the sensitivity of the wire position along the optical axis on the production of electron beams (threshold is defined here as the constant plasma density resulting in beams with $<$10% of the maximum charge observed during a pressure scan in the quasimonoenergetic regime). This window was found to be ≈ 200 μm wide only. Outside this, the beam charge is comparable to the self-injection case without density modulation.

Pressure scans were carried out at what was found to be the optimum spatial parameters, employing the 25 μm diameter wire at 0.50 mm distance to the optical axis and at a longitudinal z position 0.07 mm from the nozzle center towards the off-axis parabolic mirror. The wire injection scheme was found to be rather robust with regard to backing pressure. Below the self-modulated laser wakefield accelerator (LWFA) regime at 11 bar, the beam charge is increased by 1 order of magnitude, as illustrated in Fig. 2. With the wire, electron beam divergence is not affected by the overall plasma density but is on average only 75% compared to the self-injection case. On rare occasions, a beam divergence down to 2 mrad could be demonstrated, which is less than the minimum divergence achieved without wire.

Example spectra can be seen in Fig. 3, showing the spectral range from 43 MeV to infinity. A relative spectral spread $\frac{\Delta E}{E} \leq 4\%$ can be calculated. Note however, that

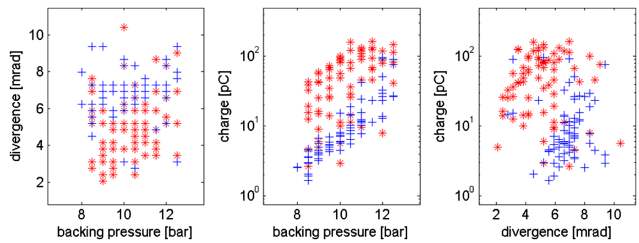

FIG. 2. Comparison of divergence and charge of electron beams using hydrogen as target gas. The red stars represent shots with the wire 0.5 mm below the laser axis, and blue crosses represent LWFA with nonlinear wave breaking and self-injection. Every data point corresponds to one shot. The failure rate with wire is below 5% and thus comparable to the wireless self-injection. Note the increased brightness indicated by the results in the figure to the right.

spectrometer dispersion and divergence have not been deconvoluted here. In fact, 4 mrad FWHM (see Fig. 3) produces an apparent $\frac{\Delta E}{E} \approx 4\%$ (FWHM) at 100 MeV, thus the real relative spectral spread is below what can be resolved with this particular spectrometer but less than a few percent. Electron beam mean energies are generally lower with the wire. The effect of the wire is threefold: It injects a charge $\sim$10 times higher than that available without wire while at the same time providing beams with clean quasimonoenergetic spectra and reduced divergence, thus brightness is increased dramatically. A weak self-injected background charge can be identified in most of the shots. Within limits, energy tuning becomes possible by altering the z position of the wire as illustrated in Fig. 3. From this a field of ≈ 250 GV/m and an acceleration length of ≈ 0.4 mm may be estimated, indicating that acceleration for the wire-injected beams effectively only takes place in stage III. The background charge, which is higher in energy, must therefore result from injection in an earlier stage, or resemble an injected dark current exposed to higher acceleration fields. If we assume this background not to be accelerated over a much longer distance than the wire-injected charge, this indicates that acceleration of the wire-injected charge takes place in a later plasma wave period as field strengths decrease with increasing number of plasma wave oscillation periods behind the laser driver. This is supported by beam profile measurements that show an ellipticity in the beam divergence for the self-injected beams only, as illustrated in Fig. 4, which can be understood as an effect due to the interaction of the injected electrons with the laser field inside the first plasma wave period [32].

Figure 5 shows spectra with and without wire at backing pressures that result in comparable beam charges for both cases. Wire injection at 9 bar is thus compared to self-injection at 12 bar. Note that low-energy artifacts, carrying a significant amount of charge, appear >20 pC in the spectra of self-injected beams, while spectra of wire-injected beams are cleaner. The tendency of decreasing peak energy with increasing charge due to beam loading [10] is clearly visible in the wire injection case and indicates that injection probably occurs at the same z position.

The 3D fully relativistic parallel PIC code ELMIS [33] was used to investigate the physical mechanisms in the modulated density during laser propagation. In the simulation 140 attoseconds corresponded to one time step and an $80 \times 80 \times 80$ μm^3 box was represented by

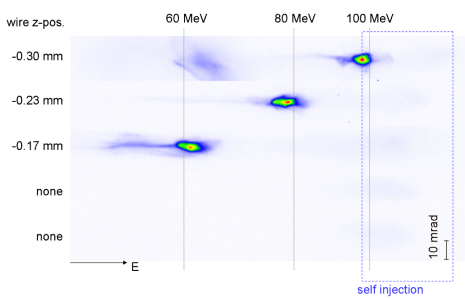

FIG. 3. Example spectra with comparable charge and variable wire position as recorded on the Lanex screen using 9.5 bar backing pressure. Besides the rather strong peak when the wire is present, a weak background self-injection can be seen in all spectra.

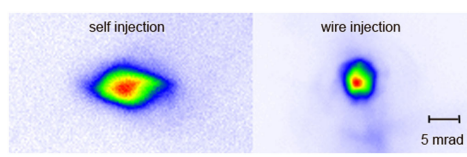

FIG. 4. Beam profile measurements acquired with helium illustrate different eccentricities for the two cases without wire on the left and with wire on the right, shown on an equal lateral and normalized color scale.

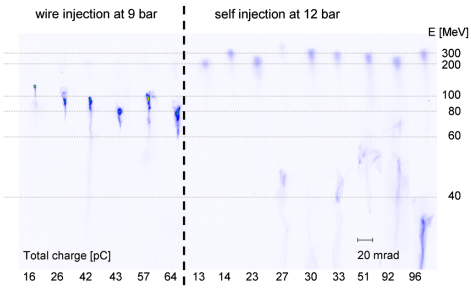

FIG. 5. Example spectra of beams with variable charge and fixed wire position; left: wire injection at 9 bar backing pressure; right: self-injection at 12 bar backing pressure to compensate for the charge increase in the wire injection case as indicated in Fig. 2. Each group has been sorted according to integrated charge and the spectra are displayed on an equal lateral and normalized color scale.

$1024 \times 256 \times 256$ cells. The ions (H^+) were mobile. During the simulation the average number of virtual particles was 1 billion. Laser parameters were taken from the experiment. As the resolution for the measured plasma densities was limited to $\sim$100 μm, the exact distribution is unknown. Still, the interferometric data does provide useful information about densities and lengths of each section while steeper gradients such as shock fronts remain concealed. In combination with theoretical considerations and fluid simulations by Wang *et al.* [34], a profile resembled by the broken line function in Fig. 6 is very likely and thus used for the simulations. This density distribution is fully consistent with the acquired interferometric data. It should be noted though that estimated gas jet temperatures in the experiment are in the range 10–50 K only, and are thus 1 order of magnitude lower than those simulated by Wang *et al.* [34]. Moreover, in our case, the distance between wire and plasma channel was about 3 times larger than what was presented in that particular paper.

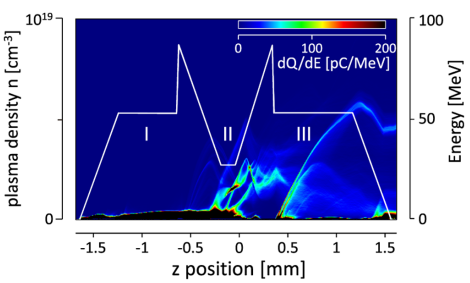

FIG. 6. Electron energy distribution as a function of the laser pulse z position and plasma density distribution (white curve).

Additionally, those simulations were carried out with helium while we used hydrogen, which at these low temperatures requires a different equation of state.

With the proposed density distribution, simulations show that when traversing region I, the laser pulse gets focused transversely and generates a highly nonlinear plasma wave, which does not reach breaking and thus facilitates neither longitudinal nor transverse self-injection of electrons. In line with previous studies [21,22,35] at the density downramp, which is the expansion fan originating from the wire, the cavities of the nonlinear plasma wave rapidly expand behind the laser pulse and thereby catch electrons accumulated between the buckets. In region II these electrons form an electron bunch. At the entry to region III, the cavity size shrinks again. With the assumed shallow inward gradients however, injected electrons are dephased after the transition and are not accelerated further. The following outward density shock wave enables a second injection of a new bunch into the second plasma wave period, which is accelerated throughout region III.

The initial dephasing and renewed injection of electrons upon entering stage III, followed by a rapid acceleration over no more than half a millimeter until the end of the gas jet, explains the rather short acceleration distances that can be derived from the field estimates related to Fig. 3. This also leads to the observed lower final energy of the electrons compared to the self-injection case. The localized injection results in highly monoenergetic beams both in simulation and experiment. When increasing the height above the wire, a decrease in gradient strengths together with an extension of region II explains the reduced probability for the production of electron beams when operating at too large a distance. That the electrons are accelerated in the second plasma wave period, isolated from the laser pulse, as suggested by simulations and indicated experimentally, may as well explain the reduced divergence.

In conclusion, a wire injection scheme has successfully been demonstrated as an alternative to some more complex setups facilitating controlled injection. Beam features include a reduction in divergence by 25% and an increase in bunch charge by up to 1 order of magnitude if compared to beams of electrons accelerated in the quasimonoenergetic, nonlinear, self-injection regime. Their spectra are tunable and show less than a few percent relative spread. Simulations confirm the experimental findings with respect to external injection control, acceleration in the second plasma wave period, and resulting spectral distribution.

ACKNOWLEDGMENTS

We acknowledge the support of the Swedish Research Council, the Knut and Alice Wallenberg Foundation, the Lund University X-Ray Centre, the European Research Council Contract No. 204059-QPQV, the Swedish Research Council Contract No. 2010-3727, and the Swedish National Infrastructure for Computing.

[1] T. Tajima and J. Dawson, Phys. Rev. Lett. **43**, 267 (1979).
[2] S. Backus, C. G. Durfee, M. M. Murnane, and H. C. Kapteyn, Rev. Sci. Instrum. **69**, 1207 (1998).
[3] C. G. R. Geddes, Cs. Toth, J. van Tilborg, E. Esarey, C. B. Schroeder, D. Bruhwiler, C. Nieter, J. Cary, and W. P. Leemans, Nature (London) **431**, 538 (2004).
[4] J. Faure, Y. Glinec, A. Pukhov, S. Kiselev, S. Gordienko, E. Lefebvre, J.-P. Rousseau, F. Burgy, and V. Malka, Nature (London) **431**, 541 (2004).
[5] S. P. D. Mangles *et al.*, Nature (London) **431**, 535 (2004).
[6] K. Nakajima *et al.*, Nat. Phys. **4**, 92 (2008).
[7] H.-P. Schlenvoigt *et al.*, Nat. Phys. **4**, 130 (2007).
[8] M. Fuchs *et al.*, Nat. Phys.**5**, 826 (2009).
[9] M. Tzoufras, W. Lu, F. Tsung, C. Huang, W. Mori, T. Katsouleas, J. Vieira, R. Fonseca, and L. Silva, Phys. Rev. Lett. **101**, 145002 (2008).
[10] C. Rechatin, X. Davoine, A. Lifschitz, A. Ben Ismail, J. Lim, E. Lefebvre, J. Faure, and V. Malka, Phys. Rev. Lett. **103**, 194804 (2009).
[11] C. Rechatin, J. Faure, A. Ben-Ismail, J. Lim, R. Fitour, A. Specka, H. Videau, A. Tafzi, F. Burgy, and V. Malka, Phys. Rev. Lett. **102**, 164801 (2009).
[12] I. Kostyukov and E. Nerush, Phys. Rev. Lett. **103**, 175003 (2009).
[13] S. V. Bulanov, F. Pegoraro, A. M. Pukhov, and A. S. Sakharov, Phys. Rev. Lett. **78**, 4205 (1997).
[14] A. Zhidkov, J. Koga, T. Hosokai, K. Kinoshita, and M. Uesaka, Phys. Plasmas **11**, 5379 (2004).
[15] E. Esarey, R. Hubbard, W. Leemans, A. Ting, and P. Sprangle, Phys. Rev. Lett. **79**, 2682 (1997).
[16] V. Malka, J. Faure, C. Rechatin, A. Ben-Ismail, J. K. Lim, X. Davoine, and E. Lefebvre, Phys. Plasmas **16**, 056703 (2009).
[17] A. Beck, X. Davoine, and E. Lefebvre, New J. Phys. **13**, 093016 (2011).
[18] J. Faure, C. Rechatin, A. Norlin, A. Lifschitz, Y. Glinec, and V. Malka, Nature (London) **444**, 737 (2006).
[19] A. Pak, K. A. Marsh, S. F. Martins, W. Lu, W. B. Mori, and C. Joshi, Phys. Rev. Lett. **104**, 025003 (2010).
[20] C. McGuffey *et al.*, Phys. Rev. Lett. **104**, 025004 (2010).
[21] S. Bulanov, N. Naumova, F. Pegoraro, and J. Sakai, Phys. Rev. E **58**, R5257 (1998).
[22] H. Suk, N. Barov, J. Rosenzweig, and E. Esarey, Phys. Rev. Lett. **86**, 1011 (2001).
[23] C. G. R. Geddes, K. Nakamura, G. Plateau, Cs. Toth, E. Cormier-Michel, E. Esarey, C. Schroeder, J. Cary, and W. Leemans, Phys. Rev. Lett. **100**, 215004 (2008).
[24] A. J. Gonsalves *et al.*, Nat. Phys. **7**, 862 (2011).
[25] K. Schmid, A. Buck, C. Sears, J. Mikhailova, R. Tautz, D. Herrmann, M. Geissler, F. Krausz, and L. Veisz, Phys. Rev. ST Accel. Beams **13**, 091301 (2010).
[26] J. Faure, C. Rechatin, O. Lundh, L. Ammoura, and V. Malka, Phys. Plasmas **17**, 083107 (2010).
[27] C.-T. Hsieh, C.-M. Huang, C.-L. Chang, Y.-C. Ho, Y.-S. Chen, J.-Y. Lin, J. Wang, and S.-Y. Chen, Phys. Rev. Lett. **96**, 095001 (2006).
[28] A. C. Kermode *et al.*, *Mechanics of Flight* (Pearson Education, Harlow, England, 2006).
[29] Y. Glinec, J. Faure, A. Guemnie-Tafo, V. Malka, H. Monard, J. P. Larbre, V. De Waele, J. L. Marignier, and M. Mostafavi, Rev. Sci. Instrum. **77**, 103301 (2006).
[30] A. Buck *et al.*, Rev. Sci. Instrum. **81**, 033301 (2010).
[31] K. Svensson (unpublished).
[32] S. P. D. Mangles *et al.*, Phys. Rev. Lett. **96**, 215001 (2006).
[33] URL http://www.ipfran.ru/english/structure/lab334/simlight.html.
[34] C. Wang, J. Li, J. Sun, and X. Luo, Phys. Rev. ST Accel. Beams **15**, 020401 (2012).
[35] R. G. Hemker, N. Hafz, and M. Uesaka, Phys. Rev. ST Accel. Beams **5**, 041301 (2002).

Paper V

Down-ramp injection and independently controlled acceleration of electrons in a tailored laser wakefield accelerator

M. Hansson, B. Aurand, X. Davoine, H. Ekerfelt, K. Svensson, A. Persson, C.-G. Wahlström, and O. Lundh.

Physical Review Special Topics - Accelerators and Beams **18**, 071303 (2015).

PHYSICAL REVIEW SPECIAL TOPICS—ACCELERATORS AND BEAMS **18,** 071303 (2015)

Down-ramp injection and independently controlled acceleration of electrons in a tailored laser wakefield accelerator

M. Hansson,[1,*] B. Aurand,[1] X. Davoine,[2] H. Ekerfelt,[1] K. Svensson,[1]
A. Persson,[1] C.-G. Wahlström,[1] and O. Lundh[1,†]

[1]*Department of Physics, Lund University, P.O. Box 118, S-22100 Lund, Sweden*
[2]*CEA, DAM, DIF, Bruyères-le-Châtel, 91297 Arpajon, France*

(Received 23 March 2015; published 8 July 2015)

We report on a study on controlled injection of electrons into the accelerating phase of a plasma wakefield accelerator by tailoring the target density distribution using two independent sources of gas. The tailored density distribution is achieved experimentally by inserting a narrow nozzle, with an orifice diameter of only 400 μm, into a jet of gas supplied from a 2 mm diameter nozzle. The combination of these two nozzles is used to create two regions of different density connected by a density gradient. Using this setup we show independent control of the charge and energy distribution of the bunches of accelerated electron as well as decreased shot-to-shot fluctuations in these quantities compared to self-injection in a single gas jet. Although the energy spectra are broad after injection, simulations show that further acceleration acts to compress the energy distribution and to yield peaked energy spectra.

DOI: 10.1103/PhysRevSTAB.18.071303 PACS numbers: 41.75.Jv, 52.35.-g, 52.38.-r, 52.50.Jm

Benefiting from the high electric fields that can be sustained in a plasma wave, laser wakefield accelerators [1] appear promising as compact sources of highly relativistic electrons and X-rays. Quasi-monoenergetic bunches of highly relativistic electrons were first observed in 2004 [2–4], by self-injection through wave-breaking. Since then, much effort has been made on controlling the injection of electrons into the accelerating plasma structure. Different mechanisms for injection, such as injection by colliding laser pulses [5–7] and ionization [8–11] and injection in density down-ramps [12–16] etc., have been proposed and studied both theoretically and experimentally.

The mechanism of density down-ramp injection is typically divided into two regimes; short density ramps (of the order of the plasma wavelength, λ_p) and long density ramps ($> \lambda_p$). Short density ramps have been produced experimentally, for example by optical plasma formation and expansion [17] and by shock waves [15,18] in gas jets. Due to the well-localized injection point, electron bunches with peaked energy spectra can be generated. In longer density ramps [14,16], injections occur over a longer distance, and thus initially give broad energy spectra. However, after further acceleration of the electrons, the energy spectra can become peaked.

The mechanism of density down-ramp injection relies on breaking of the plasma density wave that follows a laser pulse. This occurs when the electrons that constitute the plasma wave approaches and exceeds the phase velocity of the wave. For laser wakefield accelerators based on self-injection this is achieved by driving the plasma density oscillations to such high amplitude that wave-breaking occurs. In contrast, density down-ramp injection exploits the gradually increasing plasma wavelength in the ramp. Behind the driving laser pulse, this results in a decreased phase velocity of the plasma density wave and can thus be used to reach the conditions for wave-breaking.

In this article, we present a study, experimentally and numerically, on controlled injection of electrons into the accelerating field of a laser wakefield accelerator, based on long density down-ramps, and the subsequent acceleration of the injected electrons in the following low density plasma. The aim is to improve our understanding of the physics behind both injection in density down-ramps and the subsequent acceleration.

Controlled injection is achieved in this experiment using two separate nozzles to supply the gas in the interaction region. In contrast to the work presented in Ref. [16], where ionization-induced injection is employed in combination with a density down-ramp, the electrons are injected in this experiment solely by density down-ramp injection. Furthermore, our experimental setup allows for continuous variation of the length of the plasma after the injection point, as compared to Refs. [14,16]. We show that this density distribution can be used to separately control the amount of charge and the electron kinetic energy in the bunches of accelerated electrons. The shot-to-shot fluctuations, in total charge and energy distribution, achieved using this setup are significantly smaller compared to the beams accelerated in the self-injection scheme in a single

*martin.hansson@fysik.lth.se
†olle.lundh@fysik.lth.se

gas jet. The conclusions presented in this article are based on experiments, performed using a multi-terawatt laser at the Lund Laser Centre, and supported by particle-in-cell (PIC) simulations using the code CALDER-CIRC [19].

The laser pulses, each containing 650 mJ of energy and with a duration (FWHM) of 40 fs, are focused to an almost circular spot with 19 μm diameter (FWHM), using an $f = 0.765$ m off-axis parabolic mirror. The peak intensity of the laser pulses, when focused in vacuum, is determined to 3.7×10^{18} W/cm^2, corresponding to a normalized vector potential of 1.3.

Two separate nozzles are used to provide the desired density distribution of hydrogen gas in the interaction region, as illustrated in Fig. 1(a), and is ionized by the leading edge of each laser pulse. The main part of the gas is supplied by a nozzle with an exit diameter of 2 mm, with its orifice located 1 mm from the optical axis. This nozzle provides an almost cylindrically symmetric jet of gas toward the optical axis, and is typically positioned such that the laser pulse is focused on the front edge of the density distribution. Additionally, a narrow metallic tube, with an orifice diameter of 400 μm, is inserted into the jet, perpendicular to both the optical axis and the direction of the main jet. Gas is supplied through this tube to provide an additional, localized, contribution to the density in the interaction region with the laser pulse.

The total neutral density distribution, along the optical axis, of the gas provided from these two nozzles is characterized off-line by measuring, using a wavefront sensor, the additional optical path length introduced by the gas in an optical probe beam [20]. The optical path length introduced by the gas provided from the 2 mm nozzle is first measured and the density distribution is calculated assuming circular symmetry. The narrow tube is inserted into the flow from the 2 mm nozzle and the wavefront is again measured, first without any gas supplied from the narrow tube. By comparing the wavefront with and without the narrow tube inserted in the flow we conclude that the gas distribution is essentially unaffected by inserting this tube. Finally, the difference in optical path length is measured with gas supplied simultaneously from the main nozzle and from the narrow tube, as shown in Fig. 1(b). This allows the contribution from the narrow tube to the total gas density to be determined assuming circular symmetry close to the orifice, and the final total density profile, shown in Fig. 1(c), to be calculated.

The total density distribution along the optical axis contains a peak and a plateau joined together by a gradient. As will be shown, under suitable chosen conditions, density down-ramp injection of electrons into the accelerating phase of a laser plasma wakefield occurs in this gradient and the electrons are subsequently accelerated in the remaining plasma.

The backing pressures supplied independently to each nozzle are used to control the density in the peak and the plateau. The density profile from the 2 mm gas nozzle is approximately flat over 0.7 mm which corresponds to the maximum plateau length. The density in the plateau is used to control the plasma wavelength in this region and is also used to tune the strength of the accelerating field. Furthermore, the two nozzles are separately mounted on 3-axis translation stages which allow full control of the position of the two density distributions both relative to each other and relative to the laser focus. By moving the 2 mm nozzle along the optical axis, while keeping the narrow nozzle fixed, the length of the density plateau is varied. This degree of freedom provides a mean to perform studies of the acceleration independently of the injection of electrons.

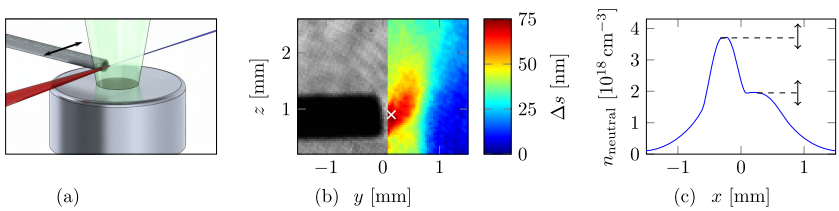

FIG. 1. A schematic illustration of the experimental setup is shown in (a). The laser pulses (red) are focused on the front edge of the gas jet provided from a 2 mm nozzle with its orifice located 1 mm from the optical axis. A narrow tube is inserted into the jet, with its orifice 0.2 mm from the optical axis, and provides locally an additional amount of gas. The electrons (blue) accelerated in the interaction propagate along the optical axis. Measurements, using a wavefront sensor, of the additional optical path length introduced by the gas in an optical probe beam allows the neutral gas density profile to be determined. In (b) the additional path length (Δs) introduced by the gas, supplied from both nozzles simultaneously, is shown in the color scale in the part not obstructed by the narrow tube. The 2 mm nozzle is located just below the edge of the image and supplies a flow of gas along the vertical (z) axis. The shadow of the narrow tube marks its position in the left part of the figure. The optical axis of the main laser beam is perpendicular to the plane of the figure and its position in the plane is marked as a white cross. The typical neutral gas density (n_{neutral}) distribution along the optical (x) axis used in this experiment is shown in (c). The tube can be moved along the optical axis to change the position of the density peak and thus also the density down-ramp. Furthermore, the density in the peak and plateau can be varied independently.

Measurements of the density distributions show that the gradient between the two regions is approximately 230 μm long and is unaffected by changing the backing pressure within the range used in this experiment. Thus, the density down-ramp becomes sharper as the backing pressure to the narrow tube is increased, which allowed for studies to be performed of the dependence of the number of injected electrons on the gradient.

The electrons accelerated in the plasma are observed by letting them impact on a scintillating screen (KODAK LANEX REGULAR), imaged onto a 16-bit CCD-camera (PRINCETON PHOTONMAX 1024). The amount of charge impacting on the scintillating screen is determined using published calibration factors for the screen [21] and by calibration of the response of the CCD-camera through the imaging optics. Furthermore, a 10 cm long dipole magnet with a peak field strength of 0.7 T can be inserted in the electron beam to disperse the electrons according to energy before impacting on the scintillating screen. This allows for the energy spectrum, above a cutoff energy of 40 MeV, of the electron beams to be determined. The electron energy dispersion on the scintillating screen was calibrated by numerically tracing electrons of different energies through the dipole magnetic field, according to the experimental geometry.

Electrons were first injected and accelerated in a target where gas was supplied only from the 2 mm gas nozzle. The threshold in electron number density in the plateau for required self-injection was found to be approximately 11×10^{18} cm^{-3}. The observed beams of electrons had the typical characteristics of self-injection in gas jets [22,23], with limited reproducibility and a bunch charge of the order of 30 pC with a standard deviation higher than 50%.

The electron number density provided from the 2 mm nozzle was lowered well below threshold for injection (to 3×10^{18} cm^{-3}). When adding gas also from the narrow tube, beams of accelerated electrons were observed [see Fig. 2(a)] for *every* laser pulse sent onto the target. The bunches of accelerated electrons injected using this composite gas target contain only of the order of 1 pC and their spectra typically contain a broad peak [see Fig. 2(b)]. Furthermore, the shot-to-shot stability in charge and energy of the electron beams, with standard deviations 13% and 5%, respectively, is far better than the stability of the beams injected through the self-injection mechanism in a single gas jet. This indicates that the local increase of gas in the interaction region facilitates the injection of electrons into the accelerating wakefield, and the reproducibility suggests that the mechanism is different from the self-injection observed when only supplying gas from one nozzle.

The kinetic energy of the accelerated electrons could be controlled by varying the remaining plasma length after the density down-ramp. This was done by moving the 2 mm gas nozzle, while keeping the position of the down-ramp

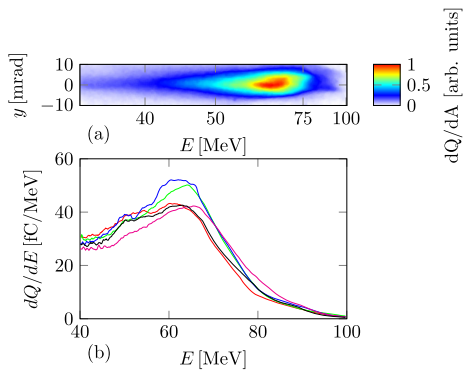

FIG. 2. Typical image of the dispersed electrons impacting on the scintillating screen (a) in a color map representing amount of charge per area. The total amount of charge is approximately 1.5 pC and the beams have a divergence of 10 mrad. Calculated energy spectra of electrons accelerated in five consecutive shots (b). The energy spectra of the electrons accelerated using this target typically contains a broad peak at an energy that is tunable from 50 to 80 MeV. The shot-to-shot fluctuations in charge and average energy achieved using this setup are significantly better compared to self-injection.

fixed with respect to the laser focus in vacuum. The resulting dependence of the peak electron energy on the length of the remaining plasma is shown in Fig. 3 for two different densities in the plateau. The result shows that a longer plasma, after the density down-ramp, provides higher energy of the electrons. This corresponds well with the estimated dephasing length [24] $L_d \approx 3$ mm, i.e., the maximum length an injected electron can stay in the accelerating phase of the wakefield, which is much longer than the plateau.

Assuming that the movement of the 2 mm gas nozzle has minor effects on the position of injection, the average accelerating electric field is estimated by fitting a line to each series of data. This gives a value of 37 MV/mm at a density of 2.6×10^{18} cm^{-3} in the plateau and 50 MV/mm at a density of 3.25×10^{18} cm^{-3}.

These accelerating electric fields are quite low compared to most other studies of laser wakefield acceleration using similar laser parameters [15]. This can be explained by two parts; first, the electron number density in the plateau is relatively low compared to studies in which the accelerator is operated close to the threshold for self-injection. This leads to a lower peak electric field in the accelerating region in our experiments. Second, as the electrons are injected when the plasma wake is growing longitudinally behind the laser pulse, in a long gradient, the electrons will be distributed longitudinally over a length approximately equal to $\Delta\lambda_p$, where $\Delta\lambda_p$ is the difference in plasma

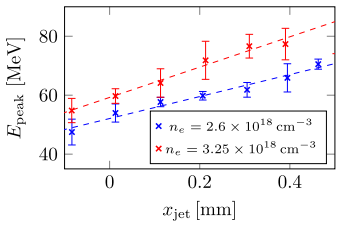

FIG. 3. Peak energy against relative jet position along the optical axis for two different plateau densities. The acceleration length in the plateau after the density down-ramp is controlled by the position of the gas jet. Zero on the x-axis corresponds to the position where the density down-ramp is approximately centered in the density distribution from the jet. Each data point corresponds to 10 consecutive shots and the error bars indicate one standard deviation in each direction. While the electron number density in the peak is kept constant at 11×10^{18} cm^{-3}, the peak energy increases linearly (dashed blue line) with the relative jet position.

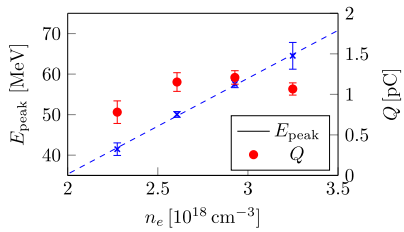

FIG. 4. Peak energy (blue) and total charge (red) against electron number density in the plateau. Each data point corresponds to 10 consecutive shots and the error bars indicate one standard deviation in each direction. The peak energy increases linearly (dashed blue line) with the electron number density, whereas the total charge shows no such trend. The electron number density in the peak is kept constant at 11×10^{18} cm^{-3}.

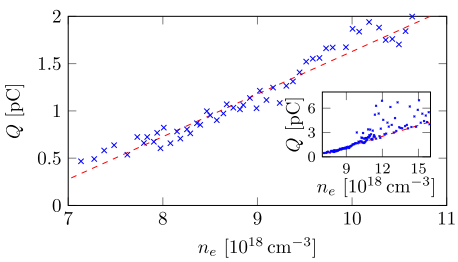

FIG. 5. Charge, above 40 MeV, as a function of electron number density in the peak. The positions of the two nozzles are kept fixed and the electron number density in the plateau is kept constant at 3.25×10^{18} cm^{-3}. At low peak densities, the amount of injected charge increases linearly with only small shot-to-shot fluctuations (standard deviation of 0.09 pC) around the fitted line (red dashed). At densities above 10×10^{18} cm^{-3} (shown in the inset), large fluctuations occur. However, the fluctuations only contribute to an increase in the total charge and indicate two different mechanisms of injection. The onset of the large fluctuations coincides with the electron number density threshold for self-injection.

wavelength in the peak and the plateau regions. As the plasma wavelength increases from 11 μm in the peak where the electron number density is 11×10^{18} cm^{-3} to 19 μm for the electron number density in the plateau of 3.25×10^{18} cm^{-3}, the injected electrons will be distributed along 8 μm in the first plasma period. Thus, the injected electrons are distributed over approximately 40% of the first plasma wave period, and the average electric field experienced by the injected electrons is lower than if they were all placed in the back of the first plasma wave period, which is the case for self-injection.

The influence of the electron number density in the plateau after the density down-ramp was studied while keeping the electron number density in the peak constant at 11×10^{18} cm^{-3}. The resulting kinetic energy of the accelerated electrons showed a strong dependence on this electron number density (see Fig. 4).

While varying the energy of the electrons, using either of the methods described above, the charge did not show significant variations compared to the standard deviation. We conclude that the energy of the electrons could be controlled independently of the amount of injected charge, by changing either the electron number density in the plateau or the length of the plateau. The amount of charge in the electron beams could be separately controlled, within a certain range, by varying the peak density while keeping the plateau density constant. No trend is observed in the electron energy spectra while varying the peak density, whereas the beam charge shows a clear dependence on the electron number density in the peak as shown in Fig. 5. Up to an electron number density of 10×10^{18} cm^{-3}, the charge increases linearly with electron number density in the peak. By increasing this density by only 40% (from 7.1×10^{18} cm^{-3} to 10×10^{18} cm^{-3}), the observed charge was increased by more than a factor of 3. Furthermore, the standard deviation of the shot-to-shot fluctuations in charge around the fitted linear dependence on peak electron number density is smaller than 0.1 pC (standard deviation). Thus, the relative charge fluctuations are significantly smaller using this setup than in our experiments for self-injection using a single gas jet.

An interesting feature is observed in the charge dependence as the electron number density in the peak is increased beyond 10×10^{18} cm^{-3}, shown in the inset in Fig. 5. At these densities the shot-to-shot fluctuations in charge are much larger than for lower densities. Remarkably, there

is not a single data point below the line that follows the charge dependence for densities below 10×10^{18} cm^{-3}. The images of the dispersed electrons on the scintillating screen show that the electron beams, for peak densities above 10×10^{18} cm^{-3} typically contain two components. One component with spectral shape and total charge similar to the ones observed at lower peak density is present on every shot. In addition, some beams contain a second component with higher charge and different spectral shape. The shot-to-shot fluctuations in this component is significantly larger than the fluctuations in the first component. We interpret this feature as injection of electrons through two different mechanisms; the stable, low charge component which is present on every shot is injected as the laser pulse propagate through the density down-ramp. The second component, which is only present above a certain threshold value for the electron number density in the peak, could be due to self-injection in the peak. This interpretation is supported by the observation that the value of the electron number density above which the second component starts to appear is the same as the electron number density threshold for self-injection observed in our experiments using a single gas jet.

To further support our interpretations of the experimental results, particle-in-cell simulations are performed using the code CALDER-CIRC [19]. In the simulations, the electron number density profile is approximated by a piecewise linear function, including two regions of constant density joined together by a linear gradient as shown in Fig. 6(a). The laser pulse parameters are chosen to correspond to those used in the experiments.

From the simulations, it is observed that the laser pulse undergoes self-focusing and self-compression in the increasing density and excite a highly nonlinear wakefield as the laser pulse reaches the density peak. However, no electrons are injected into the accelerating structure in this region [see Fig. 6(b)], as the wakefield is not yet strong enough for self-injection. As the laser pulse propagates through the linear density down-ramp, the wakefield structure increases in size and a certain portion of the background electrons become located within the electron void behind the laser pulse [see Fig. 6(c)]. The injection of electrons into the wakefield stops when the rear end of the first plasma period reaches the end of the density down-ramp, whereas the already injected electrons become further accelerated in the remaining plasma.

The observations from the simulations of injection in the density down-ramp and consecutive acceleration in the following plateau agree perfectly with the experimental observations presented above. For example, from Fig. 6(a) it is clear that the final energy of the electrons can be controlled by varying the length of the plasma after the density down-ramp.

It is further evident from the solid curves in Fig. 6(b–c) that the maximum accelerating field is much lower in the

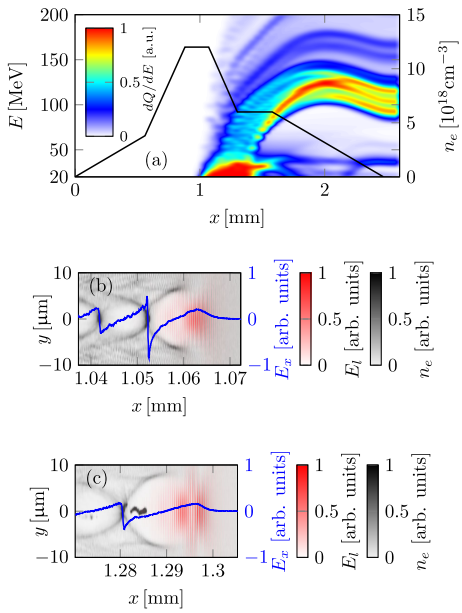

FIG. 6. Simulated evolution of the electron spectrum as the laser pulse propagates through the plasma (a) and local electron number density distribution before (b) and after (c) the density down-ramp along with the laser field (red) and accelerating electric field (blue). Injection of electrons into the wakefield structure occurs in the density down-ramp, located between ≈1.1 mm and ≈1.35 mm. The injected electrons are accelerated in the density plateau and the final electron energy spectrum contains a peak centered around 105 MeV and a FWHM of 20 MeV. In (c) electrons have been trapped after being injected as the plasma wavelength gradually increased in the density down-ramp. Thus, the electrons are distributed longitudinally over a distance approximately equal to $\Delta\lambda_p \approx 5$ μm.

low electron number density of the plateau than in the peak. Also, since the electrons are distributed longitudinally the average electric field experienced by the injected electrons is lower than if all electrons would be located at the back of the first plasma wave period.

Furthermore, it is observed in the simulations that the wakefield structure is close to breaking already before the density down-ramp and only minor changes in the parameters for the simulation result in self-injection there. This agrees well with the experimental findings, in which two populations of accelerated electrons are identified at high densities (see Fig. 5).

The results from the simulations can also be used to understand the shape of electron energy spectra of the beams of accelerated electrons. In Fig. 7, the longitudinal

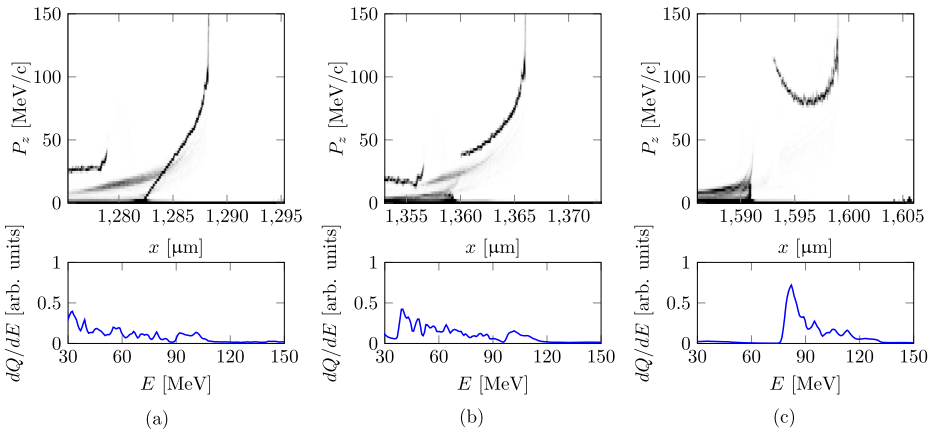

FIG. 7. Simulated compression of longitudinal phase-space distribution of injected electrons in the density plateau. In the first step (a) the laser pulse has just propagated through the density down-ramp, and the injected electrons are distributed along a line with a slope approximately equal to 12 MeV/c/μm, corresponding to a large energy spread in the total energy spectrum. After acceleration over 75 μm (b), the average energy of the injected electrons has increased, and the phase-space distribution starts to diverge from a line. After further acceleration over 240 μm (c), the phase-space distribution has deformed into a U-shape, corresponding to a peaked energy spectrum. The compression of the phase-space distribution to yield a peaked energy spectrum occurs because the injected electrons are distributed longitudinally, and thus experience different accelerating field. The slope of the front part of the injected electrons is too large, and this part of the electron distribution is not compressed.

phase-space distribution of the electrons is shown at three different locations along the optical axis following the laser pulse. Immediately after the density down-ramp [Fig. 7(a)], the injected electrons are distributed along a line in phase-space, corresponding to a spread both in energy and longitudinal position. After propagating a short distance, the average energy of the injected electrons is increased [Fig. 7(b)]. Furthermore, since the electrons have a longitudinal spread, they experience different electric field strength. Locally, this results in a rotation of the phase-space distribution of electrons, and globally the phase-space distribution appears to be bending. In the final step [Fig. 7(c)], the distribution of electrons has been deformed into a U-shape, corresponding to an increased distribution of electrons at an energy corresponding to the bottom of the U-shape. Thus, the rotation and bending of the original phase-space distribution of electrons thus acts to compress the energy spectrum.

In conclusion, we have demonstrated independent control of the number of injected electrons and their final energy distribution in a laser wakefield accelerator using a simple setup to tailor the density distribution. It has been shown that electrons are injected in the density down-ramp between two regions of different electron number density. The shot-to-shot fluctuations in both charge and energy are greatly improved in comparison to electron beams generated by self-injection. The same setup will be used in future experiments to study acceleration over longer distances and also to study localized ionization-induced injection.

ACKNOWLEDGMENTS

We acknowledge the support of the Swedish Research Council, the Knut and Alice Wallenberg Foundation, the Swedish Foundation for Strategic Research, Laserlab-Europe/CHARPAC (Grant Agreement No. 284464, EC's 7th Framework Programme) and EuCARD2/ANAC2 (Grant Agreement No. 312453, EC's 7th Framework Programme).

[1] T. Tajima and J. M. Dawson, Phys. Rev. Lett. **43**, 267 (1979).

[2] C. G. R. Geddes, C. Toth, J. van Tilborg, E. Esarey, C. B. Schroeder, D. Bruhwiler, C. Nieter, J. Cary, and W. P. Leemans, Nature (London) **431**, 538 (2004).

[3] J. Faure, Y. Glinec, A. Pukhov, S. Kiselev, S. Gordienko, E. Lefebvre, J.-P. Rousseau, F. Burgy, and V. Malka, Nature (London) **431**, 541 (2004).

[4] S. P. D. Mangles, C. D. Murphy, Z. Najmudin, A. G. R. Thomas, J. L. Collier, A. E. Dangor, E. J. Divall, P. S. Foster, J. G. Gallacher, C. J. Hooker, D. A. Jaroszynski, A. J. Langley, W. B. Mori, P. A. Norreys, F. S. Tsung,

R. Viskup, B. R. Walton, and K. Krushelnick, Nature (London) **431**, 535 (2004).

[5] D. Umstadter, J. K. Kim, and E. Dodd, Phys. Rev. Lett. **76**, 2073 (1996).

[6] E. Esarey, R. F. Hubbard, W. P. Leemans, A. Ting, and P. Sprangle, Phys. Rev. Lett. **79**, 2682 (1997).

[7] J. Faure, C. Rechatin, A. Norlin, A. Lifschitz, Y. Glinec, and V. Malka, Nature (London) **444**, 737 (2006).

[8] A. Pak, K. A. Marsh, S. F. Martins, W. Lu, W. B. Mori, and C. Joshi, Phys. Rev. Lett. **104**, 025003 (2010).

[9] C. McGuffey, A. G. R. Thomas, W. Schumaker, T. Matsuoka, V. Chvykov, F. J. Dollar, G. Kalintchenko, V. Yanovsky, A. Maksimchuk, K. Krushelnick, V. Y. Bychenkov, I. V. Glazyrin, and A. V. Karpeev, Phys. Rev. Lett. **104**, 025004 (2010).

[10] M. Chen, E. Esarey, C. B. Schroeder, C. G. R. Geddes, and W. P. Leemans, Phys. Plasmas **19**, 033101 (2012).

[11] F. G. Desforges, B. S. Paradkar, M. Hansson, J. Ju, L. Senje, T. L. Audet, A. Persson, S. Dobosz-Dufrénoy, O. Lundh, G. Maynard, P. Monot, J.-L. Vay, C.-G. Wahlström, and B. Cros, Phys. Plasmas **21**, 120703 (2014).

[12] S. Bulanov, N. Naumova, F. Pegoraro, and J. Sakai, Phys. Rev. E **58**, R5257 (1998).

[13] H. Suk, N. Barov, J. B. Rosenzweig, and E. Esarey, Phys. Rev. Lett. **86**, 1011 (2001).

[14] A. J. Gonsalves, K. Nakamura, C. Lin, D. Panasenko, S. Shiraishi, T. Sokollik, C. Benedetti, C. B. Schroeder, C. G. R. Geddes, J. van Tilborg, J. Osterhoff, E. Esarey, C. Toth, and W. P. Leemans, Nat. Phys. **7**, 862 (2011).

[15] M. Burza, A. Gonoskov, K. Svensson, F. Wojda, A. Persson, M. Hansson, G. Genoud, M. Marklund, C.-G. Wahlström, and O. Lundh, Phys. Rev. ST Accel. Beams **16**, 011301 (2013).

[16] G. Golovin, S. Chen, N. Powers, C. Liu, S. Banerjee, J. Zhang, M. Zeng, Z. Sheng, and D. Umstadter, Phys. Rev. ST Accel. Beams **18**, 011301 (2015).

[17] J. Faure, C. Rechatin, O. Lundh, L. Ammoura, and V. Malka, Phys. Plasmas **17**, 083107 (2010).

[18] K. Schmid, A. Buck, C. M. S. Sears, J. M. Mikhailova, R. Tautz, D. Herrmann, M. Geissler, F. Krausz, and L. Veisz, Phys. Rev. ST Accel. Beams **13**, 091301 (2010).

[19] A. Lifschitz, X. Davoine, E. Lefebvre, J. Faure, C. Rechatin, and V. Malka, J. Comput. Phys. **228**, 1803 (2009).

[20] G. R. Plateau, N. H. Matlis, C. G. R. Geddes, A. J. Gonsalves, S. Shiraishi, C. Lin, R. A. van Mourik, and W. P. Leemans, Rev. Sci. Instrum. **81**, 033108 (2010).

[21] A. Buck, K. Zeil, A. Popp, K. Schmid, A. Jochmann, S. D. Kraft, B. Hidding, T. Kudyakov, C. M. S. Sears, L. Veisz, S. Karsch, J. Pawelke, R. Sauerbrey, T. Cowan, F. Krausz, and U. Schramm, Rev. Sci. Instrum. **81**, 033301 (2010).

[22] S. P. D. Mangles, A. G. R. Thomas, O. Lundh, F. Lindau, M. C. Kaluza, A. Persson, C.-G. Wahlström, K. Krushelnick, and Z. Najmudin, Phys. Plasmas **14**, 056702 (2007).

[23] M. Hansson, L. Senje, A. Persson, O. Lundh, C.-G. Wahlström, F. G. Desforges, J. Ju, T. L. Audet, B. Cros, S. D. Dufrénoy, and P. Monot, Phys. Rev. ST Accel. Beams **17**, 031303 (2014).

[24] E. Esarey, C. B. Schroeder, and W. P. Leemans, Rev. Mod. Phys. **81**, 1229 (2009).

Paper VI

Dynamics of ionization-induced electron injection in the high density regime of laser wakefield acceleration

F. G. Desforges, B. S. Paradkar, M. Hansson, J. Ju, L. Senje, T. L. Audet, A. Persson, S. Dobosz Dufrénoy, O. Lundh, G. Maynard, P. Monot, J.-L. Vay, C.-G. Wahlström, and B. Cros.

Physics of Plasmas **21**, 120703 (2014).

PHYSICS OF PLASMAS 21, 120703 (2014)

Dynamics of ionization-induced electron injection in the high density regime of laser wakefield acceleration

F. G. Desforges,[1] B. S. Paradkar,[1,a)] M. Hansson,[2] J. Ju,[1] L. Senje,[2] T. L. Audet,[1] A. Persson,[2] S. Dobosz-Dufrénoy,[3] O. Lundh,[2] G. Maynard,[1] P. Monot,[3] J.-L. Vay,[4] C.-G. Wahlström,[2] and B. Cros[1,b)]
[1]*Laboratoire de Physique des Gaz et des Plasmas, CNRS-Université Paris-Sud, 91405 Orsay, France*
[2]*Department of Physics, Lund University, P. O. Box 118, S-22100 Lund, Sweden*
[3]*Laboratoire Interactions, Dynamique et Lasers, CEA Saclay, 91191 Gif-sur-Yvette, France*
[4]*Lawrence Berkeley National Laboratory, Berkeley, California 94720, USA*

(Received 23 September 2014; accepted 23 November 2014; published online 8 December 2014)

The dynamics of ionization-induced electron injection in high density ($\sim 1.2 \times 10^{19}$ cm^{-3}) regime of laser wakefield acceleration is investigated by analyzing the betatron X-ray emission. In such high density operation, the laser normalized vector potential exceeds the injection-thresholds of both ionization-injection and self-injection due to self-focusing. In this regime, direct experimental evidence of early on-set of ionization-induced injection into the plasma wave is given by mapping the X-ray emission zone inside the plasma. Particle-In-Cell simulations show that this early on-set of ionization-induced injection, due to its lower trapping threshold, suppresses the trapping of self-injected electrons. A comparative study of the electron and X-ray properties is performed for both self-injection and ionization-induced injection. An increase of X-ray fluence by at least a factor of two is observed in the case of ionization-induced injection due to increased trapped charge compared to self-injection mechanism. © *2014 AIP Publishing LLC*.
[http://dx.doi.org/10.1063/1.4903845]

One of the exciting applications of Laser Wakefield Acceleration (LWFA)[1] is the development of next generation compact X-ray sources with femtosecond pulse duration and source size of the order of few microns. For this application, LWFA is operated in the extremely non-linear regime, typically known as the bubble regime,[2] where electrons from the background plasma are injected and accelerated in the ion cavity formed by the near-total expulsion of electrons initially located in the path of the laser. Accelerated electrons emit X-rays while performing transverse oscillatory betatron motion due to the radial focusing force exerted by the ions.[3]

For the successful realization of a practical LWFA based X-ray source, it is crucial to improve the efficiency of X-ray generation (from laser to X-ray). Typically, current experiments,[4–8] relying on self-injection mechanism, have been able to produce a maximum of $\sim 10^9$ photons with peak spectral brightness in the range of $10^{20} - 10^{22}$ photons/(s mm^{2}mrad^{2}0.1%BW) using 50–100 TW laser systems. For given laser parameters, wavelength (λ_L), and power (P_L), the self-injection mechanism is controlled by varying the parameter $P_{eff} = \alpha P_L / P_c$, where α is the fraction of laser energy within full-width-at-half-maximum (FWHM) intensity of focal spot and P_c is the critical power for self-focusing. Therefore, in order to achieve a specific P_{eff} for a given laser power αP_L, the required plasma density (n_0) can be calculated as $n_0(\text{cm}^{-3}) \simeq 1.94 P_{eff} \times 10^{19} / [\alpha P_L(\text{TW}) \lambda_L^2(\mu\text{m}^2)]$. Recent experiments[9] have shown that self-injection mechanism starts at $P_{eff} \simeq 2$ whereas the injected charge saturates at $P_{eff} \geq 4$ due to the beam-loading effect. For example, for a 20 TW Gaussian laser pulse ($\alpha = 0.5$) operating at 0.8 μm wavelength, self-injection is expected to start at $n_0 \simeq 6 \times 10^{18}$cm^{-3} whereas beam-loading should occur for $n_0 \gtrsim 1.2 \times 10^{19}$cm^{-3}. Since X-ray production is directly proportional to trapped charge, high density operation near beam loading limit is essential to maximize the trapped charge and X-ray fluence.

In addition to high-density operation near beam loading limit, the ionization-induced injection mechanism[11–15] offers an attractive alternative to the self-injection mechanism for the optimization of X-ray generation. In this mechanism, inner shell electrons of high atomic number gas are preferentially trapped into the plasma wave. Although these electrons are ionized near the laser axis, they have a non-zero transverse momentum which is necessary for betatron oscillations. In addition, the number of trapped electrons can be controlled by adjusting the length of the plasma column. On this background, we examined the use of this injection mechanism for the optimization of X-ray beam properties. This offers a new perspective as previous experimental studies of the ionization-induced injection mechanism[12–14] were so far focused on electron acceleration to produce low emittance, quasi-monoenergetic GeV energy electron bunches.

In this letter, we present a comparative study of electron and X-ray properties for both self-injection and ionization-induced injection mechanisms in the high density regime near beam-loading threshold. In this regime, for moderate laser intensity, self-focusing plays an important role to control ionization-induced injection.[16,17] Here, self-focusing is used to initiate both ionization-induced injection and self-injection with a laser initially having an intensity below the

[a)]Electronic mail: bsparadkar@gmail.com
[b)]Electronic mail: brigitte.cros@u-psud.fr

injection thresholds. By analysing betatron radiation, we give the first experimental demonstration of an early onset of ionization-induced injection due its lower injection threshold compared to self-injection. This result is obtained by using a technique similar to pinhole imaging of the betatron radiation inside a long dielectric capillary tube.[8,18,19] Previous experiments[11–14] have demonstrated ionization-induced injection by operating below self-injection threshold. With the help of numerical simulations, we demonstrate that this early ionization-induced injection of electrons in the ion cavity suppresses self-injection. We also report a significant increase, by at least a factor of two, of X-ray fluence when ionization-induced injection is used compared to self-injection. The improvement of the X-ray yield is predominantly due to an increase of trapped charge.

Experiments were performed using the Lund Laser Centre (LLC) multi-terawatt titanium-doped sapphire (Ti:Sa) laser, delivering pulses with a duration of 40 fs FWHM at a wavelength of 800 nm. The laser beam was focused to a spot with radius (w_0) at e^{-2} of the maximum intensity of 17 μm. The energy in the focal plane was measured[20] to be $E_L = (830 \pm 30)$ mJ, 88% of which was contained within a circle of radius equal to the waist size (w_0). The corresponding peak intensity and normalized vector potential are estimated to be $I_L = (38 \pm 02) \times 10^{18}$ W/cm^2 and $a_0 \approx 1.3$–1.4, respectively. A glass capillary tube, with a length of 20 mm and an inner radius $r_{cap} = 73$ μm was used to confine and control the gas distribution.[21] The gas was let in through two slits located at 2.5 mm from the tube exits, providing a 15 mm long plateau with constant pressure between the two slits. The gas used for studying self-injection was pure hydrogen whereas it was a mixture composed of 99% hydrogen (H_2) and 1% nitrogen (N_2) for ionization-induced injection. The gas density was calibrated off-line;[21] the corresponding electron number density of the plateau, with and without nitrogen, is $n_0 = (12 \pm 2) \times 10^{18}$ cm^{-3}, assuming a complete ionization of the atoms. Note that this density is the same as the estimated density for near beam-loading limit operation for 20 TW laser system. The electron bunch energy characterization was performed by combining a deflecting dipole magnet with a scintillating screen imaged by a 16-bit CCD camera. The lowest energy that could be measured was about 40 MeV. The charge was calculated from the image of the scintillating screen using published calibration factors.[22] The X-ray emission was recorded with a 16-bit X-ray CCD camera located 1.20 meter away from the emission source. An array of thin metallic filters[23] was inserted between the source and the camera in order to allow estimation of the critical energy, assuming a synchrotron-like spectrum.[6]

The energy spectra of electron bunches accelerated in pure H_2 (blue curves) and mixture (red curves) media are given in Fig. 1(a). The mean spectra obtained from a sequence of 30 shots for the same parameters are represented by solid and dashed lines. The shaded areas illustrate the standard deviation of electron spectra from the mean curves. For these experimental parameters, electron bunches with broad energy spectra were measured, indicating a continuous injection. The resulting detected charge was estimated to be

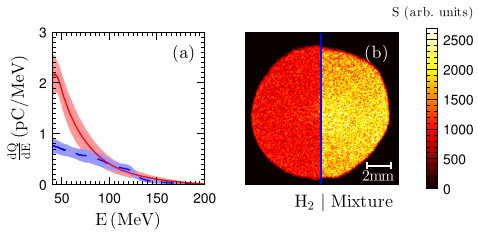

FIG. 1. (a) Mean energy spectra of electron bunches for a sequence of 30 shots performed at $n_0 = (12 \pm 2) \times 10^{18}$ cm^{-3} with pure H_2 (blue dashed line) and gas mixture (red solid line). The colored areas indicate the standard deviation from the mean spectra. (b) Typical X-ray half-beam images for H_2 (left part) and gas mixture (right part).

55 pC for pure H_2 and 100 pC for mixture whereas the average energy was found to be approximately 70 MeV for both gases. The X-ray beams generated during the acceleration process are illustrated by two typical X-ray half-beam images in Fig. 1(b) for pure H_2 (left part) and mixture (right part). It shows that the amplitude of the X-ray signal (S) is at least twice higher when the gas mixture is used, leading to a maximum peak fluence of $\sim 10^5$ ph/mrad^2. The fluence of betatron radiation emitted by an electron bunch oscillating within an ion plasma channel scales as[3] $\Gamma_X \propto N_\beta \gamma_e^2 Q$ where Q and γ_e are the bunch charge and energy, respectively. The number of oscillations can be estimated as $N_\beta = L_\varphi / \lambda_\beta \propto n_0^{-1} \gamma_e^{-1/2}$, where L_φ is the dephasing length of electrons and λ_β is the betatron oscillation wavelength. As γ_e and n_0 are similar for both gases, the higher fluence observed in the presence of the mixture is pre-dominantly due to an increase of the electron bunch charge.

The characterization of the X-ray beam provides a valuable insight on the electron injection and dynamics during acceleration. The critical energy is defined[25] as $E_c = 3\gamma_e^2 r_\beta \hbar \omega_p^2 / 2$, where r_β and ω_p are the source size and the plasma frequency, respectively. The critical energy was found to be independent of the type of gas. The average critical energy for all the shots shown in Fig. 1(a) was computed to be 5.2 ± 1.0 keV. Assuming a synchrotron-like spectrum, it was estimated from a least squares method[7] using the transmission data of the filters and the sensitivity of the imaging system. The corresponding X-ray source size is estimated to be $r_\beta \approx 2.6 \pm 0.5$ μm, using the critical energy definition given above.

By analyzing the spatial distribution of the X-ray signal as detailed in Refs. 18 and 19, we can determine the betatron X-ray radiating zone inside the plasma. As the capillary tube plays a role similar to a pinhole for X-rays, the radial variation of the X-ray signal in the detector plane is directly transformed into the longitudinal variation (dI/dz) of the X-ray emission intensity inside the plasma, assuming emission on the capillary axis.

The azimuthal average of the X-ray signal on the detector (Fig. 2(a)) shows that the peak value of the X-ray fluence for the mixture (red solid and dotted-dashed lines) is twice that of pure H_2 (blue dashed line), as it can be seen in Fig. 1(b). The corresponding emission lengths (Fig. 2(b)) for

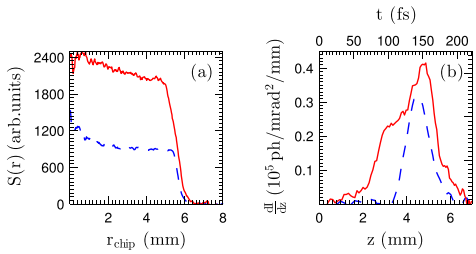

FIG. 2. Experimental profiles of X-ray beams for pure H_2 (blue dashed line) and gas mixture (red solid line) at $(11\pm1)\times10^{18}$ cm^{-3}: (a) Azimuthal average of the X-ray signal on the detector, and (b) corresponding calculated longitudinal profile of emission.

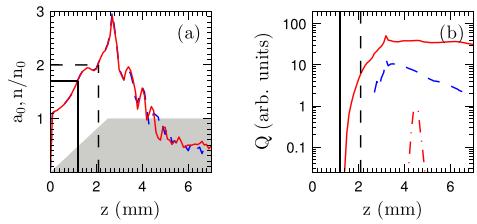

FIG. 3. Simulated normalized vector potential of the laser beam and gas profile (grey area) (a), bunch charge (b) as functions of plasma length for a pure H_2 (blue dashed line) and a $99\%H_2+1\%N_2$ gas (red solid and dotted-dashed lines for inner and outer shell electrons, respectively). The black dashed and solid lines indicate the theoretical thresholds of self-injection and ionization-induced injection, respectively.

mixture and pure H_2 are about 5 mm and 3 mm, respectively. Typically, a single electron injected at a position "z" inside the plasma will radiate over a distance of the order of the dephasing length. Beyond dephasing length, the radiated power by the electron should reduce considerably due to the reduction in energy.[10] Therefore, an X-ray emission length significantly larger than the dephasing length[24] ($L_\varphi \simeq 400\,\mu$m), is indicative of multiple electron injections as the laser pulse propagates through the plasma. In addition, Fig. 2(b) shows that the typical variation of the measured emission occurs on a scale length much longer than the longitudinal bunch size of electrons, which is of the order of the plasma wavelength. Therefore, the X-ray source can be assumed to be a point source moving inside the plasma with the group velocity of the laser pulse (v_{gr}). Consequently, photons emitted at longitudinal locations separated by distance a dz will reach the detector with a time difference of $dt = dz(v_{gr}^{-1} - c^{-1})$. In other words, we can compute the temporal profile of the X-ray pulse from the longitudinal spatial profile using the transformation $t = z(v_{gr}^{-1} - c^{-1})$. The corresponding time scale is shown on the top horizontal axis of Fig. 2(b). The analysis of 10 shots for each gas type shows that, on average, ionization-induced injection is triggered earlier than self-injection by around 1 mm. The FWHM of X-ray emission duration is found to be on average 47 fs for pure H_2 and 53 fs for the mixture. The corresponding peak brightness for gas mixture case is estimated to be $\sim5\times10^{20}$ photons/(s mm^{2}mrad^{2}0.1%BW) and the number of photons $\sim10^9$.

These experimental results are qualitatively analyzed using Particle-In-Cell (PIC) simulations in two dimensional Cartesian geometry (2DXZ) with the code WARP.[26] Ionization dynamics is described by a field ionization model[27] implemented in WARP. Different electron species for each possible ionization state are created in order to identify the electrons coming from inner shell ionization. For example, for the simulation of H_2 and N_2 gas mixture, we have a total of 8 electron species, 1 for H_2 and 7 for N_2. The glass capillary tube (dielectric constant = 2.25) is modelled by two dielectric slabs separated by a distance equal to the inner diameter of the capillary tube. The longitudinal profile of plasma density, shown by the grey area in Fig. 3, is modelled as a linear density ramp near the capillary entrance followed by a plateau of density $n_0 = 11\times10^{18}$ cm^{-3}. Here, the density at the entrance rises from zero to n_0 in 2.5 mm. The laser pulse with $a_0 = 1.3$, waist size $w_0 = 17\,\mu$m and duration (FWHM) $\tau = 40$ fs is focused at $z = 1$ mm. The grid resolution in Z and X directions is 0.04 μm and 0.33 μm, respectively, with 4 macro-particles per cell.

The simulated evolution of the laser a_0 and accelerated charge (with energy above 40 MeV) along the longitudinal direction are plotted in Fig. 3 for pure H_2 (blue dashed line) and gas mixture (red solid line). In both cases, self-focusing of the laser causes a_0 to increase above the thresholds of self-injection and ionization-induced injection (see Fig. 3(a)). Typically, for our operating conditions, the ionization-induced injection is expected[15] at $a_0 \approx 1.7$ whereas the self-injection will occur for[24] $a_0 \gtrsim 2$. In the case of gas mixture, all the electrons above 40 MeV energy are found to come from N_2 inner shell (N^{5+}, N^{6+}) ionization. Indeed, the amount of these electrons is two orders of magnitude higher than the quantity of accelerated electrons coming from outer shell ionization (H and N to N^{4+}), as illustrated by the comparison of the red dotted-dashed and solid lines in Fig. 3(b). These negligibly small number of outer shell electrons (shown by red dotted-dashed line) are trapped in a wakefield produced by a beam of trapped inner shell electrons. This result indicates that ionization-induced injection of N_2 inner shell electrons suppresses the self-injection of H_2 electrons. We observe that the ionization-induced injection starts $\sim$1 mm before self-injection (see Fig. 3(b)) which is consistent with the experimental results. In both cases, the process of injection stops with the decrease of a_0 after 3 mm. The continuous injection of inner shell electrons over a longer distance results in the observed increase of trapped charge in ionization-induced injection compared to the self-injection process.

One important consequence of early injection due to ionization-induced injection is the suppression of self-injection of electrons coming from outer shell ionization (H and N to N^{4+}). The mechanism of such suppression is shown in Fig. 4. PIC simulations studies[24] have demonstrated that in the case of self-injection, trapped electrons typically enter the bubble transversely to the laser pulse propagation. This is referred as transverse injection whereas the injection of

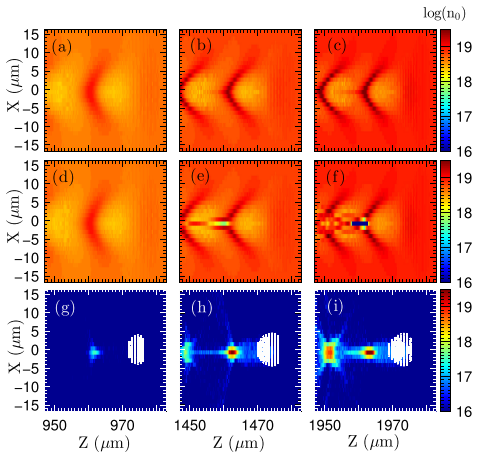

FIG. 4. Modification of wakefield structure leading to suppression of transverse injection by ionization-induced injection. For different longitudinal locations, the densities of electrons in pure Hydrogen case are plotted in (a), (b), and (c). Corresponding densities of electrons coming from outer shell ionization (H^+ and N^+ to N^{4+}) are plotted in (d), (e), and (f) while the electron densities from inner shell ionization (N^{5+} and N^{6+}) are shown in (g), (h), and (i). The laser pulse is shown by white contour lines in the bottom plots.

electrons along the axis of the laser propagation is called longitudinal injection.[4] In Figs. 4(a)–4(c), the electron densities for the pure Hydrogen case are plotted at three different longitudinal locations whereas outer shell electron densities in the gas mixture case are shown in Figs. 4(d)–4(f). The corresponding inner shell electron densities in the gas mixture case can be seen in Figs. 4(g)–4(i). The laser pulse is shown by white contour lines in the bottom graphs. During the onset of ionization-induced injection at $Z \sim 950\,\mu$m, the outer shell electron density is identical to the pure hydrogen case as can be seen from Figs. 4(a) and 4(d). The inner shell electrons (Fig. 4(g)) are injected longitudinally as they are ionized inside the bubble near $X = 0$ at the peak intensity of the laser pulse. During the laser pulse propagation, the laser self-focusing (see Fig. 3(a)) makes the plasma wave increasingly non-linear as can be seen from Figs. 4(a)–4(c). However, in the case of gas mixture, due to the presence of longitudinally injected inner shell trapped electrons near the axis (Figs. 4(h) and 4(i)), the outer shell electrons coming transversely to the axis are repelled. This can be seen by comparing Figs. 4(b) and 4(c) with Figs. 4(e) and 4(f). The reduction in electron density near the axis seen in Figs. 4(e) and 4(f) is due to the expulsion of outer-shell electrons by the already injected inner-shell electrons. This modification of transverse wakefield structure eventually results in the suppression of transverse injection due to longitudinal ionization-induced injection.

In conclusion, by observing betatron X-ray radiation we have experimentally demonstrated early onset of ionization-induced injection in a LWFA regime in which both ionization-induced injection and self-injection are possible. We found that a higher X-ray fluence ($\sim 10^5$ ph/mrad^2) is achieved in the case of ionization-induced injection compared to the case of self-injection. The FWHM X-ray pulse duration was estimated to be approximately 53 fs. The increase in X-ray fluence is primarily due to the increased amount of trapped charge in the case of ionization-induced injection, attributed to a longer injection length due to its lower injection threshold. Finally, we observe that in the regime where both self-injection and ionization-induced injection are possible, the early on-set of ionization-induced injection suppresses the transverse self-injection process thereby leading to pre-dominantly longitudinal injection. These are key results for understanding the dynamics of ionization-induced injection, and also for the development of future X-ray sources based on betatron radiation, as it demonstrates that the efficiency of X-ray generation can be significantly increased by using ionization-induced injection instead of self-injection.

This project has benefited from financial support from the Triangle de la Physique, the Labex PALM, ARC, the Swedish Research Council, the Knut and Alice Wallenberg Foundation, the Swedish Foundation for Strategic Research, the Lund University X-ray Centre (LUXC), Laserlab-Europe/CHARPAC (Grant Agreement No. 284464, EC's 7th Framework Programme), EuCARD2/ANAC2 (Grant Agreement No. 312453, ECs 7th Framework Programme), and US-DOE (Contract No. DE-AC02-05CH11231). J. Ju acknowledges financial support from the Chinese Scholarship Council (CSC).

[1]E. Esarey, C. B. Schroeder, and W. P. Leemans, Rev. Mod. Phys. **81**, 1229 (2009).
[2]A. Pukhov and J. Meyer-ter-Vehn, Appl. Phys. B **74**, 355 (2002).
[3]I. Kostyukov, S. Kiselev, and A. Pukhov, Phys. Plasma **10**, 4818 (2003).
[4]S. Corde, C. Thaury, A. Lifschitz, G. Lambert, K. Ta Phuoc, X. Davoine, R. Lehe, D. Douillet, A. Rousse, and V. Malka, Nat. Commun. **4**, 1501 (2013).
[5]A. Rousse, K. Ta Phuoc, R. Shah, A. Pukhov, E. Lefebvre, V. Malka, S. Kiselev, F. Burgy, J. Rousseau, D. Umstadter *et al.*, Phys. Rev. Lett. **93**, 135005 (2004).
[6]S. Fourmaux, S. Corde, K. Ta Phuoc, P. Leguay, S. Payeur, P. Lassonde, S. Gnedyuk, G. Lebrun, C. Fourment, V. Malka *et al.*, New. J. Phys. **13**, 033017 (2011).
[7]S. Kneip, S. R. Nagel, C. Bellei, N. Bourgeois, A. E. Dangor, A. Gopal, R. Heathcote, S. P. D. Mangles, J. R. Marques, A. Maksimchuk *et al.*, Phys. Rev. Lett. **100**, 105006 (2008).
[8]J. Ju, K. Svensson, H. Ferrari, A. Döpp, G. Genoud, F. Wojda, M. Burza, A. Persson, O. Lundh, C-G. Wahlström *et al.*, Phys. Plasmas **20**, 083106 (2013).
[9]S. P. D. Mangles, G. Genoud, M. S. Bloom, M. Burza, Z. Najmudin, A. Persson, K. Svensson, A. G. R. Thomas, and C.-G. Wahlström, Phys. Rev. ST Accel. Beams **15**, 011302 (2012).
[10]S. Corde, K. Ta Phuoc, G. Lambert, R. Fitour, V. Malka, A. Rousse, A. Beck, and E. Lefebvre, Rev. Mod. Phys. **85**, 1 (2013).
[11]M. Chen, Z.-M. Sheng, Y.-Y. Ma, and J. Zhang, J. Appl. Phys. **99**, 056109 (2006).
[12]C. McGuffey, A. G. R. Thomas, W. Schumaker, T. Matsuoka, V. Chvykov, F. J. Dollar, G. Kalintchenko, V. Yanovsky, A. Maksimchuk, K. Krushelnick *et al.*, Phys. Rev. Lett. **104**, 025004 (2010).
[13]C. E. Clayton, J. E. Ralph, F. Albert, R. A. Fonseca, S. H. Glenzer, C. Joshi, W. Lu, K. A. Marsh, S. F. Martins, W. B. Mori *et al.*, Phys. Rev. Lett. **105**, 105003 (2010).
[14]A. Pak, K. A. Marsh, S. F. Martins, W. Lu, W. B. Mori, and C. Joshi, Phys. Rev. Lett. **104**, 025003 (2010).
[15]M. Chen, E. Esarey, C. B. Schroeder, C. G. R. Geddes, and W. P. Leemans, Phys. Plasmas **19**, 033101 (2012).

[16]C. Xia, J. Liu, W. Wang, H. Lu, W. Cheng, A. Deng, W. Li, H. Zhang, X. Liang, Y. Leng *et al.*, Phys. Plasmas **18**, 113101 (2011).
[17]M. Zeng, M. Chen, Z-M. Sheng, W. B. Mori, and J. Zhang, Phys. Plasmas **21**, 030701 (2014).
[18]G. Genoud, K. Cassou, F. Wojda, H. E. Ferrari, C. Kamperidis, M. Burza, A. Persson, J. Uhlig, S. Kneip, S. P. D. Mangles *et al.*, Appl. Phys. B **105**, 309 (2011).
[19]S. Corde, C. Thaury, K. T. Phuoc, A. Lifschitz, G. Lambert, J. Faure, O. Lundh, E. Benveniste, A. Ben-Ismail, L. Arantchuk *et al.*, Phys. Rev. Lett. **107**, 215004 (2011).
[20]F. G. Desforges, M. Hansson, J. Ju, L. Senje, T. L. Audet, S. Dobosz-Dufrénoy, A. Persson, O. Lundh, C.-G. Wahlström, and B. Cros, Nucl. Instrum. Methods Phys. Res., Sect. A **740**, 54 (2013).
[21]J. Ju and B. Cros, J. Appl. Phys. **112**, 113102 (2012).
[22]A. Buck, K. Zeil, A. Popp, K. Schmid, A. Jochmann, S. D. Kraft, B. Hidding, T. Kudyakov, C. M. S. Sears, L. Veisz *et al.*, Rev. Sci. Instrum. **81**, 033301 (2010).
[23]P. Kirkpatrick, Rev. Sci. Instrum. **10**, 186 (1939).
[24]W. Lu, M. Tzoufras, C. Joshi, F. S. Tsung, W. B. Mori, J. Vieira, R. A. Fonseca, and L. O. Silva, Phys. Rev. ST Accel. Beams **10**, 061301 (2007).
[25]E. Esarey, B. A. Shadwick, P. Catravas, and W. P. Leemans, Phys. Rev. E **65**, 056505 (2002).
[26]J.-L. Vay, D. P. Grote, R. H. Cohen, and A. Friedman, Comput. Sci. Discovery **5**, 014019 (2012).
[27]G. L. Yudin and M. Y. Ivanov, Phys. Rev. A **64**, 013409 (2001).

Paper VII

Investigation of ionization-induced electron injection in a wakefield driven by laser inside a gas cell

T. L. Audet, M. Hansson, P. Lee, F. G. Desforges, G. Maynard, S. Dobosz Dufrénoy, R. Lehe, J.-L. Vay, B. Aurand, A. Persson, I. Gallardo González, A. Maitrallain, P. Monot, C.-G. Wahlström, O. Lundh, and B. Cros.

Physics of Plasmas **23**, 023110 (2016).

PHYSICS OF PLASMAS **23**, 023110 (2016)

Investigation of ionization-induced electron injection in a wakefield driven by laser inside a gas cell

T. L. Audet,[1,a)] M. Hansson,[2] P. Lee,[1] F. G. Desforges,[1] G. Maynard,[1] S. Dobosz Dufrénoy,[3] R. Lehe,[4] J.-L. Vay,[4] B. Aurand,[2] A. Persson,[2] I. Gallardo González,[2] A. Maitrallain,[3] P. Monot,[3] C.-G. Wahlström,[2] O. Lundh,[2] and B. Cros[1,b)]
[1]*Laboratoire de Physique des Gaz et des Plasmas, CNRS, Univ. Paris-Sud, Université Paris-Saclay, 91405 Orsay, France*
[2]*Department of Physics, Lund University, P.O. Box 118, S-22100 Lund, Sweden*
[3]*Laboratoire Interactions, Dynamique et Lasers, CEA, Université Paris-Saclay, 91191 Gif-sur-Yvette, France*
[4]*Lawrence Berkeley National Laboratory, Berkeley, California 94720, USA*

(Received 22 September 2015; accepted 3 February 2016; published online 16 February 2016)

Ionization-induced electron injection was investigated experimentally by focusing a driving laser pulse with a maximum normalized potential of 1.2 at different positions along the plasma density profile inside a gas cell, filled with a gas mixture composed of $99\%H_2 + 1\%N_2$. Changing the laser focus position relative to the gas cell entrance controls the accelerated electron bunch properties, such as the spectrum width, maximum energy, and accelerated charge. Simulations performed using the 3D particle-in-cell code WARP with a realistic density profile give results that are in good agreement with the experimental ones. The interest of this regime for optimizing the bunch charge in a selected energy window is discussed. © *2016 AIP Publishing LLC*.
[http://dx.doi.org/10.1063/1.4942033]

I. INTRODUCTION

The mechanism of laser wakefield acceleration (LWFA) in a plasma[1] can produce electric fields 3 orders of magnitude higher than in conventional RF accelerators. LWFA thus appears as a promising way to achieve compact relativistic electron sources. In this scheme, the plasma wave is excited by the ponderomotive force of a short intense laser pulse. At sufficiently high intensity gradient (typically achievable with an ultrashort laser pulse with intensity above $\sim 10^{19}$ W/cm^2), plasma electrons are blown out of the laser axis behind the laser pulse. A cavity or "bubble" where only ions remain is created behind the laser pulse leading to strong transverse and longitudinal electrostatic fields. Plasma electrons can be trapped in this field and accelerated to high energy. This mechanism can occur continuously or several times over the plasma length as long as the laser intensity is high enough, which leads to accelerated electron bunches with a wide energy spread.

Several methods to increase the number of electrons and reduce the electron bunch energy spread have been proposed and tested such as the use of colliding pulses,[2,3] density ramp injection,[4,5] density transition injection,[6,7] or ionization-induced injection.[8–10] The mechanism of ionization-induced injection can be implemented simply by adding a small proportion of high-Z gas to the low-Z gas constituting the target medium. During the interaction with the intense laser pulse, the outer shell electrons of the high-Z gas are ionized in the front of the laser pulse and mostly contribute to the plasma wave, without being trapped. Electrons from the inner-shell of the high-Z atoms, having a much higher ionization threshold, are ionized closer to the intensity peak in a region where they can be more easily trapped by the plasma wave. This mechanism has shown its ability to increase the trapped charge[11] and lower the transverse emittance of the electron bunches[12] and is thus a promising candidate as an injector for multi-stage laser plasma accelerators. Although previous studies have used it in injector-accelerator experiments,[13,14] a detailed specific study of the injection mechanism and the physics controlling the electron bunch properties in the experiments needed to be performed.

In this paper, the properties of electron bunches with energy in the range of 50–200 MeV, produced by ionization-induced injection using a single laser pulse focused in a gas cell target, are reported. The laser normalized vector potential and maximum plasma density are such that electron injection is dominated by ionization-induced injection, as shown in the previous work.[11] The focal spot position was varied along the propagation axis to explore different injection conditions along the plasma density profile.

The use of gas cells has been shown to contribute to the stability of electron production[15–18] as the gas confined in the cell is relatively homogeneous. Nevertheless, windows cannot be used to confine the gas on the intense short-pulse laser path, and density gradients are established due to gas leakage between the higher pressure volume of the gas cell and the low pressure chamber around it. Direct experimental measurement of these gradients is particularly difficult due to the small volume and large range of density to be probed. We have thus evaluated the gradients by their calculation through fluid simulations.

We performed experimental measurements of electron properties inside short gas cells, for which the focal plane position of the laser pulse was varied along the gradient. Experimental results were analyzed and compared with

[a)]Electronic mail: thomas.audet@u-psud.fr
[b)]Electronic mail: brigitte.cros@u-psud.fr

numerical modeling with the Particle-In-Cell (PIC) code WARP.[19] It shows that the density profile and the focus position play a major role in the regime of intensity studied. The remaining of the paper is organized as follows: in Section II, the experimental set-up and parameters are described; Section III presents experimental results of the cell position scan and their analysis with the help of simulations; the influence of other parameters such as the cell length and laser energy on the bunch properties is discussed in Section IV.

II. EXPERIMENTAL CONDITIONS

Experiments were performed at the Lund Laser Centre (LLC), using a Ti:sapphire multi-terawatt laser system. Linearly polarized laser pulses, with duration $\tau_L = (37 \pm 3)$ fs full-width-at-half-maximum (fwhm), were focused using a 78 cm focal length off-axis parabola to a fwhm spot size of 17 μm. The laser wavefront was corrected using a deformable mirror to achieve a symmetrical circular distribution of energy in the transverse focal plane in vacuum. The laser envelope was close to the envelope of a Gaussian pulse and the measured Rayleigh length was $z_R \simeq 1$ mm. The laser energy on target was $E_L = (585 \pm 65)$ mJ and the resulting peak intensity in the focal plane was $I_L = (3.1 \pm 0.5) \times 10^{18}$ W/cm^2, which corresponds to a normalized vector potential of $a_0 = (e/m_e c^2) \times (2I_L/\varepsilon_0 \omega_L)^{1/2} = 1.2 \pm 0.1$.

The target gas was contained in a variable length gas cell placed in the experimental vacuum chamber. The cell was made as a large diameter cylinder with replaceable entrance and exit faces, at the center of which 200 μm diameter holes were drilled to let the laser and electron bunches pass through. The thickness of the entrance and exit plates was 500 μm. A gas mixture composed of 99%H_2 + 1%N_2 was let in through an electrovalve opened 40 ms before the laser pulse. The stationary state plateau gas density in the cell was characterized prior to the experiment using interferometric measurements similar to the ones described in Ref. 20. Calculation of the profile with fluid simulations was performed using a transient turbulent sonic solver in OpenFOAM (sonicFoam).[21] The normalized density profile n_e/n_{e0} obtained from simulations is plotted as a function of the position along the laser propagation axis as a solid line in Fig. 1.

The grey areas represent schematically the areas occupied by the walls of the gas cell; the laser is propagating from left to right. The density profile consists of a maximum in the inner part of the cell which length can be varied by moving the exit plate; on each side, sharp gradients at the transition with the plates are followed by smoother gradients in the vicinity of the holes, and sharp gradients outside the cell. The colored circles, labeled (a) to (d), represent the different positions of the focal plane in-vacuum relative to the gas cell, used to achieve results shown in Section III.

The focal plane is at a maximum distance of 1.4 mm from the 200 μm entry hole (in the case where it is located at 0.9 mm). In vacuum, the fwhm laser spot size at 1.4 mm from the focal plane is ~41 μm; in this case, all the detected laser energy is entering the gas cell. At the LLC facility, the laser pointing is actively stabilized to cancel drift of the laser

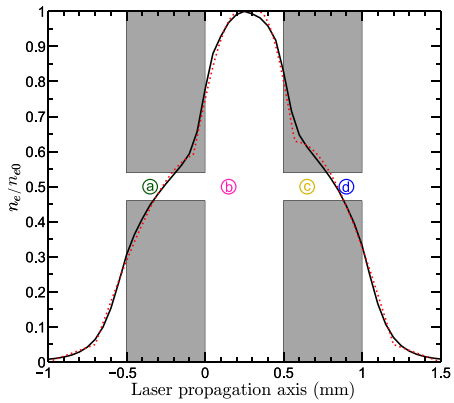

FIG. 1. Normalized density profile for an inner cell length of $L_{cell} = 0.5$ mm calculated with OpenFOAM (black solid line) and approximated density profile used in WARP simulations (red dotted line). The grey areas represent the entrance and exit plates. The colored circles are the in-vacuum focal plane positions of the laser pulse in the experimental study used for the numerical study.

spot in the focal plane, ensuring alignment of the gas cell to be optimized and stable over time of measurement duration. For the experimental results presented in this paper, the maximum electron number density in the cell was $n_{e0} = 8.3 \times 10^{18}$ cm^{-3}, and the corresponding plasma frequency is $\omega_p = 1.6 \times 10^{14}$ rad/s which leads to $\omega_p \tau_L \simeq 6$. The critical power for self-focusing associated to this density is $P_C = 3.6$ TW, which gives a ratio of laser power to critical power $P_L/P_C = (P_L[GW]/17) \times (n_e/n_c) \simeq 4.1$, where n_c is the critical density. Self-focusing is thus expected to occur mainly in the area where the density is close to its maximum.

The generated electron bunches were characterized using a 12 cm-long magnetic dipole with a maximum field strength of 0.7 T and a LANEX screen imaged by a 16 bits CCD. The charge was calculated from LANEX images using published calibration factor[22] and the lowest energy that could be measured was ~50 MeV.

III. VARYING THE FOCAL PLANE POSITION

In this section, electron properties are presented for different positions of the focal plane relative to the entrance of the gas cell. Experimentally, the inner length of the cell was below 1 mm but was not known precisely. As the electron energy distribution is sensitive to the plasma length, measured electron spectra were compared with the results of simulations performed for several values of the plasma length. The best fit of experimental spectra was achieved for a cell length value of $L_{cell} = 0.5$ mm.

Experimental results at different focus positions were then analyzed by comparison to quasi-three-dimensional, electromagnetic PIC simulations with the numerical code WARP, which uses a Fourier decomposition of the electromagnetic fields in the azimuthal direction with respect to the laser-propagation direction.[23] Two Fourier modes were

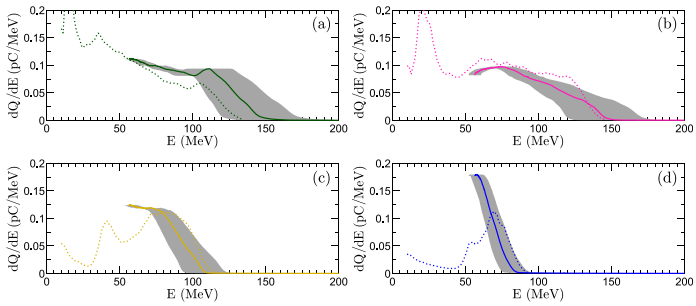

FIG. 2. Electron spectra for different positions z_f of the focal plane in vacuum (a) $z_f = -0.35$ mm, (b) $z_f = 0.15$ mm, (c) $z_f = 0.65$ mm, and (d): $z_f = 0.9$ mm. Solid lines represent the experimental spectra (averaged over 2 shots), gray areas represent the experimental energy uncertainty, and dotted lines represent WARP simulation results for a maximum density in the cell of $n_{e0} = 7.8 \times 10^{18}$ cm^{-3} and an inner cell length of $L_{cell} = 0.5$ mm. Simulation spectra are normalized to the maximum value of the experimental spectrum for the position $z_f = -0.35$ mm.

included in the simulations. A field ionization module based on the Ammosov-Delone-Krainov model was used to model ionization dynamics.[24] The longitudinal profile calculated with OpenFOAM was used in the WARP simulations, with a maximum electron density of $n_{e0} = 7.8 \times 10^{18}$ cm^{-3}, for a gas mixture of 99% of H_2 and 1% of N_2. The laser was linearly polarized. The driving laser parameters are $a_0 = 1.1$, a spot size of 17 μm fwhm, and a duration of 40 fs. All simulations were carried out with 36 macroparticles per cell with a grid resolution of $1.25 \times \lambda_L/2\pi$ and $0.05 \times \lambda_L/2\pi$ in r- and z-directions, respectively.

In Figs. 2(a)–2(d) are displayed electron spectra, obtained from experimental data and from PIC simulation results, for different positions of the in-vacuum focal plane z_f corresponding to the circles labeled (a) to (d) in Fig. 1. Only electrons with energy above ∼50 MeV could be detected experimentally and grey areas around the experimental spectra represent the uncertainty on the energy determination estimated from typical electron pointing fluctuations and divergence. We can observe for all focus positions a good agreement between experimental and simulation data. The electron spectrum shape is shown to be strongly dependent on the parameter z_f. At $z_f = -0.35$ mm, the spectra exhibit a plateau up to ∼110 MeV and then a quasi-linear decrease up to ∼150 MeV. As the value of z_f is increased, the extension of the plateau is reduced, and it vanishes at $z_f = 0.9$ mm.

Fig. 3 shows experimental and simulation results for (a) the total charge above 50 MeV, Q_{tot} and (b) the maximum energy, E_{max}, of the electron bunch; crosses indicate experimental points for gas mixture and open circles with lines simulation results; E_{max} is defined as the energy above which the charge density becomes less than 10% of the maximum. The value of the charge obtained by simulations was normalized to the average of the experimental values at $z_f \simeq -0.35$ mm. Triangles in Fig. 3(a) are experimental results for pure H_2 for similar n_e (8.5×10^{18} cm^{-3}) and L_{cell} (0.8 ± 0.5 mm, respectively). These data show that the addition of 1% N_2 increases the accelerated charge by up to a factor of 10 for the range of parameters studied here, so that the injection of most electrons can be attributed to ionization-induced injection.

Simulation results and experimental data for gas mixture exhibit the same behavior. Experimental data show that both E_{max} and Q_{tot} are increasing from $z_f \simeq -0.6$ mm to $z_f \simeq -0.35$ mm. $z_f = -0.6$ mm corresponds to a position of the focal plane in vacuum in front of the entrance of the cell, so that during the propagation, the laser diffracts significantly before the density is high enough for laser pulse self-focusing to occur; consequently, the maximum intensity is relatively low, leading to a low amplitude accelerating field. From $z_f \simeq -0.6$ mm to $z_f \simeq -0.35$ mm, the maximum energy is increasing, from $z_f = -0.35$ mm to $z_f = 0.15$ mm it is nearly constant, and it decreases for z_f larger than 0.15 mm. The reduction of the maximum energy for z_f larger than 0.15 mm indicates a reduction of the accelerating length and/or of the accelerating field.

The evolution of the normalized vector potential a_0 along the propagation axis, as given by PIC simulations, is

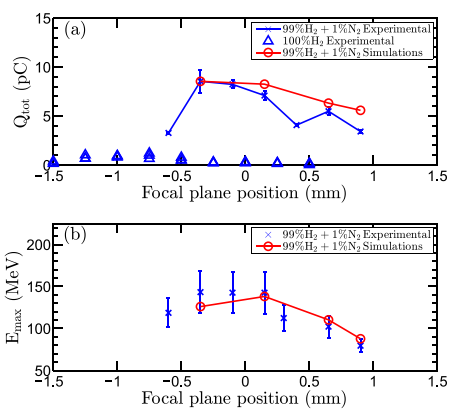

FIG. 3. Simulation and experimental results comparison for charge and energy as a function of focal plane position, blue crosses are experimental data points, and red circles with solid line are simulation results: (a) Q_{tot}: bunch charge for electrons with energy higher than 50 MeV; Blue triangles represent the experimental values of the charge obtained with pure hydrogen and (b) E_{max}: electron maximal energy.

plotted in Fig. 4 with the focal plane position as a parameter. The evolution of a_0 is similar for the four cases corresponding to the spectra of Fig. 2. It shows that laser focusing and defocusing are in these cases dominated by the density profile. Indeed, a_0 starts to increase around the same location for all cases which corresponds to the beginning of the laser self-focusing and decreases when the density is dropping. The variation of z_f changes the maximum absolute values of a_0, which are decreasing when z_f is increased above $z_f = 0.15$ mm.

The locations where electron injection begins are indicated by vertical dashed lines in Fig. 4, and they are defined as the first locations at which electrons with an energy higher than 10 MeV are present. It can be seen that the beginning of injection occurs around the same value of $a_0 \simeq 1.7 \pm 0.1$ for all cases which is consistent with the ionization-induced trapping threshold given in Ref. 10 (in our case at the injection we have $\gamma_p \simeq 15$ and $k_p L_{RMS} \simeq 2.1$, where γ_p is the Lorentz factor of the plasma wave, k_p its wave number, and L_{RMS} the longitudinal root-mean-square laser pulse length). As z_f is increased above 1.15 mm, this value of a_0 is reached after a longer propagation distance; injection then starts later and the acceleration length is reduced as the plasma length is constant.

In the simulation, we also observe that the largest maximum longitudinal electric field of the wake is obtained for $z_f = 0.15$ mm. Therefore, a shift of z_f away from $z_f = 0.15$ mm leads to a reduction of the length available to inject and accelerate electrons and of the amplitude of the electric field responsible for the trapping and acceleration processes. The consequence is that both the charge and the maximum energy of accelerated electrons are reduced when z_f is shifted away from $z_f = 0.15$ mm, as observed in Fig. 3. These results show that a change of the laser focal plane position along the density profile allows control of the position of injection, and subsequently the accelerated charge and energy distribution.

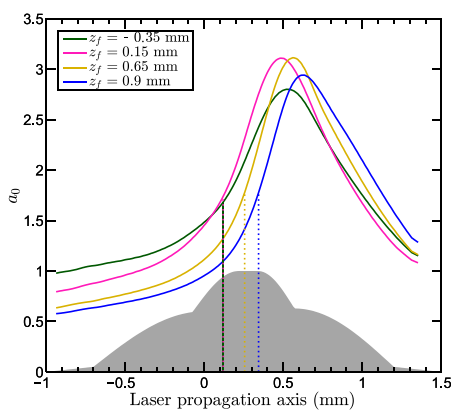

FIG. 4. Normalized vector potential obtained from WARP simulations along the propagation axis for different positions of the focal plane in vacuum. Solid lines represent the value of the normalized vector potential and vertical dashed lines indicate the start of injection in each case (for cases $z_f = -0.35$ mm and $z_f = 0.15$, vertical lines are superimposed).

TABLE I. Parameters of 4 different cases for comparison of accelerated charge in experiments; n_e is the maximum value of the plateau, and the nonlinear dephasing length L_φ is evaluated for this density.

Case No.	Case 1	Case 2	Case 3	Case 4
n_e (10^{18} cm^{-3})	8.3	9.5	8.5	9.3
L_{cell} (mm)	0.5	0.7	10	5
L_{cell} (L_φ)	0.9	1.5	18.5	10.5
L_φ (mm)	0.56	0.46	0.54	0.48
z_f (mm)	0.9	−0.25	−0.25	−0.5

IV. VARYING THE DENSITY, CELL LENGTH, AND LASER INTENSITY

In addition to the focus position, in the regime of interest for an injector, other parameters, such as the plasma density and length, and the laser strength, have a significant role in determining the accelerated charge and the energy of the electron bunch. In this section, we examine the influence of these parameters on the total charge and in a limited energy range suitable for an injector. The energy window 60–70 MeV is of interest as it contains a significant charge for all parameter sets. Table I summarizes the parameters of 4 different cases that were studied experimentally.

The laser vector potential is $a_0 = 1.2$ and the corresponding values of the total charge, Q_{tot} (blue bars), and of the charge in the [60–70 MeV] energy range, $Q_{[60-70\text{MeV}]}$ (red bars), for these 4 cases are plotted in Fig. 5(a). For all cases, the selected value of z_f corresponds to the focal position maximizing the charge in the 60–70 MeV energy range. Case 1 is extracted from the study presented in Section III (i.e., $z_f = 0.9$ mm). We then compare three other sets of parameters to case 1. We first increase the density (case 2) keeping the cell length in the same range and observe a strong increase on both Q_{tot} and $Q_{[60-70\text{MeV}]}$: Q_{tot} is increased

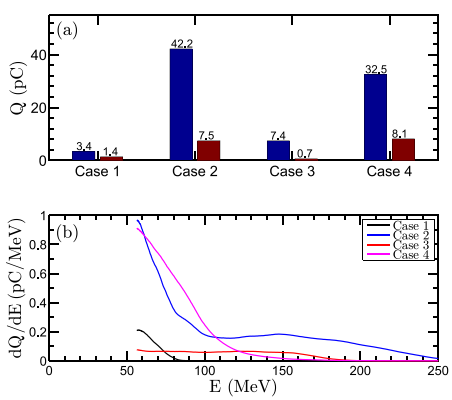

FIG. 5. Experimental cases comparison. (a) Total charge Q_{tot} (blue bars) and charge in the 60–70 MeV energy range $Q_{[60-70\text{MeV}]}$ (red bars) for parameters of cases 1 to 4 listed in Table I. (b) Corresponding energy spectra.

by a factor of ∼12 and $Q_{[60-70\mathrm{MeV}]}$ by a factor of ∼5. Then, we increase the length at a similar density (case 3), and we can observe a significant increase for Q_{tot} but a decrease for $Q_{[60-70\mathrm{MeV}]}$. Finally, we increase both the density and the cell length (case 4) and observe an increase for both Q_{tot} and $Q_{[60-70\mathrm{MeV}]}$.

To further understand this behavior, we plotted the electron spectra for cases 1–4 in Fig. 5(b). Compared with case 1 (solid black line), case 2 (solid blue line) exhibits a higher charge density over the whole spectrum and extends to higher electron energy. For case 2, as the density is higher, the laser self-focuses earlier in the profile, leading to higher charge and higher accelerating field amplitude. The length for case 3 is much longer than the dephasing length and the ionization-induced injection process is in this case continuous which explains the broad spectrum observed in Fig. 5(b) (solid red line). Both the dephasing length and the depletion length at this density ($n_{e0} \sim 8.3 \times 10^{18}\,\mathrm{cm}^{-3}$, $L_D \simeq 2.3$ mm, and $L_\varphi \simeq 0.6$ mm (Ref. 25)) are larger than the cell length of case 1; therefore, an increase in length compared with case 1 leads to an increase of E_{max} as seen in Fig. 5(b) for case 3. For case 4, density and length are both increased, leading to an increase of accelerated charge (similar to case 2) and energy spectrum broadening (similar to case 3). In comparison with case 2, case 4 presents a lower high energy charge density which is probably due to the dephasing effect. The comparison of these 4 cases shows that the charge in the range of 60–70 MeV is maximized for larger n_{e0}, although for the set of parameters studied it reaches only 25% of the total measured charge at a value around 8 pC.

The effect of a_0 variations was studied numerically using WARP simulations, as the laser energy could not be increased in the experiment. In Fig. 6 are plotted Q_{tot} and $Q_{[60-70\mathrm{MeV}]}$ and the associated spectra at $n_{e0} = 7.8 \times 10^{18}\,\mathrm{cm}^{-3}$ and $z_f = 0.65$ mm and for different values of a_0 indicated on the horizontal axis. Q_{tot} and $Q_{[60-70\mathrm{MeV}]}$ are normalized to the same value as in Fig. 3(a) to be comparable to experimental values in pC and the spectra are normalized to the same value as in Fig. 2 to be comparable to experimental spectra in pC/MeV. Fig. 6(a) shows that an increase of a_0 from 1.1 to 2 multiplies Q_{tot} by 13.7 and $Q_{[60-70\mathrm{MeV}]}$ by 8.3. In Fig. 6(b), we observe that the spectra exhibit higher charge density over all the spectrum for higher a_0 and a higher E_{max}. We also observe a peak appearing around 50 MeV for $a_0 = 2$ which can be of interest for an injector at this energy.

Fig. 7 presents the evolutions of a_0 along the propagation axis and the beginning of injection for the different cases. For all simulation results, injection is observed when $\triangle\phi = \phi_i - \phi_{min} \simeq 1$, where ϕ_i is the normalized electrostatic potential of the plasma wave ($\phi = e\Phi/m_e c^2$) at the position of creation of electrons ionized from N^{5+} and N^{6+} and ϕ_{min} its first minimum. To satisfy this condition at a density lower than n_{e0}, i.e., to drive a similar amplitude plasma wave at lower density, the laser amplitude must be higher.[26] For a value in-vacuum of $a_0 = 2$, the laser power is high enough for self-focusing to occur in the entry gradient. In this case, injection is observed at $n_e \simeq 0.4 \times n_{e0}$ when $a_0 \simeq 1.9$. It thus shows that increasing the initial value of a_0 and keeping z_f constant lead to injection earlier during the propagation.

For $a_0 = 1.5$ and 2, we observe significant injection of hydrogen electrons although their contribution to the spectrum is smaller than the contributions of electrons coming from ionized N^{5+} and N^{6+}. Indeed, electrons from hydrogen represent ∼9% and ∼17% of the total charge in case of an initial a_0 of 1.5 and 2, respectively. We also observe that the maximum longitudinal electric field is ∼1.9 and ∼2.7 times higher for $a_0 = 1.5$ and $a_0 = 2$, respectively. Both effects, earlier injection and the excitation of larger amplitude electric fields over a longer distance, contribute to produce higher charge and electron bunches with higher energy.

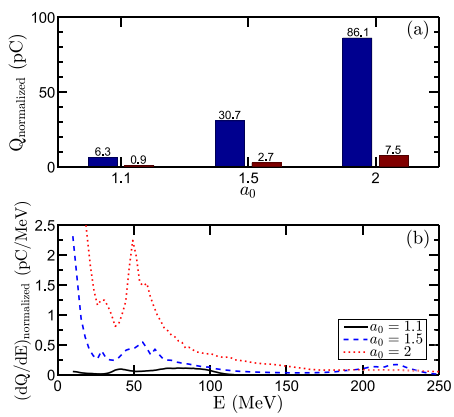

FIG. 6. (a) Simulated electron bunches total charge Q_{tot} (blue bars) and charge in the 60–70 MeV energy range $Q_{[60-70\mathrm{MeV}]}$ (red bars) and (b) associated electron energy distribution for different values of a_0. Normalization is the same as in Fig. 3.

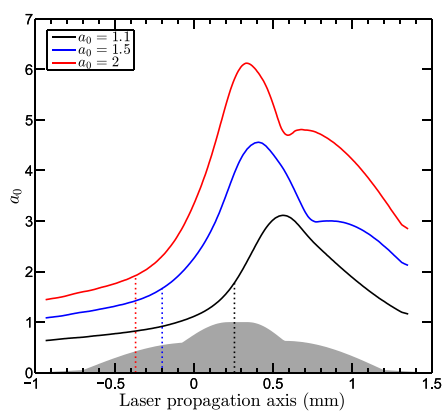

FIG. 7. Evolution of a_0 along the propagation axis for different values of a_0 in vacuum. Solid lines represent the value of the normalized vector potential and dashed lines indicate the start of injection in each case.

V. CONCLUSION

In conclusion, we showed that the position of the laser focal plane along the density profile of a gas cell plays a major role in triggering the ionization-induced injection of electrons and controlling acceleration processes, and therefore on determining the properties of generated electron bunches. Especially, we showed that the focal plane position relative to the cell entrance changes the maximum value of a_0, which has an impact on the longitudinal position of injection and electrostatic fields magnitude. By changing the focal plane position, the electron bunch charge and energy distribution can be tuned, either to optimize the electron bunch total charge or the charge in a given energy range, for example, 60–70 MeV optimized to 41% of the total measured charge for the case of Fig. 2(d) (case 1). For this case, the focal plane in vacuum is located in the exit density gradient ($z_f = 0.9$ mm) and $a_0 = 1.1$, simulation results show a distribution centered at ∼68 MeV. The charge in the 60–70 MeV range can be increased by a factor of ∼5 by increasing the density (case 2). When a_0 is increased from 1.1 to 2, simulations predict 13.6 times higher charge electron bunch exhibiting a peaked distribution at ∼50 MeV.

ACKNOWLEDGMENTS

Authors acknowledge the use of the computing facility clusters GMPCS of the LUMAT federation (FR LUMAT 2764). This work was supported by the Triangle de la Physique under Contract No 2012-032TELISA. Authors also acknowledge the support of the Swedish Research Council, the Knut and Alice Wallenberg Foundation, the Swedish Foundation for Strategic Research, Laserlab-Europe/CHARPAC, and EuCARD2/ANAC2 (Grant Agreements Nos. 284464 and 312453, EC's 7th Framework Programme). This work was supported in part by the Director, Office of Science, Office of High Energy Physics, U.S. Dept. of Energy under Contract No. DE-AC02-05CH11231.

[1]T. Tajima and J. M. Dawson, Phys. Rev. Lett. **43**, 267 (1979).
[2]E. H. Esarey, R. F. Hubbard, W. P. Leemans, A. Ting, and P. Sprangle, Phys. Rev. Lett. **79**, 2682 (1997).
[3]J. Faure, C. Rechatin, A. Norlin, A. F. Lifschitz, Y. Glinec, and V. Malka, Nature **444**, 737 (2006).
[4]S. V. Bulanov, N. Naumova, F. Pegoraro, and J. Sakai, Phys. Rev. E **58**, R5257 (1998).
[5]C. G. R. Geddes, K. Nakamura, G. R. Plateau, C. Tóth, E. Cormier-Michel, E. H. Esarey, C. B. Schroeder, J. R. Cary, and W. P. Leemans, Phys. Rev. Lett. **100**, 215004 (2008).
[6]K. Schmid, A. Buck, C. M. S. Sears, J. M. Mikhailova, R. Tautz, D. Herrmann, M. Geissler, F. Krausz, and L. Veisz, Phys. Rev. Spec. Top. - Accel. Beams **13**, 091301 (2010).
[7]M. Burza, A. Gonoskov, K. Svensson, F. Wojda, A. Persson, M. Hansson, G. Genoud, M. Marklund, C.-G. Wahlström, and O. Lundh, Phys. Rev. Spec. Top. -Accel. Beams **16**, 011301 (2013).
[8]M. Chen, Z.-M. Sheng, Y.-Y. Ma, and J. Zhang, J. Appl. Phys. **99**, 056109 (2006).
[9]A. Pak, K. A. Marsh, S. F. Martins, W. Lu, W. B. Mori, and C. Joshi, Phys. Rev. Lett. **104**, 025003 (2010).
[10]M. Chen, E. H. Esarey, C. B. Schroeder, C. G. R. Geddes, and W. P. Leemans, Phys. Plasmas **19**, 033101 (2012).
[11]F. G. Desforges, B. S. Paradkar, M. Hansson, J. Ju, L. Senje, T. L. Audet, A. Persson, S. D. Dufrénoy, O. Lundh, G. Maynard, P. Monot, J.-L. Vay, C.-G. Wahlström, and B. Cros, Phys. Plasmas **21**, 120703 (2014).
[12]C. McGuffey, A. G. R. Thomas, W. Schumaker, T. Matsuoka, V. Chvykov, F. J. Dollar, G. Kalintchenko, V. Y. A. Maksimchuk, K. Krushelnick, V. Y. Bychenkov, I. V. Glazyrin, and A. V. Karpeev, Phys. Rev. Lett. **104**, 025004 (2010).
[13]C. E. Clayton, J. E. Ralph, F. Albert, R. A. Fonseca, S. H. Glenzer, C. Joshi, W. Lu, K. A. Marsh, S. F. Martins, W. B. Mori, A. Pak, F. S. Tsung, B. B. Pollock, J. S. Ross, L. O. Silva, and D. H. Froula, Phys. Rev. Lett. **105**, 105003 (2010).
[14]B. B. Pollock, C. E. Clayton, J. E. Ralph, F. Albert, A. Davidson, L. Divol, C. Filip, S. H. Glenzer, K. Herpoldt, W. Lu, K. A. Marsh, J. Meinecke, W. B. Mori, A. Pak, T. C. Rensink, J. S. Ross, J. Shaw, G. R. Tynan, C. Joshi, and D. H. Froula, Phys. Rev. Lett. **107**, 045001 (2011).
[15]J. Osterhoff, A. Popp, Z. Major, B. Marx, T. P. Rowlands-Rees, M. Fuchs, M. Geissler, R. Hörlein, B. H. S. Becker, E. A. Peralta, U. Schramm, F. Grüner, D. Habs, F. Krausz, S. M. Hooker, and S. Karsch, Phys. Rev. Lett. **101**, 085002 (2008).
[16]M. Vargas, W. Schumaker, Z.-H. He, Z. Zhao, K. Behm, V. Chvykov, B. Hou, K. Krushelnick, A. Maksimchuk, V. Yanovsky, and A. G. R. Thomas, Appl. Phys. Lett. **104**, 174103 (2014).
[17]F. G. Desforges, M. Hansson, J. Ju, L. Senje, T. L. Audet, S. Dobosz-Dufrénoy, A. Persson, O. Lundh, C.-G. Wahlström, and B. Cros, Nucl. Instrum. Methods Phys. Res., Sect. A **740**, 54 (2014).
[18]M. Hansson, L. Senje, A. Persson, O. Lundh, C.-G. Wahlström, F. G. Desforges, J. Ju, T. L. Audet, B. Cros, S. D. Dufrénoy, and P. Monot, Phys. Rev. Spec. Top. -Accel. Beams **17**, 031303 (2014).
[19]J.-L. Vay, D. P. Grote, R. H. Cohen, and A. Friedman, Comput. Sci. Discovery **5**, 014019 (2012).
[20]J. Ju and B. Cros, J. Appl. Phys. **112**, 113102 (2012).
[21]See http://www.openfoam.com for Openfoam documentation, 2014.
[22]A. Buck, K. Zeil, A. Popp, K. Schmid, A. Jochmann, S. D. Kraft, B. Hidding, T. Kudyakov, C. M. S. Sears, L. Veisz, S. Karsch, J. Pawelke, R. Sauerbrey, T. Cowan, F. Krausz, and U. Schramm, Rev. Sci. Instrum. **81**, 033301 (2010).
[23]A. Lifschitz, X. Davoine, E. Lefebvre, J. Faure, C. Rechatin, and V. Malka, J. Comput. Phys. **228**, 1803 (2009).
[24]G. L. Yudin and M. Y. Ivanov, Phys. Rev. A **64**, 013409 (2001).
[25]W. Lu, M. Tzoufras, C. Joshi, F. S. Tsung, W. B. Mori, J. M. Vieira, R. A. Fonseca, and L. O. Silva, Phys. Rev. Spec. Top. -Accel. Beams **10**, 061301 (2007).
[26]L. M. Gorbunov and V. I. Kirsanov, Sov. Phys. - JETP **93**, 509–518 (1987).

Paper VIII

Localization of ionization-induced trapping in a laser wakefield accelerator using a density down-ramp

M. Hansson, T. L. Audet, H. Ekerfelt, B. Aurand, I. Gallardo González, F. G. Desforges, X. Davoine, A. Maitrallain, S. Reymond, P. Monot, A. Persson, S. Dobosz Dufrénoy, C.-G. Wahlström, B. Cros, and O. Lundh.

Plasma Physics and Controlled Fusion **58**, 055009 (2016).

OPEN ACCESS
IOP Publishing
Plasma Physics and Controlled Fusion
Plasma Phys. Control. Fusion **58** (2016) 055009 (7pp)
doi:10.1088/0741-3335/58/5/055009

Localization of ionization-induced trapping in a laser wakefield accelerator using a density down-ramp

M Hansson[1], T L Audet[2], H Ekerfelt[1], B Aurand[1], I Gallardo González[1], F G Desforges[2], X Davoine[3], A Maitrallain[4], S Reymond[1,5], P Monot[4], A Persson[1], S Dobosz Dufrénoy[4], C-G Wahlström[1], B Cros[2] and O Lundh[1]

[1] Department of Physics, Lund University, PO Box 118, 22100 Lund, Sweden
[2] Laboratoire de Physique des Gaz et des Plasmas, CNRS, Univ. Paris-Sud, Université Paris-Saclay, 91405 Orsay, France
[3] CEA, DAM, DIF, Bruyères-le-Châtel, 91297 Arpajon, France
[4] Laboratoire Interactions, Dynamique et Lasers, CEA, Université Paris-Saclay, 91191 Gif-sur-Yvette, France
[5] ENSTA ParisTech, Université Paris-Saclay, 828 boulevard des Maréchaux, 91762 Palaiseau, France

E-mail: martin.hansson@fysik.lth.se

Received 19 February 2016
Accepted for publication 26 February 2016
Published 23 March 2016

Abstract
We report on a study on controlled trapping of electrons, by field ionization of nitrogen ions, in laser wakefield accelerators in variable length gas cells. In addition to ionization-induced trapping in the density plateau inside the cells, which results in wide, but stable, electron energy spectra, a regime of ionization-induced trapping localized in the density down-ramp at the exit of the gas cells, is found. The resulting electron energy spectra are peaked, with 10% shot-to-shot fluctuations in peak energy. Ionization-induced trapping of electrons in the density down-ramp is a way to trap and accelerate a large number of electrons, thus improving the efficiency of the laser-driven wakefield acceleration.

Keywords: laser, wakefield, trapping, down-ramp, ionization

(Some figures may appear in colour only in the online journal)

1. Introduction

With the breakthrough in 2004 [1–3], the research on laser wakefield accelerators [4] has shown the possibility of generating beams of relativistic electrons with peaked electron energy spectra. The energy of the electrons in the beams depends strongly on the laser system in use, but also on other experimental parameters, such as length and density of the interaction medium, with energies ranging from a few tens of keV [5] up to a few GeV [6]. Much effort is now focused on controlling the properties of the generated beams [7], such as the energy and number of accelerated electrons as well as the divergence and pointing, and on reducing the shot-to-shot fluctuations of these beams [8]. Several techniques to control the injection and trapping of electrons in an excited plasma wave have been demonstrated experimentally to decrease the shot-to-shot fluctuations in charge and energy of the electrons in the generated beams. These methods include trapping by colliding pulses [9], trapping in density transitions [10, 11] and down-ramps [7, 12, 13] and ionization-induced trapping [14, 15].

Trapping of electrons in a density down-ramp is similar to the mechanism of self trapping, which occurs when the electrons that constitute the plasma wave approach and exceed the phase velocity of the wave. In a density down-ramp the phase velocity of the plasma wave behind the driving laser pulse is decreased and the threshold for trapping is thereby

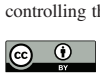

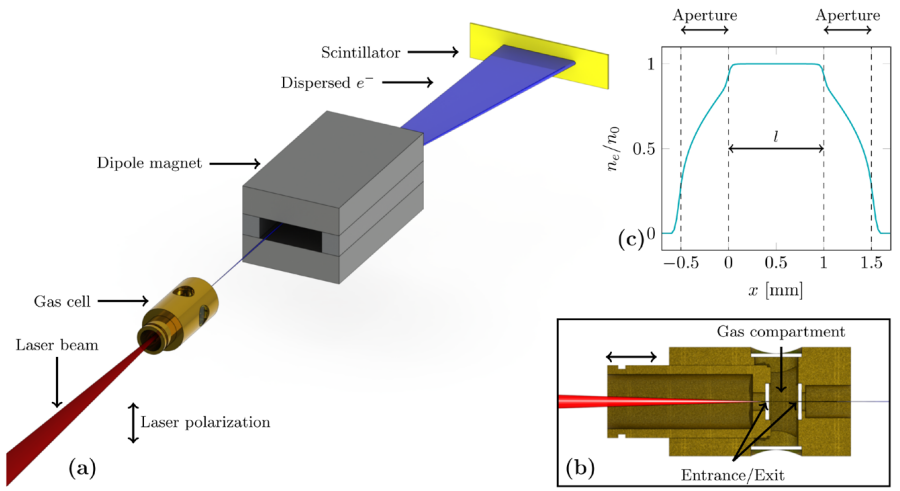

Figure 1. Schematic illustration of the experimental set-up. The laser pulses are focused, through an entrance aperture, into a cell filled with gas. The electrons, accelerated in the interaction, propagate along the optical axis and are then dispersed by a dipole magnetic field before impacting on a scintillating screen and recorded with a 16-bit CCD-camera. (b) Detailed cross section view of the gas cell. The gas cell allows the length to be varied under vacuum during the experiment. (c) Density distribution along the optical axis of the laser beam. The dashed lines marks the entrance and exit apertures through the windows confining the gas, and l is the inner length of the cell, i.e. the distance between the inner surfaces of the windows. The density gradients are characterized using computational fluid dynamics.

also decreased. A drawback of using this technique is that the amount of charge in the bunches of accelerated electrons is relatively small as compared to other mechanisms for injection.

The method of ionization-induced trapping is instead based on the release of free electrons, by field ionization of ions, close to the peak of the laser pulse inside the first period of the excited plasma wave. In contrast to trapping due to a density down-ramp, beams containing a large number of electrons are typically observed when using ionization-induced trapping. However, this type of trapping typically occurs over an extended length, and the electron energy distribution is therefore usually wide. Methods to localize ionization-induced injection and thereby generate quasi-monoenergetic electron energy spectra are certainly of interest including self-truncation of ionization-induced trapping and ionization-induced trapping in a shock [16, 17].

In this paper we present an experimental study, supported by particle-in-cell simulations, on controlled trapping of electrons using a combination of the mechanisms described above. This way, the advantage of higher charge due to ionization-induced trapping is combined with the localization of trapping in a density down-ramp, to produce peaked spectra with high charge. The accelerated beams of relativistic electrons are shown to be reproducible with respect to charge and energy.

2. Experimental setup

Experiments are conducted using the multi-terawatt laser at the Lund Laser Centre, based on chirped pulse amplification (CPA) in Ti:sapphire crystals. The duration of the laser pulses, when fully re-compressed after amplification, that are used in this experiment is (37 ± 3) fs full width at half maximum (FWHM) and each pulse contains approximately (585 ± 60) mJ of energy. The pulses are focused using an off-axis parabolic mirror with an effective focal length of 0.75 m. Furthermore, closed loop wave-front optimization is performed using a wave-front sensor (Phasics SID4) and a deformable mirror in the beam line. With this optimization the focal spot is almost circularly symmetric with a diameter of 17 μm (FWHM).

From the measured pulse duration and energy together with images of the focused laser pulse, the peak intensity is estimated to $(3.0 \pm 0.5) \times 10^{18}$ W cm^{-2} when the laser pulse is focused in vacuum, corresponding to a peak normalized vector potential $a_0 = 1.2 \pm 0.1$.

The leakage through the final dielectric folding mirror of a co-propagating reference beam is focused using a lens, and the focal plane is imaged onto a camera. The images of the focus of the reference beam is used, together with a piezo-electrically actuated mirror, to lock the position of the focused pulses and thus prevent long term drifts of the pointing.

The laser pulses are focused through an entrance aperture, with a diameter of either 100 μm or 200 μm, into a gas cell of variable length (see figures 1(a) and (b)). The gas cell is mounted using a 5-axis holder to allow accurate positioning of the cell along the optical axis, with the entrance of the cell at the beam waist. Gas is filled from a reservoir through an electronically controlled valve that is opened well before the laser pulse arrives at the target, to reach a stationary density of gas

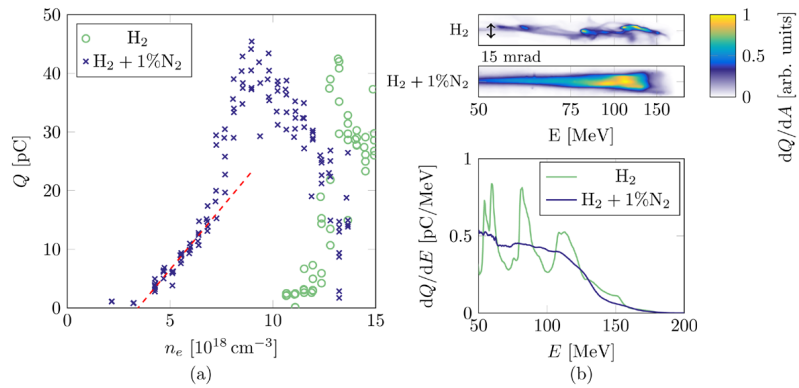

Figure 2. (a) Accelerated charge as a function of electron number density in the density plateau of the cell with the inner length set to 2 mm. The threshold in electron number density is clearly lower when 1% of nitrogen is present in the gas as compared to pure hydrogen. Furthermore the threshold for trapping is not as sharp as when pure hydrogen is used. The red dashed line is fitted to the accelerated charge using the gas mixture at electron number densities between 4×10^{18} cm^{-3} and 7×10^{18} cm^{-3}. (b) Typical shape of dispersed electron beams of electrons, and corresponding spectra, accelerated in the gas mixture and in pure hydrogen for beams containing approximately 40 pC of charge. The electron number density is set to 9×10^{18} cm^{-3} when the gas mixture is used and 13×10^{18} cm^{-3} when pure hydrogen is used. The colormap in each image is normalized to its maximum value. The beams of electrons accelerated in the gas mixture typically have a large divergence and a wide electron energy spectrum whereas the beams of electrons accelerated in pure hydrogen typically consist of multiple peaked features.

in the cell. The number density of neutral gas molecules was characterized using interferometry as a function of backing pressure off-line before the experiment started. Furthermore, the density gradients at the entrance and exit were characterized using computational fluid dynamics simulations (using both OpenFOAM SonicFOAM solver and COMSOL CFD). The length of the gradients (from 10% to 90% of the plateau density) are between 0.5 mm and 0.7 mm depending on the size of the apertures. The normalized gas density distribution along the optical axis of the laser beam is shown in figure 1(c).

To compare self-trapping with ionization-induced trapping, two types of gases are used in the experiment. Pure hydrogen gas is used to allow only self-trapping, whereas a mixture of hydrogen and 1% nitrogen is used to enable ionization-induced trapping.

The electrons accelerated in the interaction co-propagate with the laser pulse along the optical axis onto a scintillating screen (Kodak Lanex regular), covered with an aluminum foil that blocks the laser light. The light emitted from the rear side of the scintillating screen is recorded using a 16-bit CCD-camera, and the total response of the system is calibrated and used together with published calibration factors for the screen [18] to determine the amount of charge in the beams of electrons impacting on the screen. Furthermore, a dipole magnet is mounted on a manual linear translation stage and can be moved into the electron beam under vacuum to disperse the electrons depending on their energy. Numerically tracing the electrons through the dipole magnetic field allows electron energy spectra to be determined from the acquired images of the dispersed electrons impacting the scintillating screen.

Before acquiring a series of data, the longitudinal laser focus position, with respect to the gas cell is fine tuned, either by moving the cell or by changing the curvature of the deformable mirror, to yield the best quality of the beams of accelerated electrons. Similarly, the pulse compression is optimized by fine tuning the grating separation.

3. Experiments and results

3.1. Self trapping and ionization-induced trapping

The inner length of the cell, i.e. the distance between the inner surfaces of the front and back windows, is set to 2 mm and a sequence of shots is recorded while the backing pressure supplied to the gas cell is varied using either pure hydrogen or a gas mixture containing 1% of nitrogen.

As shown in figure 2(a), the electron number density threshold for trapping of electrons is significantly lower for the gas mixture than for pure hydrogen. This is expected, since the threshold for ionization-induced trapping is lower than for self-trapping [19]. Furthermore, it is observed that the threshold for trapping is much sharper in the case of self-trapping in pure hydrogen than for ionization-induced trapping in the gas mixture. Using the gas mixture at low electron number density, 4×10^{18} cm^{-3} to 7×10^{18} cm^{-3}, the amount of charge in the beams of accelerated electrons scales almost linearly with the electron number density in the plasma, indicated by the red dashed line in figure 2(a). The shot-to-shot fluctuations in charge, as deviations from a fitted linear dependence on the density, is only 1.2 pC here. At higher electron number densities the charge increases more rapidly with density but the relative shot-to-shot fluctuations in charge remains low, and is on average 14.5% at each selected value of electron number density.

A typical image of a dispersed electron beam accelerated when the cell is filled with the gas mixture to provide

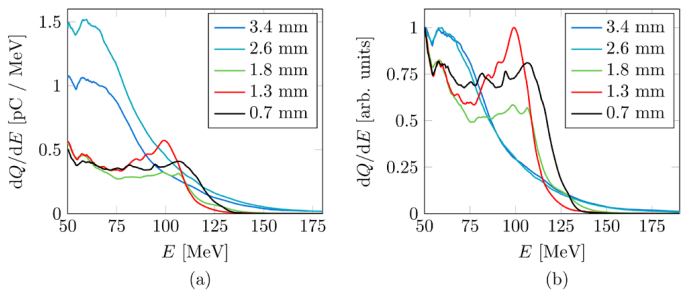

Figure 3. (a) Evolution of the electron energy spectrum for beams accelerated using the gas mixture at an electron number density of 12×10^{18} cm^{-3} as the length of the gas cell is varied. A peaked feature is observed for cell lengths between 0.7 mm and 1.8 mm. The visibility of the peaked feature is highest at a cell length of 1.3 mm as shown in (b) where the spectra are normalized at 50 MeV. For longer cells the amount of charge is larger but no peak is observed in the electron energy spectra.

an electron number density of 9×10^{18} cm^{-3} is shown in figure 2(b). This image shows the reproducible features of the beams of accelerated electrons trapped by ionization, with a large energy spread up to a cut-off energy of approximately 150 MeV and a rather large divergence that is increasing with electron energy (≈12 mrad at 100 MeV). The beam charge, of electrons with energy above 50 MeV, is in this case 38 pC.

Beams with similar amount of charge are produced using pure hydrogen at a higher electron number density, 13×10^{18} cm^{-3}. A typical image of a dispersed electron beam accelerated under these conditions is shown in figure 2(b). Due to oscillations of the peak normalized vector potential, a_0, these beams typically contain multiple, peaked, components as self trapping occurs at multiple locations along the plasma and the energy and number of peaks are fluctuating from shot to shot. Each of these components has an energy spread of about 10% and a divergence smaller than 10 mrad.

3.2. Trapping in a density down-ramp

The length of the cell is varied in a sequence of shots with the cell filled with the gas mixture of hydrogen and 1% of nitrogen and the typical spectral shapes are studied. The electron number density is set to 12×10^{18} cm^{-3} to operate the accelerator well above the threshold for ionization-induced trapping [20]. At this density, the power of the laser pulse exceeds the critical power for self-focusing, $P/P_c \approx 4$. The peak normalized vector potential is therefore expected to increase rapidly as the laser pulse enters the gas cell and reaches approximately the value for a matched pulse, for which the transverse size of the laser pulse is approximately equal to the transverse size of the electron void. For a laser pulse containing 585 mJ of energy this corresponds to $a_0 = 3.2$, according to the theory by Lu *et al* [21]. Under these conditions, the dephasing length is $L_d \approx 0.6$ mm. Thus, for regular ionization-induced trapping, broad electron energy spectra, without peaked features are expected.

In figure 3(a), spectra are shown for five shots at different inner cell lengths. For inner cell lengths of above 1.8 mm, the electron energy spectra are wide and monotonically decreasing with energy. For cell lengths of 1.8 mm and lower, the charge distribution is modified and a peak builds up at energies around 100 MeV. The visibility of the peak is largest for a cell length of 1.3 mm as made clear in figure 3(b), in which the spectra are normalized to the charge at 50 MeV.

For cell length below 1.8 mm, it is observed that the shape of the distribution is not sensitive to the cell length and with a peak in the range 100–110 MeV, which suggests that the distance from the point of trapping to the end of acceleration is unaffected by changes in the cell length. This is consistent with the assumption that these electrons are trapped in the density down-ramp at the back of the gas cell.

For a cell length of 0.7 mm, after re-optimizing both longitudinal laser focus position, using the deformable mirror, and pulse compression by adjusting the grating separation, and after decreasing the electron number density to 9.6×10^{18} cm^{-3}, the peaked features in the spectrum are even more clear (see figure 4(a)). In addition, another peaked feature at higher energy is observed. The peak at lower energy is reproducible and appeared in 73 of 100 shots in a sequence. For these shots the energy of the peak is 90 MeV ± 10% and the energy spread is 20 MeV ± 48%. For the remaining 27 shots, a component at similar energy and divergence is still observed, but is not contributing to a peak in the spectrum but rather a wide distribution of energies up to ≈ 120 MeV. In both cases the divergence was only approximately 3 mrad.

The peak at higher energy is observed on all shots in this sequence at an energy of 150 MeV ± 7%, with an energy spread of 50 MeV ± 18%. This second peaked feature has a larger divergence (≈10 mrad) than the component at lower energy. The total amount of detected charge is on average 9 pC ± 28% in this series of shots.

Under the same conditions, but switching to pure hydrogen, only the peak at 150 MeV remain, as shown in figure 4(b). In this series of shots, the amount of charge is on average 1.0 pC ± 29%, but increases to 2.0 pC when moving the cell only 0.25 mm along the optical axis.

Typical spectra from the two cases, normalized at the peak at high energy, are shown in figure 4(c). Here it can be observed that the energy spread of the component at 150 MeV

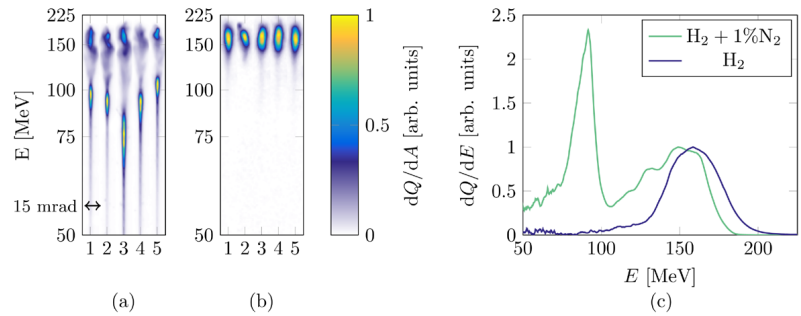

Figure 4. Typical traces of the dispersed electron beams using (a) a mixture of hydrogen and 1% nitrogen and (b) pure hydrogen, at an electron number density of 9.6×10^{18} cm^{-3} in a cell with an inner length of 0.7 mm. Each trace is normalized to its peak value. The total amount of detected charge is 9 pC $\pm$ 28% in the case of the gas mixture and 1.0 pC $\pm$ 29% in the case of the pure hydrogen. Typical energy spectra of beams of electrons accelerated in pure hydrogen and in a mixture of 1% nitrogen in hydrogen are shown in (c). The energy spectra of all beams feature a peak at approximately 150 MeV. In addition, the beams accelerated in the gas mixture typically contain another peak at a lower energy ($\approx$ 90 MeV). Each curve is normalized to its corresponding value at the peak around 150 MeV, to allow the shapes to be compared.

is approximately 50 MeV (FWHM) in both cases. The component at low energy, for this shot at 90 MeV, has a significantly smaller energy spread of only 15 MeV.

3.3. Three-dimensional particle-in-cell simulations

Simulations are performed using the fully relativistic three-dimensional particle-in-cell code CALDER-CIRC [22], which is exploiting the fact that only a low number of azimuthal Fourier components are required to model laser wakefield acceleration. In the simulations the time step is set to 52 attoseconds and a window following the laser pulse, with a size of 50 μm longitudinally and 75 μm radially, is used. The spatial grid size is set to 16 nm in the longitudinal direction and 190 nm in the radial direction, and three azimuthal Fourier modes are used.

The laser pulse is defined in the simulations to have a pulse duration of 34 fs and a transversal size of 17 μm (FWHM) when focused in vacuum, with a peak normalized vector potential of 1.25, approximately corresponding to laser parameters in the experiment. The waist of the laser beam, when not affected by the propagation in the plasma, is chosen in the simulations to be located at the beginning of the density plateau inside the cell. Furthermore, the shape of gradients of the density distribution in the entrance and exit of the cell are fitted as piece-wise linear functions, consisting of three parts, from the results from the characterization of the gradients using computational fluid dynamics. The length of the gradient is chosen to be 500 μm, in the fall from 90% to 10% of the plateau density, which corresponds to the shortest possible gradient determined using computational fluid dynamics.

First, simulations are performed at different electron number densities to determine the threshold of self trapping in the density plateau. A simulation is then performed for a cell with an inner length of 0.8 mm at an electron number density of 9.1×10^{18} cm^{-3} to avoid self-trapping in the density plateau. The results from this simulation are summarized in figure 5 (a). Here, the evolution of the electron energy spectra are shown for the electrons released by ionization from H and $N - N^{4+}$ in black (upper) and the electrons released by ionization from N^{5+} and N^{6+} green (lower). Also, the evolution of the peak normalized vector potential inside the plasma is shown in red and the electron number density is shown in blue. Each of these curves are normalized to the corresponding maximum value of the simulation. Furthermore, in figures 5(c) and (d), the electron distribution is shown, both in real space and longitudinal phase-space, close to the laser pulse before (b), in the middle (c) and in the end (d) of the density down-ramp together with the corresponding electron energy spectrum at each position.

Under these conditions, ionization-induced trapping occurs continuously in the plateau between the input and exit of the cell and provide a wide, but very weak, background in the electron energy spectrum.

An increased rate of trapping of electrons is observed in the density down-ramp, both for electrons from the background plasma and for electrons ionized from N^{5+} and N^{6+}. The electron energy spectrum at the end of the density down-ramp contains two slightly separated peaks, consistent with the experimental results. The peak at higher energy is identified to contain electrons from ionization of hydrogen and from the first ionization states of nitrogen ($N - N^{4+}$). These electrons are released into the plasma, by ionization from their corresponding atoms or ions, far from the peak of the laser pulse, and the simulation shows that these electrons are injected and trapped in the density down-ramp at the exit of the gas cell by density down-ramp injection. The spectral peak at lower energy is due entirely to electrons from ionization of N^{5+} and N^{6+}, which occur much closer to the peak of the laser pulse. The simulation shows that these electrons are also trapped in the density down-ramp at the exit from the gas cell.

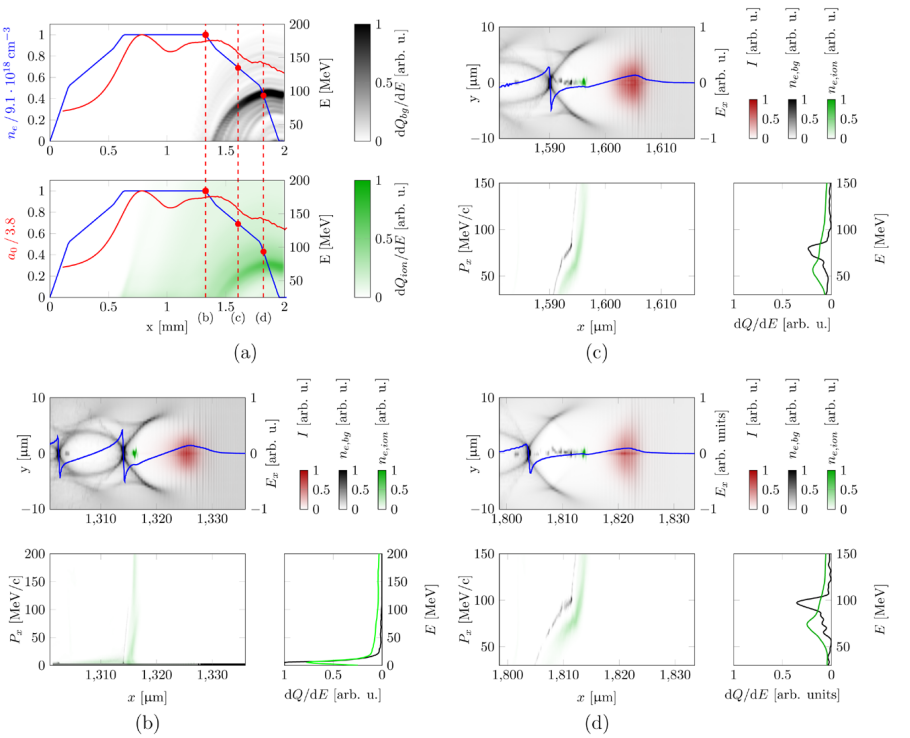

Figure 5. Summary of a particle-in-cell simulation (a) showing the evolution of the spectrum of the trapped electrons released by ionization from H and $N - N^{4+}$ (black) and from N^{5+} and N^{6+} (green). Three snapshots ((b)–(d)) from the simulation showing trapping of electrons in the density down-ramp at the exit of the cell, with the corresponding position of each snapshot marked in the density profile in (a). For each snapshot, the density distribution of the background electrons is shown in black, and the electrons released from N^{5+} and N^{6+} in green. The intensity distribution of the laser pulse is shown in red. Before the density down-ramp (b), only a small fraction of electrons, mainly released by ionization of N^{5+} and N^{6+}, has been trapped. The electrons released from H and $N - N^{4+}$ and trapped in the density down-ramp (c) are well separated in phase-space from the electrons released from N^{5+} and N^{6+} that are also trapped in this ramp. After further acceleration, and phase-space rotation due to the longitudinal extent of the injected electrons, these two populations form two peaks in the energy spectrum (d).

The simulation further reveals a longitudinal separation of the electrons that build up the two components after they have been trapped in the plasma wave. During the subsequent acceleration in the density down-ramp, the electrons from ionization of N^{5+} and N^{6+} are located closer to the center of the electron void, and thus experience a lower accelerating field than the trapped electrons ionized from H and $N - N^{4+}$, which are located further to the back of the electron void.

The reason for this separation is a fundamental difference in the injection and trapping mechanism. The electrons, already released from the atoms far from the peak of the laser pulse, are injected at the back of the electron void following the laser pulse, as the size of the bubble is growing in the density down-ramp. In contrast, ionization of N^{5+} and N^{6+} releases electrons into the plasma closer to the peak of the laser pulse and they are able to pass through the rest of the laser field into the electron void. The released electrons are then accelerated by the longitudinal electric field and catch up with and exceeds the speed of the laser pulse (corresponding to a relativistic factor $\gamma_l \approx 14$).

Overall, the final electron energy spectrum of the simulation agrees qualitatively well with the experimental findings under similar conditions. However, the energy of the two spectrally peaked features are lower than observed in the experiments. We attribute those differences to discrepancies in the parameters of the laser pulse and/or density distribution between the experiment and simulation. In particular, the effect of a longer density ramp is two-fold: (I) the effective length of acceleration becomes longer. (II) The plasma wavelength is increasing more slowly, which means that the dephasing of the electrons due to the expansion of the plasma wave is slower.

4. Discussions

Our experiment using a gas mixture shows two different regimes of laser wakefield acceleration of ionization-induced trapped electrons. For cells longer than approximately 2 mm, a large number of electrons are trapped by ionization-induced trapping, after self-focusing of the laser pulse, in the density plateau. This process occurs over an extended length, as long as the conditions for trapping are fulfilled, and the resulting electron energy spectra are therefore wide without peaked features. Under these conditions, the threshold, in electron number density, for ionization-induced trapping is lower than for self-trapping. For electron number densities in the range between 4×10^{18} cm^{-3} and 7×10^{18} cm^{-3}, the amount of charge in the bunches of accelerated electrons scales linearly with electron number density in the plateau, with only small shot-to-shot fluctuations. This regime is therefore favorable when good control over the charge is desired, but has the drawback of generating beams of electrons with wide energy spectra.

For shorter cells, only few electrons are trapped in the density plateau and provide broad and weak distributions in the energy spectra. However, the density down-ramp at the exit of the cell increases the rate of trapping by ionization, as observed in the simulations. The reason for this increased rate of trapping is the decreased phase velocity of the wake, as the wake period increases behind the laser pulse as it propagates through the density down-ramp, which facilitates trapping of electrons. The region from which electrons can be ionized to become trapped in the wake therefore locally increases in a density down-ramp. Localization of the trapping, together with phase-space rotation of the distribution of trapped electrons [7], yield a peak in the electron energy spectrum.

Similarly, the threshold for trapping of electrons from the background plasma also decreases in the density down-ramp at the exit of the cell, and these trapped electrons also contribute to a peak in the electron energy spectrum (see figures 4(b) and (c)). The electrons trapped from the background plasma are subject to a stronger accelerating field in the wake which results in a higher energy for these electrons compared to the electrons from ionization from N^{5+} and N^{6+}.

While the electron energy is higher for the electrons trapped from the background plasma in the density down-ramp, the amount of charge is significantly higher when also ionization-induced trapping occurs in the density down-ramp.

Due to pump depletion, as the length of the cell is increased, the strength of the laser pulse as it reaches the exit down-ramp is decreased. Therefore, the amount of charge injected in the down-ramp is expected to decrease, which agrees well with our observation of no peaked features for cells longer than approximately 1.8 mm.

5. Conclusions

We have shown experimentally, and supported by simulations, that the advantage of ionization-induced trapping to provide high charge in beams of accelerated electrons can be combined with a density down-ramp to localize the injection and thereby providing peaked electron energy spectra. Higher charge in the accelerated beams, as compared to pure density down-ramp injection, also implies a better efficiency of the accelerator. The peak energy of the electrons trapped by field ionization of N^{5+} and N^{6+} at the back of a gas cell shows only small shot-to-shot fluctuations and the method is therefore a suitable choice for a stable wakefield accelerator.

Acknowledgments

We acknowledge the support of the Swedish Research Council, the Knut and Alice Wallenberg Foundation, the Swedish Foundation for Strategic Research, the Triangle de la Physique (Grant Agreement No. 2012-032TELISA), Laserlab-Europe/LEPP (Grant Agreement No. 654148, EC's Horizon 2020) and EuCARD2/ANAC2 (Grant Agreement No. 312453, EC's 7th Framework Programme). The simulations were performed on resources provided by the Swedish National Infrastructure for Computing (SNIC) at Lunarc. SR acknowledges support from the ERASMUS programme.

References

[1] Faure J, Glinec Y, Pukhov A, Kiselev S, Gordienko S, Lefebvre E, Rousseau J P, Burgy F and Malka V 2004 *Nature* **431** 541–4
[2] Geddes C G R, Toth C, van Tilborg J, Esarey E, Schroeder C B, Bruhwiler D, Nieter C, Cary J and Leemans W P 2004 *Nature* **431** 538–41
[3] Mangles S P D *et al* 2004 *Nature* **431** 535–8
[4] Tajima T and Dawson J M 1979 *Phys. Rev. Lett.* **43** 267–70
[5] He Z H, Thomas A G R, Beaurepaire B, Nees J A, Hou B, Malka V, Krushelnick K and Faure J 2013 *Appl. Phys. Lett.* **102** 064104
[6] Leemans W P *et al* 2014 *Phys. Rev. Lett.* **113** 245002
[7] Hansson M, Aurand B, Davoine X, Ekerfelt H, Svensson K, Persson A, Wahlström C G and Lundh O 2015 *Phys. Rev. ST Accel. Beams* **18** 071303
[8] Hansson M *et al* 2014 *Phys. Rev. ST Accel. Beams* **17** 031303
[9] Faure J, Rechatin C, Norlin A, Lifschitz A, Glinec Y and Malka V 2006 *Nature* **444** 737–9
[10] Schmid K, Buck A, Sears C M S, Mikhailova J M, Tautz R, Herrmann D, Geissler M, Krausz F and Veisz L 2010 *Phys. Rev. ST Accel. Beams* **13** 091301
[11] Burza M, Gonoskov A, Svensson K, Wojda F, Persson A, Hansson M, Genoud G, Marklund M, Wahlström C G and Lundh O 2013 *Phys. Rev. ST Accel. Beams* **16** 011301
[12] Gonsalves A J *et al* 2011 *Nat. Phys.* **7** 862–6
[13] Golovin G, Chen S, Powers N, Liu C, Banerjee S, Zhang J, Zeng M, Sheng Z and Umstadter D 2015 *Phys. Rev. ST Accel. Beams* **18** 011301
[14] McGuffey C *et al* 2010 *Phys. Rev. Lett.* **104** 025004
[15] Desforges F G *et al* 2014 *Phys. Plasmas* **21**
[16] Mirzaie M *et al* 2015 *Sci. Rep.* **5** 14659
[17] Thaury C *et al* 2015 *Sci. Rep.* **5** 16310
[18] Buck A *et al* 2010 *Rev. Sci. Instrum.* **81** 033301
[19] Pak A, Marsh K A, Martins S F, Lu W, Mori W B and Joshi C 2010 *Phys. Rev. Lett.* **104** 025003
[20] Chen M, Esarey E, Schroeder C B, Geddes C G R and Leemans W P 2012 *Phys. Plasmas* **19** 033101
[21] Lu W, Tzoufras M, Joshi C, Tsung F S, Mori W B, Vieira J, Fonseca R A and Silva L O 2007 *Phys. Rev. ST Accel. Beams* **10** 061301
[22] Lifschitz A, Davoine X, Lefebvre E, Faure J, Rechatin C and Malka V 2009 *J. Comput. Phys.* **228** 1803–14

Paper IX

Shock assisted ionization injection in laser-plasma accelerators

C. Thaury, E. Guillaume, A. Lifschitz, K. Ta Phuoc, M. Hansson, G. Grittani, J. Gautier, J.-P. Goddet, A. Tafzi, O. Lundh, and V. Malka.
Scientific Reports **5**, 16310 (2015).

www.nature.com/scientificreports

OPEN

Shock assisted ionization injection in laser-plasma accelerators

C. Thaury[1,*], E. Guillaume[1,*], A. Lifschitz[1], K. Ta Phuoc[1], M. Hansson[2], G. Grittani[3,4], J. Gautier[1], J.-P. Goddet[1], A. Tafzi[1], O. Lundh[2] & V. Malka[1]

Received: 07 September 2015
Accepted: 12 October 2015
Published: 09 November 2015

Ionization injection is a simple and efficient method to trap an electron beam in a laser plasma accelerator. Yet, because of a long injection length, this injection technique leads generally to the production of large energy spread electron beams. Here, we propose to use a shock front transition to localize the injection. Experimental results show that the energy spread can be reduced down to 10 MeV and that the beam energy can be tuned by varying the position of the shock. This simple technique leads to very stable and reliable injection even for modest laser energy. It should therefore become a unique tool for the development of laser-plasma accelerators.

Laser plasma wakefield accelerators can produce femtosecond electron beams[1] with energies up to a few GeV[2–4], in only a few centimeters. A critical issue with plasma accelerators is to trap electrons into the wakefield in a reliable and controllable way. Ionization injection is one of the most effective methods for achieving this trapping[5–9]. This technique is based on the use of a high-Z gas or a gas mixture (low and high Z gases). While outer shell electrons of the high-Z gas are ionized by the rising edge of the laser pulse, inner shell electrons are released only when the laser reaches its peak intensity. At that time, a wakefield cavity is already formed. Electrons from inner shells can therefore be released in the middle of the cavity. They are then accelerated as they slip toward the back of the cavity and possibly injected if their velocity exceeds the wakefield velocity. This injection technique allows to accelerate electron beams with high charge[10] and low emittance[11] but large energy spread[6–8].

This large energy spread comes from the fact that the laser field remains above the threshold for inner shell ionization over a significant length (possibly a few millimeters), leading to continuous electron injection. Several techniques have been proposed to control the trapping length and hence the energy spread in ionization injection. They include the use of moderate power laser pulses[12], multiple beams setups[5,13–15], and plasma density tailoring[16] notably in staged laser-plasma accelerators[17–19]. Yet, energy spreads obtained in experiments are at best about 10 MeV[17], which remains relatively large compared to best controlled injection techniques[20,21].

Here we propose and demonstrate a controlled ionization injection technique which is simpler to set up than existing ones and leads to mean energy spreads of about 10 MeV, with room for improvement. It is based on the creation of a shock front in a supersonic gas jet. Electrons ionized when the laser crosses the shock front spend more time in the accelerating field because the cavity expands, as illustrated in Fig. 1. They can thus be injected below the threshold for regular ionization injection, leading to localized trapping and low energy spreads. This technique is quite similar to density-transition injection[22], except for the use of a gas mixture instead of a pure light gas. We show in the following that this simple change stabilizes the injection and improves the beam quality significantly.

[1]LOA, ENSTA ParisTech, CNRS, École Polytechnique, Université Paris-Saclay, 828 bd des Maréchaux, 91762 Palaiseau France. [2]Department of Physics, Lund University, P. O. Box 118, S-22100 Lund, Sweden. [3]Institute of Physics ASCR, v.v.i. (FZU), ELI Beamlines project, Na Slovance 2, 18221 Prague, Czech Republic. [4]Czech Technical University in Prague, FNSPE, Brehova 7, 11519 Prague, Czech Republic. *These authors contributed equally to this work. Correspondence and requests for materials should be addressed to C.T. (email: cedric.thaury@ensta-paristech.fr)

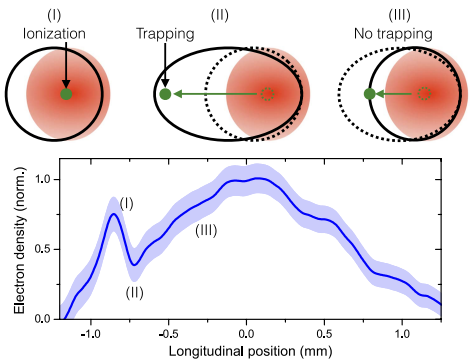

Figure 1. Principle of shock assisted ionization injection and typical density profile. Electrons ionized close to the center of the plasma cavity when the laser crosses the density transition (between I and II) spend a long time in the accelerating field due to the expansion of the cavity in the shock front. Therefore, they are much more likely to be trapped than electrons ionized in the up-ramp density gradient (III) which have to catch up a shrinking (accelerating) cavity. For low enough laser intensity and plasma density the injection can thus be restricted to the shock front. The shaded area indicates the standard error on the measurement. Note that the measured shock front is not fully resolved; it may actually be significantly sharper and denser (the resolution is about 40 μm).

Results

The experiment was performed at LOA using the *salle jaune* laser facility. The laser duration and focal spot were 28 fs and $12.2 \times 15.7\,\mu m^2$ full width at half maximum (FWHM) respectively. The peak laser intensity in vacuum was $I = (5 \pm 2) \times 10^{18}$ W cm^{-2}. The shock front was formed by inserting a 500 μm thick silicon wafer into the supersonic gas flow from a 1.5 mm nozzle, 3 mm from the nozzle exit. Its position along the laser propagation axis was varied in order to tune the electron beam energy. The density profile was characterized at every shot by plasma interferometry and Abel inversion. Note that the shock front is almost perpendicular to the optical axis within the plasma (which radial extension is about 160 μm FWHM), Abel inversion can therefore be performed using the optical axis as a symmetry axis. A typical density profile is shown in Fig. 1. Unless otherwise stated, the gas is a mixture composed of 99% of helium and 1% of nitrogen. Helium is fully ionized in the rising edge of the laser, while nitrogen is ionized to N^{5+} ; electrons from upper levels can be ionized when the laser reaches its peak intensity, leading to ionization injection. Electron spectra were measured with a spectrometer consisting of a permanent magnet (1.1 T with a length of 100 mm) combined with a phosphor screen imaged on a 16 bit CCD camera. The spectral resolution varies between 2.7% and 3.8% for electron energy between 75 and 200 MeV. All measurement precisions were obtained from the standard deviation.

Ten consecutive electron spectra obtained with a shock and a gas mixture are shown in the left side of Fig. 2. Electrons are injected at every shot (over hundreds of consecutive shots). The beam charge is about 1 pC. The mean energy spread is 14 ± 2 MeV (11% at 123 MeV), while the energy spread of the best shots is about 10 MeV. This is much smaller than typical energy spread obtained with regular ionization injection, as exemplified in Fig. 5d. The accelerated beam is elliptic[9] with a divergence of 5 ± 0.6 mrad in the laser polarization direction and 2.6 ± 0.7 mrad in the perpendicular direction. The beam stability is compared with that of shock front injection in pure helium in Fig. 2. The charge and the energy spread are similar in both cases. In contrast, the stability is much better in the gas mixture; the standard deviation of the electron beam energy and charge are 2.5% and 12% respectively, while in pure helium they are 7% and 24%. The use of gas mixture improves also significantly the rms pointing stability; it is 1.5 mrad in the gas mixture versus 3.2 mrad in pure helium (in other series the rms pointing stability is as low as 0.7 mrad and it is never larger than 1.8 mrad with the gas mixture). Beam fluctuations in pure helium are likely due to a deficient laser wavefront[23], to inhomogeneities in the laser spot or to imperfect shock fronts. In the gas mixture, ionization injection restricts the injection close to the optical axis[7,9]; therefore it produces an electron beam which is less sensitive to radial inhomogeneities, similar to longitudinal injection[24]. Accordingly, shock assisted ionization injection was also observed to depend much less on shock and laser conditions than regular shock injection; for many conditions, there was no injection with pure helium while electrons were injected at every shot with the gas mixture.

Particle-In-Cell simulations were used to get some insight into the injection mechanism. They were performed with the 3D, fully electromagnetic code CALDER-CIRC which uses cylindrical coordinates and a Fourier decomposition in the poloidal direction[25]. Two Fourier modes were used with 70

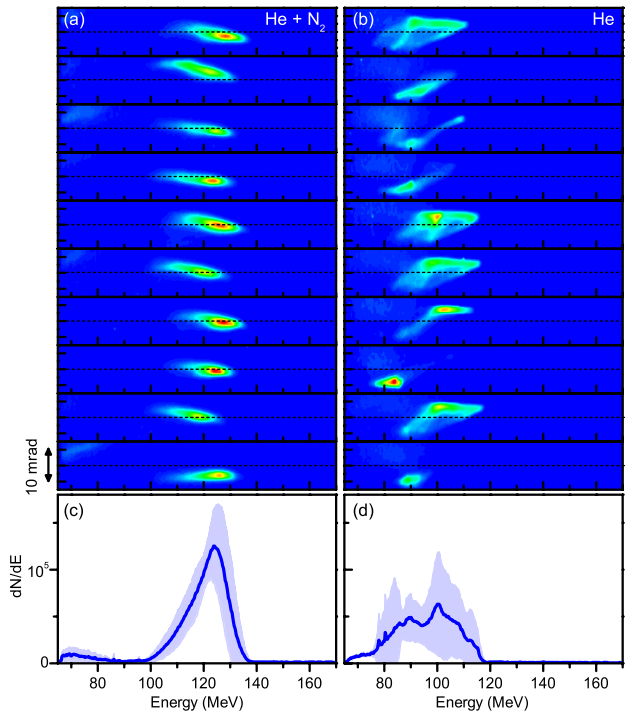

Figure 2. Angularly resolved electron spectra of ten consecutive shots, with a shock front and a gas mixture **(a)** or pure helium **(b).** The electron density at the center of the density profile is $4 \pm 0.1 \times 10^{18}\,\mathrm{cm}^{-3}$ in (**a**) and $3 \pm 0.1 \times 10^{18}\,\mathrm{cm}^{-3}$ in (**b**). The shock front is located 1.03 ± 0.02 mm from the center of the density profile in (**a**) and 1.34 ± 0.02 mm in (**b**). The small differences in density and shock front position explain the difference in the electron beam energy between (**a**,**b**). The spectra are corrected from the spectrometer dispersion. The color bar goes from 0 (blue) to 83000 electrons per MeV per mrad (red). (**c**,**d**) Corresponding mean electron spectra, with standard deviation in colored area.

macro-particles by cell, and mesh sizes $\Delta z = 0.2k_0^{-1}$ and $\Delta r = 1.5k_0^{-1}$ in the longitudinal and radial directions respectively, with k_0 the laser wavenumber. The laser intensity was $I = 3.3 \times 10^{18}\,\mathrm{W\,cm}^{-2}$ and the focal spot radius was 16 μm FWHM. Ionization was described using a modified ADK model[26]. The density profile used in the simulation is shown in Fig. 3a. Because of moderate plasma density and laser intensity, the laser weakly self-focuses; the peak intensity does not exceed $I = 1.5 \times 10^{19}\,\mathrm{W\,cm}^{-2}$ and a wakefield is efficiently excited over $\approx$1.5 mm only (from $x \approx -0.7$ mm). Yet, an electron beam with a 1 pC charge is trapped and accelerated up to $\approx$110 MeV, with an energy distribution similar to the experimental one (Fig. 3b). Figure 3a shows the ionization position of accelerated electrons. Most of them originate from a short region just before the density transition. They gain some energy from the wakefield before the shock front. Then, they shift back towards the center of the plasma cavity in the density transition, because of the cavity expansion; they are thus further accelerated and gain enough energy to be trapped. Note that the peak around 55 MeV in Fig. 3b is due to regular ionization injection occurring well after the density transition; similar peaks were also observed in the experiment.

In addition to improving the stability, shock assisted ionization injection preserves most of the advantages of shock front injection, notably its simplicity (single stage, single laser pulse) and the possibility to change the electron energy by varying the shock position. For instance, in Fig. 4(a) the energy increases from 70 MeV to 120 MeV when the shock position is moved from -0.26 mm to -0.9 mm from the center of the density profile. The charge and energy spread are almost constant, except for $z = -0.26$ where they are reduced by a factor of 10 and 4 respectively (probably because of a smoother shock front). From Fig. 4(a), the mean longitudinal field and the effective acceleration length are estimated to be about

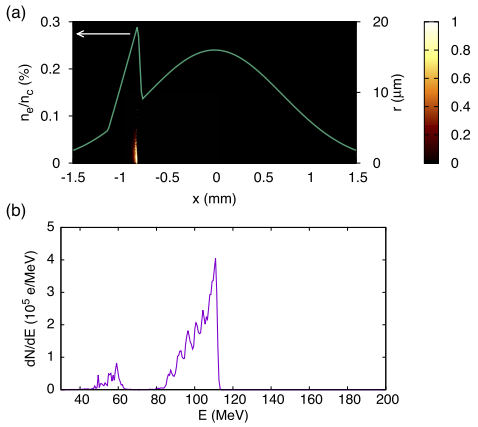

Figure 3. Simulation of ionization injection in a shock front. (**a**) Density profile (left axis) and initial radius of trapped electrons (right axis). The color scale indicates the density of trapped electrons in arbitrary unit. (**b**) Corresponding electron spectrum.

67.5 ± 8 GeV/m and 1.65 ± 0.32 mm respectively. This length is much smaller than the dephasing length, indicating that acceleration is limited by laser diffraction, as observed in the simulation. The longitudinal field is also relatively weak, pointing out that the accelerator is operated in the quasi-linear regime, consistently with the moderate laser intensity.

Figure 4(b) shows that electrons can be injected even with modest laser energy, down to ≈670 mJ. While the electron beam energy increases slightly with the laser energy E_L for $E_L \lesssim 1.07$ J, the rise is most significant for larger energies, likely because of better laser self-focusing and hence longer acceleration length. The beam charge (integrated over two FWHM) increases more steadily with E_L, from 38 ± 7 fC up to 8.6 ± 1.5 pC. This increase goes along a growth of the energy spread from 9 ± 1 MeV up to 25 ± 4 MeV. These findings are consistent with injection ionization close to the injection threshold (the injected volume in the phase space increases with the laser intensity).

The charge and the energy of the beam also depend on the electron density n_e, as shown in Fig. 4c. From $n_e = 3.1 \times 10^{18}\,\mathrm{cm}^{-3}$ to $n_e = 9.2 \times 10^{18}\,\mathrm{cm}^{-3}$, the charge and energy increase from 0.5 ± 0.2 to 14.2 ± 1 pC and from 98 ± 4 to 193 ± 3 MeV respectively. The charge growth arises likely from the increase of the nitrogen density and of the laser intensity (resulting from self-focusing). The beam energy increases because of rising accelerating field originating from the increase of the density and enhanced laser self-focusing. It confirms that the acceleration is not limited by dephasing (in the opposite case, the energy would decrease with increasing density).

As the plasma density increases some electrons can be released after the density transition, leading to injection over a long length and hence to broad energy distributions. This effect is illustrated in Fig. 5. Whereas all the charge is concentrated in a single peak at low density (Fig. 5a), a second peak with a large energy spread is also accelerated when the density is risen above $\sim 5.3 \times 10^{18}\,\mathrm{cm}^{-3}$ (Fig. 5b,c). Note that at the threshold density (Fig. 5b), a second beam is not trapped at each shot. In contrast, for $n_e \sim 9.2 \times 10^{18}\,\mathrm{cm}^{-3}$ the spectra presents always a low energy tail (Fig. 5c). The energy spread of the tail is very similar to that of electron beams obtained without shock at the same density (Fig. 5d), confirming that this tail is due to regular ionization injection. The total charge is also similar with or without the shock, about 30 pC, probably because of beam loading. Thus, the drawback of rising the plasma density to increase the beam charge is that it can also increase the charge in the low energy tail. A way to increase the beam charge while avoiding this detrimental effect is to rise the fraction of nitrogen in the gas mixture. This is exemplified in Fig. 5b–e which shows that doubling the proportion of nitrogen leads to the injection of more electrons in the electron beam without changing significantly the energy distribution nor the divergence.

Discussion

In conclusion, we demonstrated a controlled injection technique which gathers most of the advantages of ionization and shock front injections. It is easy to setup and works for a large range of parameters without requiring a complex alignement. Compared to ionization injection, electron trapping is confined to a small region, leading to the injection of electron beams with rather low energy spreads (down

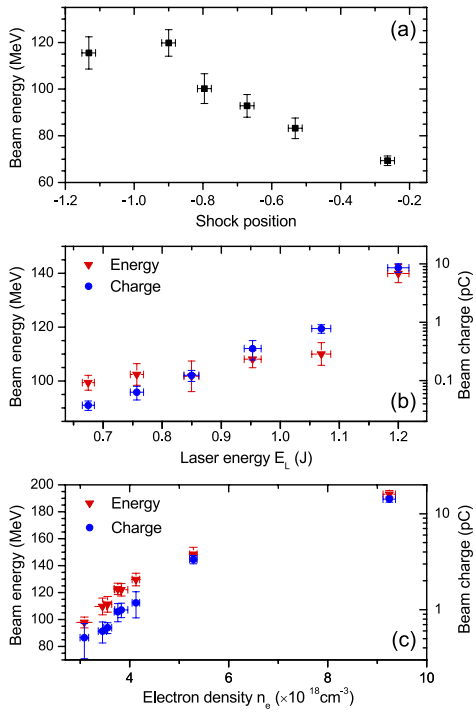

Figure 4. Influence of the shock position, the laser energy and the electron density on the beam properties. (**a**) Peak energy as a function of the shock position, for $n_e = 5.3 \pm 0.4 \times 10^{18}\,\mathrm{cm}^{-3}$. (**b**) Electron beam energy and charge as a function of the laser energy, for $n_e = 5.6 \pm 0.3 \times 10^{18}\,\mathrm{cm}^{-3}$. (**c**) Beam charge and energy as a function of the electron density. In (**b**,**c**) the shock position is $z_s = -1.02 \pm 0.02\,\mathrm{mm}$. Error bars indicate the standard deviation.

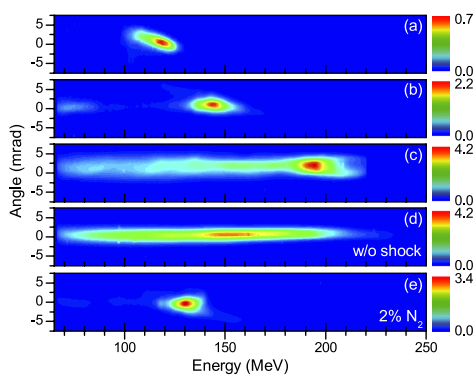

Figure 5. Angularly resolved electron spectra for different conditions. (**a**) Electron density $n_e = 3.7 \times 10^{18}\,\mathrm{cm}^{-3}$. (**b**) $n_e = 5.3 \times 10^{18}\,\mathrm{cm}^{-3}$. (**c**) $n_e = 9.2 \times 10^{18}\,\mathrm{cm}^{-3}$. (**d**) $n_e = 9.2 \times 10^{18}\,\mathrm{cm}^{-3}$, without shock. (**e**) $n_e = 5.3 \times 10^{18}\,\mathrm{cm}^{-3}$, mixture 2% nitrogen, 98% helium.

to 10 MeV). The electron beams were also observed to be much more stable than those obtained by shock front injection. In particular the pointing stability was as low as 0.7 mrad. Further optimization of the shock may lead to higher charge and to smaller energy spread, down to 5 MeV as obtained with density-transition injection[20]. Moreover, a laser-plasma lens could be used to reduce the divergence below 2 mrad[27,28].

References

1. Lundh, O. *et al.* Few femtosecond, few kiloampere electron bunch produced by a laser-plasma accelerator. *Nature Phys.* **7,** 219–222, doi: 10.1038/nphys1872 (2011).
2. Wang, X. *et al.* Quasi-monoenergetic laser-plasma acceleration of electrons to 2 GeV. *Nature Comm.* **4,** 1988, doi: 10.1038/ncomms2988 (2013).
3. Kim, H. T. *et al.* Enhancement of electron energy to the multi-gev regime by a dual-stage laser-wakefield accelerator pumped by petawatt laser pulses. *Phys. Rev. Lett.* **111,** 165002, doi: 10.1103/PhysRevLett.111.165002 (2013).
4. Leemans, W. P. *et al.* Multi-gev electron beams from capillary-discharge-guided subpetawatt laser pulses in the self-trapping regime. *Phys. Rev. Lett.* **113,** 245002, doi: 10.1103/PhysRevLett.113.245002 (2014).
5. Chen, M., Sheng, Z.-M., Ma, Y.-Y. & Zhang, J. Electron injection and trapping in a laser wakefield by field ionization to high-charge states of gases. *J. Appl. Phys.* **99,** 056109, doi: 10.1063/1.2179194 (2006).
6. McGuffey, C. *et al.* Ionization Induced Trapping in a Laser Wakefield Accelerator. *Phys. Rev. Lett.* **104,** 025004, doi: 10.1103/PhysRevLett.104.025004 (2010).
7. Pak, A. *et al.* Injection and Trapping of Tunnel-Ionized Electrons into Laser-Produced Wakes. *Phys. Rev. Lett.* **104,** 025003, doi: 10.1103/PhysRevLett.104.025003 (2010).
8. Clayton, C. E. *et al.* Self-Guided Laser Wakefield Acceleration beyond 1 GeV Using Ionization-Induced Injection. *Phys. Rev. Lett.* **105,** 105003, doi: 10.1103/PhysRevLett.105.105003 (2010).
9. Chen, M., Esarey, E., Schroeder, C. B., Geddes, C. G. R. & Leemans, W. P. Theory of ionization-induced trapping in laser-plasma accelerators. *Phys. Plasmas* **19,** 033101, doi: 10.1063/1.3689922 (2012).
10. Guillaume, E. *et al.* Physics of fully-loaded laser-plasma accelerators. *Phys. Rev. ST Accel. Beams* **18,** 061301, doi: 10.1103/PhysRevSTAB.18.061301 (2015).
11. Schroeder, C. B. *et al.* Thermal emittance from ionization-induced trapping in plasma accelerators. *Phys. Rev. ST Accel. Beams* **17,** 101301, doi: 10.1103/PhysRevSTAB.17.101301 (2014).
12. Kamperidis, C., Dimitriou, V., Mangles, S. P. D., Dangor, A. E. & Najmudin, Z. Low energy spread electron beams from ionization injection in a weakly relativistic laser wakefield accelerator. *Plasma Phys. Contr. Fusion* **56,** 084007, doi: 10.1088/0741-3335/56/8/084007 (2014).
13. Li, F. *et al.* Generating High-Brightness Electron Beams via Ionization Injection by Transverse Colliding Lasers in a Plasma-Wakefield Accelerator. *Phys. Rev. Lett.* **111,** 015003, doi: 10.1103/PhysRevLett.111.015003 (2013).
14. Bourgeois, N., Cowley, J. & Hooker, S. M. Two-pulse ionization injection into quasilinear laser wakefields. *Phys. Rev. Lett.* **111,** 155004, doi: 10.1103/PhysRevLett.111.155004 (2013).
15. Yu, L.-L. *et al.* Two-color laser-ionization injection. *Phys. Rev. Lett.* **112,** 125001, doi: 10.1103/PhysRevLett.112.125001 (2014).
16. Zeng, M. *et al.* Controlled ionization-induced injection by tailoring the gas-density profile in laser wakefield acceleration. *J. Plasma Phys.* **78,** 363–371, doi: 10.1017/S0022377812000098 (2012).
17. Liu, J. S. *et al.* All-Optical Cascaded Laser Wakefield Accelerator Using Ionization-Induced Injection. *Phys. Rev. Lett.* **107,** 035001, doi: 10.1103/PhysRevLett.107.035001 (2011).
18. Pollock, B. B. *et al.* Demonstration of a narrow energy spread, ~0.5 GeV electron beam from a two-stage laser wakefield accelerator. *Phys. Rev. Lett.* **107,** 045001, doi: 10.1103/PhysRevLett.107.045001 (2011).
19. Golovin, G. *et al.* Tunable monoenergetic electron beams from independently controllable laser-wakefield acceleration and injection. *Phys. Rev. ST Accel. Beams* **18,** 011301, doi: 10.1103/PhysRevSTAB.18.011301 (2015).
20. Buck, A. *et al.* Shock-Front Injector for High-Quality Laser-Plasma Acceleration. *Phys. Rev. Lett.* **110,** 185006, doi: PhysRevLett.110.185006 (2013).
21. Faure, J. *et al.* Controlled injection and acceleration of electrons in plasma wakefields by colliding laser pulses. *Nature (London)* **444,** 737–739, doi: 10.1038/nature05393 (2006).
22. Schmid, K. *et al.* Density-transition based electron injector for laser driven wakefield accelerators. *Phys. Rev. ST Accel. Beams* **13,** 091301, doi: 10.1103/PhysRevSTAB.13.091301 (2010).
23. Beaurepaire, B. *et al.* Effect of the laser wave front in a laser-plasma accelerator. *Phys. Rev. X* **5,** 031012, doi: 10.1103/PhysRevX.5.031012 (2015).
24. Corde, S. *et al.* Observation of longitudinal and transverse self-injections in laser-plasma accelerators. *Nature Comm.* **4,** 1501, doi: 10.1038/ncomms2528 (2013).
25. Lifschitz, A. F. *et al.* Particle-in-cell modelling of laser-plasma interaction using fourier decomposition. *J. Comput. Phys.* **228,** 1803, doi: 10.1016/j.jcp.2008.11.017 (2009).
26. Nuter, R. *et al.* Field ionization model implemented in Particle In Cell code and applied to laser-accelerated carbon ions. *Phys. Plasmas* **18,** 033107, doi: 10.1063/1.3559494 (2011).
27. Lehe, R., Thaury, C., Guillaume, E., Lifschitz, A. & Malka, V. Laser-plasma lens for laser-wakefield accelerators. *Phys. Rev. ST Accel. Beams* **17,** 121301, doi: 10.1103/PhysRevSTAB.17.121301 (2014).
28. Thaury, C. *et al.* Demonstration of relativistic electron beam focusing by a laser-plasma lens. *Nature Comm.* **6,** doi: 10.1038/ncomms7860 (2015).

Acknowledgements

This work was supported by the European Research Council through the ERC projects X-Five (Contract No. 339128), and by the Agence Nationale pour la recherche through the project LUCEL-X (ANR-13-BS04-0011) and CILEX (ANR-10-EQPX-CILEX). O.L. and M.H. acknowledge support by the Swedish Research Council, the Swedish Foundation for Strategic Research and the Knut and Alice Wallenberg Foundation.

Author Contributions

C.T., E.G. and K.T.P. conceived the experiment, C.T., E.G., K.T.P., M.H., G.G. and O.L. conducted the experiment, A.L. wrote the code CALDER-CIRC and ran the simulation, J.-P.G. and A.T. operated the

laser, C.T. and E.G. analyzed the results, C.T. wrote the paper and V.M. supervised the project. All authors reviewed the manuscript.

Additional Information

Competing financial interests: The authors declare no competing financial interests.

How to cite this article: Thaury, C. *et al.* Shock assisted ionization injection in laser-plasma accelerator. *Sci. Rep.* **5**, 16310; doi: 10.1038/srep16310 (2015).

Paper X

Injection of electrons by colliding laser pulses in a laser wakefield accelerator

M. Hansson, B. Aurand, H. Ekerfelt, A. Persson, and O. Lundh.

In press: *Nuclear Instruments and Methods in Physics Research A (2016) DOI:10.1016/j.nima.2016.02.070.*

ARTICLE IN PRESS

Nuclear Instruments and Methods in Physics Research A ∎ (∎∎∎∎) ∎∎∎–∎∎∎

Contents lists available at ScienceDirect

Nuclear Instruments and Methods in Physics Research A

journal homepage: www.elsevier.com/locate/nima

Injection of electrons by colliding laser pulses in a laser wakefield accelerator

M. Hansson*, B. Aurand, H. Ekerfelt, A. Persson, O. Lundh

Department of Physics, Lund University, P.O. Box 118, S-22100 Lund, Sweden

ARTICLE INFO

Article history:
Received 14 November 2015
Received in revised form
18 February 2016
Accepted 22 February 2016

Keywords:
Laser
Wakefield
Injection
Trapping
Colliding pulses

ABSTRACT

To improve the stability and reproducibility of laser wakefield accelerators and to allow for future applications, controlling the injection of electrons is of great importance. This allows us to control the amount of charge in the beams of accelerated electrons and final energy of the electrons. Results are presented from a recent experiment on controlled injection using the scheme of colliding pulses and performed using the Lund multi-terawatt laser. Each laser pulse is split into two parts close to the interaction point. The main pulse is focused on a 2 mm diameter gas jet to drive a nonlinear plasma wave below threshold for self-trapping. The second pulse, containing only a fraction of the total laser energy, is focused to collide with the main pulse in the gas jet under an angle of 150°. Beams of accelerated electrons with low divergence and small energy spread are produced using this set-up. Control over the amount of accelerated charge is achieved by rotating the plane of polarization of the second pulse in relation to the main pulse. Furthermore, the peak energy of the electrons in the beams is controlled by moving the collision point along the optical axis of the main pulse, and thereby changing the acceleration length in the plasma.

1. Introduction

The research on laser wakefield accelerators, first proposed by Tajima and Dawson [1] in 1979, has been highly active since the break-through in 2004 when it was demonstrated that laser wakefield accelerators could produce electron beams with quasi-monoenergetic spectra in the so-called bubble regime [2–4]. However, laser wakefield accelerators still suffer from several issues, and in particular large shot-to-shot fluctuations, large energy spread and divergence. One of the causes of the fluctuations is the injection and trapping of electrons, which in many experiments is achieved by self-trapping. Self-trapping occurs as the velocity of the electrons constituting the plasma wave approaches and exceeds the phase-velocity of the wave. Since the evolution of the laser pulse in the plasma and the excitation of the plasma wave is highly non-linear, both the number of trapped electrons and the final energy of the electrons tends to be hard to control. For this reason, several techniques for externally triggered injection and trapping of electrons in laser wakefield accelerators have been developed and proved to be successful to decrease shot-to-shot fluctuations and to improve the quality of the beams. These include, among others, injection in density down-ramps [5–7] or density transitions [8,9], injection by ionization from inner shells [10,11] and injection by colliding laser pulses [12–14].

In the scheme of injection by colliding laser pulses, a focused laser pulse drives a plasma wave in its wake to a large amplitude, but below the threshold for self-trapping. A second focused counter-propagating laser pulse, with lower intensity, is spatially and temporally overlapped with the main pulse at a certain time and position in the plasma. During the collision of the two pulses, a beat-wave is formed which exerts a large ponderomotive force on the plasma electrons. For amplitudes of the two pulses over a certain threshold [14], this force stochastically heats the plasma electrons and a fraction of these electrons gain sufficiently large forward momentum to become trapped in the wake driven by the main pulse.

The technique of injection by colliding laser pulses has been shown to generate high quality beams [15–17], regarding divergence, energy spread of the quasi-monoenergetic spectra and electron pulse duration. However, this technique is experimentally challenging since two laser pulses of high intensity have to be spatially and temporally overlapped at the desired point of injection and requires high control and stability of the pointing of the two laser pulses.

In this article we report on our experiments on colliding pulse injection, and our efforts to decrease the complexity in the experimental set-up. We anticipate that such simplified set-up

* Corresponding author.
E-mail address: martin.hansson@fysik.lth.se (M. Hansson).

http://dx.doi.org/10.1016/j.nima.2016.02.070

Please cite this article as: M. Hansson, et al., Nuclear Instruments & Methods in Physics Research A (2016), http://dx.doi.org/10.1016/j.nima.2016.02.070

allows the technique to become more approachable for further studies including studies of applications of the electron beams.

2. Experimental set-up and methods

The experiments were conducted at the Lund Laser Centre, using a multi-terawatt laser operating at 10 Hz at a central wavelength of 800 nm. The laser system produces pulses of up to 1 J after compression in a single 50 mm diameter beam. The beam position and pointing is monitored at several points in the laser system and, using piezoelectric actuated mirrors, an automated system compensates for long term drifts.

The experimental set-up is illustrated in Fig. 1(a), showing the incoming beam from the laser system from bottom left. The pulse duration is estimated from autocorrelation measurements to (40 ± 4) fs full width at half maximum (FWHM). The beam is split into two parts using a small pick-up mirror close to the interaction point. The pick-up mirror is elliptical such that it reflects a circular 1/2 in. beam perpendicular to the optical axis of the main beam. Also, the substrate of this mirror is cut to leave a circular shade in the main beam without blocking any additional part of the main beam.

The main laser beam, used for the pulses that drive the plasma wake, is focused using an off-axis parabolic mirror with an effective focal length of 750 mm. The beam reflected by the pick-up mirror is used for the pulses that trigger the injection and is focused using an off-axis parabolic mirror with an effective focal length of 100 mm. The injection pulses are focused onto the optical axis of the main beam at, or at the vicinity of, the main beam waist. The optical axes of the two focused beams are both in the horizontal plane, in which they make an angle of 150°. The beam line used for the injection pulses include a motorized linear translation stage to move the collision point along the optical axis of the main beam, and a second motorized linear translation stage to allow for re-focusing of the injection pulses under vacuum. A manually actuated delay stage allows for coarse adjustment of the temporal overlap of the two pulses at the interaction point before the experimental chamber is pumped to vacuum. The fine adjustment is then made by a motorized linear translation stage that moves the pick-up mirror along the direction of the reflected beam. Furthermore, a rotatable zero-order mica $\lambda/2$ wave retarder is inserted, for specific data series, in the beam line and allows rotation of the plane of polarization of the injection pulses. The wave retarder is approximately 80 μm thick and is not expected to affect the duration of the injection pulses significantly. However, the transmittance of the wave retarder is measured to 0.8 and the peak intensity of the injection pulses is decreased by the same factor.

The foci of the two beams are imaged simultaneously using a microscope by reflecting the beams on the top edge of a prism, shaped to reflect both beams vertically in the direction of the microscope objective (see Fig. 1(b)). This imaging system is used to spatially overlap the two pulses, by inserting the prism edge and imaging the desired position for the collision, and then steering the two foci there. Fig. 1(c) shows a typical image of the two foci on the top edge of the prism after the spatial overlap has been tuned. In order to clearly see both foci in this figure, the normalization of the color map is different in the two regions separated by the dashed line, which also marks the position of the edge of the prism.

By fitting Gaussian distributions to the intensity distribution of each foci, the diameter (FWHM) of the foci of the main and injection beam are determined to be 20 μm and 11 μm, respectively. Furthermore, the amount of energy fitted into each Gaussian is 470 mJ and 42 mJ, respectively. Assuming a Gaussian

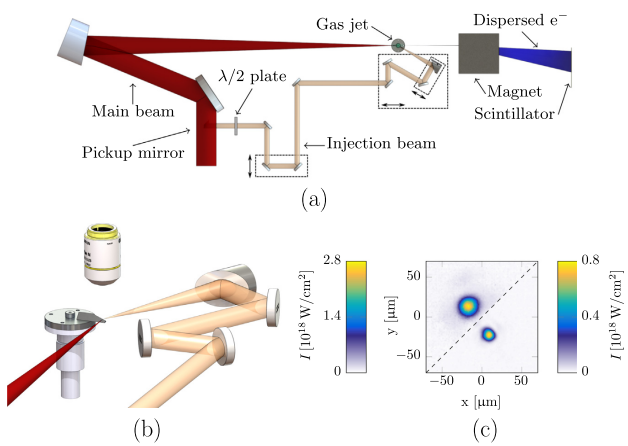

Fig. 1. (a) Schematic illustration of the experimental set up. The main beam of pulses driving the wakefield is focused using an $f=750$ mm parabolic mirror onto a jet of hydrogen gas. The beam of pulses to trigger injection is generated using a pick-up mirror in the single beam from the laser system and is focused using an $f=100$ mm parabolic mirror on the optical axis of the main beam close to its waist. The electrons, trapped and accelerated in the interaction in the plasma, propagate along the optical axis of the main beam out of the plasma and are dispersed by a dipole magnetic field according to energy before they impact on a scintillating screen. The pick-up mirror is mounted on a motorized linear translation stage, with the translation axis in the direction of the reflected beam, which allows for fine tuning of the temporal overlap of the pulses at the position of spatial overlap. For specific data series, a rotatable zero-order mica $\lambda/2$ wave retarder is inserted in the beam line and allows rotation of the plane of polarization of the injection pulses. (b) Imaging system used to observe the foci of the main and injection beam simultaneously. The upper edge of a prism, cut to reflect both beams vertically towards a microscope objective, is inserted at the desired position of collision. The foci of the beams are then steered to this position using motorized actuators. (c) Image acquired using the system shown in (b), showing the intensity distribution of the foci from the two pulses. Note that the scale of the color map is different for the two parts of the image. The wavefront of the laser beam is corrected using a deformable mirror. (For interpretation of the references to color in this figure caption, the reader is referred to the web version of this paper.)

Please cite this article as: M. Hansson, et al., Nuclear Instruments & Methods in Physics Research A (2016), http://dx.doi.org/10.1016/j.nima.2016.02.070

distribution temporally, with the determined pulse duration, the peak intensities are 2.8×10^{18} W/cm^2 and 0.8×10^{18} W/cm^2, for the main and injection pulse respectively, corresponding to normalized vector potentials of 1.1 and 0.6.

A gas nozzle with an orifice diameter of 2 mm located approximately 1 mm from the optical axis, provides a jet of hydrogen gas with its front edge at the waist of the main beam. The neutral density distribution is characterized off-line by measuring, using a wavefront sensor, the additional optical path length introduced by the gas in an optical probe beam [18], and by assuming circular symmetry in the plane of the two laser pulses.

The accelerated electrons exit the plasma along the optical axis of the main laser pulse, and are dispersed by a dipole magnetic field before impacting on a scintillating screen. Images of the scintillating screen are acquired for each shot and are used to determine the electron energy spectra. The response of the imaging system is absolutely calibrated, which is used together with published calibration factor for the scintillating screen [19] to determine the amount of charge in the beams of accelerated electrons.

3. Results

During the experiment, the pick-up mirror is first removed from the beamline. In this case, beams of accelerated electrons are observed for electron number densities above 1.1×10^{19} cm^{-3}. The beams of electrons show the typical features of self-trapped beams, with electron energy spectra containing one or more peaked features [20]. The energy value of these peaks are fluctuating from shot to shot in the range from approximately 50 MeV to 200 MeV and the amount of detected charge is of the order of 50 pC with fluctuations (standard deviation) of 50%.

The density is then lowered well below this threshold, to 8×10^{18} cm^{-3}, to make sure that no accelerated electrons in the succeeding shots are due to self-trapping, and the pick-up mirror is inserted. After optimizing both spatial and temporal overlap of the main and injection pulses at the desired position of injection, quasi-monoenergetic beams of accelerated electrons with low divergence (≈ 3 mrad) are observed. These beams of accelerated electrons have a small energy spread, typically below 5 MeV (FWHM). Due to the lower peak intensity of the main pulse, the density can be increased to 1.2×10^{19} cm^{-3}, while still observing high-quality electron beams. Images of dispersed electron beams on the scintillating screen for two shots at the same plasma electron number density and with the collision point approximately in the center of the gas jet are shown in Fig. 2(a), together with the electron energy spectra for each beam. It is confirmed, by blocking the injection pulse, that no beams of accelerated electrons are generated due to self-trapping. It is observed in this figure that the beams impacting on the scintillating screen are close to circular symmetric. This suggests that the measured energy spread is most likely limited by the resolution of the electron spectrometer and divergence of the electron beams.

To confirm that the trapped charge is due to the interference of the two colliding pulses, the plane of polarization of the injection pulses is rotated. The amount of detected charge as a function of angle of rotation (θ) of the plane of polarization of the injection pulse with respect to the horizontal plane, is shown in Fig. 2(b), for a sequence of shots taken using a plasma electron number density of 1.1×10^{19} cm^{-3}. Maximum amount of charge is detected with both pulses polarized in the horizontal plane (θ=0°), for which the interference between the pulses is maximal. In contrast, with the injection pulse polarized in the vertical plane, there is minimal interference between the two pulses as they cross each other, and as a result no charge is detected on any of these shots.

The energy of the accelerated electrons is controlled by changing the position of collision in the plasma along the optical axis of the main beam, while still maintaining the temporal overlap of the two pulses. This is achieved in the experiment using either of two methods. (I) By moving the translation stage holding the focusing mirror of the injection pulse, the position of collision is changed while keeping the plasma fixed with respect to the main beam focus. The drawback of this method is that both the spatial and temporal overlap had to be re-checked after every change of collision point. This prevented systematic studies of the properties of the beams as a function of collision point. (II) By instead moving the gas nozzle, the length of the remaining plasma after the collision point is thus varied. Since no fine tuning of the spatial and temporal overlap needs to be done between different positions of the plasma, this method allowed for systematic studies of the properties of the beams of accelerated electrons as a function of collision point. However, moving the plasma with respect to the

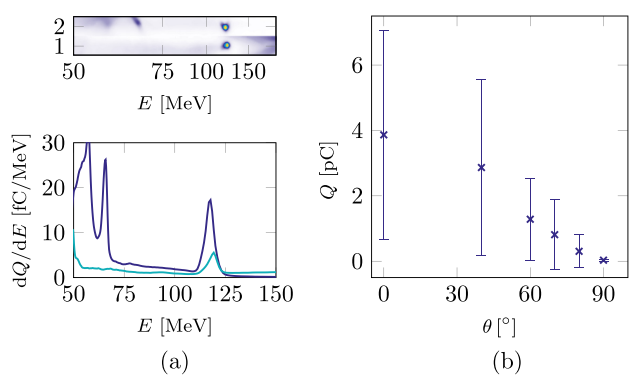

Fig. 2. (a) High quality beams of accelerated electrons, trapped by the collision of the two laser pulses in the plasma. The divergence (FWHM) of the beams is 3 mrad and the beams are quasi-monoenergetic at 120 MeV. The amount of detected charge is controlled by rotating the plane of polarization of the injection beam (b). The error bars mark the standard deviation of 10 shots. At θ=0°, the plane of polarization of the injection pulse is horizontal, which allows for maximum interference with the main pulse. At an angle θ=90° of the plane of polarization of the injection pulse, with respect to the horizontal plane, there is no interference of the two pulses and no trapped charge is observed at this angle.

Please cite this article as: M. Hansson, et al., Nuclear Instruments & Methods in Physics Research A (2016), http://dx.doi.org/10.1016/j.nima.2016.02.070

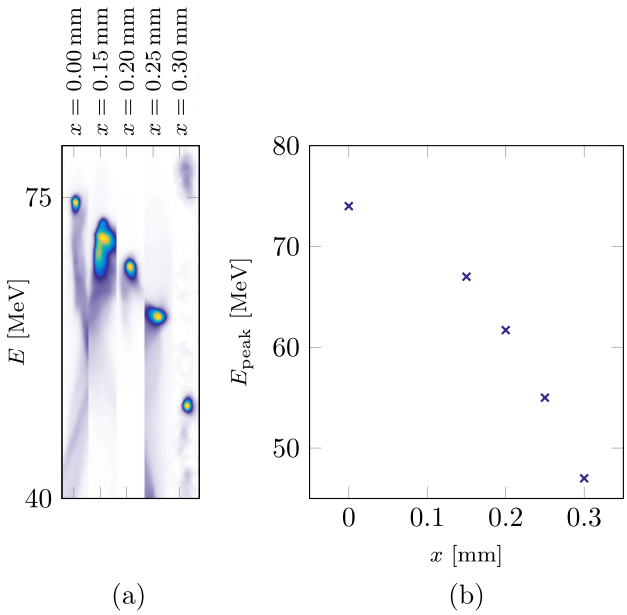

Fig. 3. The electron energy is controlled by varying the collision point in the plasma. (a) Images of the scintillating screen showing the dispersed electron beams for different collision points. (b) Corresponding peak electron energy plotted for selected points of collision. Each data point corresponds to a single shot. The peak energy decreases for collision points further back of the plasma.

focus of the main beam is expected to affect also the propagation of the main laser pulse in the plasma.

In Fig. 3(a), images of five dispersed electron beams are shown with for different collision points, x, relative to the center of the jet, tuned using method (II) of moving the gas jet. Correspondingly, the peak energy for these shots are plotted in Fig. 3(b) as a function of collision point, x. During this sequence, the $\lambda/2$ wave retarder is removed from the injection beam path and the plasma electron number density is set to 1.0×10^{19} cm^{-3}. Although the magnitude of the accelerating field is varying over during the full acceleration distance, the average, effective, accelerating field is estimated to 90 MV/mm from this figure.

4. Discussion

It is clear from the results that injection and trapping of electrons is triggered by the interaction between the two laser pulses. Furthermore, it is confirmed that the injection is triggered due to the interference between the fields of the two laser pulses, since no beams of accelerated electrons were observed with crossed polarization of the two pulses.

The experiment still suffers from large fluctuations in the resulting beams of accelerated electrons. These fluctuations most likely comes from scatter and drift of the pointing of the two beams, which was observed during the experiment on images of the scattered light from the two laser pulses as they propagate through the plasma. Although, the experimental results show that beams with low divergence and small energy spread can be achieved by this method, the experiment still suffers from large fluctuations.

5. Summary and outlook

We have demonstrated a compact set-up for the colliding pulse injection scheme for laser wakefield accelerators, by picking off part of the main laser pulse, close to the point of interaction, to trigger the injection. The colliding pulse injection scheme provides electron beams with excellent quality, regarding divergence and energy spread. The scheme also provides means to control both the electron energy and amount of charge in the beams of accelerated electrons.

Future experiments on the colliding pulse injection scheme are planned, aiming to decrease the shot-to-shot fluctuations of the beams of accelerated electrons.

Acknowledgments

We acknowledge the support of the Swedish Research Council (Grant agreement no. 2015-03749), the Knut and Alice Wallenberg Foundation (Grant agreement no. ICA10-0077), the Swedish Foundation for Strategic Research (Grant agreement no. 2014.0170), Laserlab-Europe/CHARPAC (Grant agreement no. 284464, EC's 7th Framework Programme) and EuCARD2/ANAC2 (Grant agreement no. 312453, EC's 7th Framework Programme).

References

[1] T. Tajima, J.M. Dawson, Physical Review Letters 43 (1979) 267.
[2] J. Faure, Y. Glinec, A. Pukhov, S. Kiselev, S. Gordienko, E. Lefebvre, J.-P. Rousseau, F. Burgy, V. Malka, Nature 431 (2004) 541.

Please cite this article as: M. Hansson, et al., Nuclear Instruments & Methods in Physics Research A (2016), http://dx.doi.org/10.1016/j.nima.2016.02.070

[3] C.G.R. Geddes, C. Toth, J. van Tilborg, E. Esarey, C.B. Schroeder, D. Bruhwiler, C. Nieter, J. Cary, W.P. Leemans, Nature 431 (2004) 538.
[4] S.P.D. Mangles, C.D. Murphy, Z. Najmudin, A.G.R. Thomas, J.L. Collier, A. E. Dangor, E.J. Divall, P.S. Foster, J.G. Gallacher, C.J. Hooker, D.A. Jaroszynski, A. J. Langley, W.B. Mori, P.A. Norreys, F.S. Tsung, R. Viskup, B.R. Walton, K. Krushelnick, Nature 431 (2004) 535.
[5] A.J. Gonsalves, K. Nakamura, C. Lin, D. Panasenko, S. Shiraishi, T. Sokollik, C. Benedetti, C.B. Schroeder, C.G.R. Geddes, J. van Tilborg, J. Osterhoff, E. Esarey, C. Toth, W.P. Leemans, Nature Physics 7 (2011) 862.
[6] G. Golovin, S. Chen, N. Powers, C. Liu, S. Banerjee, J. Zhang, M. Zeng, Z. Sheng, D. Umstadter, Physical Review Special Topics - Accelerators and Beams 18 (2015) 011301.
[7] M. Hansson, B. Aurand, X. Davoine, H. Ekerfelt, K. Svensson, A. Persson, C.-G. Wahlström, O. Lundh, Physical Review 18 (2015) 071303.
[8] M. Burza, A. Gonoskov, K. Svensson, F. Wojda, A. Persson, M. Hansson, G. Genoud, M. Marklund, C.-G. Wahlström, O. Lundh, Physical Review Special Topics - Accelerators and Beams 16 (2013) 011301.
[9] K. Schmid, A. Buck, C.M.S. Sears, J.M. Mikhailova, R. Tautz, D. Herrmann, M. Geissler, F. Krausz, L. Veisz, Physical Review Special Topics—Accelerators and Beams 13 (2010) 091301.
[10] C. McGuffey, A.G.R. Thomas, W. Schumaker, T. Matsuoka, V. Chvykov, F. J. Dollar, G. Kalintchenko, V. Yanovsky, A. Maksimchuk, K. Krushelnick, V. Y. Bychenkov, I.V. Glazyrin, A.V. Karpeev, Physical Review Letters 104 (2010) 025004.
[11] F.G. Desforges, B.S. Paradkar, M. Hansson, J. Ju, L. Senje, T.L. Audet, A. Persson, S. Dobosz-Dufrénoy, O. Lundh, G. Maynard, P. Monot, J.-L. Vay, C.-G. Wahlström, B. Cros, Physics of Plasmas 21 (2014) 120703.
[12] E. Esarey, R.F. Hubbard, W.P. Leemans, A. Ting, P. Sprangle, Physical Review Letters 79 (1997) 2682.
[13] G. Fubiani, E. Esarey, C.B. Schroeder, W.P. Leemans, Physical Review E 70 (2004) 016402.
[14] Z.-M. Sheng, K. Mima, Y. Sentoku, M.S. Jovanović, T. Taguchi, J. Zhang, J. Meyer-ter Vehn, Physical Review Letters 88 (2002) 055004.
[15] J. Faure, C. Rechatin, A. Norlin, A. Lifschitz, Y. Glinec, V. Malka, Nature 444 (2006) 737.
[16] C. Rechatin, J. Faure, A. Ben-Ismail, J. Lim, R. Fitour, A. Specka, H. Videau, A. Tafzi, F. Burgy, V. Malka, Physical Review Letters 102 (2009) 164801.
[17] O. Lundh, J. Lim, C. Rechatin, L. Ammoura, A. Ben-Ismail, X. Davoine, G. Gallot, J.-P. Goddet, E. Lefebvre, V. Malka, J. Faure, Nature Physics 7 (2011) 219.
[18] G.R. Plateau, N.H. Matlis, C.G.R. Geddes, A.J. Gonsalves, S. Shiraishi, C. Lin, R. A. van Mourik, W.P. Leemans, Review of Scientific Instruments 81 (2010) 033108.
[19] A. Buck, K. Zeil, A. Popp, K. Schmid, A. Jochmann, S.D. Kraft, B. Hidding, T. Kudyakov, C.M.S. Sears, L. Veisz, S. Karsch, J. Pawelke, R. Sauerbrey, T. Cowan, F. Krausz, U. Schramm, Review of Scientific Instruments 81 (2010) 033301.
[20] M. Hansson, L. Senje, A. Persson, O. Lundh, C.-G. Wahlström, F.G. Desforges, J. Ju, T.L. Audet, B. Cros, S. Dobosz Dufrénoy, P. Monot, Physical Review Special Topics - Accelerators and Beams 17 (2014) 031303.

Please cite this article as: M. Hansson, et al., Nuclear Instruments & Methods in Physics Research A (2016), http://dx.doi.org/10.1016/j.nima.2016.02.070

Paper XI

A setup for studies of laser-driven proton acceleration at the Lund Laser Centre

B. Aurand, M. Hansson, L. Senje, K. Svensson, A. Persson, D. Neely, O. Lundh, and C.-G. Wahlström.

Laser and Particle Beams **33**, 59 (2015).

Laser and Particle Beams (2015), *33*, 59–64.

doi:10.1017/S0263034614000779

A setup for studies of laser-driven proton acceleration at the Lund Laser Centre

B. AURAND,[1] M. HANSSON,[1] L. SENJE,[1] K. SVENSSON,[1] A. PERSSON,[1] D. NEELY,[2] O. LUNDH,[1] AND C.-G. WAHLSTRÖM[1]

[1]Department of Physics, Lund University, Lund, Sweden
[2]Central Laser Facility, STFC Rutherford Appleton Laboratory, Didcot, United Kingdom

(RECEIVED 8 September 2014; ACCEPTED 26 October 2014)

Abstract

We report on a setup for the investigation of proton acceleration in the regime of target normal sheath acceleration. The main interest here is to focus on stable laser beam parameters as well as a reliable target setup and diagnostics in order to do extensive and systematic studies on the acceleration mechanism. A motorized target alignment system in combination with large target mounts allows for up to 340 shots with high repetition rate without breaking the vacuum. This performance is used to conduct experiments with a split mirror setup exploring the effect of spatial and temporal separation between the pulses on the acceleration mechanism and on the resulting proton beam.

Keywords: Laser-ion acceleration; Mirror design; Radiation detectors

INTRODUCTION

Within the last decade, tremendous progress has been made in the field of laser ion acceleration. First demonstrated *Wilks et al.*, 2001 by the mechanism of target normal sheath acceleration (TNSA) nowadays provides a source for ultra-short proton bunches with energies up to several tens of MeV (Daido *et al.*, 2012; Passoni *et al.*, 2010). An ultra-intense laser pulse ($I > 10^{16}$ W/cm^2) which interacts with the front-side of a μm-thick target foil drives a massive electron current toward the rear-side of the target. The electrons exiting the target on the scale of the Debye-length create a charge separation field between them and the positively charged remaining bulk. This generates an electric field in the order of a few TV/m. In this field, which can be considered static on the timescale of a several 100's of fs up to a few ps (Schreiber *et al.*, 2006), protons and heavier ions like carbon or oxygen — mainly from the hydrocarbon contamination layer on the target — are accelerated.

Numerous studies on the mechanism of TNSA have been made so far, e.g., the investigation of the dependence on laser parameters like the focal spot size (Brenner *et al.*, 2011), energy (Coury *et al.*, 2012), or pulse duration (Robson *et al.*, 2007), studies on the electron current driven in the target (Tresca *et al.*, 2011; Coury *et al.*, 2013), or different target geometry (Schwoerer *et al.*, 2006; Ramakrishna *et al.*, 2010; Hegelich *et al.*, 2006; Burza *et al.*, 2011). In our current study on TNSA acceleration, we focus on the influence of two independent laser pulses with different temporal and spatial separation, interacting with the target and driving the acceleration. In this paper we describe the technical part of the setup, which includes laser and particle diagnostics as well as the target and optical probing system.

Address correspondence and reprint request to Bastian Aurand, Department of Physics, Lund University, 22100 Lund, Sweden.
E-mail: bastian.aurand@uni-duesseldorf.de

LASER SYSTEM

The Lund terawatt laser is a Ti:Sapphire based CPA (Strickland & Mourou, 1985) laser system with four amplification stages situated in the basement of the Physics Department at Lund university. A dedicated diagnostic table setup next to the compressor allows the verification of the laser beam parameters on a daily basis. The pulse duration is measured with a second order single-shot autocorrelator. A third order scanning autocorrelator (Amplitude, Sequoia®) is used to measure the laser contrast. Besides that, the spectrum (RGB, Qwave®) and the spectral phase (Avesta, SPIDER SP-120) are recorded. A mirror in the beam line with a designed leakage of 1.5% allows for on-shot recording of autocorrelation and laser spectrum. Typical pulse parameters are an energy $E_L = 0.9$ J at a pulse duration of $\tau_L = 35$ fs. The laser contrast is $0.5–1 \times 10^{-9}$ up to 50 ps before the main

pulse. A beam position system controls piezo mirrors in the amplifier chain and compensates for long term drifts which helps to keep laser parameters stable during operation.

A deformable mirror (DM) with a clear aperture of 65 mm, segmented in 32 piezo controlled areas (NightN Ltd., DM2-65-32) in the beam line enables corrections of the wavefront downstream. The 45 mm diameter beam is guided in vacuum and can be delivered into two different target areas by flipping one of the beam line mirrors. One of the target areas is mainly dedicated to laser wakefield acceleration (LWFA) (Desforges *et al.*, 2014; Hansson *et al.*, 2014) experiments, whereas the other target area mainly for proton experiments. The radiation shielding allows simultaneous experiments on electrons in one room and preparation of ion acceleration experiments in the other room. Both cylindrical experimental chambers with an inner diameter of 108 cm and a height of 37 cm are accessible by removing the lid or flanges on the side of the vacuum vessel. In the following, we will focus on the proton setup only (Fig. 1).

TARGET SYSTEM

Below the proton chamber is a housing containing an electrically insulated and Faraday-shielded xyz-linear stage system (Newport, GTS70). Using optical encoded position sensors and double-shielded cables, malfunction events due to electro-magnetic pulses do not occur. All stages have a travel range of 70 mm at a velocity of up to 50 mm/s with an on-axis accuracy of ±1μm and a bi-directional position reproducibility of 100 nm. The upper part of the target mount holds a three-point load, multi-purpose holder on which different kinds of self-centering targets can be mounted. Additional tip/tilt screws enable target adjustments perpendicular to the motion axis which is checked for every target with a micrometer caliper. Primarily used is an matrix target mount with 340 (17 × 20) independent target positions of 1 mm diameter and 2.5 mm separation (Fig. 2a). The mount consists of two comb shaped plates where a target foil can be clamped in between (Fig. 2b). Using an additional spacer, double layered target configurations or grids for proton imaging purposes can be realized.

The position of the target chamber center (TCC) which is the dedicated focus position is defined by the overlap of two external lasers beams, each referenced to the center of two opposed flanges on the chamber wall. This position is transferred to an alignment needle on the target mount and verified during major rebuilds. The target is aligned in the TCC using the laser focus diagnostic, observing the

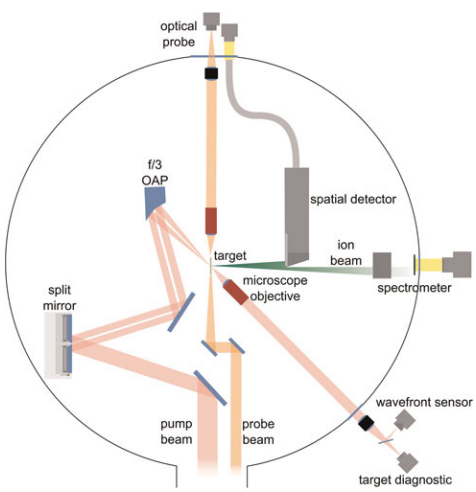

Fig. 1. Experimental setup for proton acceleration in the TNSA regime. The incident laser pulse is divided by a split-mirror into two beams which can be spatially and temporally shifted with respect to each other. Both beams are focused by the same OAP onto the target. The accelerated protons can be sent to a spectrometer for an energy measurement or a spatial detector in order to determine the beam profile. An independent optical probe can be used to do shadowgraphy or interferometry of the target rear surface.

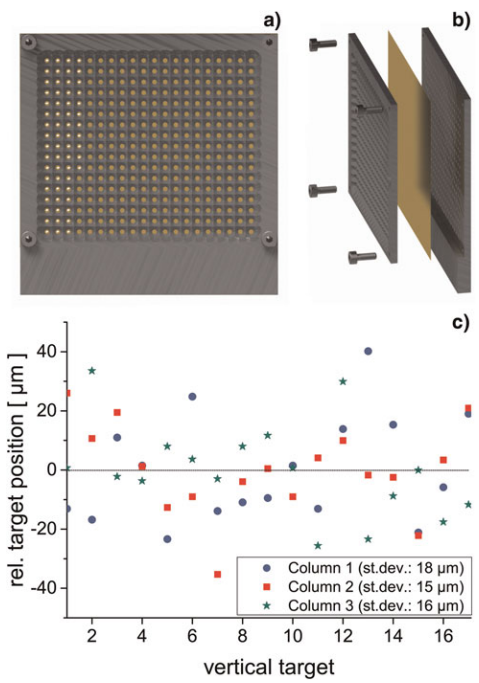

Fig. 2. (**a**) Matrix target mount with 340 (17 × 20) independent target positions. (**b**) The mount consists of two comb shaped plates in where the target foil is clamped in between (**c**) Scan of the relative focal position for a column wise vertical movement of a 3 μm Al foil. The standard deviation in each column is less than 18 μm.

reflection of a monochromatic light source from the target rear surface at an angle of 45°. This diagnostic is based on an infinity corrected 10× objective (Mitutoyo, Plan Apo NIR) with a working distance of 31 mm, imaging the laser focal plane onto a camera outside the vacuum vessel. Alternatively, for the laser alignment, the beam can be sent to a modified Hartmann sensor (Hartmann, 1900; Primot *et al*., 1995) (Phasics, SID4) to measure the wavefront. Note that within this setup using a DM, wavefront corrections for all optical elements up to the final focusing parabola can be included. The small depth of the focus diagnostic (4.1 μm) and the additional observation angle allow for a position accuracy of 2–3 μm with respect to the objective.

The typical procedure in order to take a series of shots is a columnwise pre-inspection of the target, regarding foil condition and possible wrinkles. This allows for a burst-mode of up to 17 shots within 1 min by moving the target vertically to the next position without any further inspection. Measurements of the focus position (Fig. 2c) for a pre-aligned target show a deviation of less than 18 μm, which is significantly smaller than the Rayleigh-length. This deviation is mainly given by imperfections during manufacturing of the target mount. The complete remote control of the target alignment enables a scan with a complete target in less than 1.5 h. Simultaneous monitoring and controlling of the laser parameters guarantee stable laser conditions. Further automated control of the target system, e.g., by target positioning via chromatic-confocal sensing (Ruprecht, A.K. *et al.* 2005) could increase the repetition rate and precision of the alignment.

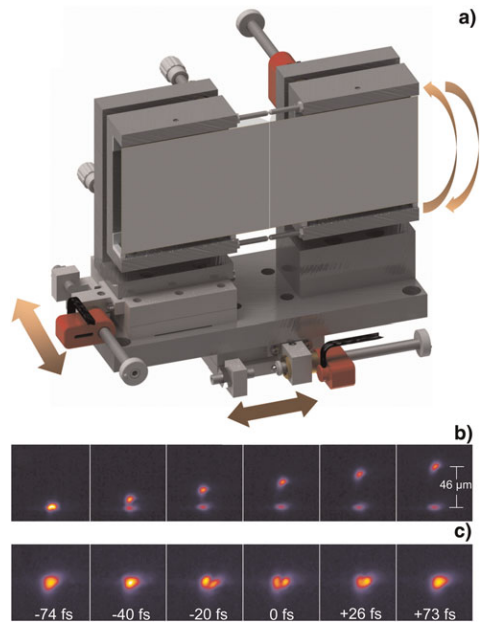

Fig. 3. (**a**) Split mirror setup generating two independent beams, which can be spatially and temporally shifted against each other. In addition the amount of energy in both parts can be changed. (**b**) Vertical focus separation by movement of one beam. (**c**) Interference structures are visible when the beams overlap within $\Delta t = \pm 20$ fs relative timing.

SPLIT MIRROR SETUP

Focusing of the laser is done by an off-axis parabolic mirror with 152 mm focal length (SORL, OAP 06-02-03/MMOA-3) giving a focal spot of 5 μm (FWHM) corresponding to a maximum intensity of 2×10^{19} W/cm^2 on the target and a measured Rayleigh-length of ($z_R \approx 50$ μm). One of the mirrors inside the experimental chamber consists of a specially designed split-mirror to generate two independent beams which can be spatially and temporally shifted with respect to each other (Fig. 3a). The setup is based on two protected silver mirrors sized 70×90 mm which have a thin edge to place them side by side, leaving a vertical gap of only a few tenths of a millimetre. Both mirrors are mounted separately and can be tilted horizontally and vertically using piezo-linear actuators (Newport, Picomotor). In addition, one of the mirrors is mounted on a linear stage allowing for a translation perpendicular to its surface. The introduced path difference of up to 20 mm in either direction at an incidence angle of ≈12° correspondes to a temporal delay of max. ±68 ps with respect to the fixed pulse. Finally, both mirrors can be moved sideways simultaneously to change the fraction of the incident beam on each mirror and therefore the energy ratio between the two pulses.

We deduce the minimal vertical movement of the beam in the focal plane to 150 nm/steps of the piezomotor tilting the mirror. In the given geometry, a vertical separation does not significantly change the length of each beam path, so it is not changing the relative timing between the two pulses. The bi-directional repeatability due to hysteresis effects in the mount is in the order of 5–6 μm. To avoid this effect, scans are always performed in one direction of movement (Fig. 3b).

The temporal overlap of the pulses is verified by the observation of an interference structure while both beams are spatially overlapped. The interference pattern is visible within a spatial range of 20 μm corresponding to ≈60 fs temporal range, showing a symmetric maximum (Fig. 3c). This method allows for a relative timing with a sub-pulse duration accuracy which is higher compared to methods like transverse probing of the generated plasma (Aurand *et al*., 2014).

Advantageous for all kinds of measurement series done with this setup are the common beam line and the focusing system downstream of the split-mirror, making the measurements insensitive to beam pointing fluctuations. Even if the absolute focus position of the system undergoes a small spatial jitter, the relative spatial and temporal separation of the beams remained fixed.

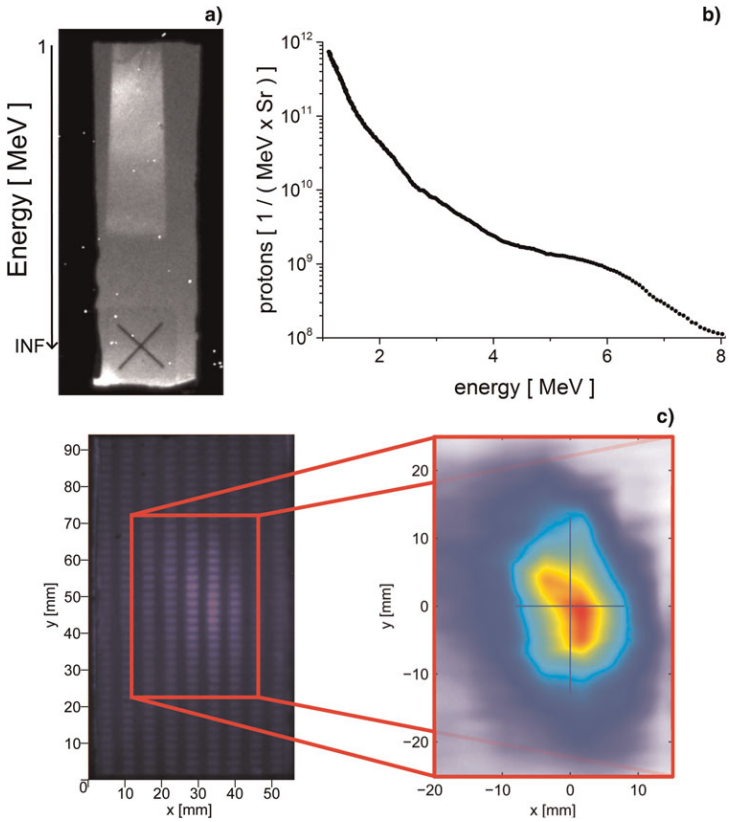

Fig. 4. Proton energy measurement from a 3 μm Al foil. (**a**) The raw data image obtained by the fluorescence of energy dispersed protons in a BC-408 scintillator in target normal direction. (**b**) Evaluated proton spectra using the calculated deflection curve and a cross calibration with CR-39 to get the absolute particle number. (**c**) Using the spatial detector, a beam profile of the accelerated particles can be taken. An Al filter grid in front of the detector allows for the subtraction of the electron background and a reconstruction of the proton beam profile.

ION DIAGNOSTIC

Ions are accelerated from the target rear surface. In order to be able to match the high repetition rate and the high number of shots per target, all diagnostics used in this setup have digital readouts.

The proton energy is determined by deflection of the proton beam in a magnetic field with an effective strength of $B_{Eff} = 0.69$ T and a length of 6 cm, which is situated in the target normal direction (47 ± 0.5) cm behind the target. A 1 mm horizontal entrance slit covers a solid angle of (8×10^{-5}) sr. Heavier ions are blocked by a 6 μm Al filter in front of the scintillator (St. Gobain, BC-408). The fluorescence signal is imaged by a 16-bit camera (Princeton, "PhotonMAX 1024")(Fig. 4a). To obtain the absolute particle number, a cross-calibration using a CR-39 trace detector was done (Cartwright *et al*., 1978) (Fig. 4b). The lowest detectable energy, determined by the setup geometry, is 1.2 MeV. The highest resolvable energy is ≈10 MeV.

The proton beam profile is measured by moving a scintillator (St. Gobain, BC-408) with a thickness of 500 μm into to the beam at a position of (65 ± 2) mm behind the target. The scintillator is placed in a light-shielded aluminum box with a 12 μm thick Al entrance window and an acceptance angle of 28°. The scintillator is imaged by an objective inside the box onto an optical fiber bundle, which transfers the signal out of the vacuum chamber onto a camera (Fig. 4c). Using a grid of Al bars with different thicknesses in front of the scintillator allows for an analytical subtraction of the electron background, superimposed with the signal, by taking the different stopping power for electrons and protons into account. In

contrast to a stack of radiochromic film (RCF), the energy selectivity of the scintillator is not very high. The signal is a superposition of all protons which are passing the filter and thus being transmitted or being stopped in the scintillator (d_{Scint} = 0.5 mm; 0.9 MeV ≤ E_{Stop} ≤ 7 MeV). In the future, a stack of scintillators with various thickness which are fluorescing at different wavelengths could be used to obtain an energy resolved signal (Green *et al*., 2011). Note that the response from a scintillator depends both on particle number and particle energy, which needs to be taken into account calculating absolute particle numbers (Green *et al*., 2011).

OPTICAL PROBE SETUP

A small amount (≈10 mJ) of the stretched pulse can be coupled from the last amplification stage of the laser system and sent to a separate pulse compressor. This part is compressed to roughly 60 fs and can optionally be frequency doubled ($\lambda_{2\omega}$= 400 nm). A specially designed curved target mount allows for probing along the target rear surface without being affected by the bright plasma on the front surface (Fig. 5a). A motorized linear stage with 150 mm travel enables controlled delay scans in a time window of up to 1 ns. The probe imaging system consists of a 20× infinity corrected objective (Mitutoyo, Plan Apo NIR) with a working distance of 20 mm. The image is collected by a camera outside the vacuum vessel. In this configuration, shadowgraphy can be obtained, with a resolution of 1 μm (Fig. 5b). By adding a Wollaston prism (Small *et al*., 1973) and two polarizers outside the chamber, Nomarski-interferometry can be done to determine the electron density (Fig. 5c).

OUTLOOK

The double pulse setup described above was developed and implemented within the last year and has been used for experiments. More than 4000 shots on targets have been conducted so far, investigating changes in particle-energy distribution and proton beam profile. Tentative results show a clear dependence of particle energy and proton beam divergence on the spatial separation of the two foci. A detailed analysis and comparison to numerical simulations is currently under investigation and will be reported accordingly.

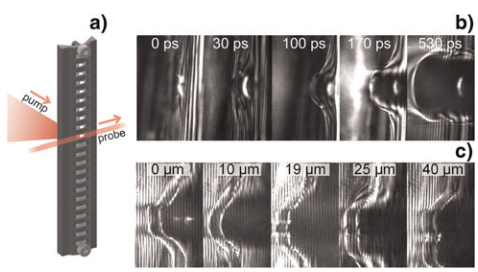

Fig. 5. (**a**) Curved target mount for transverse optical probing of the target rear surface. (**b**) High resolution shadowgraphy of an evolving plasma-plume, probed at different times compared to the pump-pulse. (**c**) Raw image by the Nomarski interferometric setup of two plasma-plumes for a fixed time but different separations, done by the split-mirror setup.

ACKNOWLEDGMENTS

We gratefully thank the Knut and Alice Wallenberg Foundation, the Swedish Research Council and the Swedish Foundation for Strategic Research for financial support. D. Neely acknowledges financial support by the UK Grant program: EP/K022415/1 (Advanced laser-ion acceleration strategies towards next generation healthcare).

REFERENCES

Aurand, B., Kuschel, S., Jäckel, O., Rödel, C., Zhao, H.Y., Herzer, S., Paz, A.E., Bierback, J., Polz, J., Elkin, B., Kamakar, A., Gibbon, P., Kaluza, M.C. & Kuehl, T. (2014). Enhanced radiation pressure-assisted acceleration by temporally tuned counter-propagating pulses. *Nucl. Inst. Meth. A* **740**, 033031.

Brenner, C.M., Green, J.S., Robinson, A.P.L., Carroll, D.C., Dromey, B., Foster, P.S., Kar, S., Li, Y.T., Markey, K., Spindloe, C., Streeter, M.J.V., Tolley, M., Wahlström, C.-G., Xu, M.H., Zepf, M., McKenna, P. & Neely, D. (2011). Dependence of laser accelerated protons on laser energy following the interaction of defocused, intense laser pulses with ultra-thin targets. *Lasers Part. Beams* **29**, 345–351.

Burza, M., Gonoskov, A., Genoud, G., Persson, A., Svensson, K., Quinn, M., McKenna, P., Marklund, M. & Wahlström, C.-G. (2011). Hollow microspheres as targets for staged laser-driven proton acceleration. *New J. Phys.* **13**, 013030.

Cartwright, B.G. & Shirk, E.K. (1978). A nuclear-track-recording polymer of unique sensitivity and resolution. *Nucl. Inst. Meth. A* **153**, 457–460.

Coury, M., Carroll, D.C., Robinson, A.P.L., Yuan, X.H., Brenner, C.M., Burza, M., Gray, R.J., Quinn, M.N., Lancaster, K.L., Li, Y.T., Lin, X.X., Tresca, O., Wahlström, C.-G., Neely, D. & McKenna, P. (2012). Influence of laser irradiated spot size on energetic electron injection and proton acceleration in foil targets. *Appl. Phys. Lett.* **100**, 074105.

Coury, M., Carroll, D.C., Robinson, A.P.L., Yuan, X.H., Brenner, C.M., Burza, M., Gray, R.J., Quinn, M.N., Lancaster, K.L., Li, Y.T., Lin, X.X., Tresca, O., Wahlström, C.-G., Neely, D. & McKenna, P. (2013). Injection and transport properties of fast electrons in ultra-intense laser-solid interactions. *Phys. Plasmas* **20**, 043104.

Daido, H., Nishiuchi, M. & S. Pirozhkov, S. (2012). Review of laser-driven ion sources and their applications. *Rep. Prog. Phys.* **75**, 056401.

Desforges, F.G., Hansson, M., Ju, J. Senje, L., Auder, T.L., Dobosz-Dufrenoy, S., Persson, A., Lundh, Wahlström, C.-G. & Cros, B. (2014). Reproducibility of electron beams from laser wakefield acceleration in capillary tubes. *Nucl. Instrum. Meth. A* **740**, 54–59.

Green, J., Borghesi, M., Brenner, C.M., Carroll, D.C., Dover, N.P., Foster, P.S., Gallegos, Pl., Green, S., Kirby, D., Kirkby, K.J., McKenna, P., Merchant, M.J., Najmudin, Z., Palmer, C.A.J., Parker, D., Prasad, R., Quinn, K.E., Rajeev,

P.P., Read, M.P., Romagnani, L., Schreiber, J., Streetse, M.J.V., Tresca, O., Wahlström, C.-G., Zeft, M. & Neely, D. (2011). Scintillator-based ion beam profiler for diagnosing laser-accelerated ion beams. *SPIE Proc.* **8079**, 807991.

Hansson, M., Senje, L., Persso, A., Lundh, O., Wahlström, C.-G., Desforges, F.G., Ju, J., Audet, T.L., Cros, B., Dobosz, S. & Monot, P. (2014). Enhanced stability of laser wakefield acceleration using dielectric capillary tubes. *Phys. Rev. ST AB* **17**, 031303.

Hartmann, J. (1900). Bemerkungenüber den Bau und die Justirung von Spektrographen. *Z. Instrumentenkunde* **20**, 17–27, 47–58.

Hegelich, B.M., Albright, B.J., Cobble, J., Flippo, K., Letzring, S., Paffett, M., Ruhl, H., Schreiber, J., Schulze, R.K. & Fernández, J.C. (2006). Laser acceleration of quasi-monoenergetic MeV ion beams. *Nat.* **439**, 441–444.

Passoni, M., Bertagna, L. & Zani, A. (2010). Target normal sheath acceleration: Theory, comparison with experiments and future perspectives. *New J. Phys.* **12**, 045012.

Primot, J. & Sogno, L. (1995). Achromatic three-wave (or more) lateral shearing interferometer. *Z. JOSA A* **12**, 2679–2685.

Ramakrishna, B., Murakami, M., Borghesi, M., Ehrentraut, L., Nickles, P.V., Schürer, M., Steinke, S., Psikal, J., Tikhonchuk, V. & Ter-Avetisyan, S. (2010). Laser-driven quasimonoenergetic proton burst from water spray target. *Phys. Plasmas* **17**, 083113.

Robson, L., Simpson, P.T., Clarke, R.J., Ledingham, K.W.D., Lindau, F., Lundh, O., McCanny, T., Mora, P., Neely, D., Wahlström, C.-G.,, Zepf, M. & McKenna, P. (2007). Scaling of proton acceleration driven by petawatt-laser plasma interactions. *Nat. Phys.* **3**, 58–62.

Ruprecht, A.K., Pruss, C., Tiziani, H.J., Wolfgan, O., Peter, L., Arndt, L., Mohr, J. & Lehmann, P. (2005). Confocal micro-optical distance sensor: Principle and design. *Z. SPIE Proc.* **5856**, 128–135.

Schreiber, J., Bell, F. Grüner, F., Schramm, U., Geissler, M., Schnüger, Ter-Avetisyan, S., Hegelich, B.M., Cobble, J., Brambrink, E., Fuchs, J., Auderbert, P. & Habs, D. (2006). Analytical model for ion acceleration by high-intensity laser pulses. *Phys. Rev. ST AB* **97**, 045005.

Schwoerer, H., Pfotenhauer, S. Jäckel, O., Amthor, K.-U., Liesfeld, B., Ziegler, W., Sauerbrey, R., Ledingham, K.W.D. & Esirkepov, T. (2006). Laser-plasma acceleration of quasi-monoenergetic protons from microstructured targets. *Nat.* **439**, 445–448.

Small, R.D., Sernas, V.A. & Page, R.H. (1972). Single beam Schlieren interferometer using a Wollaston prism. *Appl. Opt.* **11**, 858–862.

Strickland, D. & Mourou, G. (1985). Compression of amplified chirped optical pulses. *Opt. Commun.* **56**, 219–221.

Tresca, O., Carroll, D.C., Yuan, X.H., Aurand, B., Bagnoud, V., Brenner, C.M., Coury, M., Fils, J., Gray, R.J., Kühl, T., Li, C., Li, Y.T., Lin, X.X., Quinn, M.N., Evans, R.G., Zielbauer, B., Roth, M., Neely, D. & McKenna, P. (2011). Controlling the properties of ultra-intense laser proton sources using transverse refluxing of hot electrons in shaped mass-limited targets. *Plasma Phys. Contr. Fusion* **53**, 105008 .

Wilks, S.C., Langon, A.B., Cowan, T.E., Roth, M., Singh, M., Hatchett, S., Key, M.H., Pennington, D., MacKinnon, A. & Snaverly, R.A. (2001). Energetic proton generation in ultra-intense laser solid interactions. *Phys. Plasmas* **8**, 542–549.

Paper XII

Manipulation of the spatial distribution of laser-accelerated proton beams by varying the laser intensity distribution

B. Aurand, L. Senje, K. Svensson, M. Hansson, A. Higginson, A. Gonoskov, M. Marklund, A. Persson, O. Lundh, D. Neely, P. McKenna, and C.-G. Wahlström.

Physics of Plasmas **23**, 023113 (2016).

PHYSICS OF PLASMAS 23, 023113 (2016)

Manipulation of the spatial distribution of laser-accelerated proton beams by varying the laser intensity distribution

B. Aurand,[1,2,a] L. Senje,[1] K. Svensson,[1] M. Hansson,[1] A. Higginson,[3] A. Gonoskov,[4] M. Marklund,[4] A. Persson,[1] O. Lundh,[1] D. Neely,[5] P. McKenna,[3] and C.-G. Wahlström[1]
[1]*Department of Physics, Lund University, P.O. Box 118, 22100 Lund, Sweden*
[2]*Institut für Laser- und Plasmaphysik, Heinrich-Heine Universität, 40225 Düsseldorf, Germany*
[3]*SUPA Department of Physics, University of Strathclyde, Glasgow G4 0NG, United Kingdom*
[4]*Department of Applied Physics, Chalmers University of Technology, 41296 Gothenburg, Sweden*
[5]*Central Laser Facility, STFC, Rutherford Appleton Laboratory, OX11 0QX Didcot, United Kingdom*

(Received 25 October 2015; accepted 20 January 2016; published online 18 February 2016)

We report on a study of the spatial profile of proton beams produced through target normal sheath acceleration using flat target foils and changing the laser intensity distribution on the target front surface. This is done by either defocusing a single laser pulse or by using a split-pulse setup and irradiating the target with two identical laser pulses with variable spatial separation. The resulting proton beam profile and the energy spectrum are recorded as functions of the focal spot size of the single laser pulse and of the separation between the two pulses. A shaping of the resulting proton beam profile, related to both an increase in flux of low-energy protons in the target normal direction and a decrease in their divergence, in one or two dimensions, is observed. The results are explained by simple modelling of rear surface sheath field expansion, ionization, and projection of the resulting proton beam.
[http://dx.doi.org/10.1063/1.4942032]

I. INTRODUCTION

More than a decade ago, first experimental results[1,2] showed the possibility to accelerate protons to tens of MeV kinetic energy over a sub-mm length by using ultra-intense laser pulses irradiating the front side of μm-thick metal foils. The laser pulse forms a megaampere electron current inside the target penetrating through the rear surface and expanding into vacuum, leading to a charge separation on the scale of the Debye length. In the resulting electric field—which is of the order of up to a few TV/m—protons, mainly from the hydrocarbon contamination layer on the target rear surface, are quickly accelerated to high energies.[3,4]

This process, the target-normal-sheath-acceleration (TNSA) mechanism,[5] creates a continuous, Boltzmann-like, energy distribution up to a cut-off energy, which has attracted considerable interest, partly from a fundamental plasma physics point of view and partly because of its great potential for novel applications. It represents a very compact source of energetic ions. The pulse duration, at the source, is short, and the transverse emittance is very low.[6–8] Potential applications in medicine, material science, accelerator physics, and industry, for example, have been widely discussed.[3,9] However, in order to become a useful source for applications, a number of parameters must be greatly improved. For example, the shot-to-shot stability, the maximum proton energies, and the laser-to-proton energy conversion efficiencies must be increased. At the same time, the beam divergence should be reduced. In addition, for many applications, the proton energy distributions must be reduced, and ideally, a narrow energy spread achieved. All these improvements require further experimental and theoretical studies and enhanced understanding of the fundamental processes involved.

In typical TNSA experiments, using a flat metallic target foil irradiated on the front surface by a tightly focused laser pulse, the beam of protons leaves the target's rear surface centred along the target's normal (TN) direction. The maximum proton energy, E_{Prot}, within the beam depends on the peak laser intensity I_{L} and, thus, for a given laser pulse duration, both on the pulse energy and the irradiated spot size on the target. Brenner *et al.*[10] show that increasing I_{L} by increasing the pulse energy has a significantly larger influence on the total flux of protons than the same increase in intensity obtained by reducing the laser spot size. Xu *et al.*[11] and Green *et al.*[12] show that, with constant laser pulse energy and pulse duration, the total flux of protons can be increased by defocusing the laser at the target, even though the peak laser intensity is decreased. The proton beam divergence depends on the laser parameters and on the proton energies; the most energetic protons exhibit the smallest divergence.[13] Schollmeier *et al.*[14] used micro-structured target foils as a tool to demonstrate the effect of defocusing the laser beam on the generated proton beam. Several more studies have been reported in the literature regarding the proton beam divergence and laminarity[15] and how they can be manipulated, e.g., via the use of curved targets.[16,17] In this paper, we report on experimental studies of how the angular/spatial distribution of the proton beams can be manipulated without changing the target shape or composition, and instead by varying spatially the laser intensity distribution on the target's front surface. We keep the target and laser parameters fixed and vary the intensity distribution while monitoring the

[a]Electronic mail: Bastian.Aurand@uni-duesseldorf.de

spatial proton beam profile. In recent studies, it was shown that by using a fixed, hollow, doughnut-like laser beam profile, the beam divergence, and energy profile could be manipulated.[18] Here, we vary the intensity distribution either by defocusing the laser on the target or by dividing the focused laser pulse into two spatially separated pulses, with a separation that can be continuously varied. In the first case, we find that the proton beam divergence can be significantly reduced by optimally defocusing the laser pulse, and in the second case that, with optimized separation between the two foci, the proton beam divergence is reduced in the direction of the separation of the foci, resulting in an elliptically shaped proton beam. These collimation effects, in one or two dimensions, are found to be mainly affecting the relatively large number of low energy protons. The number of low energy protons in the target's normal direction increases while their divergence decreases, resulting in intense beams of low-energy protons, collimated in one or two dimensions.

II. EXPERIMENTAL SETUP AND METHODS

The experiments were carried out using the Lund 10 Hz multi-terawatt laser system; a chirped-pulse amplification (CPA) based Ti:sapphire laser with a pulse duration of 35 fs and a temporal contrast better than 1×10^{-9} 50 ps before the main pulse. In the experiments presented here, the energy per pulse, on target, was kept fixed at 0.6 J. The experimental setup[19] is shown in Fig. 1(a). After compression, the 45 mm diameter beam was guided into the interaction chamber and sent onto a split-mirror setup (Figure 1(b)) before reaching an off-axis parabolic (OAP) focusing mirror. For the first part of the investigation, the split-mirror setup was positioned in a way that the full laser beam was reflected on one of the mirrors, and thus, only one focal spot was produced. Instead, the target foil was moved to different positions along the optical axis around the beam waist. For the second part of the investigation, the split-mirror setup was positioned such that each laser pulse was divided into two halves, resulting in two identical focused laser pulses hitting the target foil. The foil was then positioned in the focal plane of the focusing mirror while the separation between the two foci was varied between shots.

The split-mirror setup consists of two planes, protected silver mirrors of standard optical quality ($\lambda/10$ flatness). They have a vertically oriented wedged shaped edge in order to enable the mirrors to be mounted very close to each other, with a gap of only a few tenths of a millimetre, but with the possibility to move freely relative to each other. Due to a separate mounting, the mirrors can be tilted independently in vertical and horizontal directions. In addition, one of the mirrors is mounted on a linear translation stage, which moves the mirror perpendicular to its surface, enabling the relative optical path length and therefore the relative timing of the pulses to be accurately controlled. The complete split-mirror setup is further mounted on another linear translation stage moving it transversely with respect to the laser beam. This enables the split ratio of the pulses to be varied. Both beams are sent onto the same off-axis parabolic mirror, with 152 mm focal length and focused to a circular spot with radius $r_L = 2.5\ \mu$m (HWHM) reaching a peak intensity of $I_L = 2 \times 10^{19}$ W/cm^2.

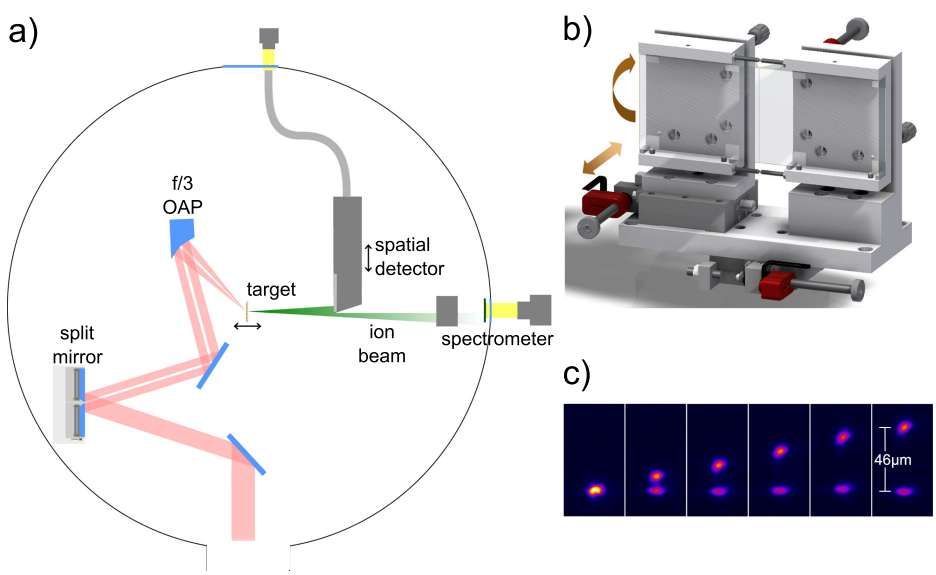

FIG. 1. (a) Experimental setup: The laser beam is guided onto the split-mirror and separated into two parts which are focused by an f/3 parabolic mirror onto the target. For diagnostics, either a spectrometer, consisting of a dipole magnetic field, a scintillator, and a camera, or a spatial detector to image the beam profile is used. (b) The split-mirror consists of two independently adjustable rectangular mirrors with a gap of a few tenths of a millimetre in between. (c) By tilting one of the mirrors, the spatial separation of the beams and the resulting foci can be varied.

Applying angular tilts in one direction to one of the mirrors, the two foci can be separated in that direction of the focal plane (Figure 1(c)). Note that this tilt is induced more than 1 m upstream of the interaction point and is in the order of some μ-rad. Neither a significant pulse front tilt nor a significant relative temporal difference between the beams is induced. By use of a deformable mirror in the beam line, the phase was corrected to ensure a good quality of the focus in the overlapped case. The slight horizontal elongation of the beam, which can be seen in Figure 1(c), is independent of the tilt direction. Fine adjustment of the temporal overlap can be done by adjustments of the relative path length while monitoring the interference patterns occurring in the focal plane when the foci have a spatial overlap. In the studies reported here, the splitting ratio was fixed at either 100:0 or 50:50, and the relative time delay $\Delta t = 0$.

As a target, we used 3 μm-thick Al foils mounted in a matrix target holder realizing 340 independent targets and where each new target can be aligned within a few seconds, with an accuracy of better than 18 μm (standard deviation) with respect to the laser focus position. The target is mounted at 45°, horizontally tilted, with respect to the laser axis.

In order to take advantage of the high repetition rate of the laser and the fast target alignment procedure, only online proton diagnostics were used. A magnetic-field based proton spectrometer disperses the protons, after passing through a 1 mm entrance pinhole, depending on their energy onto a scintillator (St. Gobain: BC-408; 500 μm thick), wrapped in a 12 μm thick aluminum foil to block heavy ions, which is monitored by a 16-bit camera (Princeton: PhotonMAX1024). The proton signal is collected in the target's normal direction covering a solid angle of 8×10^{-5} sr, and the energy uncertainty due to the pinhole size is $\Delta E/E \approx 10\%$. In addition, a spatial detector is used to monitor the spatial-intensity distribution of the proton beam.[20] A scintillator (St. Gobain: BC-408; 500 μm thick) is positioned (65 ± 2) mm behind the target in a light shielded box with a 12 μm thick and light tight Al entrance window. The scintillator emission is imaged onto an optical fibre bundle, which allows for the image to be transferred onto a 12-bit CCD camera placed outside the vacuum chamber. This enables a reconstruction of the two-dimensional proton beam spatial profile. With this detector setup, the signal is not energy selective, but represents a superposition of all protons, which are stopped in the scintillator (0.9 MeV $< E_{\mathrm{Stop}} <$ 7 MeV). We typically investigate protons with maximum kinetic energies of $E \leq 6$ MeV, so most protons are stopped in the scintillator. The signal from the detector is thus not representing the number of protons, but rather the deposited energy. By adding additional bars of aluminum with different thicknesses in front of the detector allowed us to distinguish between electrons and protons in the detector, which was used to calibrate the device.

III. EXPERIMENTAL RESULTS

A. Defocus scan with a single laser focus

When we use only one laser focus and move the target foil along the laser propagation axis, i.e., through the focus, we find, as expected, that the highest proton energy is obtained with the target at best focus ($r_{0\mu m} \approx 2.5\,\mu$m), where the peak intensity is the highest. The proton beam is then centered along the TN direction, and the profile, integrating over all protons with $E > 0.9$ MeV, is spatially round and smooth. However, the divergence dramatically decreases when the target foil is positioned at ±375 μm ($r_{375\mu m} \approx 8.5\,\mu$m) or at ±450 μm ($r_{450\mu m} \approx 10.5\,\mu$m) from best focus (see Figure 2(a)). This corresponds to approximately three to four Rayleigh lengths, and the peak laser intensity is reduced by roughly one order of magnitude. The laser beam profile was carefully investigated in order to ensure a homogeneous distribution of energy over the enlarged irradiated spot. The small difference in the intensity of the proton beam distribution. which can be seen in Figure 2(a) for target positions before and behind the focus, is not systematically different for the full measurement campaign, but they differ systematically within one measurement run with the same laser alignment. This might result mainly from the fact that a laser beam profile for a real laser is not only perfectly Gaussian but also to a smaller extent that a real focussing element is not perfectly parabolic. In this case, it can be shown by ray-tracing that there are small differences in local divergence and intensities on small scales within the beam profile.

The observed decrease in the proton beam divergence is not due to the decrease in the laser intensity, which is easily verified by reducing the laser energy with the target at a best

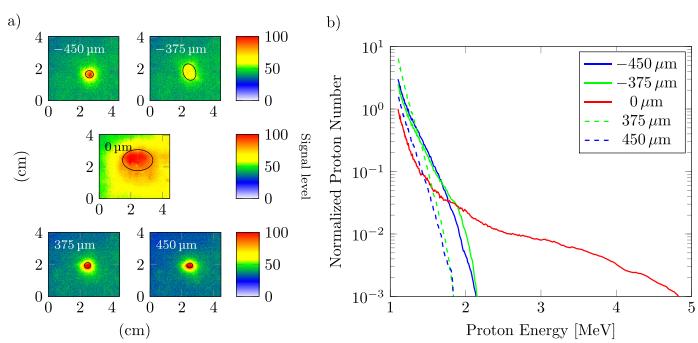

FIG. 2. (a) The proton beam profile for five representative shots measured with the spatial detector for the target foil positioned at best focus (middle) ($r_{0\mu m} \approx 2.5\,\mu$m), 375 μm ($r_{375\mu m} \approx 8.5\,\mu$m), and 450 μm ($r_{450\mu m} \approx 10.5\,\mu$m) before and after the focus (upper/lower). In the defocused case, the proton beam is collimated compared to best focus. The corresponding proton energy distribution in the TN direction is shown in (b).

focus. Instead, it represents a significant relative increase in the number of low energy protons propagating close to the TN direction. The overall lower proton energy results from the de-focusing and therefore the reduced sheath field strength.

Figure 2(b) shows the proton energy distribution observed in the TN direction with the target both at the best focus and defocused by 375 μm. This shows the significant relative increase in the number of low energy protons and a corresponding decrease in protons with the highest energies. This resembles the finding in Ref. 11, but here, it is evident that the increase in low-energy protons in the TN direction is partly due to a reduction in divergence of these protons. Defocusing the laser pulse thus leads to reduced divergence and a significantly increased relative flux of low energy protons in the centre of the beam, even though the maximum proton energy is reduced. Using different aluminum filters in front of the spatial detector reveals as well the finding that in the defocused case, the energy of the protons in the center of the beam decreases, while their particle number increases.

B. Two foci of equal intensity and variable separation with the target foil at the best focus

Using similar measurement methods compared to the previous paragraph, we find as expected that the highest proton energy is obtained with zero separation, i.e., when the two foci overlap and give rise to the highest peak intensity on target. The spatial beam profile is then round in the TN direction, and with the highest energy protons having the smallest divergence, consistent with several previous reports.[2,21,22] When separating the two foci in one direction, we find that the proton beam shape changes from circular to elliptical, with the minor axis in the direction of separation. When the separation is increased further, the proton beam profile becomes round again (see Figure 3(a)). Since this effect occurs both for horizontal and vertical tilt, it is concluded that it is not due to the incidence angle between the laser and target, e.g., caused by an elongated beam profile due to the projection on the target surface. The degree of ellipticity, defined as the ratio between the major and the minor axis of an ellipse fitted to 80% level in each proton dose distribution, is shown in Figure 3(a) for different separation of the foci. When placing a filter in front of the spatial detector, stopping protons with energy below 1.7 MeV, we find that the elliptical shape disappears and we are left with a significantly weaker but circular proton beam, for all values of foci separation.

This observation is similar to the case of defocusing as discussed above, where we observed a collimation in two dimensions of low energy protons when defocusing the laser on the target foil. Here, we also find a collimation of low energy protons, but now only in one direction. This is further verified by measuring the proton energy distribution in the TN direction, as a function of separation between the two foci. Figure 3(b) shows two plots of the proton energy distribution in the TN direction with the two foci separated at 9 μm and 30 μm divided by the distribution obtained with the two overlapping foci. The inset shows the original signal. These plots show the significant increase in the number of low energy protons obtained with the optimum separation, accompanied by a relative decrease in protons with the highest energies. With large separation (30 μm) between the two foci, two independent proton sources are obtained, with the

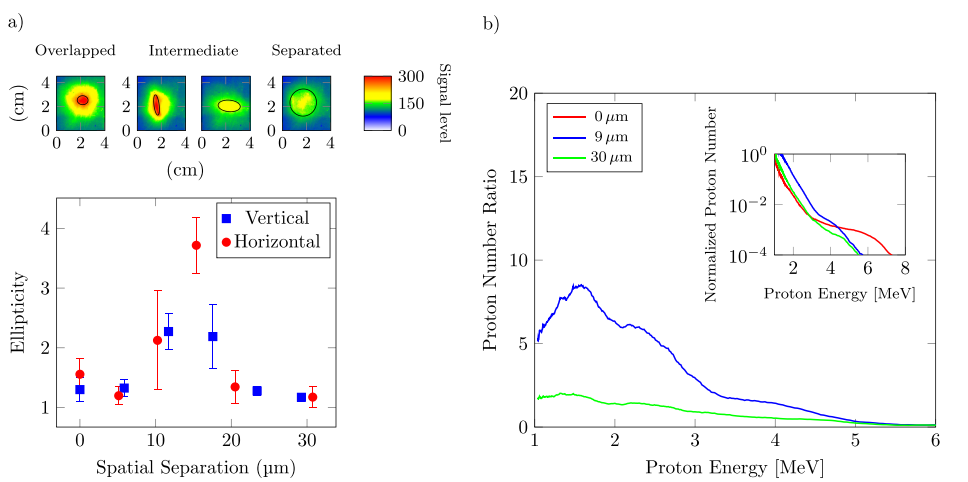

FIG. 3. (a) The upper figures show the measured proton beam profile for the case of two foci being overlapped or separated (horizontally or vertically). For an intermediate separation of ~3 focus diameters, the resulting beam profile becomes elliptical. Overlapping or separating the foci further results in a circular shaped profile. Calculating the ellipticity from the beam profile for different spatial separations in horizontal and vertical direction illustrates the change in the beam profile. (b) The inset shows the proton energy distribution in the forward direction for three different separations between the two focal spots. The large plot gives the energy distribution measured for the different separations divided by the corresponding distribution obtained in the case that both foci overlap (red curve 0 μm separation). For a separation of 9 μm, the number of low energy protons is increased.

same reduction in the maximum energy as for the optimum separation, but without the enhancement in proton flux at low energies. These graphs show that the elliptical shape observed with the spatial detector actually represents a collimation effect, with an increase in proton number in TN direction, and that this collimation mainly affects the low energy protons.

IV. MODELLING

A numerical model was developed to investigate how the size of the laser focus and the separation of the laser foci in the case of two beams may be expected to influence the resulting proton beam distribution. The model (an earlier version of which is described in Ref. 23) calculates how the evolving fast electron density distribution on a grid corresponding to the target rear surface maps into the beam of protons accelerated by TNSA. Fast electrons produced at the target front side in a given laser focus are assumed to be ballistically transported through the target in a beam with a fixed divergence angle. Transport phenomena such as collisions and self-generated fields are not accounted for, but are expected to have a limited effect in relatively thin targets.[24] Recirculation or refluxing of fast electrons within the foil is also neglected. It was validated in simulations that refluxing for a 35 fs-duration laser pulse will occur essentially only for target thicknesses of more than 3 μm. The rear-surface fast electron sheath dynamics, field-ionization of hydrogen, and the direction of projection of the resulting protons are calculated. Unlike more computationally intensive 3D Particle-in-Cell (PIC) modelling, this simpler approach enables a range of parametric scans to be performed relatively quickly, to explore the expected changes to the proton beam profile.

The initial diameter of the fast electron distribution at the target rear side, arising from a laser focal spot of radius r_L at the front side, is given by $d_e = 2(r_L + D\tan\theta_{1/2})$, where $\theta_{1/2}$ is the divergence half-angle of the electron beam as it propagates within the target of thickness D. The sheath profile due to the single laser focus is assumed to be parabolic.[24] In the case of two laser foci, two fast electron distributions are generated at the target rear, with the degree of overlap depending on the separation of the laser foci and the magnitude of $\theta_{1/2}$. In the calculations below, $D = 3\,\mu$m and $\theta_{1/2}$ is set to 30°. The target rear surface is defined as a spatial grid of 80×80 cells of 0.025 μm size, centred at $X = Y = 0$. Electrons arrive over the duration of the laser pulse, which is set equal to 35 fs. The magnitude of the sheath field increases with the increase in the fast electron number density over the first half (rising edge) of the laser pulse and thereafter decreases with time due to lateral expansion of the electron population. The maximum field strength is calculated (assuming a sharp boundary) as $E_{max} = E_0\sqrt{2/e_N}$, where e_N is Euler's number (2.7183), $E_0 = \sqrt{n_{e0}k_BT_e/\epsilon_0}$, ϵ_0 is the vacuum permittivity, and T_e and n_{e0} are the fast electron temperature and maximum density, respectively (as derived in Ref. 25). The fast electron temperature is determined from ponderomotive scaling.[26] The number of fast electrons generated, and thus the fast electron density, is calculated assuming a laser pulse energy of 0.6 J and a laser-to-fast electron energy conversion efficiency of 20%. The conversion efficiency is fixed at this value in the intensity range explored in this study, based on measurements reported in Ref. 27. The initial transverse sheath expansion velocity is set equal to 0.7c (as determined from a previous experiment[8] and simulations[28]), and it decreases exponentially with a 1/e time constant of 60 fs. The rate of reduction in the transverse expansion velocity is based on time- and space-resolved interferometry measurements of a probe beam reported in Ref. 8, scaled to the shorter laser pulse used in the present work. The sheath evolution is calculated in 0.8 fs steps.

Free protons are released by field ionization of a uniform layer of hydrogen, as calculated using the Ammosov-Delon-Krainov (ADK) rate[29] at each time step. Changes in the proton front due to the evolving electric field are calculated, and the local gradient to this front is used to determine the projection of the resulting beam of protons. The detector plane is defined by a 3 cm × 3 cm spatial grid with a resolution equal to 100 μm and is set 6.5 cm from target, to match the experimental conditions. The 2D proton beam spatial-intensity distributions calculated after 200 fs are compared with the measurements.

A. Defocusing

The simulations show that as the laser pulse is defocused, the maximum kinetic energy in the proton beam is reduced, but the number of low-energy protons increases. In addition, more gradual gradients in the sheath field lead to a reduction in the beam divergence. The result is therefore, at the optimum amount of defocusing, a narrow and intense beam of low energy protons. This is illustrated in Figure 4. Further defocusing reduces the laser intensity too much, and the proton beam quickly reduces in brightness. In the simulation, the proton distribution can be analyzed separately for different proton energies. When this is done, it is found that the observed intense and narrow beam is due to protons with kinetic energy less than 70% of the maximum energy obtained at best focus. This is in agreement with the experimental finding.

B. Two spatially separated foci

For the purposes of modelling the case of the two spatially separated foci, it is assumed that the fast electron population produced by each laser spot passes through the thin foil without interaction with the other and emerges at the rear side. The electron density at the rear surface is summed in regions of overlap, which enhances the sheath field. The results of these simulations show that as the spot separation is increased, the proton beam becomes elliptical, with the minor axis in the direction parallel to the separation direction (Figure 5). The maximum degree of ellipticity is obtained when the separation is ~3 focal spot diameters. As the separation is further increased, the two spots each give rise to independent circular proton beams. The spatial separation of these is not noticeable in the far-field detection plane, where a single round proton distribution is therefore observed. These simulation results are in excellent agreement with the experimental finding. In the simulation, the proton distribution can be analyzed separately for different proton energies. When this is done, it is found that the observed ellipticity is

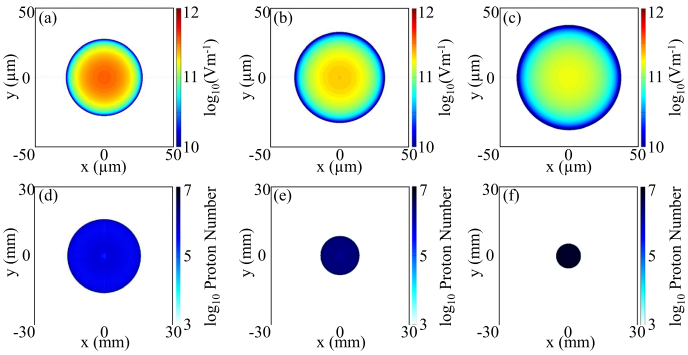

FIG. 4. Simulation results showing the electrostatic sheath field distribution after 200 fs for: (a) $r_L = 5\,\mu$m, (b) $r_L = 10\,\mu$m, and (c) $r_L = 15\,\mu$m. The corresponding proton beam profiles, integrated over the full proton energy range, are shown in (d)–(f), respectively. In the defocused case, the sheath field is larger and weaker, resulting in a proton beam with smaller divergence.

due to protons with kinetic energy less than 70% of the maximum energy. Analyzing only the high energy range of the proton energy distribution, circular beam profiles are found independently of spot separation. This is also in agreement with the experimental findings.

V. CONCLUSION

This article addresses the influence of defocusing and focus shaping of the laser pulse on the generated proton beam profile and the proton energy distribution. Defocusing a single laser beam by a few Rayleigh lengths on the target front surface results in a spatially larger electron distribution directed towards the target rear surface, which has a lower average energy due to the lower initial laser intensity. As a result, the created sheath field on the rear surface covers a larger area, resulting in a larger proton source size, but is weaker than in the case of a focused laser beam. The secondary accelerated beam of protons is more collimated, due to the larger electron distribution at the target rear side leading to a lesser electrostatic sheath field gradient, and therefore more directed electric field distribution. At the same time, the proton flux is increased due to the larger source size of protons being accelerated. This however results in a reduction of the electric field strength, leading to an overall lower proton energy.

By using two laser beams, to create two foci separated by a few laser spot diameters, we could transfer this effect of beam-shaping to a tool in order to generate a customized proton beam of high flux in one direction. In that case, the superposition of the shape of the two foci as well as the resulting electron distribution driven through the target forms an expanded sheath field in one direction at the target rear surface. The beam of accelerated protons is produced with a lower divergence in only one direction. We demonstrated that for our experimental parameters, this effect occurs for a focal spot separation between the two foci of approximately three focal spot diameters. A larger beam separation results in two independent proton sources,[30] each

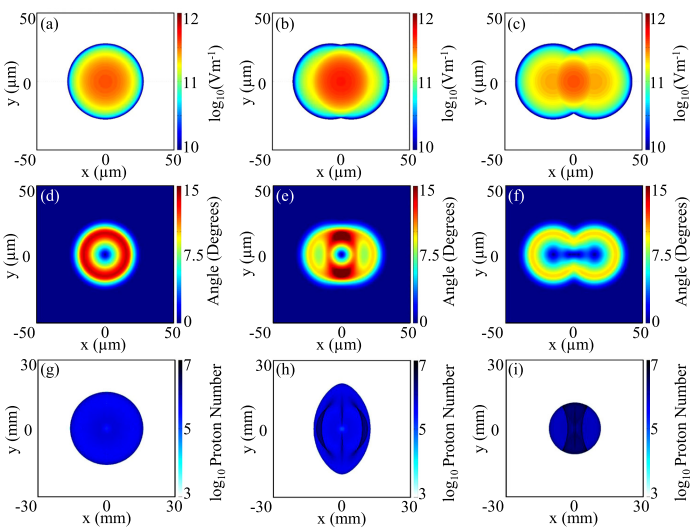

FIG. 5. Simulation results showing the electrostatic sheath field distribution after 200 fs for focal spot separation equal to: (a) 0 μm, (b) 15 μm, and (c) 30 μm. The corresponding angular proton distributions at the target surface are shown in (d)–(f), respectively, and the resulting proton beam distributions in the detector plane are shown in (g)–(i), respectively. At an optimum foci separation, corresponding to case (b), the divergence in the x-direction is significantly reduced.

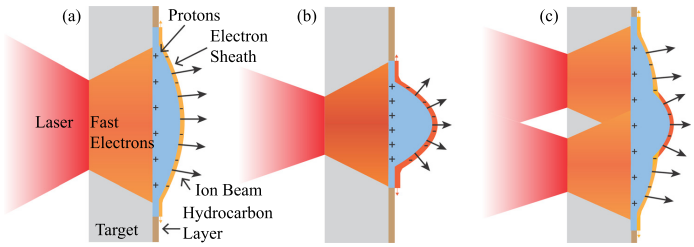

FIG. 6. Schematic illustration of the sheath fields formed by (a) a single defocused laser pulse; (b) two overlapped laser foci; and (c) two laser foci at a separation close to optimum to modify the sheath profile.

with high divergence but relative low energy. A smaller separation results in one proton source with high divergence and high energy, due to the addition of both laser beams. Figure 6 illustrates schematically the sheath expansion in three of the cases investigated experimentally. These results obtained by laser beam splitting presents an indirect measurement of the sheath field size, which was estimated to be in the order of 20 μm. This is in agreement with the results obtained in Ref. 31 using a laser system with a similar pulse duration as in our study, i.e., a few tens of femtoseconds. For longer laser pulse durations, where the electrons can be accelerated and recirculated within the target during the pulse duration, the sheath field becomes larger, as, e.g., obtained in Refs. 32 and 33.

In summary, the proton beam can be shaped by this effect, increasing the proton flux for the low energy proton part. The cost of this effect is a reduction in the maximum proton energy. For distinct applications which do not need high proton energies but a high proton flux with a shaped beam profile (e.g., proton beam writing[34] or radioisotope production[35]), this method might be sufficient to at least preform the beam profile before using collimators to create the desired shape. This enhances the process efficiency and reduces the number of protons which need to be dumped away creating unnecessary activation or radiation at the collimator. Using this technique on high energy lasers could be a scheme to accelerate protons as a fast ignition driver. Here, as well primarily a high proton flux is needed.

In the case studied above, both laser beams interact with the target at the same time. In further studies, one can introduce a temporal delay between the two pulses, which may result not only in a collimation but also in a change of direction of the proton beam due to a possible tilt of the sheath field front at the target rear surface. This may allow for a new method of combined beam collimation and shaping. Exploring the influence of varying the relative intensities of the two pulses is additional options for further studies.

ACKNOWLEDGMENTS

We gratefully thank the Knut and Alice Wallenberg Foundation, including their funding of the PLIONA project, the Swedish Research Council, and the Swedish Foundation for Strategic Research for financial support. We also acknowledge support from EPSRC (Grant No. EP/J003832/1) and Laserlab-Europe/CHARPAC (Grant Agreement No. 284464).

[1]E. L. Clark, K. Krushelnick, J. R. Davies, M. Zepf, M. Tatarakis, F. N. Beg, A. Machacek, P. A. Norreys, M. I. K. Santala, I. Watts, and A. E. Dangor, Phys. Rev. Lett. **84**, 670 (2000).
[2]R. A. Snavely, M. H. Key, S. P. Hatchett, T. E. Cowan, M. Roth, T. W. Phillips, M. A. Stoyer, E. A. Henry, T. C. Sangster, M. S. Singh, S. C. Wilks, A. MacKinnon, A. Offenberger, D. M. Pennington, K. Yasuike, A. B. Langdon, B. F. Lasinski, J. Johnson, M. D. Perry, and E. M. Campbell, Phys. Rev. Lett. **85**, 2945 (2000).
[3]H. Daido, M. Nishiuchi, and A. S. Prizhkov, Rep. Prog. Phys. **75**, 056401 (2012).
[4]M. Passoni, L. Bertagna, and A. Zani, New J. Phys. **12**, 045012 (2010).
[5]S. C. Wilks, A. B. Langdon, T. E. Cowan, M. Roth, M. Singh, S. Hatchett, M. H. Key, D. Pennington, A. MacKinnon, and R. A. Snavely, Phys. Plasmas **8**, 542 (2001).
[6]J. Fuchs, P. Antici, E. d'Humilres, E. Lefebvre, M. Borghesi, E. Brambrink, C. A. Cecchetti, M. Kaluza, V. Malka, M. Manclossi, S. Meyroneinc, P. Mora, J. Schreiber, T. Toncian, H. Pepinm, and P. Audebert, Nat. Phys. **2**, 48 (2006).
[7]J. Fuchs, C. A. Cecchetti, M. Borghesi, T. Grismayer, E. d'Humilres, P. Antici, S. Atzeni, P. Mora, A. Pipahl, L. Romagnani, A. Schiavi, Y. Sentoku, T. Toncian, P. Audebert, and O. Willi, Phys. Rev. Lett. **99**, 015002 (2007).
[8]S. Buffechoux, J. Psikal, M. Nakatsutsumi, L. Romagnani, A. Andreev, K. Zeil, M. Amin, P. Antici, T. Burris-Mog, A. Compant-La-Fontaine, E. d'Humieres, S. Fourmaux, S. Gaillard, F. Gobet, F. Hannachi, S. Kraft, A. Mancic, C. Plaisir, G. Sarri, M. Tarisien, T. Toncian, U. Schramm, M. Tampo, P. Audebert, O. Willi, T. E. Cowan, H. Pépin, V. Tikhonchuk, M. Borghesi, and J. Fuchs, Phys. Rev. Lett. **105**, 015005 (2010).
[9]K. W. D. Ledingham, P. R. Bolton, N. Shikazono, and C. M. C. Ma, Appl. Sci. **4**, 402 (2014).
[10]C. M. Brenner, J. S. Green, A. P. L. Robinson, D. C. Carroll, B. Dromey, P. S. Foster, S. Kar, Y. T. Li, K. Markey, C. Spindloe, M. J. V. Streeter, M. Tolley, C.-G. Wahlström, M. H. Xu, M. Zepf, P. McKenna, and D. Neely, Laser Part. Beams **29**, 345 (2011).
[11]M. H. Xu, Y. T. Li, D. C. Carroll, P. S. Foster, S. Hawkes, S. Kar, F. Liu, K. Markey, P. McKenna, M. J. V. Streeter, C. Spindloe, Z. M. Sheng, C.-G. Wahlström, M. Zepf, J. Zheng, J. Zhang, and D. Neely, Appl. Phys. Lett. **100**, 084101 (2012).
[12]J. S. Green, D. C. Carroll, C. Brenner, B. Dromey, P. S. Foster, S. Kar, Y. T. Li, K. Markey, P. McKenna, D. Neely, A. P. L. Robinson, M. J. V. Streeter, M. Tolley, C.-G. Wahlström, M. H. Xu, and M. Zepf, New J. Phys. **12**, 085012 (2010).
[13]J. Fuchs, T. E. Cowan, P. Audebert, H. Ruhl, L. Gremillet, A. Kemp, M. Allen, A. Blazevic, J.-C. Gauthier, M. Geissel, M. Hegelich, S. Karsch, P. Parks, M. Roth, Y. Sentoku, R. Stephens, and E. M. Campbell, Phys. Rev. Lett. **91**, 255002 (2003).
[14]M. Schollmeier, K. Harres, F. Nürnberg, A. Blazevic, P. Audebert, E. Brambrink, J. C. Fernández, K. A. Flippo, D. C. Gautier, M. Geißel, B. M. Hegelich, J. Schreiber, and M. Roth, Phys. Plasmas **15**, 053101 (2008).
[15]T. E. Cowan, J. Fuchs, H. Ruhl, A. Kemp, P. Audebert, M. Roth, R. Stephens, I. Barton, A. Blazevic, E. Brambrink, J. Cobble, J. Fernández, J.-C. Gauthier, M. Geissel, B. M. Hegelich, J. Kaae, S. Karsch, G. P. Le Sage, S. Letzring, M. Manclossi, S. Meyroneinc, A. Newkirk, H. Pépin, and N. Renard-LeGalloudec, Phys. Rev. Lett. **92**, 204801 (2004).
[16]P. K. Patel, A. J. Mackinnon, M. H. Key, T. E. Cowan, M. E. Foord, M. Allen, D. F. Price, H. Ruhl, P. T. Springer, and R. Stephens, Phys. Rev. Lett. **91**, 125004 (2003).
[17]M. Roth, A. Blazevic, M. Geissel, T. Schlegel, T. E. Cowan, M. Allen, J.-C. Gauthier, P. Audebert, J. Fuchs, J. Meyer-ter-Vehn, B. M. Hegelich,

S. Karsch, and A. Pukhov, Phys. Rev. Spec. Top. - Accel. Beams **5**, 061301 (2002).
[18]C. Brabetz, S. Busold, T. Cowan, O. Deppert, D. Jahn, O. Kester, M. Roth, D. Schumacher, and V. Bagnoud, Phys. Plasmas **22**, 013105 (2015).
[19]B. Aurand, M. Hansson, L. Senje, K. Svensson, A. Persson, D. Neely, O. Lundh, and C.-G. Wahlström, Laser Part. Beams **33**, 59 (2015).
[20]J. S. Green, M. Borghesi, C. M. Brenner, D. C. Carroll, N. P. Dover, P. S. Foster, P. Gallegos, S. Green, D. Kirby, K. J. Kirkby, P. McKenna, M. J. Merchant, Z. Najmudin, C. A. J. Palmer, D. Parker, R. Prasad, K. E. Quinn, P. P. Rajeev, M. P. Read, L. Romagnani, J. Schreiber, M. J. V. Streeter, O. Tresca, C.-G. Wahlström, M. Zepf, and D. Neely, Proc. SPIE **8079**, 807991 (2011).
[21]F. Nürnberg, M. Schollmeier, E. Brambrink, A. Blazevic, D. C. Carroll, K. Flippo, D. C. Gautier, M. Geißel, K. Harres, B. M. Hegelich, O. Lundh, K. Markey, P. McKenna, D. Neely, J. Schreiber, and M. Roth, Rev. Sci. Instrum. **80**, 033301 (2009).
[22]J. Schreiber, S. Ter-Avetisyan, E. Risse, M. P. Kalachnikov, P. V. Nickles, W. Sandner, U. Schramm, D. Habs, J. Witte, and M. Schnürer, Phys. Plasmas **13**, 033111 (2006).
[23]M. N. Quinn, D. C. Carroll, X. H. Yuan, M. Borghesi, R. J. Clarke, R. G. Evans, J. Fuchs, P. Gallegos, L. Lancia, and K. Quinn, Plasma Phys. Controlled Fusion **53**, 124012 (2011).
[24]X. H. Yuan, A. P. L. Robinson, M. N. Quinn, D. C. Carroll, M. Borghesi, R. J. Clarke, R. G. Evans, J. Fuchs, P. Gallegos, L. Lancia, D. Neely, K. Quinn, L. Romagnani, G. Sarri, P. A. Wilson, and P. McKenna, New J. Phys. **12**, 063018 (2010).
[25]T. Grismayer and P. Mora, Phys. Plasmas **13**, 032103 (2006).
[26]S. C. Wilks, W. L. Kruer, M. Tabak, and A. B. Langdon, Phys. Rev. Lett. **69**, 1383 (1992).
[27]P. M. Nilson, W. Theobald, J. Myatt, C. Stoeckl, M. Storm, O. V. Gotchev, J. D. Zuegel, R. Betti, D. D. Meyerhofer, and T. C. Sangster, Phys. Plasmas **15**, 056308 (2008).
[28]P. McKenna, D. C. Carroll, R. J. Clarke, R. G. Evans, K. W. D. Ledingham, F. Lindau, O. Lundh, T. McCanny, D. Neely, A. P. L. Robinson, L. Robson, P. T. Simpson, C.-G. Wahlström, and M. Zepf, Phys. Rev. Lett. **98**, 145001 (2007).
[29]M. V. Ammosov, N. B. Delone, and V. P. Krainov, Sov. Phys. - JETP **64**, 1191 (1986).
[30]O. Lundh, Y. Glinec, C. Homann, F. Lindau, A. Persson, C.-G. Wahlström, D. C. Carroll, and P. McKenna, Appl. Phys. Lett. **92**, 011504 (2008).
[31]O. Jäckel, J. Polz, S. M. Pfotenhauer, H.-P. Schlenvoigt, H. Schwoerer, and M. C. Kaluza, New J. Phys. **12**, 103027 (2010).
[32]J. Schreiber, M. Kaluza, F. Grüner, U. Schramm, B. M. Hegelich, J. Cobble, M. Geissler, E. Brambrink, J. Fuchs, P. Audebert, D. Habs, and K. Witte, Appl. Phys. B **79**, 1041 (2004).
[33]M. Borghesi, A. J. Mackinnon, D. H. Campbell, D. G. Hicks, S. Kar, P. K. Patel, D. Price, L. Romagnani, A. Schiavi, and O. Willi, Phys. Rev. Lett. **92**, 055003 (2004).
[34]F. Watt, M. B. H. Breese, A. A. Bettiol, and J. A. van Kan, Mater. Today **10**(6), 20 (2007).
[35]R. Clarke, S. Dorkings, D. Neely, and I. Musgrave, Proc. SPIE **8779**, 87791C (2013).